



UNIVERSITY OF
BIRMINGHAM

**Hydrogen Storage Properties of Nitrogen- and
Halogen-Containing Materials**

by

Rachel Frances Du Plessis

Supervisor: Dr Paul Anderson

A thesis submitted to The University of Birmingham
for the degree of Doctor of Philosophy

The School of Chemistry
College of Engineering and Physical Sciences
University of Birmingham
September 2016

UNIVERSITY OF
BIRMINGHAM

University of Birmingham Research Archive

e-theses repository

This unpublished thesis/dissertation is copyright of the author and/or third parties. The intellectual property rights of the author or third parties in respect of this work are as defined by The Copyright Designs and Patents Act 1988 or as modified by any successor legislation.

Any use made of information contained in this thesis/dissertation must be in accordance with that legislation and must be properly acknowledged. Further distribution or reproduction in any format is prohibited without the permission of the copyright holder.

Abstract

The Li-Mg-N-H system represents a promising all-round system for a solid-state hydrogen store. Kinetic and thermodynamic improvements are still required to bring the properties of this system to a suitable position. The effect of preparation conditions and the addition of dopant materials into this system were investigated by a variety of experimental techniques. The preparation method of the sample was found to be very important. The choice of initial preparation and desorption conditions can be used to control the phase of $\text{Li}_2\text{Mg}(\text{NH})_2$ formed. Pressurised milling conditions (under 100 bar H_2) appeared to be successful in reducing gas release during milling, but changed the reaction pathway. This was apparent from DSC measurements where an exothermic area was observed around 200°C indicating the crystallisation of $\text{Mg}(\text{NH}_2)_2$ and LiH was occurring preferentially before desorption at these temperatures.

The addition of 0.1 mole fraction of either calcium halide dopant, CaCl_2 or CaBr_2 lowered the peak hydrogen desorption temperature from this system. The addition of these dopants did not appear to improve the hydrogenation properties of the major desorption product, $\text{Li}_2\text{Mg}(\text{NH})_2$. The activation energies of all the doped samples were reduced relative to the undoped samples prepared in the same manner, however the calculated enthalpy of hydrogen desorption was not reduced by the addition of CaCl_2 .

The reactions between MgH_2 and NH_4Cl at various temperatures and stoichiometry's were also investigated using several techniques. Solid-state reactions between these two reagents have not been carried out before. An unknown set of peaks was observed by powder XRD and a new phase, $\text{Mg}(\text{NH}_4)_2\text{Cl}_4$ was identified which was found to be iso-structural with $\text{Mg}(\text{NH}_4)_2\text{F}_4$.

Acknowledgements

I've finally come to the end of my thesis, and no matter what anyone tells you, it's certainly a journey! I would like to thank Paul Anderson, my supervisor, who has guided me throughout the arduous process of research and subsequent analysis and writing up of the work, and who took me on after a 4th year project! I would also like to thank the other members of the group, both past (Phil Chater) and present for your discussions around work and many other topics!

To the members of 5th floor chemistry, thanks for spontaneous hydrogen fuel cell car races around the office floor, and Chemball antics. Thanks also to the Department of Met and Mat, to David Book for equipment use and especially to Dan Reed for all his patience, time and problem solving.

On a personal level, thanks to my husband, Andy, for telling me if he can; I can and saintly tolerance as the submission deadline loomed. Thanks always to my parents for everything; I know mum would have been so proud.

Contents

Contents	i
List of Figures	viii
List of Tables	xxii
Abbreviations	xxvi
1 Introduction.....	1
1.1 The hydrogen economy	1
1.2 Introduction to hydrogen storage	2
1.3 Thermodynamics of hydrogen storage.....	4
1.4 Kinetics of solid-state hydrogen storage.....	6
1.5 Separating thermodynamics and kinetics	8
1.6 Complex light metal hydrides.....	9
1.6.1 Li-N-H systems.....	9
1.6.2 Li-Mg-N-H systems.....	11
1.6.3 Mechanistic pathways of the 2Li-Mg-N-H system.....	19
1.6.4 Improving the Li-Mg-N-H system	21
1.7 Aims.....	26

2	Experimental.....	27
2.1	Solid-state synthesis.....	27
2.1.1	Thermal synthesis under inert gas.....	27
2.1.2	Ball-milling under inert gas.....	27
2.2	Temperature programmed desorption.....	28
2.2.1	TPD-MS	28
2.2.2	Calibration.....	29
2.2.3	TGA-MS	31
2.3	Mass spectrometry.....	32
2.3.1	Ionisation	32
2.3.2	Separation.....	33
2.3.3	Detection.....	33
2.4	Hydrogenation.....	34
2.4.1	Crude hydrogenation.....	34
2.5	Raman spectroscopy	35
2.6	Differential scanning calorimetry	36
2.7	Crystallography ¹	37
2.7.1	Lattice points.....	38
2.7.2	Crystal systems.....	39
2.7.3	Lattice planes and Miller indices.....	40
2.8	Diffraction.....	41

2.8.1	Bragg Equation.....	42
2.8.2	Powder X-ray diffraction ^{112, 113}	43
2.8.3	X-ray generation.....	46
2.8.4	Monochromation.....	47
2.8.5	Detection.....	48
2.8.6	Data collection.....	48
2.8.7	Synchrotron powder X-ray diffraction.....	48
2.9	Rietveld analysis ¹¹⁵⁻¹¹⁷	49
2.10	Quantitative phase analysis	52
3	Effects on the Li–Mg–N–H system of various preparation methods and reaction conditions.....	54
3.1	Introduction	54
3.2	Experimental.....	55
3.3	Comparing TPD–MS and TGA–MS of Li–Mg–N–H samples.....	57
3.3.1	Thermal desorption	57
3.4	Comparing preparation methods of Li–Mg–N–H samples.....	60
3.4.1	Thermal desorption	60
3.4.2	Activation energies.....	75
3.4.3	Differential scanning calorimetry	79

3.4.4	Powder XRD.....	82
3.4.4.1	Hand ground.....	82
3.4.4.2	Ball-milled under 1 bar argon.....	87
3.4.4.3	Ball-milled under 100 bar hydrogen.....	91
3.4.4.4	Cycling experiments.....	95
3.4.5	Raman spectra	103
3.5	Overall discussion	105
3.6	Conclusions.....	111
3.7	Further work.....	113
4	Storage properties of the Li-N-H and Li-Mg-N-H system doped with CaBr ₂ or CaCl ₂	115
4.1	Introduction.....	115
4.2	Experimental.....	117
4.3	Thermal desorption.....	118
4.3.1	TPD-MS	118
4.3.1.1	Li-N-H hand-ground samples.....	118
4.3.1.2	Li-Mg-N-H hand-ground samples	121
4.3.1.3	TPD-MS hand-ground sample summary.....	126
4.3.2	TGA-MS	128
4.3.2.1	Li-Mg-N-H ball-milled samples.....	128

4.3.2.2 TGA-MS ball-milled summary.....	138
4.3.3 Kinetic calculations	143
4.4 Differential scanning calorimetry	147
4.5 Powder XRD	152
4.5.1 Hand-ground.....	152
4.5.2 Ball-milled under 1 bar argon pressure	158
4.5.3 Ball-milled under 100 bar hydrogen	163
4.5.4 Cycling experiments.....	166
4.6 Raman spectroscopy	173
4.7 Overall discussion	174
4.8 Conclusions.....	180
4.9 Further work.....	183

5 Reactions of Magnesium Hydride and Ammonium

Chloride 185

5.1 Introduction	185
5.2 Experimental.....	186
5.3 Reactions of NH_4Cl with MgH_2	187
5.3.1 Powder X-ray diffraction	187
5.3.1.1 <i>Ex-situ</i> under flowing argon	187

5.3.1.1 <i>Ex-situ</i> under flowing ammonia	197
5.4 Investigations across a stoichiometry range	199
5.4.1 Powder X-ray diffraction.....	199
5.5 Reactions of NH_4Cl with 2MgH_2	201
5.5.1 Powder X-ray diffraction.....	201
5.6 Powder XRD summary	203
5.7 Raman spectroscopy	204
5.8 Differential scanning calorimetry	207
5.8.1 Results.....	207
5.8.2 Summary.....	211
5.9 Thermal desorption.....	212
5.9.1 TPD-MS	212
5.9.1.1 $(1-x)\text{NH}_4\text{Cl}$ with $x\text{MgH}_2$	212
5.9.1.2 NH_4Cl with alternative hydrides	216
5.9.1.3 $(1-y)\text{NH}_4\text{Cl}$ with $y\text{LiH}$	216
5.9.1.4 $(1-z)\text{NH}_4\text{Cl}$ with $z\text{KH}$	217
5.9.1.5 $(1-v)\text{NH}_4\text{Cl}$ with $v\text{LiH}$	218
5.9.2 TGA-MS	219
5.9.2.1 $(1-x)\text{NH}_4\text{Cl}$ with $x\text{MgH}_2$	219
5.9.3 Post-desorption powder XRD.....	228
5.9.4 Desorption summary	230

5.10 Rehydrogenation.....	232
5.11 Crystal structure determination.....	233
5.11.1 Indexing.....	234
5.11.2 Producing a model.....	238
5.12 Discussion.....	242
5.13 Conclusions.....	245
5.14 Further work.....	247
6 Summary.....	249
References.....	253
List of Publications.....	260

List of Figures

Figure 1-1: Enlarged Van't Hoff plot of materials, the box shows the materials which satisfy the operating conditions required for PEM fuel-cells. Figure taken from a review by W.I.F David. ²	5
Figure 1-2: Structures of α -Li ₂ Mg(NH) ₂ (1), β -Li ₂ Mg(NH) ₂ (2), Li ₂ NH (3) and LiNH ₂ (4). Nitrogen sites (green), lithium-only sites (blue), magnesium or lithium sites (pink), fixed site vacancies (grey) shown. The nitrogen-cation lattice is indicated. Structural data taken from Rijssenbeek <i>et al.</i> ⁴	15
Figure 2-1: Schematic Diagram of TPD-MS equipment ³	29
Figure 2-2: Schematic diagram of a quadrupole mass analyser ²	33
Figure 2-3: Schematic diagram of Raman and Rayleigh scattering showing the states and transitions involved.	35
Figure 2-4: Generalisation of a 3-D unit cell.	38
Figure 2-5: Unit cells of the five plane lattices ¹	39
Figure 2-6: Examples of the notation of Miller indices ¹¹⁰	41
Figure 2-7: The 2-D geometry used to show the derivation of Braggs law.....	42
Figure 2-8: Diffraction cones of two lattice planes with d-spacing's d ₁ and d ₂ ¹¹⁴	43
Figure 2-9: Schematic X-ray emission spectrum from a copper target showing the relative intensities of K β and K α and the presence of background "bremsstrahlung" white radiation ¹¹³ . .47	
Figure 3-1: TPD-MS trace of the 2LiNH ₂ + MgH ₂ hand-ground control sample heated at 2°C min ⁻¹ , showing gas release against time, H ₂ (red), NH ₃ (green) and temperature (blue).	57
Figure 3-2: TGA-MS trace of the 2LiNH ₂ + MgH ₂ hand-ground control sample, heated at 2°C min ⁻¹ , showing gas release against time, H ₂ (red), NH ₃ (green) and temperature (blue).	58

Figure 3-3: Schematic diagrams showing the gas flow routes around the samples in TGA (1) and TPD (2) set-ups.....	59
Figure 3-4: Mass loss and MS traces of two $2\text{LiNH}_2 + \text{MgH}_2$ samples, (preparation as described), heated at 2°C min^{-1} , showing hydrogen (red) and ammonia (green) release and % mass loss (purple) against temperature.....	61
Figure 3-5: Mass loss and MS traces of the two ball-milled $2\text{LiNH}_2 + \text{MgH}_2$ samples, (preparation as described), heated at 2°C min^{-1} , showing hydrogen release (red) and % mass loss (purple) against temperature.....	62
Figure 3-6: Mass loss and MS trace of $2\text{LiNH}_2 + \text{MgH}_2$ sample ball-milled under 100 bar hydrogen pressure, heated at 2°C min^{-1} , showing hydrogen (red) and ammonia (green) release and % mass loss (purple) against temperature.....	64
Figure 3-7: Powder XRD pattern of two of the prepared $2\text{LiNH}_2 + \text{MgH}_2$ samples, with Rietveld fit showing the difference (grey), calculated (red) and observed (blue, ball-milled under 1 bar argon; and black, ball-milled under 100 bar hydrogen) with the peak positions indicated for LiNH_2 (blue) and MgH_2 (black), MgO (green) and Li_2NH (pink).....	66
Figure 3-8: Raman spectra recorded after milling of two of the prepared $2\text{LiNH}_2 + \text{MgH}_2$ samples, (blue, ball-milled under 1 bar argon; and black ball-milled under 100 bar hydrogen) with key peaks labelled.....	68
Figure 3-9: Powder XRD pattern of synthesised $\text{Mg}(\text{NH}_2)_2$, with Rietveld fit showing the difference (grey), calculated (red) and observed (green) with the peak positions indicated for MgH_2 (blue), MgO (black), and $\text{Mg}(\text{NH}_2)_2$ (green and highlighted).....	69
Figure 3-10: Powder XRD pattern of cycled sample before the desorption experiment, with Rietveld fit showing the difference (grey), calculated (red) and observed (pink) with the peak positions indicated for LiNH_2 (blue), Li_2NH (black), MgH_2 (green), LiH (purple) and $\text{Mg}(\text{NH}_2)_2$ (light green).....	70

Figure 3-11: Mass loss and MS traces of the two ball-milled samples, one made from $\text{Mg}(\text{NH}_2)_2 + 2\text{LiH}$ and the other after 3 cycles of de- and re-hydrogenation, showing hydrogen (red) and ammonia (green) release and % mass loss (purple) against temperature.....71

Figure 3-12: Kissinger's plot showing five samples prepared in different ways (described in text), prepared from 2LiNH_2 and MgH_2 (blue) and from $\text{Mg}(\text{NH}_2)_2$ and 2LiH (orange).....76

Figure 3-13: DSC heating segment of $2\text{LiNH}_2 + \text{MgH}_2$ and $\text{Mg}(\text{NH}_2)_2 + 2\text{LiH}$ samples prepared by previously described methods.81

Figure 3-14: Powder XRD pattern of $2\text{LiNH}_2 + \text{MgH}_2$ sample heated at 275°C for 12 hours, with Rietveld fit showing the difference (grey), calculated (red) and observed (black) traces with the peak positions indicated for LiNH_2 (blue), MgH_2 (black), Li_2O (green), MgO (pink) and $\alpha\text{-Li}_2\text{Mg}(\text{NH})_2$ (purple).....82

Figure 3-15: Powder XRD pattern of $2\text{LiNH}_2 + \text{MgH}_2$ sample heated at 375°C for 12 hours, with Rietveld fit showing the difference (grey), calculated (red) and observed (black) traces with the peak positions indicated for MgH_2 (blue), Li_2O (black), MgO (green), MgO (pink), $\beta\text{-Li}_2\text{Mg}(\text{NH})_2$ (purple), $\text{Li}_{0.48}\text{Mg}_{2.52}\text{N}_{1.84}$ (light green) and LiMgN (brown).....83

Figure 3-16: Powder XRD pattern of $2\text{LiNH}_2 : \text{MgH}_2$ sample ball-milled under 1 bar argon heated at 200°C for 12 hours, with Rietveld fit showing the difference (grey), calculated (red) and observed (purple) traces with the peak positions indicated for Li_2NH (blue), MgO (black), $\beta\text{-Li}_2\text{Mg}(\text{NH})_2$ (green), $\text{Li}_{0.48}\text{Mg}_{2.52}\text{N}_{1.84}$ (pink), and LiMgN (purple).....88

Figure 3-17: Powder XRD pattern of $2\text{LiNH}_2 + \text{MgH}_2$ sample ball-milled under 1 bar argon, heated at 400°C for 12 hours, with Rietveld fit showing the difference (grey), calculated (red) and observed (purple) traces with the peak positions indicated for Li_2O (blue), MgO (black), $\beta\text{-Li}_2\text{Mg}(\text{NH})_2$ (green) and Mg_3N_2 (pink).....89

Figure 3-18: Powder XRD pattern of $2\text{LiNH}_2 + \text{MgH}_2$ sample ball-milled under 100 bar hydrogen, heated at 200°C for 12 hours, with Rietveld fit showing the difference (grey), calculated (red) and observed (black) traces with the peak positions indicated for LiNH_2 (blue),

MgH ₂ (black), Li ₂ O (green), MgO (pink), α-Li ₂ Mg(NH) ₂ (purple), Li ₂ NH (light green) and LiH (brown) and Mg(NH ₂) ₂ (dark blue).....	92
Figure 3-19: Powder XRD pattern of 2LiNH ₂ + MgH ₂ sample ball-milled under 100 bar hydrogen, heated at 350°C for 12 hours, with Rietveld fit showing the difference (grey), calculated (red) and observed (dark blue) traces with the peak positions indicated for MgO (blue), β-Li ₂ Mg(NH) ₂ (black), LiMgN (green), Li _{0.48} Mg _{2.52} N _{1.84} (pink).....	93
Figure 3-20: Powder XRD pattern of 2LiNH ₂ + MgH ₂ sample ball-milled under 100 bar hydrogen, heated at 220°C under flowing argon for 50 hours, with Rietveld fit showing the difference (grey), calculated (red) and observed (black) traces with the peak positions indicated for Li ₂ O (blue), MgO (black), α-Li ₂ Mg(NH) ₂ (green), β-Li ₂ Mg(NH) ₂ (pink) and Li _{0.48} Mg _{2.52} N _{1.84} (purple).....	96
Figure 3-21: Powder XRD pattern of 2LiNH ₂ + MgH ₂ sample ball-milled under 1 bar argon, heated at 220°C under flowing argon for 50 hours, with Rietveld fit showing the difference (grey), calculated (red) and observed (green) traces with the peak positions indicated for Li ₂ O (blue), MgO (black), α-Li ₂ Mg(NH) ₂ (green), β-Li ₂ Mg(NH) ₂ (pink), LiMgN (purple and Li _{0.48} Mg _{2.52} N _{1.84} (light green).....	97
Figure 3-22: Powder XRD pattern of 2LiNH ₂ + MgH ₂ sample ball-milled under 100 bar hydrogen, heated at 220°C under vacuum for 50 hours, with Rietveld fit showing the difference (grey), calculated (red) and observed (green) traces with the peak positions indicated for LiNH ₂ (blue), MgH ₂ (black), Li ₂ O (green), MgO (pink), β-Li ₂ Mg(NH) ₂ (purple), Li ₂ NH (light green), LiH (brown) and Mg(NH ₂) ₂ (dark blue).....	98
Figure 3-23: Powder XRD pattern of 2LiNH ₂ + MgH ₂ sample ball-milled under 1 bar argon, heated at 220°C under vacuum for 50 hours, with Rietveld fit showing the difference (grey), calculated (red) and observed (purple) traces with the peak positions indicated for MgH ₂ (blue), MgO (black), Li ₂ O (green), β-Li ₂ Mg(NH) ₂ (pink), LiH (purple) and Li ₂ NH (light green). ...	99

Figure 3-24: Powder XRD pattern of $2\text{LiNH}_2 + \text{MgH}_2$ sample ball-milled under 100 bar hydrogen, after rehydrogenation at 200°C for 24 hours at 100 bar H_2 of sample shown in Figure 3-20 with Rietveld fit showing the difference (grey), calculated (red) and observed (turquoise) traces with the peak positions indicated for LiNH_2 (blue), MgH_2 (black), Li_2O (green), MgO (pink), LiH (purple), and $\text{Mg}(\text{NH}_2)_2$ (light green)..... 101

Figure 3-25: Powder XRD pattern of $2\text{LiNH}_2 + \text{MgH}_2$ sample ball-milled under 1 bar argon, after rehydrogenation at 200°C for 24 hours at 100 bar H_2 of sample shown in Figure 3-21, with Rietveld fit showing the difference (grey), calculated (red) and observed (blue) traces with the peak positions indicated for LiNH_2 (blue), Li_2NH (black), MgH_2 (green), MgO (pink), Li_2O (purple), LiH (light green) and $\text{Mg}(\text{NH}_2)_2$ (brown)..... 102

Figure 3-26: Raman spectrum of $2\text{LiNH}_2 + \text{MgH}_2$ sample ball-milled under 1 bar argon, heated at 220°C for 50 hours recorded at room temperature. 104

Figure 3-27: Schematic diagram of reaction pathway energy changes when a reaction is under kinetic or thermodynamic control..... 108

Figure 4-1: TPD–MS trace of the control sample ($\text{LiNH}_2 + 2\text{LiH}$) and $\text{LiNH}_2 + 2\text{LiH} + 0.1\text{CaX}_2$, samples heated at 2°C min^{-1} , showing gas release against time, H_2 (red), NH_3 (green) and temperature (blue)..... 119

Figure 4-2: TPD–MS trace of $2\text{LiNH}_2 + \text{MgH}_2 + x\text{CaCl}_2$ samples heated at 2°C min^{-1} , showing gas release against time, H_2 (red), NH_3 (green) and temperature (blue). 122

Figure 4-3: TPD–MS trace of $2\text{LiNH}_2 + \text{MgH}_2 + x\text{CaBr}_2$ samples heated at 2°C min^{-1} , showing gas release against time, H_2 (red), NH_3 (green) and temperature (blue). 124

Figure 4-4: TPD–MS trace of $2\text{LiNH}_2 + \text{MgH}_2 + 0.1\text{Ca}(\text{BH}_4)_2$ sample heated at 2°C min^{-1} , showing gas release against time, H_2 (red), NH_3 (green) and temperature (blue)..... 125

Figure 4-5: PXRD pattern of the $2\text{LiNH}_2 + \text{MgH}_2$ CaCl_2 -doped sample ball-milled under 100 bar hydrogen, when $x = 0.1$ directly after milling with Rietveld fit showing the difference (grey), calculated (red) and observed (green) with the peak positions indicated for LiNH_2 (blue), MgH_2 (black), Li_2NH (green), MgO (pink), and $\text{Ca}(\text{NH}_2)_2$ (purple).129

Figure 4-6: Raman spectra recorder after milling of two $\text{LiNH}_2 + \text{MgH}_2$ CaCl_2 -doped samples when $x = 0.1$ (green, ball-milled under 100 bar hydrogen; and blue ball-milled under 1 bar argon) with key peaks labelled.130

Figure 4-7: Mass loss and mass spectrometry traces of doped samples ball-milled under 1 bar argon (control, $2\text{LiNH}_2 + \text{MgH}_2$ sample for reference) where 0.1 mole fraction of CaCl_2 or CaBr_2 was added, heated at 2°C min^{-1} , showing hydrogen release (red) and % mass loss (purple) against temperature.132

Figure 4-8: Normalised integrated hydrogen mass spectrometry profiles from doped samples ball-milled under 1 bar argon (control, $2\text{LiNH}_2 + \text{MgH}_2$ sample for reference) where 0.1 mole fraction of CaCl_2 or CaBr_2 was added, showing the linear regions of the hydrogen release against temperature.133

Figure 4-9: Mass loss and mass spectrometry traces of doped samples (control - $2\text{LiNH}_2 + \text{MgH}_2$ sample for reference) ball milled under 100 bar hydrogen where 0.1 mole fraction of CaCl_2 or CaBr_2 was added, heated at 2°C min^{-1} , showing hydrogen release (red) and % mass loss (purple) against temperature.134

Figure 4-10: Normalised integrated hydrogen mass spectrometry profiles from doped samples ball-milled under 100 bar hydrogen (control, $2\text{LiNH}_2 + \text{MgH}_2$ sample for reference) where 0.1 mole fraction of CaCl_2 or CaBr_2 was added showing the linear regions of the 1st step of hydrogen release against temperature.135

Figure 4-11: Mass loss and mass spectrometry traces of ball-milled (control, $\text{Mg}(\text{NH}_2)_2 + 2\text{LiH}$ sample for reference) doped sample where 0.1 mole fraction of CaCl_2 was added, heated at 2°C min^{-1} , showing hydrogen release (red) and % mass loss (purple) against temperature.137

Figure 4-12: Normalised integrated hydrogen mass spectrometry profiles from ball-milled (control, $\text{Mg}(\text{NH}_2)_2 + 2\text{LiH}$ sample for reference) doped sample where 0.1 mole fraction of CaCl_2 was added, showing the linear areas of the hydrogen release against temperature..... 138

Figure 4-13: Kissinger's plot showing five samples which were all ball-milled under 1 bar argon, all starting from $2\text{LiNH}_2 + \text{MgH}_2$ (dark blue) including samples doped with various amounts of CaCl_2 or CaBr_2 (as stated). 143

Figure 4-14: Kissinger's plot showing three samples which were all ball-milled under 100 bar H_2 pressure, all starting from $2\text{LiNH}_2 + \text{MgH}_2$ (dark blue) including samples doped with 0.1 mole fraction of CaCl_2 or CaBr_2 (as stated)..... 144

Figure 4-15: Kissinger's plot showing two samples which were all ball-milled under atmospheric argon pressure, starting from $\text{Mg}(\text{NH}_2)_2 + 2\text{LiH}$ (dark blue) including a sample doped with 0.1 mole fraction CaCl_2 146

Figure 4-16: DSC heating segment of control ($2\text{LiNH}_2 + \text{MgH}_2$ ball-milled under 1 bar argon) and 0.1 mole fraction CaCl_2 doped sample. 147

Figure 4-17: DSC heating segment of control ($2\text{LiNH}_2 + \text{MgH}_2$ ball-milled under 100 bar hydrogen) and 0.1 mole fraction CaCl_2 doped sample..... 148

Figure 4-18: DSC heating segment of control ($\text{Mg}(\text{NH}_2)_2 + 2\text{LiH}$ ball-milled) and 0.1 mole fraction CaCl_2 -doped sample. 149

Figure 4-19: Powder XRD pattern of 0.1 mole fraction CaCl_2 -doped ($2\text{LiNH}_2 + \text{MgH}_2$) hand-ground sample heated at 200°C for 12 hours, with Rietveld fit showing the difference (grey), calculated (red) and observed (purple) traces with the peak positions indicated for LiNH_2 (blue), MgH_2 (black), Li_2O (green), Mg (pink), CaCl_2 (purple) and CaNH (light green)..... 153

Figure 4-20: Powder XRD pattern of 0.1 mole fraction CaCl_2 -doped ($2\text{LiNH}_2 + \text{MgH}_2$) sample heated at 275°C for 12 hours, with Rietveld fit showing the difference (grey), calculated (red) and observed (green) traces with the peak positions indicated for LiNH_2 (blue), MgH_2 (black), Li_2O (green), Mg (pink), CaCl_2 (purple) and CaNH (light green). 154

Figure 4-21: Powder XRD pattern of 0.1 mole fraction CaCl_2 -doped ($2\text{LiNH}_2 + \text{MgH}_2$) hand-ground sample heated at 350°C for 12 hours, with Rietveld fit showing the difference (grey), calculated (red) and observed (green) traces with the peak positions indicated for MgH_2 (blue), Li_2O (black), MgO (green), $\alpha\text{-Li}_2\text{Mg}(\text{NH})_2$ (pink), $\beta\text{-Li}_2\text{Mg}(\text{NH})_2$ (purple), CaNH (light green), Mg_3N_2 (brown), LiMgN (dark blue) and $\text{Li}_{0.48}\text{Mg}_{2.52}\text{N}_{1.84}$ (brown-green).155

Figure 4-22: Powder XRD pattern of 0.1 mole fraction CaCl_2 -doped sample ($2\text{LiNH}_2 + \text{MgH}_2$) ball-milled under 1 bar argon heated at 200°C for 12 hours, with Rietveld fit showing the difference (grey), calculated (red) and observed (black) traces with the peak positions indicated for Li_2NH (blue), MgO (black), $\beta\text{-Li}_2\text{Mg}(\text{NH})_2$ (green), CaH_2 (pink) and CaNH (purple).158

Figure 4-23: Powder XRD pattern of CaCl_2 -doped sample ($2\text{LiNH}_2 + \text{MgH}_2$) ball-milled under 1 bar argon, heated at 400°C for 12 hours, with Rietveld fit showing the difference (grey), calculated (red) and observed (dark blue) traces with the peak positions indicated for Li_2O (blue), MgO (black), $\beta\text{-Li}_2\text{Mg}(\text{NH})_2$ (green) and CaNH (pink). Unfitted peaks indicated.....159

Figure 4-24: Powder XRD pattern of CaCl_2 -doped sample ($2\text{LiNH}_2 + \text{MgH}_2$) ball-milled under 1 bar argon, heated at 400°C for 12 hours, with Rietveld fit showing the difference (grey), calculated (red) and observed (dark blue) traces with the peak positions indicated for Li_2O (blue), MgO (black), $\beta\text{-Li}_2\text{Mg}(\text{NH})_2$ (green), CaO (pink) and Pawley fit with peak positions indicated for unknown F222 phase (blue and highlighted).....161

Figure 4-25: Powder XRD pattern of CaCl_2 -doped ($2\text{LiNH}_2 + \text{MgH}_2$) sample ball-milled under 100 bar hydrogen, heated at 250°C for 12 hours, with Rietveld fit showing the difference (grey), calculated (red) and observed (dark blue) traces with the peak positions indicated of Li_2O (blue), MgO (black), $\alpha\text{-Li}_2\text{Mg}(\text{NH})_2$ (green), $\beta\text{-Li}_2\text{Mg}(\text{NH})_2$ (pink), CaNH (purple), CaO (green) and Li_2MgCl_4 (brown) and Pawley fit with peak positions indicated for unknown F222 phase (blue).163

Figure 4-26: Powder XRD pattern of CaCl₂-doped sample (2LiNH₂ + MgH₂) ball-milled under 100 bar hydrogen, heated at 400°C for 12 hours, with Rietveld fit showing the difference (grey), calculated (red) and observed (blue) traces with the peak positions indicated of Li₂O (blue), MgO (black), β-Li₂Mg(NH)₂ (green), CaNH (pink) CaO (purple), Li_{0.48}Mg_{2.52}N_{1.84} (light green) and Pawley fit with peak positions indicated for unknown F222 phase (blue). 165

Figure 4-27: Powder XRD pattern CaCl₂-doped sample (2LiNH₂ + MgH₂) ball-milled under 1 bar argon, heated at 220°C under flowing argon for 50 hours, with Rietveld fit showing the difference (grey), calculated (red) and observed (purple) traces with the peak positions indicated for α-Li₂Mg(NH)₂ (blue), β-Li₂Mg(NH)₂ (black) and MgO (green), CaO (pink) and CaNH (purple) and Pawley fit with peak positions indicated for unknown F222 phase (blue). 166

Figure 4-28: Comparison of powder XRD patterns of CaCl₂-doped samples (2LiNH₂ + MgH₂) ball milled under 1 bar argon (blue) and 100 bar hydrogen (purple). 167

Figure 4-29: Powder XRD pattern of CaBr₂-doped sample (2LiNH₂ + MgH₂) ball-milled under 100 bar hydrogen, heated at 220°C under flowing argon for 50 hours, with Rietveld fits showing the difference (grey), calculated (red) and observed (blue) traces with the peak positions indicated for α-Li₂Mg(NH)₂ (blue), β-Li₂Mg(NH)₂ (black) and MgO (green), CaO (pink) and Pawley fits with peak positions indicated for Li₇(NH₂)₆Br (blue and highlighted) and unknown F222 phase (black). 168

Figure 4-30: Typical Raman spectra of CaCl₂- and CaBr₂-doped (2LiNH₂ + MgH₂) ball-milled samples heated at 220°C under flowing argon for 50 hours. 169

Figure 4-31: Powder XRD pattern of CaCl₂-doped sample (2LiNH₂ + MgH₂) ball-milled under 1 bar argon after rehydrogenation at 200°C for 24 hours at 100 bar H₂ of sample in Figure 4-28 with Rietveld fits showing the difference (grey), calculated (red) and observed (blue) traces with the peak positions indicated for Li₂NH (blue), MgO (black), Li₂O (green), α-Li₂Mg(NH)₂ (pink), β-Li₂Mg(NH)₂ (purple), CaNH (light green), Mg(NH₂)₂ (brown) and Pawley fits with peak positions indicated for unknown F222 phase (blue). 170

Figure 4-32: Powder XRD pattern of CaBr₂-doped sample (2LiNH₂ + MgH₂) ball-milled under 100 bar hydrogen after rehydrogenation at 200°C for 24 hours at 100 bar H₂ of sample in Figure 4-28 with Rietveld fits showing the difference (grey), calculated (red) and observed (green) traces with the peak positions indicated for LiNH₂ (blue), MgH₂ (black), Mg(NH₂)₂ (green), Li₂O (pink), MgO (purple), β-Li₂Mg(NH)₂ (light green), CaNH (brown) and Pawley fits with peak positions indicated for Li₇(NH₂)₆Br (blue) and unknown F222 phase (black).....171

Figure 4-33: Typical Raman spectra of CaCl₂- and CaBr₂-doped (2LiNH₂ + MgH₂) ball-milled samples after rehydrogenation at 200°C under 100 bar H₂ for 24 hours.....172

Figure 4-34: Illustration of how the thermodynamics can be changed by the formation of alternative intermediates.....175

Figure 5-1: Powder XRD pattern of NH₄Cl + MgH₂ sample after heating at 175°C for 12 hours, with Rietveld fit showing the difference (grey), calculated (red) and observed (purple) traces with the peak positions indicated for MgH₂ (blue) and NH₄Cl (black).....188

Figure 5-2: Stacked PXRD powder XRD traces of NH₄Cl + MgH₂ samples heated for 12 hours at 175°C (red), 185°C (green) and 195°C (blue) with the appearance of new small peaks indicated (starred) with peak positions indicated for MgH₂ (blue) and NH₄Cl (black).....189

Figure 5-3: Powder XRD pattern of NH₄Cl + MgH₂ sample heated at 215°C for 12 hours, with Rietveld fit showing the difference (grey), calculated (red) and observed (blue) traces with the peak positions indicated for MgH₂ (blue), NH₄Cl (black) and Mg(NH₃)₂Cl₂ (green highlighted trace).....189

Figure 5-4: Powder XRD pattern of NH₄Cl + MgH₂ sample heated at 225°C for 12 hours showing the observed (black) trace with the peak positions indicated for MgH₂ (blue) and MgO (black).....191

Figure 5-5: Stacked powder XRD plot of NH₄Cl + MgH₂ samples heated for 12 hours at 225°C (green) 250°C (red) and 275°C (blue), 300°C (black), 325°C (pink) and 350°C (burgundy).....192

Figure 5-6: Stacked powder XRD plot of $\text{NH}_4\text{Cl} + \text{MgH}_2$ samples heated for 72 hours at 185°C (red), 200°C (black) and 215°C (blue) with the peak positions indicated for MgH_2 (blue) and MgO (black).....	193
Figure 5-7: Powder XRD pattern of $\text{NH}_4\text{Cl} + \text{MgH}_2$ sample heated at 300°C for 12 hours under flowing ammonia gas with Rietveld fit showing the difference (grey), calculated (red) and observed (blue) traces with the peak positions indicated for NH_4Cl (blue), $\text{Mg}(\text{NH}_3)_2\text{Cl}_2$ (black) and $\text{Mg}(\text{NH}_3)_6\text{Cl}_2$ (green and highlighted).....	196
Figure 5-8: Powder XRD pattern of $\text{NH}_4\text{Cl} + \text{MgH}_2$ sample heated at 300°C for 12 hours under flowing ammonia gas with Rietveld fit showing the difference (grey), calculated (red) and observed (purple) traces with the peak positions indicated for NH_4Cl (blue), $\text{Mg}(\text{NH}_3)_2\text{Cl}_2$ (black) and $\text{Mg}(\text{NH}_3)_6\text{Cl}_2$ (green and highlighted).....	197
Figure 5-9: Powder XRD pattern of the sample where $x = 0.5$, heated at 200°C for 12 hours, with Rietveld fit showing the difference (grey), calculated (red) and observed (black) traces with the peak positions indicated for MgH_2 (blue), NH_4Cl (black).....	198
Figure 5-10: Comparison of the resulting mol% of $\text{MgH}_2 + \text{NH}_4\text{Cl}$ after heating at 200°C for 12 hours against starting mol% of MgH_2	199
Figure 5-11: Powder XRD pattern of sample when $x = 0.66$ was heated at 200°C for 12 hours, with Rietveld fit showing the difference (grey), calculated (red) and observed (green) traces with the peak positions indicated for MgH_2 (blue).....	200
Figure 5-12: Stacked PXRD powder XRD plot of $\text{NH}_4\text{Cl} + 2\text{MgH}_2$ samples heated for 12 hours at 215°C (green), 225°C (pink), 250°C (burgundy) and 275°C (orange) and the expanded section (A) also includes the sample heated at 200°C (blue) for 12 hours.....	201
Figure 5-13: Powder XRD plots of $\text{NH}_4\text{Cl} + 2\text{MgH}_2$ samples heated for 12 hours at 275°C (orange) and 300°C (blue) for 12 hours.....	202
Figure 5-14: Raman spectrum of $\text{NH}_4\text{Cl} + \text{MgH}_2$ heated under flowing argon for 12 hours at 325°C.....	206

Figure 5-15: DSC heating segment of $(1-x)\text{NH}_4\text{Cl} + x\text{MgH}_2$ when $x = 0.33, 0.42, 0.50, 0.58$ and 0.66	208
Figure 5-16: DSC cooling segment of $(1-x)\text{NH}_4\text{Cl} + x\text{MgH}_2$ when $x = 0.33, 0.42, 0.50, 0.58$ and 0.66	209
Figure 5-17: Close-up view of the exothermic peak that occurred during the heating segment of the DSC experiments.	210
Figure 5-18: TPD-MS trace of $(1-x)\text{NH}_4\text{Cl} + x\text{MgH}_2$ sample heated at 2°C min^{-1} where $x = 0.50$, showing gas release against time, H_2 (red), NH_3 (green) and temperature (blue).	213
Figure 5-19: TPD-MS trace of $(1-x)\text{NH}_4\text{Cl} + x\text{MgH}_2$ samples heated at 2°C min^{-1} where $x = 0.58$ and 0.66 , showing gas release against time, H_2 (red), NH_3 (green) and temperature (blue).	214
Figure 5-20: TPD-MS trace of $(1-x)\text{NH}_4\text{Cl} + x\text{MgH}_2$ samples heated at 2°C min^{-1} where $x = 0.33$ and 0.42 , showing gas release against time, H_2 (red), NH_3 (green) and temperature (blue).	215
Figure 5-21: TPD-MS trace of $(1-y)\text{NH}_4\text{Cl} + y\text{LiH}$ sample heated at 2°C min^{-1} where $y = 0.66$ showing gas release against time, H_2 (red), NH_3 (green) and temperature (blue).	217
Figure 5-22: TPD-MS trace of $(1-z)\text{NH}_4\text{Cl} + z\text{KH}$ sample heated at 2°C min^{-1} where $z = 0.66$ showing gas release against time, H_2 (red), NH_3 (green) and temperature (blue).	218
Figure 5-23: TPD-MS trace of $(1-v)\text{NH}_4\text{Cl} + v\text{CaH}_2$ sample heated at 2°C min^{-1} where $v = 0.50$ showing gas release against time, H_2 (red), NH_3 (green) and temperature (blue).	219
Figure 5-24: TGA mass loss profiles of $(1-x)\text{NH}_4\text{Cl} + x\text{MgH}_2$ samples heated at 2°C min^{-1} where $x = 0.33$ (black), 0.42 (purple), 0.5 (blue), 0.58 (red) and 0.66 (pink).	222
Figure 5-25: MS traces from TGA experiments of $(1-x)\text{NH}_4\text{Cl} + x\text{MgH}_2$ samples heated at heated at 2°C min^{-1} where $x = 0.66$ (pink), $x = 0.58$ (red), $x = 0.50$ (purple), $x = 0.42$ (blue), $x = 0.33$ (black) showing gas release against time, H_2 (solid lines), NH_3 (dashed) and temperature (orange).	223

Figure 5-26: Calculated hydrogen mass loss profiles derived from mass spectrometry data of $(1-x)\text{NH}_4\text{Cl} + x\text{MgH}_2$ samples where, $x = 0.42$ (purple), 0.5 (blue), 0.58 (red) and 0.66 (pink).. 227

Figure 5-27: Post TGA–MS powder XRD pattern of $(1-x)\text{NH}_4\text{Cl} + x\text{MgH}_2$ sample where $x = 0.42$ and the sample was heated to 400°C. Rietveld fit showing the difference (grey), calculated (red) and observed (green) traces with peak positions indicated for NH_4Cl (blue) and MgCl_2 (black)..... 228

Figure 5-28: Post TPD–MS powder XRD pattern of $\text{NH}_4\text{Cl} + 2\text{LiH}$ sample. Rietveld fit showing the difference (grey), calculated (red) and observed (blue) traces with peak positions indicated for LiCl (blue), NH_4Cl (black) and LiH (green). 229

Figure 5-29: Post rehydrogenation powder XRD pattern of $\text{NH}_4\text{Cl} + \text{MgH}_2$ sample heated to 200 °C and held for 24 hours under 100 bar H_2 . Rietveld fit showing the difference (grey), calculated (red) and observed (teal) traces with peak positions indicated for MgH_2 (blue). Inset: powder XRD pattern recorded before rehydrogenation. 232

Figure 5-30: Pre- (pink) and post- (black) rehydrogenation powder XRD patterns of an $\text{NH}_4\text{Cl} + \text{MgH}_2$ sample heated to 200°C and held for 24 hours under 100 bar H_2 233

Figure 5-31: Synchrotron powder XRD pattern of $\text{NH}_4\text{Cl} + \text{MgH}_2$ sample heated at 200°C for 12 hours with a combination of Rietveld and Pawley fits showing the difference (grey), calculated (red) and observed (black) traces with peak positions indicated for MgH_2 (blue), NH_4Cl (black) and the unknown tetragonal phase-space group $I4$ (blue and highlighted). 236

Figure 5-32: Synchrotron powder XRD pattern of $\text{NH}_4\text{Cl} + \text{MgH}_2$ sample heated at 200°C for 12 hours with a combination of Rietveld and Pawley fits showing the difference (grey), calculated (red) and observed (black) traces with peak positions indicated for MgH_2 (blue), NH_4Cl (black) and peak positions that would correspond to possible body-centred space groups for the unknown tetragonal phase with $I4$ (highlighted and blue)..... 237

Figure 5-33: Structure for $\text{Mg}(\text{NH}_4)_2\text{Cl}_4$ from atomic positions shown in Table 5-10 showing Cl, Mg and N positions in green, yellow and blue respectively..... 240

Figure 5-34: Synchrotron powder XRD pattern of $\text{NH}_4\text{Cl} + \text{MgH}_2$ sample heated at 200°C for 12 hours with Rietveld fit showing the difference (grey), calculated (red) and observed (black) traces with peak positions indicated for indicated for MgH_2 (blue), NH_4Cl (black) and $\text{Mg}(\text{NH}_4)_2\text{Cl}_4$ (highlighted and green).....241

List of Tables

Table 2-1: Crystal systems and Bravais Lattices.....	40
Table 2-2: Summary of key factors in a powder diffraction pattern and their main influences. ...	44
Table 2-3: Commonly simultaneously refinable parameters.....	50
Table 3-1: Summary of the key features from the mass spectrometry and mass losses of the samples tested to show the effects of preparation on the samples in this section.	72
Table 3-2: Estimated values of activation energies for various samples.....	77
Table 3-3: Estimated values of activation energies reported in the literature.....	79
Table 3-4: Peak temperatures and areas underneath the two main peaks from DSC data.....	80
Table 3-5: Estimated wt% by quantitative phase analysis of two phases of $\text{Li}_2\text{Mg}(\text{NH})_2$ and all nitride phases prepared from $2\text{LiNH}_2 + \text{MgH}_2$ hand ground samples.....	85
Table 3-6: Estimated wt% by quantitative phase analysis of two phases of $\text{Li}_2\text{Mg}(\text{NH})_2$ and all nitride phases prepared from $2\text{LiNH}_2 + \text{MgH}_2$ samples ball-milled under 1 bar argon.....	90
Table 3-7: Estimated wt% by quantitative phase analysis of two phases of $\text{Li}_2\text{Mg}(\text{NH})_2$ and all nitride phases prepared from $2\text{LiNH}_2 + \text{MgH}_2$ samples ball-milled under 100 bar H_2 pressure. ..	94
Table 3-8: Estimated wt% by quantitative phase analysis of two phases of $\text{Li}_2\text{Mg}(\text{NH})_2$ and nitride phases prepared from ball-milled $2\text{LiNH}_2 + \text{MgH}_2$ samples after thermal reaction at 220°C for 50 hours.....	100
Table 3-9: Summary of the effects of different conditions applied during ball milling.	106
Table 4-1: Hydrogen peak temperatures for different types of calcium dopant added to the $\text{LiNH}_2 + 2\text{LiH}$ system at mole ratio of $x = 0.1$	120

Table 4-2: Comparison of the desorption temperatures and notable features, where Li represents the Li-N-H and Li-Mg represents the Li-Mg-N-H systems.....	126
Table 4-3: Comparison of dopant content and type to the theoretical gravimetric H ₂ capacity and the measured peak desorption temperatures of the corresponding sample.....	127
Table 4-4: Comparison of the hydrogen desorption temperatures of the doped samples ball-milled under 1 bar argon and 100 bar hydrogen.	139
Table 4-5: Comparison of the gradients of the linear areas (peaks observed in the mass spectrometry traces) of integrated hydrogen release.....	139
Table 4-6: Comparison of the temperatures at which 80% of the respective hydrogen amounts (mass spec) were released from the samples.....	140
Table 4-7: Comparison of the mass loss (wt%) from samples at the respective temperatures (taken from Table 4-6) when 80% of hydrogen had been released from the samples.	141
Table 4-8: Comparison of gravimetric hydrogen capacities and the approximate mass losses recorded by TGA-MS experiments after the 1 st hydrogen desorption.....	142
Table 4-9: Estimated values of activation energies (error ± 6 kJ mol ⁻¹) for various samples where the control was 2LiNH ₂ + MgH ₂	145
Table 4-10: Estimated values of activation energies for two samples where the control was Mg(NH ₂) ₂ and 2LiH.	146
Table 4-11: Peak temperatures and areas underneath the largest low temperature peak from DSC data for several samples (estimated error was calculated to be 0.4 kJ mol ⁻¹).	150
Table 4-12: Estimated wt% by quantitative phase analysis of two phases of Li ₂ Mg(NH) ₂ and all nitride phases prepared from 0.1 mole fraction CaCl ₂ -doped 2LiNH ₂ + MgH ₂ hand-ground samples.	157
Table 4-13: Top indexing results from Topas, all to space group F222 (no. 22)	160

Table 4-14: Estimated wt% by quantitative phase analysis of two phases of $\text{Li}_2\text{Mg}(\text{NH})_2$ and nitride phases prepared from 0.1 mole fraction CaCl_2 -doped $2\text{LiNH}_2 + \text{MgH}_2$ samples ball-milled under 1 bar argon.	162
Table 4-15: Estimated wt% by quantitative phase analysis of two phases of $\text{Li}_2\text{Mg}(\text{NH})_2$ and nitride phases prepared from 0.1 mole fraction CaCl_2 -doped $2\text{LiNH}_2 + \text{MgH}_2$ samples ball-milled under 100 bar hydrogen.	166
Table 4-16: List of Raman/FTIR stretches from several amide and imide phases that might be expected to be identified in this work.	173
Table 5-1: Comparison of the lattice parameters from solid state experiments which have produced $\text{Mg}(\text{NH}_3)_2\text{Cl}_2$ to literature values from Leineweber et al. ¹¹	190
Table 5-2: Selection of peaks and top 3 (where relevant) indexing solutions for each set of peaks from Topas.....	195
Table 5-3: Preliminary Raman data recorded of $\text{NH}_4\text{Cl} + \text{MgH}_2$ samples.....	205
Table 5-4: Peak temperatures and areas (in Joules per gram of starting materials) of the exothermic peak highlighted in.....	210
Table 5-5: Comparison of theoretical wt% mass loss corresponding to one mole of ammonia and hydrogen when the amount of MgH_2 was varied.....	225
Table 5-6: Comparison of the calculated mass loss in moles attributed to ammonia and hydrogen.....	225
Table 5-7: Top indexing results from Topas ²⁷	235
Table 5-8: Variation in lattice parameters and unit cell volume for the unknown tetragonal phase using space group I4 observed from Pawley refinement of laboratory powder XRD data after heating $(1-x)\text{NH}_4\text{Cl} + x\text{MgH}_2$ samples when $x = 0.5$ for 12 hours.	238
Table 5-9: Comparison of formula unit volumes of associated phases in this work.....	239

Table 5-10: Refined crystallographic data for $\text{Mg}(\text{NH}_4)_2\text{Cl}_4$240

List of Abbreviations

Abbreviation	Description
DSC	Differential scanning calorimetry
ICE	Internal combustion engine
PCT	Pressure-composition-temperature (isotherm)
PEM	Polymer electrolyte membrane (fuel cell)
QPA	Quantitative phase analysis
TGA	Thermogravimetric analysis
TPD	Temperature programmed desorption
XRD	X-ray diffraction

1 Introduction

1.1 The hydrogen economy

The term 'Hydrogen Economy' was devised by John Bockris⁵ and refers to the effective integration of multiple systems required to deliver energy with hydrogen as the carrier. The requirements for a long term global plan to ensure varied, renewable, green energy sources that can replace the unsustainable use of non-renewable fossil fuels have been well documented^{2, 6-8}. The main drivers can be grouped into three areas, environmental effects (*e.g.* global warming and air quality), rising demand for energy which coupled with dwindling fossil fuel supplies leads to an increasing cost^{9, 10}. Although new fossil-fuel energy reserves are being discovered, ultimately a transition to renewable energy must be pursued.

In order for hydrogen to fulfil this demand, even partially, a number of different challenges are introduced compared with fossil fuels. These can be roughly grouped into three categories; production, storage and distribution, and finally the use of hydrogen. For a successful hydrogen economy to become a reality, the development of viable, zero-emission 'green' methods of hydrogen production along with a suitable delivery and distribution infrastructure are required. Additionally, appropriate storage methods, both on-board and stationary must be addressed whilst considering the safety issues surrounding the operational use of hydrogen, in particular for mobile applications.

A successful hydrogen production industry does already exist, but mainly *via* non-renewable methods such as steam methane reforming for generating hydrogen as a commercial chemical used in hydrocarbon cracking and the Haber process. Several routes exist to produce green hydrogen, using renewable energy sources such as solar, hydro-electric or wind to power electrolysis, or solar conversion through thermolysis or photolysis. An alternative option is biomass conversion; this represents a renewable source of hydrogen in the form of hydrocarbons, rather than just using sustainably generated energy to drive hydrogen production.

A distribution infrastructure to provide hydrogen as a fuel for widespread transport applications would require significant investment in pipelines, fuelling stations and transport methods. However, it should not be forgotten that for hydrogen-based transport systems, hydrogen-fuelled vehicles also need to be mass produced. Principal uses of hydrogen as a fuel are in internal combustion engines (ICEs) or fuel cells. Although ICEs are a well-developed technology for petroleum, their use with hydrogen has been limited to a few prototype vehicles, generally using ICEs built to run on both hydrogen and petrol¹¹. However, supplying and using liquid hydrogen carries a huge associated energy cost which limits the viability of this technology.

The main method of utilising hydrogen, and where much research has focused, is on powering fuel cells; cost, performance and durability are key drivers for improving fuel cells. Polymer electrolyte membrane (PEM) fuel cells are typically used with hydrogen, and they can provide power for a wide range of applications, both stationary and mobile. Currently, California is leading the global market for fuel cell electric vehicles and hydrogen fuelling stations¹². The state will have 51 stations by the end of 2016, giving approximate capacity for 13,500 hydrogen powered fuel cell vehicles^{13, 14}.

The production, distribution infrastructure and use of hydrogen have been discussed briefly above, and as such the remainder of this thesis will focus on the development of hydrogen storage methods.

1.2 Introduction to hydrogen storage

The methods for hydrogen storage can be roughly separated into two areas, physical- or containment- based, where elemental hydrogen is stored, and material- based, where hydrogen is incorporated into a chemical material. The first category consists of compression or liquefaction of hydrogen or a combination of the two, while the later includes adsorbents, interstitial and complex hydrides, organics and chemical hydrogen stores. Each existing and newly suggested storage method will have its own advantages and drawbacks, a balance of desirable properties for

various functions must be met in order to develop a range of suitable hydrogen stores. These properties include gravimetric and volumetric capacities, kinetics and thermodynamics of hydrogen de- and re-hydrogenation and the cyclic stability as well as safety and cost.

Many advances in the platforms available for hydrogen storage have been made in recent years, from compressed hydrogen storage in carbon-fibre reinforced tanks¹⁵ to physisorption in metal-organic frameworks¹⁶. More widespread research into novel materials for storage is leading to the development of viable options for real-life applications such as hydrogen fuel cell cars. Interest in light metal complex hydrides was sparked in 1997 when it was reported that Ti doped NaAlH_4 exhibited reversible hydrogen sorption¹⁷. Due to the favourably high gravimetric content of hydrogen that can be accessed in these compounds compared to metallic hydrides like LaNi_5H_6 ¹⁸, interest in solid-state materials has, in recent years focused on how to improve the hydrogen storage properties of light metal hydrides. The emphasis of the work in this thesis will be on furthering the understanding of hydrogen storage within complex light metal hydrides.

In light of these capacity considerations, compounds containing boron, nitrogen and hydrogen, such as borohydrides $[\text{BH}_4^-]$ and amides $[\text{NH}_2^-]$ have received a large amount of attention due to the formation of hydrogen rich anion groups¹⁹. Many simple systems such as lithium amide²⁰, lithium borohydride²¹ and ammonia borane²² have extremely high gravimetric contents (19.6 wt% H_2 in ammonia borane²²). Due to kinetic limitations, high temperature hydrogen desorption due to poor thermodynamics, product reversibility and ammonia evolution in addition to hydrogen, modifications are necessary in order to synthesise an optimized solid-state hydrogen storage system.

The properties of these systems can be altered to accelerate (de)hydrogenation, lower desorption/absorption temperatures, reduce ammonia production and increase hydrogen plateau pressures. For on-board storage, both the volumetric and gravimetric capacities of a potential material must be maximised as well as the operational safety of such a system^{2,23}.

1.3 Thermodynamics of hydrogen storage

The reversibility of a system for hydrogen storage is paramount. If there is no way of recharging hydrogen to a medium, then it is useless as a hydrogen store. For a system to possess facile reversible hydrogenation, the change in Gibbs free energy must be close to equilibrium i.e. $\Delta G_{dec}^{\circ} = 0$ or lower. This can be achieved by varying pressure or temperature during the reaction according to Equation 1-1 so that the entropy change (ΔS_{dec}°) is larger than the enthalpy contribution (ΔH_{dec}°). The Gibbs free energy of a reaction may also be described by equilibrium hydrogen pressure, p_{eq} (also known as plateau pressure).

$$\Delta G_{dec}^{\circ} = \Delta H_{dec}^{\circ} - T\Delta S_{dec}^{\circ} = RT \ln \left[\frac{p_{eq}}{p_0} \right] \quad \text{Equation 1-1}$$

For solid-state materials, such as metal hydrides, the simplest decomposition reaction is given in Equation 1-2.



Hence, the standard entropy of the reaction, $[\Delta S_{dec}^{\circ}]$ is due mainly to the formation of the gaseous hydrogen diatom $[S^{\circ}(H_2)]$ from a solid, and is given as $130 \text{ J K}^{-1} \text{ mol}^{-1}$ ²⁴ at 1 bar and 298 K. However, the entropy of hydrogen formation is dependent on pressure and/or temperature so this value is liable to vary^{24,2}. For a storage medium to be theoretically reversible at atmospheric pressure and 298 K, the calculated enthalpy of hydrogen release, i.e. the formation of a H_2 molecule which is equal to ΔH_{dec}° of the equation is shown in Equation 1-3.

$$\Delta H_{dec}^{\circ} = T\Delta S_{dec}^{\circ} = 298 \text{ K} \times 130 \text{ J K}^{-1} \text{ mol}^{-1} = 38.74 \text{ kJ mol}^{-1} \quad \text{Equation 1-3}$$

The enthalpy of desorption is a useful target in order to assess the reversibility of a sample but should not be considered as sacrosanct. By varying the conditions and hence the equilibrium position within a system the accessibility of the material for hydrogen storage purposes can be changed. The thermal decomposition temperature T_{dec} can also be found when ΔG_{dec}° drops below

zero, i.e. it is thermodynamically favourable the reaction to proceed above the decomposition temperature.

Often the Van't Hoff Equation is used to plot graphs; the slope gives an indication of the enthalpy change associated with a specific material. The y-intercept gives ΔS_{dec}° for a specific reaction. Re-arranging Equation 1-1 gives the Van't Hoff Equation (Equation 1-4).

$$\ln \left[\frac{p_{eq}}{p_0} \right] = \Delta H_{dec}^{\circ} / RT - \Delta S_{dec}^{\circ} / R \quad \text{Equation 1-4: Van't Hoff Equation}$$

Figure 1-1 shows a Van't Hoff plot, calculated from pressure-composition-temperature isotherms (PCT isotherms). The boxed area shows suitable materials for use in PEM cells are limited per the ideal usage conditions required, temperatures between 100°C and 250°C and hydrogen pressures of between 1 bar and 750 bar. Thermodynamics determine whether it is favourable for a reaction to proceed. For optimised performance of a hydrogen storage material, the kinetics are also important.

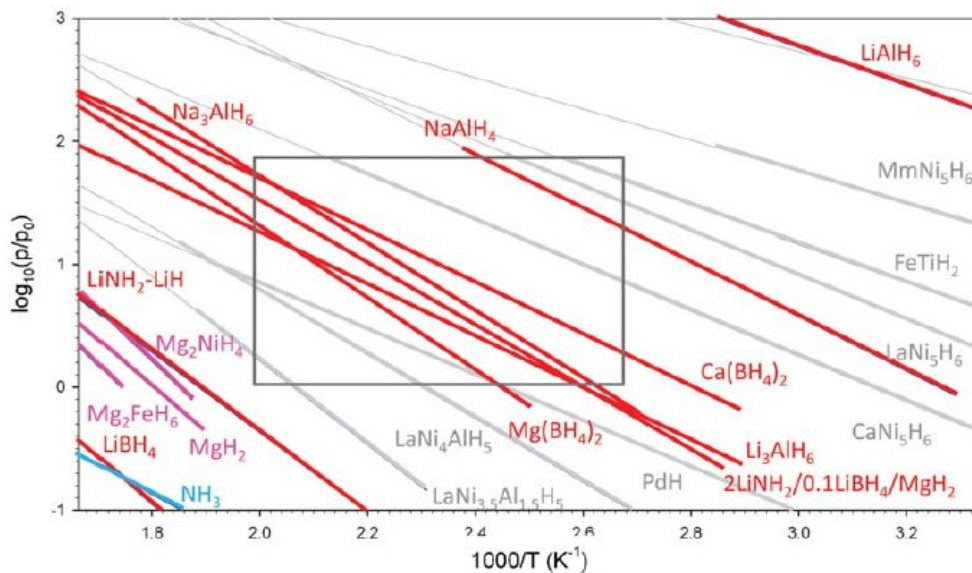


Figure 1-1: Enlarged Van't Hoff plot of materials, the box shows the materials which satisfy the operating conditions required for PEM fuel-cells. Figure taken from a review by W.I.F David.²

1.4 Kinetics of solid-state hydrogen storage

The kinetics of a reaction control how fast a reaction proceeds, due to the necessity of $\Delta G_{dec}^{\circ} \sim 0$ the kinetics of a reaction must be fast without the help of a large thermodynamic driving force²⁴. The rate at which hydrogen is re- or desorbed is critical for on-board applications. High hydrogen pressures are often needed to reduce the time required for recharging. This adds an inherent risk to the process. Reaction kinetics can be altered by the addition of a catalyst to provide reaction pathways with lower activation energies, (E_a) therefore increasing the rate of reaction compared to the uncatalysed equivalent. This may sometimes mean that due to the effectiveness of a catalyst, the reaction may be carried out at lower temperatures at a satisfactory rate, thus giving a false impression of improving thermodynamics.

Typically, two techniques are used in solid-state storage work for quantitative estimates of the activation energy of a reaction, both based around the Arrhenius Equation. The first method is based on the Arrhenius relationship between rate constant and temperature given by Equation 1-5.

$$k = A e^{-\frac{E_a}{RT}} \quad \text{Equation 1-5: Arrhenius Equation}$$

From Equation 1-5, taking the natural log of both sides gives Equation 1-6. The gradient, $[\ln k \text{ vs. } 1/T]$ is used to calculate the activation energy, where k is the rate constant at temperature, T , R is the ideal gas constant and A is the Arrhenius pre-factor. In this case, the reaction rate constants are determined at several temperatures.

$$\ln k = \ln A - \frac{E_a}{R} \cdot \frac{1}{T} \quad \text{Equation 1-6}$$

To determine the rate constants, the extent of the reaction must be taken into consideration. During the course of reaction, there may be periods (likely at the start) which exhibit a linear, that is to say a zero order, relationship between time taken and reaction extent,

and equally there may also be non-linear parts of the reaction. If the rate is assumed to be zero order, calculation of A and subsequently k will be possible.

The second equation is based on using Kissinger's method in Equation 1-7^{25,26}.

$$\ln\left(\frac{\beta}{T_m^2}\right) = -E_a/R \cdot 1/T \quad \text{Equation 1-7: Kissinger's Equation}$$

The gradient $\left[\ln\left(\frac{\beta}{T_m^2}\right) \text{ vs. } 1/T\right]$ can be used to find the activation energy by varying the heating rate, where β is the heating rate and T_m is the peak hydrogen desorption temperature. The peak hydrogen desorption temperature was determined to be the temperature at which the amount of hydrogen release peaked. Theoretically, by using a method based on rate constants (Equation 1-6) where the calculation of activation energy is based on the linear part of the reaction, which is usually at the beginning, the calculated value should be as close as possible to the true activation energy of a reaction. As the calculation for Kissinger's method is based on T_m , and does not consider the rate and extent of the reaction at T_m the value found can often be higher than through the Arrhenius calculation. Kissinger's method assumes that the reaction follows a zero-order rate during hydrogen release and gives an activation energy from the middle of the reaction. As it is unlikely that a reaction will follow a zero-order rate throughout due to various factors such as product and oxide layer formation and mass transport distances this determination is likely to be less representative of the activation energy. If however, the linear relationship holds across a larger range of the reaction, then values will be more comparable.

Several different factors including interface reaction, H_2 dissociation and oxide formation have been proposed to limit the rate of reaction kinetics; but the rate of mass transport of different ions/compounds is thought to be the rate determining step,^{24, 27} especially across the product layer as the reaction proceeds²⁸. Hydrogen release occurs across a wide range of solid-state storage systems *via* various mechanisms and intermediates^{25, 29-32}, including the diffusion of H^+ ,

H⁻, Li⁺ ^{29, 33} ions, ammonia mediating the reaction^{34, 35}, while others propose co-ordination intermediates²⁸.

1.5 Separating thermodynamics and kinetics

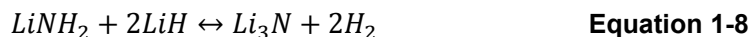
Modification of the properties of solid-state hydrogen storage systems has been achieved by a wide variety of methods. These include catalysis using a range of elements, e.g. silicon³⁶ and other compounds, such as transition metal chlorides³⁷ and transition metal nitrides³⁸. A discussion about thermodynamics and kinetics (Sections 1.3 and 1.4) is not complete without stressing that although theoretically these are two different properties, experimentally they can be difficult to separate.

Additional components which participate in the reaction can provide a lower or higher enthalpy route due to thermodynamic destabilization of the reactants, or stabilization of the products³⁴. Simultaneously, the activation energy required to form alternative products is also likely to be different. Hence, by selective partial or full substitution both properties can be tuned by changing the bonding and/or structures formed. In this work, substitution of an element of an active compound or the addition of a component whose elements were then included in intermediate compounds would be considered doping the reaction. Although these phases may induce a 'catalytic effect', i.e. providing an alternative lower energy reaction pathway, they do not appear to be regenerated after cycling. However, the introduction of dopants can give an impression of improving both properties, so careful examination of techniques used to ascertain numerical values and discussion of the factors that affect these values is needed to understand the true significance of such values that may be calculated.

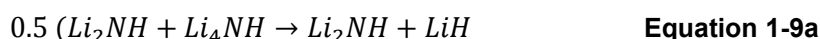
1.6 Complex light metal hydrides

1.6.1 Li–N–H systems

Many complex hydrides of light metals and combinations of light and transition metals have been investigated, many including the borohydride and amide anions. Borohydride and amide anions are favoured as they are hydrogen rich, 1B: 4H in BH_4^- and 1N: 2H in NH_2^- . One of the most widely studied solid state systems in the field of hydrogen storage is Li–N–H^{20, 39} since its discovery by Chen *et al* in 2002³⁹. The Li–N–H system can be synthesised by reacting LiNH_2 and LiH together via either inert ball milling⁴⁰ or heating. An alternative is hydrogenating Li_3N ³⁹. Equation 1-8 demonstrates the pathway originally suggested by Chen *et al.*³⁹ that can release and absorb 11.5 wt% H_2 in total through a lithium imide intermediate.



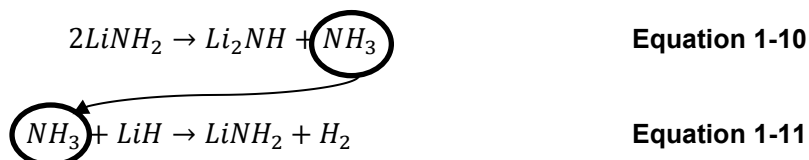
More recently Bull *et al.*⁴¹ suggested that the rehydrogenation of lithium nitride occurred through a mixture of the *quasi*-imide phase, Li_4NH and Li_2NH according to Equations 1-9 and 1-9a.



The amide to imide dehydrogenation is readily reversible at reasonably high temperatures, and dehydrogenation to the imide releases 6.5 wt% hydrogen at 285°C. However the very low plateau pressure of hydrogen⁴⁰ (0.01 bar at 255°C⁴²) released²⁰ from Equation 1-8, means that improvements are necessary for use in on-board applications or fuel cells.

There is some discussion as to the mechanism which controls hydrogen desorption from this system. One explanation for hydrogen release from a LiNH_2 -based system is that desorption occurs through ammonia mediation^{35, 43, 44}. The rate determining step³⁵ is decomposition of

lithium amide which leads to the production of ammonia and lithium imide. A rapid reaction⁴⁴ then occurs between ammonia and lithium hydride to release hydrogen and reproduce lithium amide. Equation 1-11 will occur until all lithium amide in the reaction is used up. Early experiments using deuterium labelling where the hydrogens in the amide or hydride were substituted for deuterium suggested that this pathway did occur^{35, 45}.



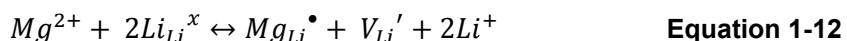
An alternative explanation is based around ion mobility of Li^+ and H^+ and a bulk solid-solid phase reaction^{20, 30}. The mechanism proposed is a result of the strong affinity between $\text{H}^{\delta+}$ contained in lithium amide and the H^- in lithium hydride which can combine to form H_2 ⁴⁶. Desorption in this case would be controlled by ion mobility of Li^+ and H^+ and the distances of mass transport between reactive interfaces of the two components. The ion migration solid based mechanism focuses on the ability of the ions to site-hop and form intermediates with varying stoichiometries such as $\text{Li}_2\text{Mg}_2(\text{NH})_3$ ⁶⁷ and $\text{Li}_4\text{Mg}_3(\text{NH}_2)_2(\text{NH})_4$ ⁶⁸ rather than the release/formation of ammonia within the storage medium through decomposition of the amide which subsequently reacts with LiH to release hydrogen.

Independently, neither mechanism can fully explain the desorption characteristics, given that desorption reactions take place in the bulk and at surface of a sample. Various experimental data has been published which supports both the ammonia-mediated and solid-solid phase mechanisms of hydrogen release from this simple system. Data includes in-situ analysis techniques such as X-ray diffraction (XRD), ^1H nuclear magnetic resonance (NMR) and infrared (IR), deuterium labelling and thermal decomposition alongside first principles calculations. It has been proposed that the temperature at which desorption is attempted, the presence of a catalyst³⁰ and particle size²⁰ can influence the mechanism of hydrogen release.

Many stoichiometric and subsequent variations of this system have been investigated, including mixed cation systems and quaternary mixed anion systems such as amide borohydrides³ and amide halides⁴⁷ which can act as a replacement for lithium amide in the reaction with lithium hydride.

1.6.2 Li-Mg-N-H systems

By substituting the Li⁺ cation with an alternative alkali, alkaline earth or transition metal of a higher electronegativity or a higher number of valence electrons, the ionic interaction between the amide anion [NH₂⁻] and Li⁺ is weakened due to charge repulsion between cations^{48, 49}. This causes destabilization of the N-H bonds in the amide anion¹⁹ and hence lowering hydrogen desorption temperatures and improving kinetics. It was found that substituting Li with Mg had a positive effect and created a novel Li-Mg-N-H system³⁴. Substitution of Li⁺ cations by Mg²⁺ cations in the amide part of the system creates vacancies and/or defects in the structure due to charge compensation⁴⁹ to maintain neutrality. By introducing vacancies into the system, empty sites are created which facilitate increased lithium ion mobility. A vacancy equation is shown in Equation 1-12 using Kroger-Vink Notation.



An alternative option is to change the cation in the hydride. When considered from a hydrogen storage point of view, the decomposition temperature of LiH is very high, around 550°C. For example, the decomposition temperature of MgH₂ is only 280°C, so this hydride, due to its lower stability, should interact more readily with other compounds, at more accessible temperatures than LiH.

In 2004, the Li-Mg-N-H medium was first synthesised by reacting Mg(NH₂)₂ and LiH^{34, 50} in addition to LiNH₂ with the binary hydride MgH₂^{40, 51}. Hydrogen release was accompanied by the appearance of an unknown set of peaks in the resulting powder XRD pattern, which were

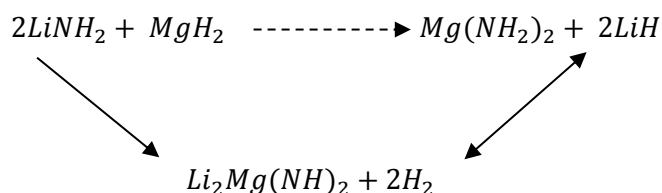
assigned to lithium magnesium imide^{40, 51}. It was found that this compound could be successfully re-hydrogenated⁵¹. Since then, many groups have investigated how the hydrogen storage properties and desorption products change when one⁵² or both^{32, 53} of the starting materials are nitrides (Li_3N and Mg_2N_3), the stoichiometries vary^{54, 55}, when additional components are used in stoichiometric amounts, e.g LiBH_4 ⁵⁶ and existing reactants are substituted with alternatives such as NaH and NaNH_2 ⁵⁷.

The ratio of $2\text{Li}:\text{Mg}$ ⁵⁸ and close derivatives such as $8\text{Li}:\text{3Mg}$ ^{34, 55} have been widely studied through various reactant routes¹. The desorption products and hydrogenation state of these phases are largely dependent on the ratio of Li and Mg as starting materials and the temperatures under which the experiments were carried out respectively. Early investigations into the $2\text{Li}-\text{Mg}-\text{N}-\text{H}$ system indicated that there appeared to be little difference on the hydrogen capacity of the material depending on which combination of starting materials is used⁵⁹, 2LiNH_2 and MgH_2 or $\text{Mg}(\text{NH}_2)_2$ and 2LiH . However, further exploration to identify intermediates and reaction pathways through *in-situ* Raman and powder XRD measurements shows that the choice of starting materials can control the reversible hydrogen content available by minimising irreversible NH_3 evolution⁶⁰.

When starting from LiNH_2 , it has been suggested that NH_3 was produced⁶¹, reducing system capacity⁶². However, although ammonia release was sometimes not observed in desorption mass spectrometry traces from samples based on lithium amide and magnesium hydride, mass loss greater than the theoretical hydrogen content was seen, leading the authors to attribute the mass loss to ammonia released below instrument detection limits⁶². LiH reacts rapidly with NH_3 ⁴⁴ and if present as a starting reagent can decrease the amount of NH_3 that escapes. Therefore starting from $\text{Mg}(\text{NH}_2)_2$; which is more stable than LiNH_2 ⁶³, and LiH instead of

¹ There are numerous references that contain data on 2 Li: 1 Mg ratio experiments, and so they will be referred to for specific details rather than for generalizations.

MgH₂, is favoured in order to maximise capacity and reduce ammonia output⁶², although the pairing of LiNH₂ and MgH₂ was thermodynamically less stable⁵⁹. Nonetheless, an *in-situ* reaction between lithium amide and magnesium hydride has been observed during high energy ball milling or heating under hydrogen pressure, which can partially or completely transform the reactants into Mg(NH₂)₂ and LiH as shown in Scheme 1-1^{78, 79}.



Scheme 1-1

A recent publication⁶⁴ made a direct quantitative comparison of reaction of the starting materials, with the respective hydrides present in slight excess. The authors identified the same phase of Li₂Mg(NH)₂ from both samples. The thermodynamic properties (enthalpy and entropy) of the first desorption step were similar regardless of starting materials, (LiNH₂ was slightly favoured). However, the kinetics (reaction rate and especially activation energy of desorption) were found to more favourable when starting from 2LiNH₂ and 1.1MgH₂. An activation energy of 42.5 kJ mol⁻¹ was measured compared to 51.7 kJ mol⁻¹ starting from Mg(NH₂)₂ and 2.2LiH.

Regardless of which set of reactants are the best starting materials, following the completion of hydrogen cycling, the only compounds produced after rehydrogenation are magnesium amide and lithium hydride,^{22, 25, 56, 59} which are the thermodynamic products^{42, 51, 65}. Luo *et al.*⁴⁰ successfully cycled a sample starting from 2LiNH₂ and MgH₂ 9 times with no loss of hydrogen capacity, an important aspect for commercial use. After heating at moderate temperatures, around 200 °C, the majority of the transformation from amide to ternary imide can be completed in around 2 hours⁶⁶.

More recently, Lamb *et al.*⁶⁷ also carried out a cycling study on Li₃N with 20 mol% nitrogen in the gas stream during short rehydrogenation cycles (30 minutes) under ~10 bar hydrogen. The

reduction of cycling capacity of the sample after over 500 cycles was only 4 wt% compared to ~7 wt% when the gas stream consisted of pure hydrogen. This is a promising finding for improving the potential for commercial application of these types of materials.

Similarly to the LiNH₂-LiH system, there is still a considerable debate as to the reaction pathway for desorption and absorption, in a system which contains significantly more variables. Further discussion on this topic will be made in Section 1.6.3.

The 2Li to Mg system stores on average 5 wt% H₂, desorption begins around 100°C^{25, 40} and peaks on average at 180–190°C,^{51, 55, 62} around 100°C lower than the Li-N-H⁴². The variations can be attributed to inconsistent ramp rates used in temperature programmed desorption experiments or the sample preparation regimes by different groups. The inclusion of magnesium into the Li-N-H system was found to significantly increase the plateau pressure of hydrogen desorption that can be achieved at temperatures of 220°C, from less than 1 bar (Li-N-H) to over 40 bar (Li-Mg-N-H)^{42, 40, 51, 66}. Hydrogen absorption also occurs at lower temperatures in the Li-Mg-N-H system compared to Li-N-H; ~80% H₂ absorption within an hour at 180°C under 90 bar H₂ has been achieved⁵¹.

Storage in this system is facilitated by low temperature formation and the stability of the ternary imide, Li₂Mg(NH)₂⁶². Computational work carried out by Michel *et al.*⁶³ predicted the formation of Li₂Mg(NH)₂ could begin at 96°C which correlated well with the temperatures that hydrogen release was first observed. Previous work by various groups^{4, 55, 57, 68, 69} has shown that several phases of Li₂Mg(NH)₂ can be formed, from either set of reactants in Scheme 1-1 and are designated α, β, γ and δ phases. It appears that temperature, pressure of synthesis⁴ and additional components⁵⁷ can control the phase produced.

The structure of α-Li₂Mg(NH)₂ was first solved by Rijssenbeek *et al.*⁴ who indexed it to an orthorhombic unit cell, space group no. 45, *Iba2*. The cation positions and anion lattice in α- and

β - $\text{Li}_2\text{Mg}(\text{NH})_2$ are based on the anti-fluorite system, similar to Li_2NH . The distribution of all Li^+ and Mg^{2+} cations is random in α - $\text{Li}_2\text{Mg}(\text{NH})_2$, while the central ion in β - $\text{Li}_2\text{Mg}(\text{NH})_2$ is always Li^+ . It can be seen in Figure 1-2 that the structures of α - $\text{Li}_2\text{Mg}(\text{NH})_2$ and β - $\text{Li}_2\text{Mg}(\text{NH})_2$ are both very like Li_2NH , with a comparable face-centred cubic nitrogen lattice where the cations sit in the tetrahedral sites. The lack of change in the basic LiNH_2 structure indicates how accommodating and versatile this anti-fluorite type system can be in terms of vacancies for cation non-stoichiometry, amide imide solid solution phases and alternative cations (further in Section 1.6.3).

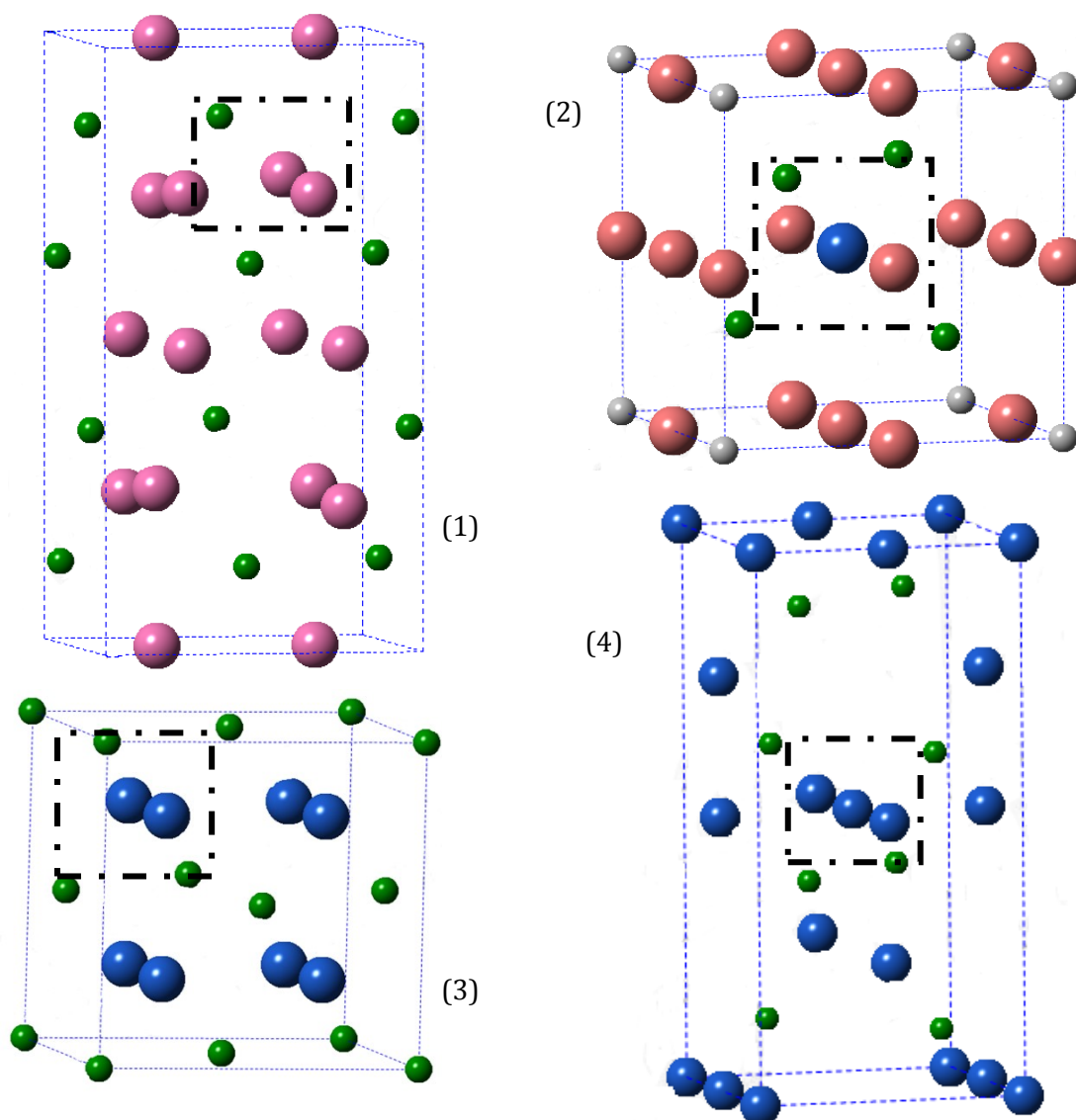


Figure 1-2: Structures of α - $\text{Li}_2\text{Mg}(\text{NH})_2$ (1), β - $\text{Li}_2\text{Mg}(\text{NH})_2$ (2), Li_2NH (3) and LiNH_2 (4). Nitrogen sites (green), lithium-only sites (blue), magnesium or lithium sites (pink), fixed site vacancies (grey) shown. The nitrogen-cation lattice is indicated. Structural data taken from Rijssenbeek *et al.*⁴

The other readily accessible structure, denoted β - $\text{Li}_2\text{Mg}(\text{NH})_2$ was identified to crystallize in a cubic unit cell when the Li–Mg–N–H system was first realised^{51, 62} and the structure solved subsequently⁴. By refining both X-ray and neutron diffraction data simultaneously, the structure was identified as a primitive cubic unit cell, space group no. 215, $P\bar{4}_3m$. The cation and vacancy ordering in this phase is more complicated than the α -phase. Another two phases of $\text{Li}_2\text{Mg}(\text{NH})_2$ have also been identified, but they require high temperature and both pressure (H_2) and temperature formation conditions respectively, γ - $\text{Li}_2\text{Mg}(\text{NH})_2$ and δ - $\text{Li}_2\text{Mg}(\text{NH})_2$ ⁴.

Conflicting information has been published on when and how the α - and β - $\text{Li}_2\text{Mg}(\text{NH})_2$ phases are formed/synthesised. The cubic β -phase was first observed in 2004⁵¹ after a thermal reaction was carried out between 2LiNH_2 and MgH_2 at temperatures up to 350°C . The same phase was also observed in 2005 by the same group after a thermal reaction carried out between $\text{Mg}(\text{NH}_2)_2$ and 2LiH at temperatures up to 250°C ²⁵ indicating that the phase type formed was independent of the starting materials. Before the structures were solved in 2008, several groups published desorption data of reactions between temperatures from 180 – 240°C ^{54, 59, 62, 66, 70} and some resulting X-ray diffraction data. Data recorded after reactions starting from both sets of reagents were consistent with the subsequent formation of one or both $\text{Li}_2\text{Mg}(\text{NH})_2$ phases, which many groups identified.

Rijssenbeek *et al.*⁴ identified that from starting materials of 2LiNH_2 and MgH_2 , α - $\text{Li}_2\text{Mg}(\text{NH})_2$ was formed and was stable after heating to 330°C . Raising the temperature above 350°C resulted in a transformation into the β - $\text{Li}_2\text{Mg}(\text{NH})_2$ phase. When the same reactions started from $\text{Mg}(\text{NH}_2)_2$ and 2LiH the formation of the α - $\text{Li}_2\text{Mg}(\text{NH})_2$ phase was less clear and β - $\text{Li}_2\text{Mg}(\text{NH})_2$ was formed at lower temperatures. Interestingly, at temperatures greater than 52°C the β -phase was the thermodynamically favoured product, as this phase did not possess a large

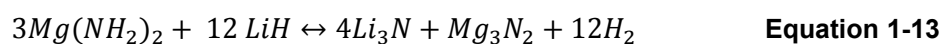
kinetic barrier to formation like the α -phase⁷¹. This may explain the direct formation of the cubic phase observed by some groups when starting from magnesium amide.

Initially, it was thought that α -Li₂Mg(NH)₂ could be converted to β -Li₂Mg(NH)₂ by simply raising the temperature as the phase transitions are as a result of the cation ordering changing within the system⁴. Several computational studies have been carried out to determine the most favourable ordering of cations and vacancies^{63, 68, 72}. First principles calculations carried out by Liang et al.⁷³ concluded that the Gibbs free energy of Li₂Mg(NH)₂ at OK was lower for the α -phase but above 325K the Gibbs free energy of the β -phase was lower⁷¹. This means at the reaction temperatures considered for this system the thermodynamically favoured phase would be the β -phase. However, the phase transition from α - to β -Li₂Mg(NH)₂ or direct formation of β -Li₂Mg(NH)₂ is kinetically unfavourable⁷³. The conversion, or direct formation of the β -phase requires temperatures greater than 400°C or high energy ball-milling whilst ensuring significant hydrogen desorption does not occur. The reversion of the β -phase of Li₂Mg(NH)₂ to the α -phase can be achieved by heating at 280°C under 9 bar H₂. Hence Liang et al.⁷¹ referred to the α -phase of Li₂Mg(NH)₂ as the kinetic product due to the high kinetic barrier to its formation and the β -phase as the thermodynamic product of their reactions which were carried out under 280°C.

Although temperature conversion can be achieved, work by Hu *et al.*⁷⁴ on the transitions between the crystal structures of the mixed imide, Li₂Mg(NH)₂ indicate that the main controlling factor being the gas back pressure during the dehydrogenation. It was observed that different phases were formed during flowing gas TPD experiments and desorption experiments carried out under vacuum⁷⁴. Liang *et al.*^{71, 73} studied in detail the effect of gas back pressure on the crystal structures and the subsequent hydrogen storage properties of the phases of Li₂Mg(NH)₂. Between 190–280°C, the crystal structure of Li₂Mg(NH)₂ was found to be independent of temperature and gas type; it was controlled by gas back pressure. Formation of the α - and β -phases of Li₂Mg(NH)₂ were preferred under high (9 bar) and low (1–3 bar) gas back pressures respectively⁶⁹.

Controlling the phase formed by managing the desorption conditions allowed the properties of hydrogenation of each phase to be examined. The cubic β -phase was found to possess higher rates of hydrogenation and a lowered operating temperature compared to the α -phase⁷¹.

Since 2004, compositional effects on the Li–Mg–N–H system have been investigated by several groups. Nakamori *et al.*^{50, 75}, Leng *et al.*⁵⁴ and Aoki *et al.*^{55, 70} all explored storage properties of the ratio $\text{Mg}(\text{NH}_2)_2 + 4\text{LiH}$. Early indications were that a multi-step reaction was occurring, intermediates such as Li_2NH were identified by powder XRD⁵⁰. Around 8 wt% H_2 was desorbed when the sample was heated to 425°C at 10°C min⁻¹ (peak at 405°C) out of a total hydrogen content of 9.1 wt% according to Equation 1-13^{53, 75}. Powder XRD data recorded at various stages throughout the hydrogen cycle confirmed that the reaction occurred according to Equation 1-13⁵³.



Rehydrogenation of the nitrides produced in Equation 1-13 was successfully carried out at 250°C under 35 MPa H_2 for 4 hours⁵³. Research carried out by Leng *et al.*⁵⁴ found that a cation disordered LiMgN phase was formed as a direct product of Li_3N reacting with Mg_3N_2 at $T > 400$ °C. The mechanism proposed is an NH_3 mediated route due to the decomposition of $\text{Mg}(\text{NH}_2)_2$ ⁵⁴. Aoki *et al.*⁷⁰ studied the low temperature range of the 1:4 system and using pressure-composition isotherms (PCI'S) found that dehydrogenating at 250°C releases 4.9 wt% H_2 . Various temperature PCIs were carried out, all showing a sloping and plateau region in the desorption profile, indicating the existence of multi-step dehydrogenation occurring⁷⁰. A Van't Hoff plot was used to calculate the enthalpy of reaction as -46 kJ mol⁻¹ H_2 and the entropy as 104 J K mol⁻¹ H_2 for the plateau region. Several complex intermediates are suggested for the plateau and sloping regions, for example $\text{Li}_4\text{Mg}_3(\text{NH}_2)_2(\text{NH})_4$ and $\text{Li}_2\text{Mg}(\text{NH})_2$ respectively⁷⁰.

When the $\text{Mg}(\text{NH}_2)_2 + 4\text{LiH}$ system is compared to systems which have lower amounts of LiH such as ratios of 1 to 2 and 3 to 8 it has been shown higher amounts of LiH suppress NH_3

formation⁵⁵ but limit the accessible low temperature hydrogen content of the sample^{55, 76, 77}. The shape of the PCI isotherm and the formation of $\text{Li}_2\text{Mg}(\text{NH})_2$ indicate the 1 to 4 system behaves in a similar manner to other ratios of Li to Mg.

Ultimately, two Li to one Mg currently appears to be the most effective ratio and overall medium for maximising low temperature reversible hydrogen storage due to the readily accessible stable mixed cation imide^{55, 74}. The volumetric capacity of this system, 56 g dm^{-3} is also comparable to that of liquid H_2 (70 g dm^{-3})⁶². Apart from work by Lamb *et al.*⁶⁷ on Li_3N , significant cyclic testing has been limited on these light-metal nitrogen hydrogen systems. Cyclic testing of this composition (2Li to Mg) was carried out. During 270 sorption cycles at 200°C under 110 bar H_2 , a capacity decrease of 25% was seen⁷⁸. The capacity was originally measured as $\sim 4 \text{ wt}\% \text{ H}_2$ and dropped to $\sim 3 \text{ wt}\%$, the drop was attributed to incomplete H_2 absorption and NH_3 formation⁷⁸. However, the time taken to complete these cycles, over 10 hours, means that kinetic improvement is imperative.

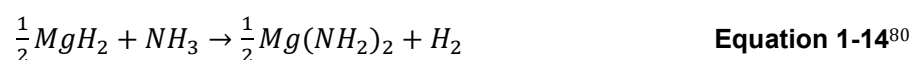
1.6.3 Mechanistic pathways of the 2Li–Mg–N–H system

As the system studied in this thesis was based on 2 to 1 lithium to magnesium ratio, only the pathways relating to this ratio will be considered in this section. As discussed in Section 1.6.2, several starting ratios have been investigated and the desorption products and routes to them are varied. Several groups have investigated the various intermediates that are formed when the system is composed from LiNH_2 and MgH_2 or $\text{Mg}(\text{NH}_2)_2$ and LiH . *In-situ* structure determination methods have been used to attempt to explain the (de-)hydrogenation process in the low temperature range^{4, 27, 32, 59, 79}. Hydrogen storage in this system revolves around the formation and rehydrogenation of $\text{Li}_2\text{Mg}(\text{NH})_2$.

Looking at the first steps of hydrogen desorption from the starting materials, it was found the apparent activation energy of $\text{Mg}(\text{NH}_2)_2$ decomposition was higher than the apparent

activation energy of $\text{Mg}(\text{NH}_2)_2$ and 2LiH , indicating that it was unlikely that the first step of desorption occurred through decomposition of $\text{Mg}(\text{NH}_2)_2$ ²⁸. In contrast, the mass loss observed from TGA experiments conducted under vacuum, of a 2LiNH_2 and MgH_2 sample indicated that ammonia desorption was occurring, (Equation 1-10) as a preliminary step to produce Li_2NH ⁶².

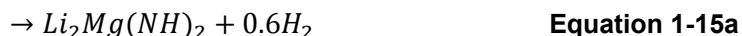
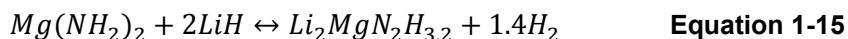
Markmaitree *et al.*⁸⁰ suggested that ammonia then becomes the key phase, favouring an ammonia-mediated mechanism, and is recycled through reaction with MgH_2 (Equation 1-14) leading to the formation of MgNH . Li_2NH and MgNH can then react to form $\text{Li}_2\text{Mg}(\text{NH})_2$ (Equation 1-14b). As $\text{Mg}(\text{NH}_2)_2$ was not observed, it was concluded that Equation 1-14 was the rate determining step⁸⁰.



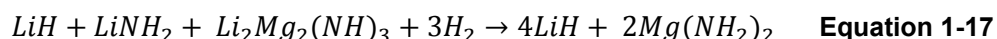
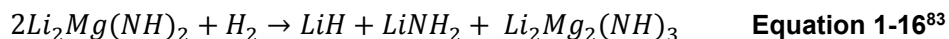
Several investigations found that when the starting materials were 2LiNH_2 and MgH_2 , they were initially transformed into $\text{Mg}(\text{NH}_2)_2$ and LiH , either during ball-milling^{81,82} or under heating into a static or over-pressured atmosphere⁶⁰. The possibility of only partial conversion between starting materials⁴ complicates the desorption mechanism as the reaction now starts from double the number of phases originally thought to be available. Although $\text{Mg}(\text{NH}_2)_2$ was formed during the dehydrogenation reaction from LiNH_2 (Equation 1-14), its formation was thought to be the rate-determining step. If $\text{Mg}(\text{NH}_2)_2$ was already partially present through a metathesis reaction during milling, this should increase the rate of hydrogen release.

Desorption was often characterised by the hydrogen desorption pressure, which was calculated from PCT isotherms, where two areas were identified, an initial sloping area and then

a plateau region^{25, 59}. During the sloping region a partially dehydrogenated, defined intermediate $\text{Li}_2\text{MgN}_2\text{H}_3$ was formed⁶², where the amide character in the phase was concentrated around the lithium cation, which then undergoes full dehydrogenation to form $\text{Li}_2\text{Mg}(\text{NH})_2$.



For the hydrogenation of $\text{Li}_2\text{Mg}(\text{NH})_2$, Weidner *et al.*⁶⁹ suggested an alternative mechanism where LiNH_2 and another mixed-cation imide phase were formed as incomplete products before the final thermodynamic products of $\text{Mg}(\text{NH}_2)_2$ and 2LiH were achieved (Equations 1-16 and 1-17). Wang *et al.*⁸³ agreed that desorption starting from $\text{Mg}(\text{NH}_2)_2$ and 2LiH also occurred following the reverse pathway in Equations 1-16 and 1-17. The structure $\text{Li}_2\text{Mg}_2(\text{NH})_3$ is similar to the other phases shown in Figure 1-2, meaning that lithium ion migration plays an important part in determining the ease of hydrogenation due to slight structural changes⁶⁹.



Kinetic studies^{28, 29, 84} on the Li–Mg–N–H system suggested that desorption favoured a solid-state reaction which is rate limited by the concentration of reactant species at the reaction interface and the diffusion rate of Li^+ from the starting materials across the phase boundary into and through $\text{Li}_2\text{Mg}(\text{NH})_2$, the product phase from desorption.

1.6.4 Improving the Li–Mg–N–H system

Recently, interest has focussed on how to improve the Li–Mg–N–H system. Several options are available in order to improve this system. For the improvements to have a lasting effect, they have to be based on changing the chemical parameters of this system, or maintaining

engineered physical properties. Mechanical ball-milling, although effective in reducing particle size in the short-term, without additives to prevent agglomeration, will not remain effective over hundreds or even tens of cycles. One such possible additive is triphenyl phosphate (TPP), but this has a negative impact on other properties⁸⁵. Milling is an important tool for assessing the initial impact of an additional or alternative component on the system.

For example, improvements have been achieved catalytically by the addition of 10 wt% TaN or TiN without compromising the hydrogen capacity³⁸. The main limitation of many solid-state hydrogen storage systems seems to be overcoming slow reaction kinetics at low temperatures. Thermodynamically, it is possible for desorption from the Li–Mg–N–H system to proceed at low temperatures; $\sim 100^\circ\text{C}$ is suitable for hydrogen release/absorption to occur for most Li: Mg starting ratios, but kinetic improvement is necessary for this to be anywhere near a commercially acceptable rate. A balance between rate and maintaining high hydrogen content in the storage medium also has to be considered.

As the link between lithium ion mobility and improved hydrogen desorption temperatures and absorption rates started to be understood²⁰, explorations began into amide and imide compounds that could be modified to improve the lithium ion conductivity by the addition of further anions such as halides^{47, 86} and borohydrides⁸⁷. When anions such as Cl^- or BH_4^- are incorporated into a structure, the interaction between the cation and the amide or imide group is weakened⁸⁸, which lowers the energy barrier to Li^+ ion migration⁸⁹ and also weakens the N–H bond relative to LiNH_2 ⁹⁰, which results in a lower hydrogen desorption temperature.

A range of transition metal chlorides was investigated by Price *et al.*³⁷ but due a metathesis reaction that occurred between the chlorides and LiNH_2 after cycling the positive kinetic effect of the modifier on the reaction was lost. Leng *et al.*⁹¹ explored the effect of adding MgCl_2 into the Li–N–H system. It was shown that 1 mol% MgCl_2 has a similar effect when compared to 1 mol%

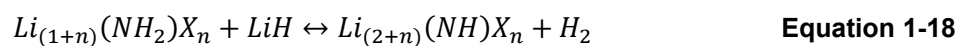
TiCl₃ but when the MgCl₂ content was increased to 50 mol% the desorption peak was shifted to 174°C⁹¹, slightly lower than the two Li to Mg system⁷⁴. An *in-situ* reaction to form Mg(NH₂)₂ and LiCl appears to be most likely, effectively creating a Cl-doped Li–Mg–N–H system, but no kinetic data was available⁹¹.

Conversely, when 0.2 mol of LiBr was added to the Li–Mg–N–H system, starting from Mg(NH₂)₂ and LiH, the de- and re-hydrogenation rates were found to be 3 and 2 times faster than the undoped sample, respectively⁹². The mechanism behind this system was found to be through the in-situ generation of LiNH₂ which reacted with LiBr to form an amide bromide, Li₂NH₂Br which then reacted with LiH to form the corresponding imide bromide. Even though the main hydrogen-releasing reaction in this system through Li₂Mg(NH)₂ still proceeds, the formation of the amide bromide reduces the volumetric capacity of this system by around 10%.

The effects of adding 2 mol of LiCl into the Li–Mg–N–H system were investigated by Gamba *et al.*⁹³ and it was found to have a positive effect on the initial rate and desorption temperature achieved. However, the formation of Li₄(NH₂)₃Cl from LiNH₂ and LiCl acts a competing reaction to the formation of dehydrogenation product, Li₂Mg(NH)₂ which increased the activation energy of the cycled product. Clearly, the amount of halide which is added to a system needs to be carefully controlled in order to balance the rate and temperature improvements these compounds can make with loss of capacity. If competing side or runaway reactions consume phases that have been identified in the main reaction, such as LiNH₂, then ultimately this will have a negative effect after cycling the system.

An alternative method employed to incorporate halides into the system was to use amide halides as the main hydrogen store. They were synthesised prior to the desorption reactions, then reacted with a hydride, and reformed from the corresponding imide halide upon rehydrogenation⁴⁷. Lithium and lithium magnesium amide halides were synthesised from

chlorine, bromine and iodine⁴⁷, but no evidence for attempts to synthesise magnesium amide halides could be found. Equation 1-18 was suggested as a general reaction for hydrogen release and uptake from these materials



The structures of several amide halides were solved and their reactions tested with LiH and MgH₂ as a direct replacement for LiNH₂ or Mg(NH₂)₂. The hydrogen desorption temperature of every amide halide tested with either hydride was reduced relative the control⁴⁷.

Due to the high hydrogen content of borohydride anions and their ability to make lithium ion mobility improvements, many studies also looked at the effectiveness of their addition into the Li–Mg–N–H systems, often with alternative cations to Li or Mg as well. Several groups^{56, 94-101} investigated the effects of adding LiBH₄ to the Li–Mg–N–H system, initially in stoichiometric amounts^{56, 98} and in catalytic amounts^{97, 99}. The addition of LiBH₄ caused several competing reactions to the formation of Li₂Mg(NH)₂ to occur, specifically the formation of Li₄(NH₂)₃BH₄⁹⁵. It can be seen the makeup of this quaternary amide borohydride, first reported in this form by Chater *et al.*¹⁰² is the same as Li₄(NH₂)₃Cl, where the [BH₄⁻] directly replaces the Cl⁻ anion. Unlike in the halide added samples⁸⁹ where the amide halide phases were only observed after heating, even from previously ball-milled samples, the quaternary amide borohydride was observed after ball-milling alone.

This existence of Li₄(NH₂)₃BH₄ seeded the formation of Li₂Mg(NH)₂ at low temperatures, between 140°C and 180°C⁵⁶. As the intermediate reaction pathway had been changed, the activation energy of hydrogen release was lowered by ~14% when 0.10 mol LiBH₄ was added¹⁰⁰ and the rates of hydrogen desorption and absorption were accelerated. The rate from the LiBH₄-added sample was around 3 times faster than the undoped sample⁵⁶, when the doped sample was

tested at 180°C compared to 220°C for the undoped sample⁶². Around 3 wt% H₂ was desorbed in 10 minutes at 180°C when LiBH₄ was added in stoichiometric amounts⁸³.

In a similar way that the addition of Mg into the Li–N–H system improved the properties, the addition of further cations¹⁰³ to the Li–Mg–N–H system often improves the hydrogen storage behaviour of these samples, often through the inclusion of the cations into key phases during the desorption process. The addition of potassium to the Li–Mg–N–H system has been studied by several groups^{83, 104, 105}, often through the addition of KH which was found to produce a kinetic and thermodynamic enhancement¹⁰⁶. Potassium can replace some of the lithium cations in Li₂Mg(NH)₂ which expands the lattice through the inclusion of a larger cation, allowing the easier movement of Li⁺ cations through the structure and also weakening the H–H bond¹⁰⁶.

The addition of sodium was also investigated, through partial substitution of LiH and Mg(NH₂)₂ with NaH and NaNH₂ respectively⁵⁷. The hydrogen desorption peak from both substituted samples was reduced by around ~15 °C compared the control sample. A reduction of around 8% in the activation energy was also achieved, but unfortunately accompanied by a 20% decrease in the hydrogen capacity⁵⁷.

As the benefits of introducing borohydrides and alternative cations into the Li–Mg–N–H system have already been discussed, the addition of phases like NaBH₄¹⁰⁷ and Ca(BH₄)₂^{90, 108} which combine the benefits of both alternative cations and anions has also been investigated. Interestingly, the activity of these two species was not the same. NaBH₄ was observed, mostly unchanged, throughout the hydrogen cycle; its behaviour more similar to a catalyst than a reactant¹⁰⁷, whereas Ca(BH₄)₂ readily underwent a metathesis reaction to produce CaH₂ and LiBH₄ during ball-milling¹⁰⁸. These phases then underwent further reaction in the system, for example allowing the formation of Li₄(NH₂)₃BH₄. The addition of 0.1 mol of Ca(BH₄)₂ resulted in large

decreases in the estimated activation energy and reaction enthalpy of ~16.5% and 28% respectively¹⁰⁸.

1.7 Aims

The project aim was to carry out a comprehensive study on the hydrogen storage properties of a Li-Mg-N-H based-system. Thermodynamically, this system possesses the attributes which could lead to the development of a viable hydrogen store for close to ambient conditions. However, due to poor kinetics the practical use of this system will be limited unless the rate of hydrogen desorption and absorption can be improved. Building on the positive results seen by the inclusion of $\text{Ca}(\text{BH}_4)_2$ into this system, research carried out in this project will look at the effectiveness of doping this complex hydride system using sub-stoichiometric amounts, between 0.1 and 0.2 mol, of CaCl_2 and CaBr_2 . These compounds were chosen to maintain the positive effects of thermodynamic destabilisation resulting from the addition of calcium into the system. The results can then be compared to those from the use of CaBH_4 ^{90, 108} and directly assess the effectiveness of the anions.

An additional area which was studied in this work included the reactions of NH_4Cl with hydrides, mainly MgH_2 . The formation of magnesium ammoniate halides¹⁰⁹ represented a possible route for hydrogen storage if a method of converting bonded NH_3 through NH_2^- to NH^{2-} and then reversing the process for rehydrogenation could be achieved.

2 Experimental

2.1 Solid-state synthesis

All samples were prepared and stored under inert conditions in an argon filled glove box (MBraun, UniLab, <10ppm O₂, <0.1ppm H₂O) due to the sensitivity of these materials to moisture and oxygen. Sample preparation for any further experimental processes was also carried out in the glove box.

2.1.1 Thermal synthesis under inert gas

Starting materials were weighed using an analytical balance (± 0.1 mg) in the required molar ratio, and hand-ground together using a porcelain pestle and mortar for approximately 5 minutes. Samples were transferred into quartz tubes (1/2" O/D) and sealed with Young's T-piece taps via Ultra-Torr fittings before removal from the glove box.

The quartz tube was then secured in a clamp stand such that the sample was centrally located in the hot zone of a vertical tube furnace (Lenton Furnaces, LFT, 12/25/250 fitted with a Eurotherm 3216P1 controller). The design of the T-piece allowed the line to be purged with argon before opening the tap, to maintain the sample under a continuous argon flow. Concentrated sulphuric acid bubblers were placed before and after the samples in the flow line to remove any residual moisture in the argon, to prevent contamination. Typically, samples were heated at a ramp rate of 2°C min⁻¹, held for a range of time periods between 4 and 72 hours and subsequently cooled naturally.

2.1.2 Ball-milling under inert gas

The starting materials were weighed using an analytical balance (± 0.1 mg) in the required molar ratio, and loaded into the chosen milling pots with stainless steel/ tungsten-carbide milling balls in a 1: 40 ratio respectively. Ball milling was carried out in 250 ml stainless steel pots loaded under atmospheric pressure in the glove box, or in 250 ml Tungsten-carbide high pressure pots,

pressurised with hydrogen to 100 bar. The pots were sealed using Viton-O rings and milling carried out in a Retzch PM400 Planetary Ball Mill at 300 rpm for 24h. To prevent temperature rises in the unpressurised milling vessel, 2 minutes of milling was followed by a 2 minute pause.

2.2 Temperature programmed desorption

Temperature Programmed Desorption (TPD) is a method used to heat samples in a controlled manner. Desorption experiments can be carried out in several different pieces of equipment, under various conditions, generally under flowing gas or vacuum and often the products are monitored using mass spectrometry. Thermogravimetric analysis (TGA) was used as a TPD method to investigate the mass loss from samples in a more controlled environment. When coupled to mass spectrometry, it is a powerful technique allowing mass losses to be assigned to known desorption products.

2.2.1 TPD-MS

A previously described³ homebuilt TPD rig coupled to a mass spectrometer was used to investigate the desorption properties of samples. The sample was heated under a continuous argon gas flow. The outlet flow of the apparatus can be connected to a mass spectrometer in order to directly analyse the desorption products.

A sample of mass approximately 0.15g was prepared inside an argon-filled glove box and loaded into a quartz reaction tube (7 mm O/D, 4 mm I/D) which was sealed at one end. The quartz tube was then loaded and sealed inside a steel reaction chamber incorporating a thermocouple, before being removed from the glove box and placed into the TPD equipment. The TPD rig had previously been repeatedly evacuated and refilled with argon.

An argon flow of 100 ml min^{-1} was established and regulated using a mass flow controller (Hastings 200 Series, Teledyne). A barrel heater was located around the reaction vessel and a thermocouple which was in contact with the sample was used to monitor the temperature, allowing the observation of any exo- or endo-thermic events. Evolved gases were monitored using a quadrupole mass spectrometer (HPR-20, Hiden Analytical) fitted with a Faraday cup ($m/z > 20$) and secondary electron multiplier for lighter ions ($m/z < 20$).

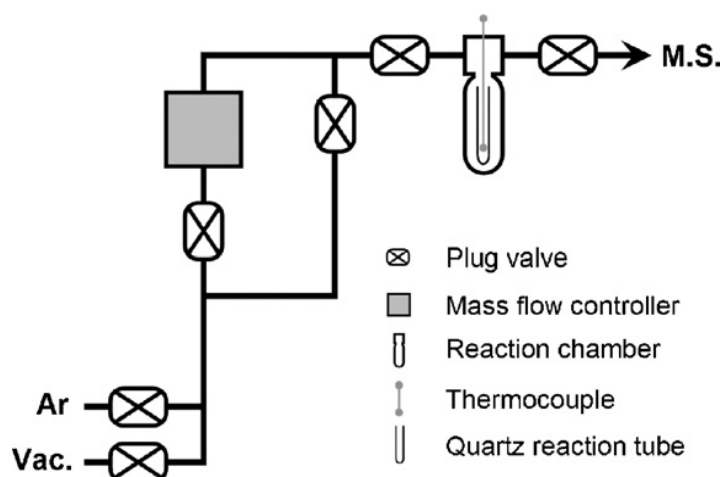


Figure 2-1: Schematic Diagram of TPD-MS equipment³.

2.2.2 Calibration

As NH_3 and H_2 levels were of specific interest in these experiments, the partial pressure of the $\text{NH}_2^{\bullet+}$ fragment was also monitored. As the $\text{NH}_3^{\bullet+}$ fragment has the same m/z ratio as $\text{OH}^{\bullet+}$ which can exaggerate readings of ammonia levels even in a high vacuum system. The $\text{NH}_2^{\bullet+}$ fragment has an intensity of $\sim 80\%$ of the $\text{NH}_3^{\bullet+}$ fragment and thus allows the determination of the correct levels of ammonia released. Carrying out calibration with standardised amounts of NH_3 and H_2 in the argon flow allows the exact ratio of detected gases to be ascertained.

To determine the sensitivity of the mass spectrometer to these gases, a standardised calibration gas (BOC Speciality Gases, 4736 ppm H_2 , 4898 ppm NH_3 , balance Ar) was used. The calibration gas was flowed through the TPD rig in the same way as the argon carrier gas used in

experiments, but at a flow rate of 65 ml min⁻¹. Partial pressures of mass channels (m/z) of 2 (H₂^{•+}), 16 (NH₂^{•+}), 17 (NH₃^{•+}/OH^{•+}), 28 (N₂^{•+}), 32(O₂^{•+}) and 40 (Ar^{•+}) were monitored until a consistent signal was achieved. A comparable data set was collected for the argon carrier gas, to allow any necessary background corrections to be made, accounting for residual H₂ or NH₃ in the argon supply before signal calibration.

To determine relative sensitivity values (Equation 2-2) for the mass spectrometer, the partial pressure channels of interest (m/z = 2 and 16), H₂⁺ (P_{H_2}) and NH₂⁺ (P_{NH_2}) were first converted to fractions (x_{H_2} and x_{NH_2} respectively) of the observed argon signal (P_{Ar}).

$$x_{H_2} = \frac{P_{H_2}}{P_{Ar}} \qquad x_{NH_2} = \frac{P_{NH_2}}{P_{Ar}} \qquad \text{Equation 2-1}$$

The background fractional amounts of H₂⁺ ($x_{b H_2}$) and NH₂⁺ ($x_{b NH_2}$) in the carrier gas normally used (Ar) were subtracted from the fractional signals observed for H₂⁺ ($x_{c H_2}$) and NH₂⁺ ($x_{c NH_2}$) in the calibration gas (473.6ppm and 498.8ppm, respectively). The relative sensitivity (R_{H_2} and R_{NH_2}) of each was found by dividing the background corrected fractional signals by the defined molar fraction of both in the calibration gas. By dividing by these values, the true values of hydrogen and ammonia released by the sample can be calculated.

$$R_{H_2} = \frac{x_{c H_2} - x_{b H_2}}{4.736 \times 10^{-3}} \qquad R_{NH_2} = \frac{x_{c NH_2} - x_{b NH_2}}{4.898 \times 10^{-3}} \qquad \text{Equation 2-2}$$

When experimental data were collected in TPD-MS experiments a background correction was also required to produce accurate results. Data were collected before the start of each heating regime until the background signals of H₂⁺ ($x_{b H_2}$) and NH₂⁺ ($x_{b NH_2}$) stabilised to give a background value. This value was deducted from the fractional signal amounts (x_{H_2} and x_{NH_2}) observed in the experiment and divided by the relative sensitivity values giving corrected molar fractions for the two channels of interest, ($x^*_{H_2}$ and $x^*_{NH_2}$).

$$X^*_{H_2} = \frac{x_{H_2} - x_{b H_2}}{R_{H_2}} \qquad X^*_{NH_2} = \frac{x_{NH_2} - x_{b NH_2}}{R_{NH_2}} \qquad \text{Equation 2-3}$$

2.2.3 TGA-MS

A Thermogravimetric analyser (TGA, Netzsch 209 TGA) consists of a thermo-microbalance which measures mass change as a function of time or temperature under an inert controlled atmosphere. The temperature of the furnace is “sample-controlled” which allows for more accurate temperature logging. The gas flows vertically from the bottom to the top of the “hot-zone” where the sample is placed, carrying any desorbed gases to the outlet. The gas outlet is connected to a mass spectrometer (Hiden Analytical, HPR20) providing gas desorption data about the sample in question (TGA-MS).

Calibration of the TGA was carried out by measuring the melting points of metal standards before baseline measurements were collected. Melting points of several metals were determined across the temperature range required for these experiments and compared to literature values, providing a multi-point calibration of measured vs. expected temperatures. Recording baseline measurements is essential to ensure the accuracy of TGA results. Baseline measurements were recorded for all heating processes using an empty alumina crucible to account for buoyancy phenomenon, and are automatically subtracted from any data produced. Several factors such as gas flow drag and velocity effects, air buoyancy and temperature gradients contribute to a buoyancy effect, where the empty crucible and lid appear to gain mass under heating. The TGA was located within a flowing argon glove box and approximately 15 mg of sample was loaded into an alumina crucible and placed on a thermo-microbalance and top-loaded vertically into the TGA. The samples were heated at 1, 2, 5, 10 and 15°C min⁻¹ to 400°C under 100 ml min⁻¹ argon and cooled back to room temperature.

2.3 Mass spectrometry

Mass spectrometry is an analytical method which measures quantitatively the mass to charge ratios (m/z) of various charged gaseous ions. A mass spectrometer can scan across a range of undefined m/z values or be pre-set to select specific m/z values, to determine the amounts of each. The m/z values which of specific interest to hydrogen storage work are 2 ($\text{H}_2^{\bullet+}$), 17 ($\text{NH}_3^{\bullet+}$) and 16($\text{NH}_2^{\bullet+}$). The mass spectrometer was used in multiple ion detection (MID) mode to maximise the amount of data collected. The analyte entered the mass spectrometer in an argon carrier gas through a heated capillary with a small diameter to restrict flow rate. This is necessary to maintain a low-pressure vacuum to avoid ion collisions inside the spectrometer. The three main components (processes) in a mass spectrometer are an ion source (ionisation), mass analyser (separation) and a detector (detection).

2.3.1 Ionisation

Samples must be ionised or charged prior to analysis. The method of ionisation usually depends on physico-chemical properties of the analyte and if ions of the molecular species or fragments are required. As analysis in this work was focused on the gas phase, only electron ionisation (Electron impact) was suitable. This technique frequently induces extensive fragmentation. In this source, a heated filament produces electrons by thermionic emission that are accelerated, and *via* energy transfer, an electron can be expelled from the gaseous analyte to create a singly charged molecule. By tuning the energy of the electrons, multiple ionisations can mostly be avoided. As the physical property, the mass-to-charge ratio (m/z), of an ion is measured, not the mass, and so the presence of singly charged species is important. Positively charged ions are then accelerated by a repeller electrode and focussed towards the mass analyser. In this work the fragmentation of NH_3 into NH_2^+ was taken into account by scanning both (m/z) = 17 and (m/z) = 16.

2.3.2 Separation

In this work a quadrupole mass analyser was used. A quadrupole mass analyser works on the principle of trajectory stability in an oscillating electric field to separate cations according to the m/z values. A quadrupole analyser consists of four parallel rods, ideally hyperbolic in shape, where each opposing pair is electrically connected. By oscillating the potentials, the cation moves towards a negatively charged rod and as the potential switches the ion changes direction. Specific combinations of potentials and frequencies will produce a stable trajectory for certain ions (with a specific m/z ratio) to reach the detector (Figure 2-2). By varying the oscillating radio field, a range of preselected m/z values can be measured.

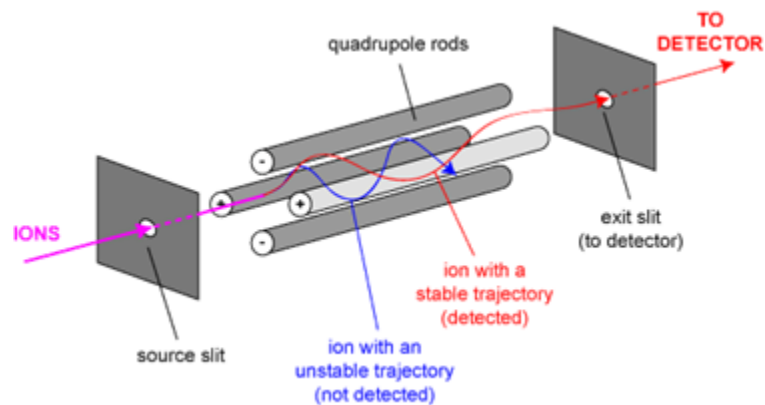


Figure 2-2: Schematic diagram of a quadrupole mass analyser².

2.3.3 Detection

The detector transforms the number of incident ions into an electric current proportional to the abundance of the m/z ratio. In a Faraday cup detector, a current is produced through electron transfer when an ion is neutralised on the surface. The current produced is proportional to the number of ions detected for each m/z value. This method of detection has low sensitivity, so a secondary electron multiplier (EM) may also be used. Positively charged ions are accelerated into a negatively charged conversion dynode at high potential, causing several negative secondary particles (*e.g.* electrons) to be released. By amplification of electrons through additional discrete or continuous dynodes, a cascade of electrons is created and the resulting current is measured.

However, the accuracy of an EM is affected by the nature (impact velocity, mass etc.) of the ions, so the precision is not as high when compared to ion detection in Faraday cups.

2.4 Hydrogenation

A crude hydrogenation method was used to determine the potential reversibility of a sample. By leaving a sample under a high hydrogen pressure and heating to a fixed temperature for between 12 and 24 hours it could usually be seen whether hydrogenation was possible. Ideally once it had been determined that a sample had the capacity to absorb hydrogen, refined hydrogenation experiments using a manometric gas sorption analyser would have been carried out. This would have allowed hydrogen absorption to be measured quantitatively as a function of pressure and/or temperature. Using a range of temperatures, a series of pressure-composition-isotherms (PCI's) could have been recorded to form a pressure-composition-temperature (PCT) diagram. Unfortunately, due to lack of sufficient equipment time, although this work was planned, it was not possible to carry out these measurements.

2.4.1 Crude hydrogenation

A previously described³ homebuilt stainless steel hydrogenation reactor vessel and gas manifold set-up were used in order to study the rough hydrogenation properties of samples. Samples of ~0.15g were prepared and loaded in quartz reaction tubes (7 mm O/D, 4 mm I/D) and sealed at one end. The quartz tubes were loaded into the bottom of the hydrogenation vessel, sealed up to 60 Nm² in the glove box and further sealed up to 90 Nm² on removal, using an adjustable torque wrench. The reactor was placed in a vertical tube furnace, then exposed to an argon-filled manifold system. The whole system (manifold and vessel) was evacuated and purged with argon several times before undergoing the same routine with low pressure hydrogen. A pressure release valve was used to vent any excess pressure build up.

A hydrogen pressure of around 80 bar was then set to allow for pressure build up due to increased temperature. As the pressure gauge was on the gas manifold system, whilst heating took

place the vessel and manifold were sealed together to allow monitoring of the hydrogen pressure. Leak checks on the whole system were carried out at different stages in the process using hydrogen monitors. On completion of the heating regime, the hydrogen pressure was vented and the system evacuated and purged again to refill it with argon before returning it to the glove box.

2.5 Raman spectroscopy

Raman spectroscopy is a technique used to measure vibrational, rotational and other low frequency phonon modes of atoms, bonds and molecules in crystals. Raman spectroscopy plots the intensity of photon scattering as a function of wavenumber. For a frequency mode to be Raman active, the thermal motion must be accompanied by a change in the direction or degree of polarisability of the molecule. Symmetric stretches are typically accompanied by the biggest change in polarisability, giving rise to the most intense bands in the spectrum whilst asymmetric movements are weaker. Whether a vibration is Raman active is governed by group theory, based on the molecules' symmetry.

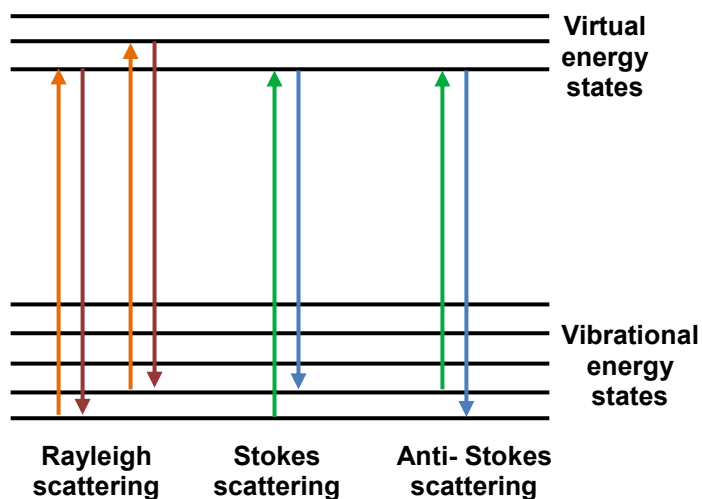


Figure 2-3: Schematic diagram of Raman and Rayleigh scattering showing the states and transitions involved.

Inelastic or Raman scattering of monochromatic light (with a wavelength within infrared, visible or ultraviolet) must be observed upon irradiation of the sample to observe a Raman spectrum. Inelastic scattering occurs when the molecule is shifted by one vibrational energy unit, as depicted in Figure 2-3. When the sample is irradiated the energy from the photon is absorbed

by the molecule, causing a polarisation of the electron cloud around the nuclei and this forms a higher (virtual) energy state. The energy of this is dependent on the wavelength of the incident radiation. Relaxation of the molecule from the unstable short lived energy state back to the vibrational energy states is accompanied by the emission of a photon. For the majority of transitions, the energy of the emitted and absorbed photons is very similar as scattering by electrons is very slight, which leads to elastic or Rayleigh scattering.

When the energy of the emitted photon is different to that of the absorbed photon, caused by inelastic interactions, this is either Stokes or Anti-Stokes scattering. When inelastic scattering is observed, induced nuclear motion may transfer some energy to the photon from the molecule or vice-versa. This can result in the molecule returning to an excited state (Stokes), or returning to the ground state from a previously excited state (Anti-Stokes). The occurrence of spontaneous Raman scattering is often very weak, around 1 in 10^6 - 10^8 photons. The observation of Stokes scattering will be dominant due to the nature of conducting experiments at close to or at room temperature, where most molecules reside in the ground vibrational state. The exchange of energy during these scattering events is depicted in Figure 2-3.

Ex-situ Raman spectra were collected using a Renishaw InVia Raman microscope using a Helium-Neon 633nm laser coupled to a grating with 1200 lines/mm. Samples were loaded and sealed into a THMS 600 cell inside an argon filled glove box before being transferred to the Raman microscope. In-situ spectra were collected using an Argon 488nm laser and an Instec HCS621V cell under 1 bar flowing argon, heated at $2\text{ }^\circ\text{C min}^{-1}$. Auto-focus was completed after every 10 spectra, which were recorded directly after one another.

2.6 Differential scanning calorimetry

Differential scanning calorimetry (DSC, Netzsch DSC204HP) is a technique used to study the thermal transitions of a sample under controlled heating, cooling and atmosphere. Data can be used to provide information on exothermic and endothermic events such as enthalpies of phase

transitions, temperatures of melting and crystallisation. In this work, DSC was used to measure the difference in heat flux between the sample pan and empty reference pan when both were subjected to identical heating and cooling regimes, under a fixed pressure. Recording the sample mass accurately, allows the calorimetric data collected to be used for calculations to calculate quantitative values (*e.g.* desorption enthalpy).

The DSC was calibrated by recording the melting points of set metal standards, the same as described in Section 2.2.2 for calibration of the TGA. Baseline correction files were measured with two empty pans under the conditions to be run, to compensate for any background readings generated from residual heat flow signal when the DSC is operated empty. This was especially important when the data were used for calculating enthalpies, as the area under or above the curve from the baseline gives the total heat flux for the thermal event in terms of sample mass.

The DSC was located within a flowing argon glove box. Approximately 15 mg of sample was loaded into a shallow aluminium pan. Consistent sample masses (within ~2 mg) were maintained to ensure no heat lag effects were observed. The sample pan and the empty reference pan were both fitted with lids and loaded into the DSC. The sample environment was controlled and maintained at 3 bar Ar, at a flow rate of 100 ml min⁻¹ throughout the experiment. Samples were heated at 2°C min⁻¹ to 400°C and cooled at 2°C min⁻¹ back to room temperature.

2.7 Crystallography¹

Crystallography is the study of the arrangement of atoms in the solid state. This can include ordered crystalline materials as well as highly disordered solids and some amorphous solids. Amorphous solids have a high degree of disorder and as such there is no specific repeating unit which can be used to describe the arrangement of atoms within an amorphous material. Nevertheless, it is possible to study the structure of the solid using, for example, total scattering techniques. The structure of these solids cannot be studied by crystallography. A crystalline material is defined as one which has long range order that extends in all directions. The essential

3-D structure and symmetry can be completely described by the smallest single repeating unit, the “Unit Cell” which, through translational symmetry gives entire crystal lattices.

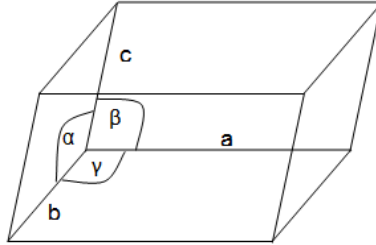


Figure 2-4: Generalisation of a 3-D unit cell.

The unit cell can be described by the lattice parameters which are the axial distances a , b and c and the angles linking them together α , β , and γ which are measured from a common origin. The unit cell is defined by lattice points which are equivalent symmetry positions in space. The environment of an atom sited at a specific location would be the same as an atom positioned at any other equivalent point in the lattice. The lattice does not include information on the atoms within the unit cell but rather shows the repeating nature of the crystal.

2.7.1 Lattice points

Lattice points are used to define the four possible lattice types, of which the simplest is a primitive cell (P) with only 1 lattice point per cell, i.e. at the corners. The introduction of additional lattice points at the centre of the unit cell produces a body-centred cell (I) and those centred on the unit cell faces give face centred cells (F & C). There are 5 two-dimensional lattices as shown in Figure 2-5 which describe all 2D patterns.

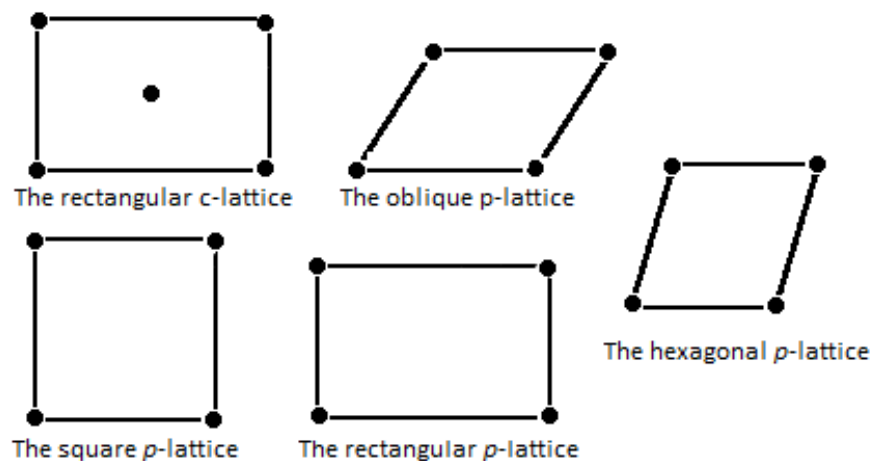


Figure 2-5: Unit cells of the five plane lattices¹.

2.7.2 Crystal systems

There are 7 crystal systems, which are constructed by stacking various plane lattices, for example, cubic or tetragonal crystal systems can be produced by stacking rectangular lattice layers in a variety of ways. By combining the crystal systems and lattice types, 14 three-dimensional Bravais lattices are produced, which include essential symmetry elements. All crystal structures are based on these lattices which are outlined in Table 2-1.

Upon addition of atoms into these seven crystal systems, supplementary information is required to fully describe the cell. By considering the symmetry elements, the structures can be further described by 32 crystal classes, also known as point groups. The associated space group symbol gives details of the main symmetry elements described by that group; such as glide and mirror planes, or inversion and screw axes.

Crystal systems are either centrosymmetric or non-centrosymmetric. Non-centrosymmetric space groups can then be further divided into non- or enantiomorphous space groups; the latter do not possess any planes/centres of symmetry. By combining symmetries, 230 three-dimensional space groups can be fashioned, which allow the symmetry elements of a crystal structure to be completely described.

Crystal System	Unit Cell Dimensions	Essential symmetry	Allowed Space lattices
Cubic	$a = b = c$ $\alpha = \beta = \gamma = 90^\circ$	Four threefold axes	P, I, F
Tetragonal	$a = b \neq c$ $\alpha = \beta = \gamma = 90^\circ$	One fourfold axes	P, I
Orthorhombic	$a \neq b \neq c$ $\alpha = \beta = \gamma = 90^\circ$	Three twofold axes	P, I, F, C
Hexagonal	$a = b \neq c$ $\alpha = \beta = 90^\circ \gamma = 120^\circ$	One sixfold axis	P
Rhombohedral/ Trigonal	$a = b = c$ $\alpha = \beta = \gamma \neq 90^\circ$	One threefold axis	R
Monoclinic	$a \neq b \neq c$ $\alpha = \gamma = 90^\circ \beta \neq 90^\circ$	One twofold axis	P, C
Triclinic	$a \neq b \neq c$ $\alpha \neq \beta \neq \gamma \neq 90^\circ$	none	P

Table 2-1: Crystal systems and Bravais Lattices.

2.7.3 Lattice planes and Miller indices

Lattice planes are made up of a repeated arrangement of lattice points which extend in three dimensions. Lattice planes in a three-dimensional unit cell are independent of symmetry and allow a face or plane within a lattice to be exactly expressed. The description of the position of a lattice plane is based on vectors which define the unit cell. Directional lattice vectors must pass through the origin and allow any point along the vector to be defined as fractions of the unit cell lengths.

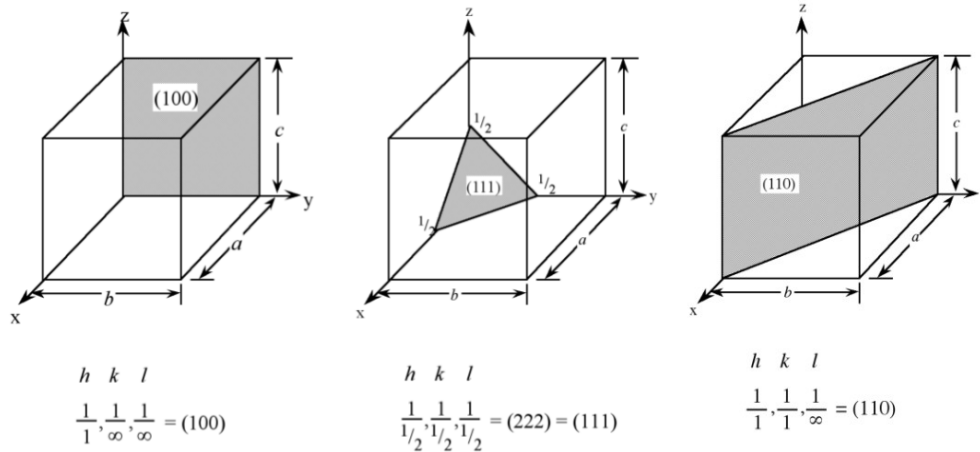


Figure 2-6: Examples of the notation of Miller indices¹¹⁰

Miller indices, such as the examples shown in Figure 2-6, are used to describe the orientation of lattice planes, and are given by the three intercepts of the plane on the unit cell vectors (or cell edges), a , b and c (as shown in Figure 2-4). The Miller index is described as the reciprocal of the fractions along the edge lengths, i.e. $(a/h, b/k, c/l)$ would be the (hkl) plane. A lattice plane extends throughout the crystal and due to the repeating nature of the unit cell, can be thought of as parallel, equally spaced planes intersecting the crystal. The perpendicular distance between these planes is denoted as the d-spacing (d_{hkl}). If the symmetry of the cell allows, i.e. in a cubic cell, various lattice planes may be equivalent to one another which gives the multiplicity of a plane. A relationship between the d-spacing, a given (hkl) plane and lattice parameters exists for all crystal systems, the simplest of which is the cubic cell shown in Equation 2-4.

$$d_{hkl} = \frac{a}{\sqrt{h^2 + k^2 + l^2}} \quad \text{Equation 2-4}$$

2.8 Diffraction

Diffraction^{1, 111} is a phenomenon that occurs when any wave, including electromagnetic radiation encounters an object. X-ray diffraction is one the most common techniques used to determine structures of crystalline solids. X-rays are part of the electromagnetic radiation

spectrum with a wavelength of approximately 1 Å. This is comparable to inter-atomic distances, making them ideal to probe the structures of crystals. The resulting diffracted data are therefore a direct representation of the arrangement of the atoms.

2.8.1 Bragg Equation

A crystal lattice of atoms acts as a 3-dimensional diffraction grating for short wavelength radiation like X-rays. However, Bragg devised a heuristic method of interpretation based on the reflection of X-rays by 2-D planes of atoms in the crystal, shown in Figure 2-7.

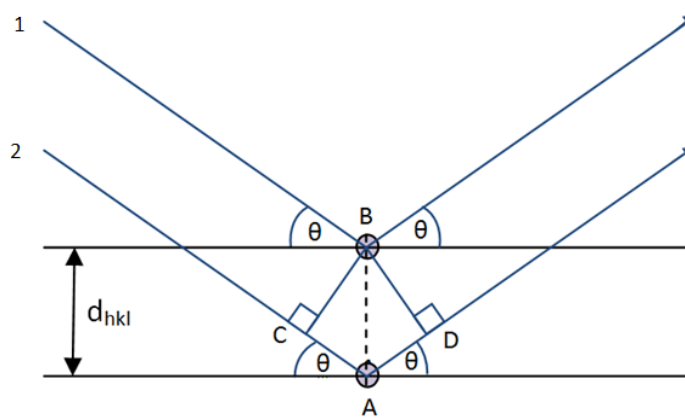


Figure 2-7: The 2-D geometry used to show the derivation of Bragg's law.

Intensity will be observed at any given 2θ when superposition of the waves occurs causing positive interference, *i.e.* when Bragg's Law is obeyed. If the X-rays (1 and 2) are incident on a surface of a crystal with angle θ and are scattered by the two consecutive planes separated by d_{hkl} one of the waves (2) must travel further than the other (distances CA and AD). By applying trigonometry using Pythagoras' theorem the difference in path length (Δ) can be expressed in terms of d_{hkl} and θ as shown in Equation 2-5.

$$\Delta = CA + AD = 2(d_{hkl} \sin \theta) \quad \text{Equation 2-5}$$

For constructive interference to occur, the path difference must be equal to an integer multiple (n) of the wavelength, which gives Bragg's Law (Equation 2-6).

$$n\lambda = 2d \sin \theta \quad \text{Equation 2-6 : Bragg's Law}$$

In all other situations, no solution exists and destructive interference is observed and no peak will appear in the diffraction pattern. However, in real applications the model is not as simple: scattering occurs from many planes in a crystallite and X-ray scattering is not from a point source, but an electron cloud around the atom. The interaction of X-rays and electrons in any given material produces a unique diffraction pattern related to the d-spacing of that specific material.

2.8.2 Powder X-ray diffraction^{112, 113}

In a powder sample, there are many crystallites which are randomly orientated. Ideally, every potential orientation is uniformly represented across the sample. The random nature of the sample means that X-rays interacting with the sample are scattered in all different directions. Diffraction from each lattice plane (100), (111), etc. instead of producing a discrete Laue spot in the reciprocal lattice, (for a single crystal) produces a diffraction cone or Debye–Scherrer ring as shown in Figure 2-8. The cone consists of many dots, each coming from a specific crystallite with the correct orientation to satisfy Bragg’s law. The data is then displayed as a function of 2θ vs the intensity of X-rays measured at the detector.

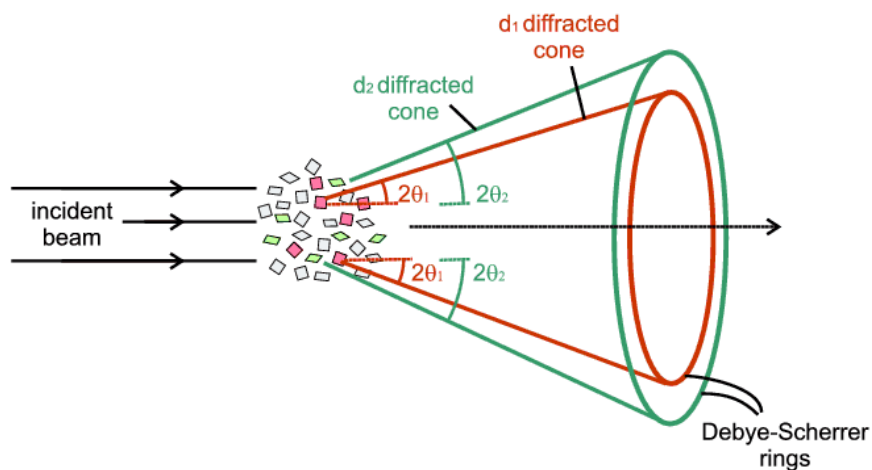


Figure 2-8: Diffraction cones of two lattice planes with d-spacing's d_1 and d_2 ¹¹⁴.

Complex 3D structural information can be elucidated from a 1-D powder diffraction pattern; there are three main components (described in Table 2-2) in powder diffraction patterns which are significant. The background is another element of the pattern that, while usually due to the contribution of external factors such as the instrument or container, should not be disregarded.

Pattern Component	Main influences	Other Factors
Peak Position	Unit cell parameters (a, b, c, α , β , γ) Symmetry Wavelength of radiation (λ)	Systematic distortions such as zero-point error, sample height or surface curvature
Peak Intensity	Structure factor Unit cell centring	Preferred orientation
Peak Shape	Particle size Crystallinity	Instrumental broadening Wavelength dispersion Micro-Strain, Structural faults

Table 2-2: Summary of key factors in a powder diffraction pattern and their main influences.

A large background signal may be caused by amorphous materials in a sample, and also absorption or fluorescence from the sample. A technique which utilises the information in the diffuse scattering part of the background is Pair Distribution Function (PDF) analysis which can, for example, help resolve local disorder in crystalline materials.

Table 2-2 shows the key aspects of a powder diffraction pattern caused by the phases present and the variables which influence the complete observed diffraction pattern. It should be noted that there is a difference between relative intensities and the global intensity of the diffraction pattern. The global intensity of a pattern is determined by experimental features, such as data collection time, intensity of the radiation and quality of the detector, as well as the scattering power of the elements within the sample. In a sample which contains multiple phases, the relative intensities of all Bragg peaks in each phase are dependent on the relative quantity of that phase. However, the relative Bragg peak intensities of a phase can be affected by broadening

caused by small crystallite sizes. If peaks undergo broadening the apparent intensity will decrease as the area under the peak will remain the same. There are several contributing factors to the intensity (I_{hkl}) of the Bragg peaks but the structure factor (F_{hkl}) contributes the largest term. Equation 2-7 demonstrates this.

$$I_{hkl} = S \cdot K_{hkl} \cdot m_{hkl} \cdot A_{hkl} \cdot Lp_{hkl} \cdot (F_{hkl}^2) \quad I_{hkl} \approx |F_{hkl}|^2 \quad \text{Equation 2-7}$$

where;

S : scale factor

K_{hkl} : proportionality constant

m_{hkl} : multiplicity of the Bragg reflection

A_{hkl} : absorption correction

Lp_{hkl} : Lorentz (angle dependence of intensities) and radiation polarization

The structure factor includes information on atomic positions, types, multiplicity and thermal parameters, the latter is necessary as it includes information on the thermal movement of the atoms which results in a reduction in observed intensity.

The structure factor (F_{hkl}) is defined as:

$$F_{hkl} = \sum_{j=1}^N f_j N_j \exp[2\pi i(hx_j + ky_j + lz_j)] \exp(-B_j \sin^2 \theta / \lambda^2) \quad \text{Equation 2-8}$$

where;

f_j : atomic scattering power of atom j

N_j : number of atoms in the unit cell

x_j, y_j, z_j : fractional co-ordinates of atom j in the unit cell

B_j : thermal isotropic displacement of atom j , $B_j = 8\pi^2(\bar{u}^2)^j$

If there are multiple phases within a sample, then the intensity at any point in the diffraction pattern will be a sum of contributions from all overlapping Bragg peaks and the background (y_{bi}). The intensity of a Bragg peak is distributed across 2θ angle according to the peak shape function used. Therefore, the intensity ($y_{i(calc)}$) at any given 2θ point can be calculated as:

$$y_{i(calc)} = \sum_n \left(\sum_{hkl} I_{hkl} \cdot P_{hkl} \cdot \Phi(2\theta_{hkl} - 2\theta_i) \right) + y_{bi} \quad \text{Equation 2-9}$$

where:

n : number of phases

P_{hkl} : preferred orientation contribution

Φ : peak profile function

2.8.3 X-ray generation

For laboratory experiments, X-rays are generated by electrons, emitted from a hot cathode, through collision with a metal target. It is a very inefficient process with less than 1% of the beam energy generating usable X-rays. Typically, the cathode is a tungsten filament and the electrons released are accelerated by a high voltage towards the anode (usually a copper metal target). Upon the collision of high energy electrons into the metal target, electrons from core

orbitals are excited and ejected, with X-ray radiation accompanying the resultant electron decay from a higher orbital.

A typical X-ray spectrum of Cu is shown in Figure 2-9, the positions of the spectral lines are characteristic for each metal. The transitions ($K_{\alpha 1}$, $K_{\alpha 2}$, K_{β}) correspond to the strongest intensity wavelengths and result from electrons in the 2p (K_{α}) and 3p (K_{β}) shells dropping down to the 1s orbital. Multiple transitions can be observed due to the number of subshells in any given orbital, if quantum selection rules are obeyed.

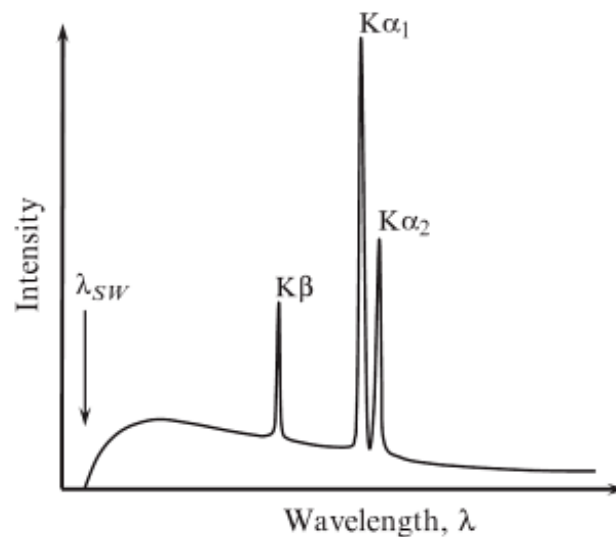


Figure 2-9: Schematic X-ray emission spectrum from a copper target showing the relative intensities of K_{β} and K_{α} and the presence of background “*bremsstrahlung*” white radiation¹¹³.

2.8.4 Monochromation

X-rays across a wide range of wavelengths, from discrete atomic transitions and continuous background radiation are produced in varying intensities, this is not ideal for XRD. In order to select the most intense wavelength of radiation a single-crystal monochromator is usually used. By careful orientation of the crystal at angle θ so that the wavelength required, normally $K_{\alpha 1}$ as the most intense, satisfies Bragg’s law, a monochromatic X-ray beam can be produced.

2.8.5 Detection

Traditionally, a scintillation point detector is used, where X-rays impact on a phosphorescent surface which subsequently releases photons. The photon signal is then amplified and recorded so that signal intensity can be directly related to the impacting X-rays at a single 2θ angle. By using a linear position sensitive detector (PSD), X-ray intensity can be continuously detected over a range of 2θ angles simultaneously. In order to ensure high accuracy of results, a goniometer was used to precisely measure the geometry of the equipment setup, particularly the angles between the X-ray source and detector. Both Bragg–Brentano (reflection) and Debye–Scherrer (transmission) geometries were used.

2.8.6 Data collection

Powder X-ray diffraction data were collected on a Bruker D8 Advance diffractometer in transmission mode and a Siemens D5005 diffractometer in capillary mode. Both machines were fitted with a germanium monochromator and copper target to produce $\text{Cu K}\alpha_1$ radiation with a wavelength of 1.5406 Å. Samples were reground and placed between amorphous Scotch-Tape or filled in polyimide tubing sealed with glue for data collection in transmission and capillary modes, respectively. The samples were spun perpendicular to the X-ray beam to ensure that a good powder average was achieved. Spinning samples reduces the effects of large crystallites in a single orientation which would not give a true representation of the sample. Spinning capillary samples allows more of the crystallites to satisfy the Bragg condition more of the time resulting in better resolved patterns for small quantity powder samples.

2.8.7 Synchrotron powder X-ray diffraction

A synchrotron works by generating and accelerating a highly-focused beam of charged particles, nominally electrons. The electrons are then accelerated, first by the linear accelerator, and then their energy is increased by electro-magnets in the booster ring, until they have enough energy to produce light. They are then injected into the storage ring and bending and wiggling

magnets are used to steer the electrons around a polygon shape, made up of straight sections. The loss of energy during the bending process produces photons which go into the experimental beamlines where the light is filtered and focused into an intense beam. Samples for testing are then placed into the path of photons on the beamline.

Powder synchrotron X-ray diffraction data were collected at Diamond Light Source, UK on I11 beamline. Samples were measured using a wavelength of 0.826205 Å. Ground samples were prepared and sealed into 0.5 mm borosilicate capillaries in an argon filled glovebox using resin and rotated in the X-ray beam during measurement.

2.9 Rietveld analysis¹¹⁵⁻¹¹⁷

Rietveld analysis provides a method allowing the refinement of several given structures simultaneously, including any overlapping peaks. The aim of the Rietveld method is to minimise the difference between observed and calculated powder diffraction patterns *via* a least squares method.

The observed intensity detected in a diffraction experiment at any point has several contributing factors that must all be described accurately to minimise the difference in the calculated intensity. Intensity contributions are described by structural models and experimental factors from the sample and instrumental set-up, which include background factors and peak shape function profiles. The background was typically described using a Chebyshev polynomial function, where the minimum number of coefficients needed to fully describe the profile observed were used. The minimum number of coefficients required was determined by an initial visual inspection followed by an assessment of the R_{wp} factor without any structural information in the fit.

The peak shapes of all phases observed in the sample must also be described. Multiple factors that influence the Bragg peak shapes include instrumental traits such as beam collimation; detector resolution and sample effects have already been described in Table 2-2.

These have been convoluted into peak shape profile functions which are linear combinations of Gaussian and Lorentzian functions, commonly such as Thompson-Cox-Hastings or Pseudo-Voigt profile functions. Although peak positions are mainly described through a relevant structural model, factors such as zero-point error should also be included in any refinement.

As Rietveld analysis is used as a structural refinement method rather than for structure solution, a reasonable starting model is required. If the structural model is unknown then by indexing Bragg peaks and determining lattice parameters, a space group and subsequently crystal structure of the phase can be generated. Finally, through Rietveld analysis a refinement to produce an accurate structure can be carried out. The structural model describes the crystal structure of a material, with information on unit cell dimensions, atomic positions, their occupancies and thermal parameters. The commonly refined parameters are shown in Table 2-3.

Phase associated	Scale factor, Unit cell parameters, Atomic co-ordinates and Occupancies, Thermal parameters (aniso- and iso-tropic), Peak profile parameters (crystallite size and strain), Preferred orientation
Global parameters	Background, Zero Point error, Instrument Profile, Sample displacement and absorption

Table 2-3: Commonly simultaneously refinable parameters.

Through variation of these factors, the residual (S_y) is reduced through a least squares refinement until the difference between calculated ($y_{i(\text{calc})}$) and observed ($y_{i(\text{obs})}$) intensities at the i^{th} step is at a minimum (Equation 2-10). A statistical weighting factor (w_i) is included.

$$S_y = \sum_i w_i [y_{i(obs)} - y_{i(calc)}]^2, \quad w_i = \frac{1}{y_{i(obs)}} \quad \text{Equation 2-10}$$

To assess the quality of the calculated diffraction pattern and observe how variations to the structural model modify the calculated data, several statistical 'R-values' can be examined. For this purpose, the 'R-weighted pattern' (R_{wp}) is a good reflection of the progression of a complete refinement due to the inclusion of the residual function (Equation 2-11)

$$R_{wp} = \sqrt{\frac{\sum w_i [y_{i(obs)} - y_{i(calc)}]^2}{\sum w_i [y_{i(obs)}]^2}} \quad \text{Equation 2-11}$$

As R_{wp} gives a measure of the complete pattern the value can be falsely manipulated, by a high background which is well fitted or strong peaks which are not included or fitted in the Rietveld phase. This may mean that a background subtracted R'_{wp} value should be examined, which includes a background term (y_{bi}), usually a polynomial term. This is a more representative value of the quality of data and the corresponding fit to the data (Equation 2-12)

$$R'_{wp} = \sqrt{\frac{\sum w_i [y_{i(obs)} - y_{i(calc)}]^2}{\sum w_i [y_{i(obs)} - y_{bi}]^2}} \quad \text{Equation 2-12}$$

The best possible value that R_{wp} could reach is 'R-expected' (R_{exp}). The R_{exp} value is mainly based on the quality of data, where N is the number of observables (which often dominates the numerator expression), P is the number of parameters and C is the number of constraints used (Equation 2-13).

$$R_{exp} = \sqrt{\frac{N-P+C}{\sum w_i [y_{i(obs)}]^2}} \approx \sqrt{\frac{N}{\sum y_i}} \quad \text{Equation 2-13}$$

By comparing differences in the values of R_{exp} and R_{wp} an additional statistical value (χ) can be defined (Equation 2-14)

$$\chi^2 = \left[\frac{R_{wp}}{R_{exp}} \right]^2 \quad \text{Equation 2-14}$$

This value is also an important indication of the quality of a refinement as it includes the number of refined parameters (degrees of freedom); the lower the value the better the fit. However, poor quality data with large step sizes and well modelled high background intensity can artificially deflate the χ^2 value. High quality data is likely to provide refinements with larger χ^2 or R_{wp} values, but the model generated is also expected to be superior quality.

Along with assessing the statistical values discussed above, a careful visual inspection of the evolution of the difference and fit lines produced should always be undertaken. Numerical R-values obtained should not be a substitute for good scientific judgement as to the global quality of the refinement and chemical soundness of the structural model produced.

2.10 Quantitative phase analysis

X-ray diffraction coupled with Rietveld analysis delivers a powerful method which provides accurate estimations of phase abundances in a sample¹¹⁸. Although techniques such as X-ray fluorescence (XRF) perform elemental analysis on a sample, phase abundances for a mixture determined using Rietveld analysis, have been found to correlate well with the overall chemical composition of a sample as determined by XRF. The weight percent (W_p) of the phase p is calculated using Equation 2-15.

$$W_p = \frac{S_p(ZMV)_p}{\sum_{i=1}^n S_i(ZMV)_i} \quad \text{Equation 2-15}$$

where:

S : scale factor

Z : number of formula units in the unit cell

M : mass of formula unit (atomic masses)

V : volume of the unit cell (\AA^3)

A refinement strategy for quantitative phase analysis (QPA) was developed for the identification of multiple phases in a sample, whereby only the lattice parameters, scale factor and peak shape profile functions were refined for each phase. The atomic positions and thermal parameters were fixed according to published crystallographic information files (.cif) of pure phases, obtained from the Inorganic Crystal Systems Database (ICSD). Since any factor that could affect Bragg peak intensities will cause an irregularity in the determined weight percent's' of the phases, consideration must be given to them, including how effects can be minimised. The most prominent of these are preferred orientation and extinction effects.

By introducing experimental controls these effects can be minimised, firstly as samples were spun during data collection, effects of preferred orientation were greatly reduced. Secondly, to diminish extinction effects, samples were all hand-ground or ball-milled prior to measurements being taken. This ensured that homogeneity of grain sizes and crystallinity was maximised across all phases in the sample. As most elements in this work were light elements, the expected absorption was already at a minimum. In addition, loading samples into capillaries reduced the cross-sectional area of the sample and helped to reduce absorption.

It should be assumed that refinements for QPA followed the strategy defined above unless explicitly indicated otherwise. In this work TOPAS Academic¹¹⁹ (Total Pattern Analysis Solutions) was used for analysis of powder X-ray diffraction data.

3 Effects on the Li–Mg–N–H system of various preparation methods and reaction conditions

3.1 Introduction

Both the Li–N–H and Li–Mg–N–H systems have been widely studied^{2, 23, 54, 55, 75, 120, 121} by many groups. There is considerable debate in the extensive literature available on this basic system as to how the hydrogen storage properties are affected by the choice and amounts of starting materials and subsequent preparation of the system. Some have concentrated on identifying the products of dehydrogenation, while others have focused on the thermodynamics and kinetics of these reversible systems. The inclusion of magnesium into the system has shown a large improvement in several properties that are of importance for hydrogen storage work.

One of the biggest topics of discussion in this system is how preparation of the system affects the results of de- and rehydrogenation. An overview of some literature was presented in Chapter 1. The work in this chapter specifically focuses on the effects of ball-milling and its conditions on the starting materials along with the identity of starting materials. The Li–Mg–N–H system can be accessed from LiNH_2 and MgH_2 or $\text{Mg}(\text{NH}_2)_2$ and LiH . While some publications⁶⁴ find little or no difference between the products and pathways observed when the starting materials are different, others¹²² suggest that $\text{Mg}(\text{NH}_2)_2$ and LiH should be the preferred starting materials. Reasons include the rapid reaction of LiH with ammonia and a lower enthalpy of decomposition of $\text{Mg}(\text{NH}_2)_2$ than LiNH_2 which lowers the desorption temperature. However, ultimately, as the thermodynamically preferred rehydrogenation products are $\text{Mg}(\text{NH}_2)_2$ and LiH , the initial choice of starting materials should be irrelevant when this system is proposed for cyclic use as a hydrogen store.

The importance of the method of preparation is also contested. While some studies focused on varying the ball-milling regime,^{82, 123, 124} others advocated that the ball-milling regime was less important but more vital were the reactions that could be facilitated during ball-milling¹²⁵. The physical changes ball-milling can make to a sample are also very important when considering the effects of hydrogen storage. For example, the particle sizes can be dramatically reduced, increasing surface area and contact between respective reactive phases. Partial desorption and/or metathesis could also occur which can enable seeding of the desired products and introduce strain into the material⁸².

More complicated versions of the Li-Mg-N-H system have now been developed, where various compounds have been substituted and/or included to improve the hydrogen storage properties. Several of these variations were investigated in this work and will be discussed in Chapter 4. Work in this chapter will focus on the effects on the basic Li-Mg-N-H system when the preparation methods are varied.

3.2 Experimental

The doped Li-Mg-N-H systems were made from either LiNH₂ (Sigma-Aldrich, 95%) and MgH₂ (Alfa-Aesar, 98%) used in 2:1 ratio or Mg(NH₂)₂ (prepared 'in-house') and LiH (Sigma-Aldrich, 95%) used in 1: 2 ratio. The samples were used for a selection of experiments, some with preparation conditions, such as hand grinding or ball-milling as described below.

Samples were ball-milled in 250 ml stainless steel milling pots in a Retsch PM400 planetary ball-mill at 300 rpm for 24 hours with a ball to sample mass ratio of 40:1. To prevent excessive temperature rises in the milling vessel, 2 minutes of milling were followed by 2 minutes paused. Samples were ball milled under two conditions, either argon gas at 1 bar or hydrogen gas at 100 bar. Some samples were heated under flowing argon to temperatures between 150°C and 400°C for up to 72 hours (preparation according to chapter 2.1.1). Magnesium amide was

synthesised from a ball-milled sample of MgH_2 . MgH_2 was heated under flowing ammonia gas at 300°C for 24 hours, reground by hand and re-heated for a further 24 hours under the same conditions. Ex-situ powder X-ray diffraction data were recorded using a Siemens D5005 instrument in capillary mode with a wavelength of 1.5406 \AA (Chapter 2.7.6).

TPD-MS samples were heated at a ramp rate of 2°C min^{-1} to 400°C and held for short time before the power was cut. Samples were reground before powder XRD measurements were collected. TGA-MS samples were heated at various ramp rates, 1, 2, 5, 10 and $15^\circ\text{C min}^{-1}$ to 400°C and cooled to room temperature. DSC samples were heated at a ramp rate of 2°C min^{-1} to 400°C and subsequently cooled to 25°C under 3 bar argon. Raman spectra were collected on a Renishaw inVia Raman microscope operating with a 633 nm laser using a cell sealed under an argon atmosphere.

Samples selected for rehydrogenation were re-ground, sealed in an airtight steel reactor and pressurised to 100 bar H_2 before being heated at a ramp rate of 2°C min^{-1} to 200°C and held for 24 hours. When post rehydrogenation powder XRD data were required, samples were reground before PRXD measurements were collected. The cycled samples were dehydrogenated at 220°C for 50 hours before being rehydrogenated as per the conditions above. The process was repeated 3 times to produce the 'cycled' sample.

3.3 Comparing TPD-MS and TGA-MS of Li-Mg-N-H samples

3.3.1 Thermal desorption

Thermal desorption data were recorded from a hand ground control sample (2LiNH_2 and MgH_2) and collected on TPD-MS and TGA-MS equipment to make a comparison of the results under identical ramping conditions.

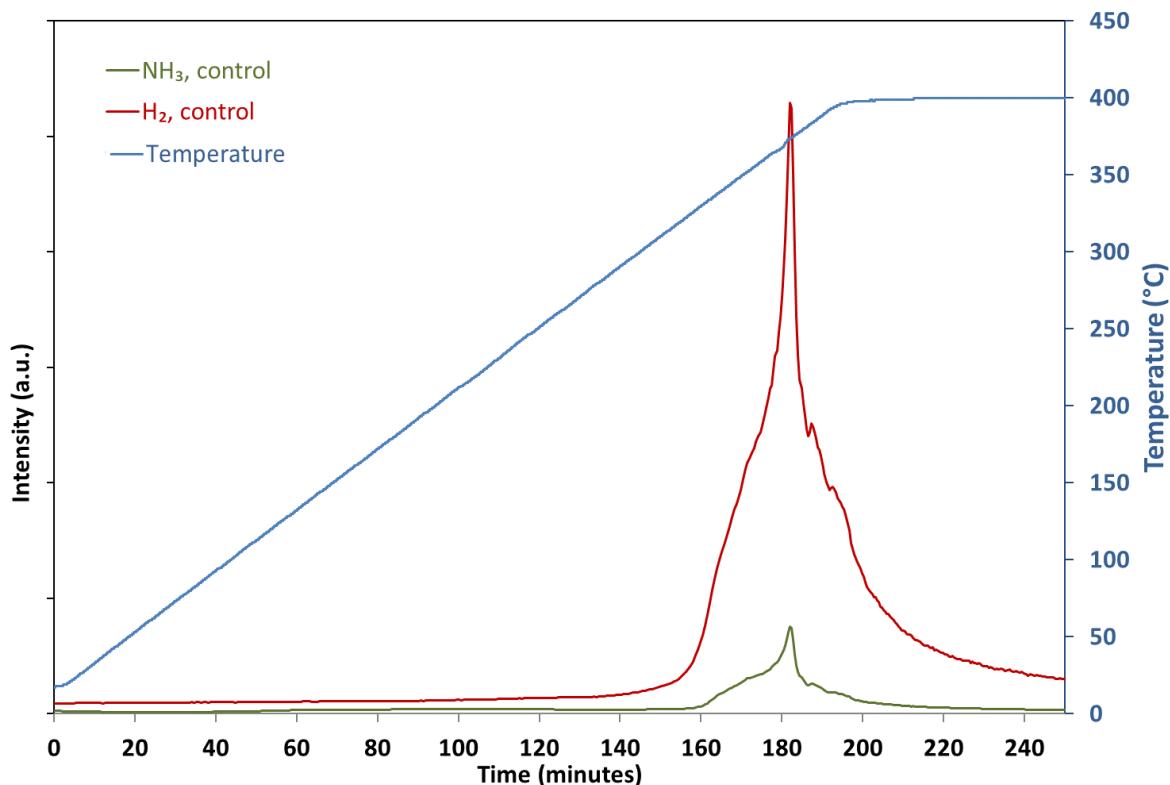


Figure 3-1: TPD-MS trace of the $2\text{LiNH}_2 + \text{MgH}_2$ hand-ground control sample heated at 2°C min^{-1} , showing gas release against time, H_2 (red), NH_3 (green) and temperature (blue).

Figure 3-1 shows the desorption trace recorded on the TPD-MS equipment. The hydrogen desorption peak was sharp and peaked at 374°C , with considerable hydrogen release continuing after the main peak. Additional details in the desorption trace were observed between 380°C and 390°C , which may indicate that two hydrogen producing reactions that peak at different temperatures were occurring. Some ammonia release was also detected and peaked at around 375°C .

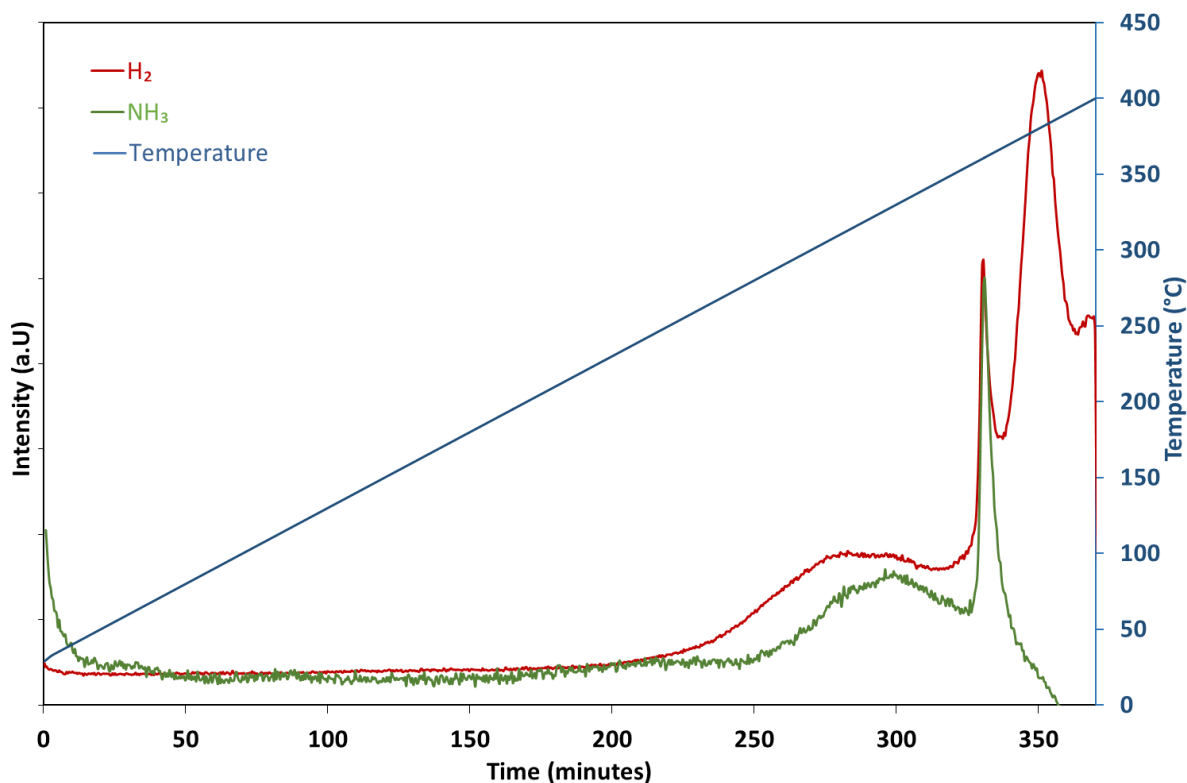


Figure 3-2: TGA-MS trace of the $2\text{LiNH}_2 + \text{MgH}_2$ hand-ground control sample, heated at 2°C min^{-1} , showing gas release against time, H_2 (red), NH_3 (green) and temperature (blue).

TGA coupled with mass spectrometry would be considered a more accurate method of collecting desorption data, because it can be accurately resolved into mass loss steps rather than making pseudo-gravimetric calculations. The desorption trace from the corresponding TGA-MS experiment is shown in Figure 3-2. The hydrogen and ammonia profiles observed in these two experiments were quite different. Although the hydrogen peak temperatures are similar (peak temperature in TGA-MS was 361°C), the ammonia release observed was significantly larger in the TGA equipment. In contrast to the TPD experiment, two clear hydrogen peaks were observed by TGA.

There are several reasons that may account for differing results in these experiments. The amount of sample used in TPD is in the region of 0.1 g compared to 0.01 g for TGA. This small amount of sample in TGA experiments reduces the chance of solid-gas reaction from gas released, which could account for the increased ammonia release in the TGA trace. The gas flow direction around the sample is also different in these two set-ups.

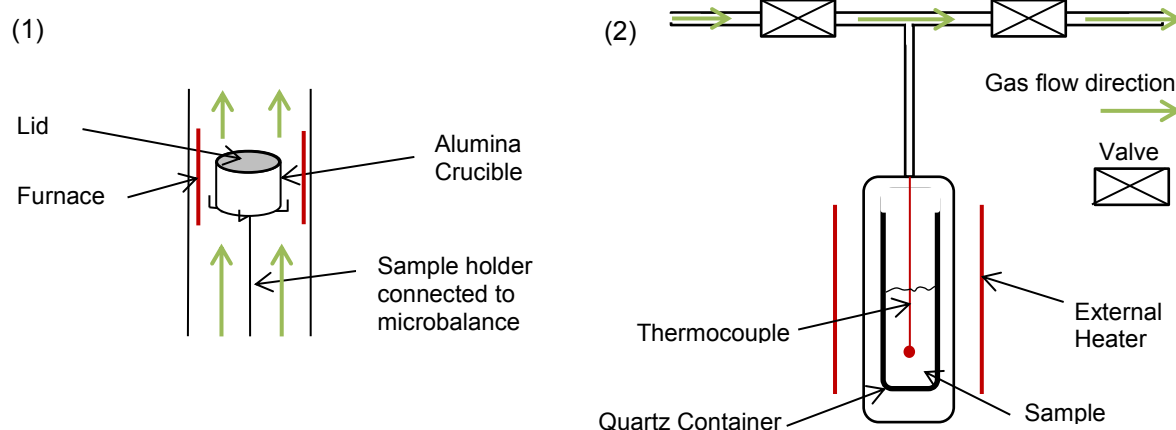


Figure 3-3: Schematic diagrams showing the gas flow routes around the samples in TGA (1) and TPD (2) set-ups.

A schematic diagram of the sample positioning and gas flow in both techniques is shown in Figure 3-3. In TPD the argon flow is across the top of a vertical quartz tube (length ~7 cm) where the sample sits at the bottom, whereas in TGA the sample is placed in an alumina crucible with a lid fitted and gas flow is vertically past the sample. The outlet gas distance to the mass spectrometer was also less in the experimental setup for the TGA compared to the TPD rig. This may account for some differences observed in the mass spectrometry traces, depending on how gas given off can flow away or remain in contact with the sample which would facilitate subsequent reactions (i.e. ammonia and sample) and drive reaction equilibria towards the products if the gas released is carried away. When combined, these two factors could account for the increased ammonia release detected in TGA experiments.

Interestingly, the TPD set up in this work appeared to encourage the release of hydrogen and suppress ammonia release. Calibration of hydrogen and ammonia gases using a calibration gas (purchased from BOC Speciality Gases) was carried out on both TPD and TGA equipment and applied to all data shown, so it is reasonable to conclude that the geometry of the desorption vessel can change the desorption pathway, mostly by affecting how easily ammonia molecules can leave the vicinity of the sample. These results were found to be reproducible. The TPD equipment was readily available and used as an initial indication of a materials behaviour under desorption conditions.

These data illustrate the difference that experimental conditions can cause to the appearance of a data-set or the reaction itself. A reaction pathway that is strongly influenced by experimental geometry is not ideal for the potential applications of this system. Ultimately, the observed variances may be an important aspect to consider when engineering a storage system for production to minimise ammonia release and maintain reversibility. Looking more widely, it shows the difficulties faced in this research area in producing and recording results that are comparable across measuring styles and set-ups, let alone to other groups around the world who may have different equipment.

3.4 Comparing preparation methods of Li–Mg–N–H samples

Several analytical techniques were used to assess the impact of preparation and identity of starting materials on the hydrogen storage abilities of this system.

3.4.1 Thermal desorption

Mass spectrometry and mass loss traces of several different samples were recorded and compared below in Figure 3-4, Figure 3-5 and Figure 3-11. The key features of the traces shown are summarised in Table 3-2. The reagents were hand ground together or ball-milled. Three ball-milling regimes were carried out: individual milling of the reagents, milling of reagents together under 1 bar argon atmosphere and milling of reagents under 100 bar hydrogen pressure. Reagents that were milled individually were then hand ground to mix them together. Mechanical-milling regimes were described in detail in Section 3.2. Sample preparation using ball-milling has become very common when studying hydrogen storage materials and amide–imide systems are no exception^{89, 104, 123, 124, 126, 127}. In order to allow direct comparisons of these results to be made to other published work, samples were ball-milled under various conditions. Physically, ball-milling should improve homogeneity of the reagents and dispersion of the reagents within the others as well as decreasing variability across the sample.

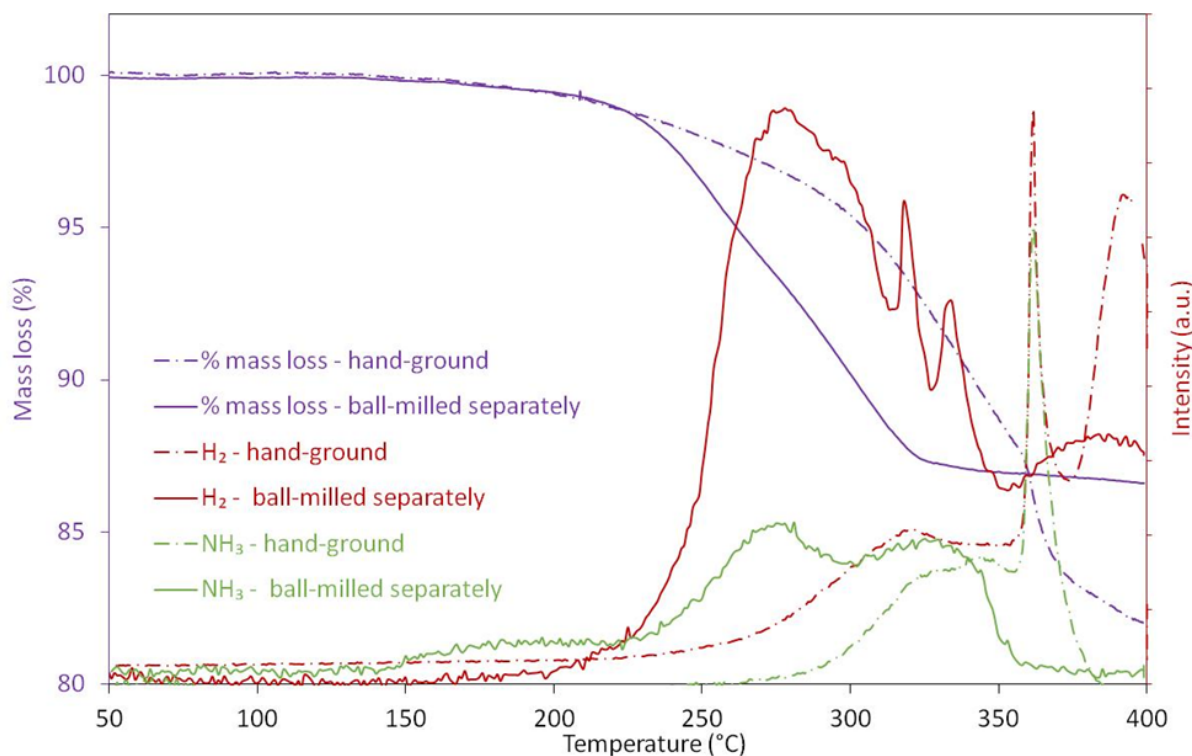


Figure 3-4: Mass loss and MS traces of two $2\text{LiNH}_2 + \text{MgH}_2$ samples, (preparation as described), heated at 2°C min^{-1} , showing hydrogen (red) and ammonia (green) release and % mass loss (purple) against temperature.

A comparison of the % mass loss and mass spectrometry profiles observed for hydrogen and ammonia for two samples is shown in Figure 3-4. The hand-ground sample did not show marked mass loss until it reached temperatures over 200°C , and significant ammonia desorption was observed in the mass spectrometry trace. Due to its mass, around 8.5 times that of H_2 , ammonia accounts for much of the mass loss per mole from this sample. A large reduction, around 120°C , in the peak hydrogen desorption temperature was observed from the sample whose components were mixed together after milling, however, substantial ammonia release was also observed.

As it had been ascertained that ball-milling the components produced a large improvement in the hydrogen desorption properties of this sample, further work was carried out to discover the effects of ball-milling the reagents together, under 1 bar argon pressure and 100 bar hydrogen pressure. Mechanical milling under a high hydrogen pressure (100 bar) was chosen to have two actions. Firstly, the physical suppression of gas release by high pressure, and secondly

an atmosphere of hydrogen forces the equilibrium position to remain with the hydrogenated starting materials. This makes the evolution of hydrogen unlikely from this sample. Depending on the conditions employed during ball-milling it has been shown it is possible to de- or re-hydrogenate a sample during energetic ball-milling¹²⁸. If dehydrogenation does take place during milling it can be difficult to measure accurately the amount of gas release. Parviz *et al.*¹²⁴ carried out a ball-milling study, which found that around 1 wt% hydrogen was desorbed from their sample after 24 hours of milling, however, that rose to almost 4 wt% H₂ after 50 hours. Ball-milling under pressure can stop gas release during milling by forcing the gas equilibria towards the starting materials.

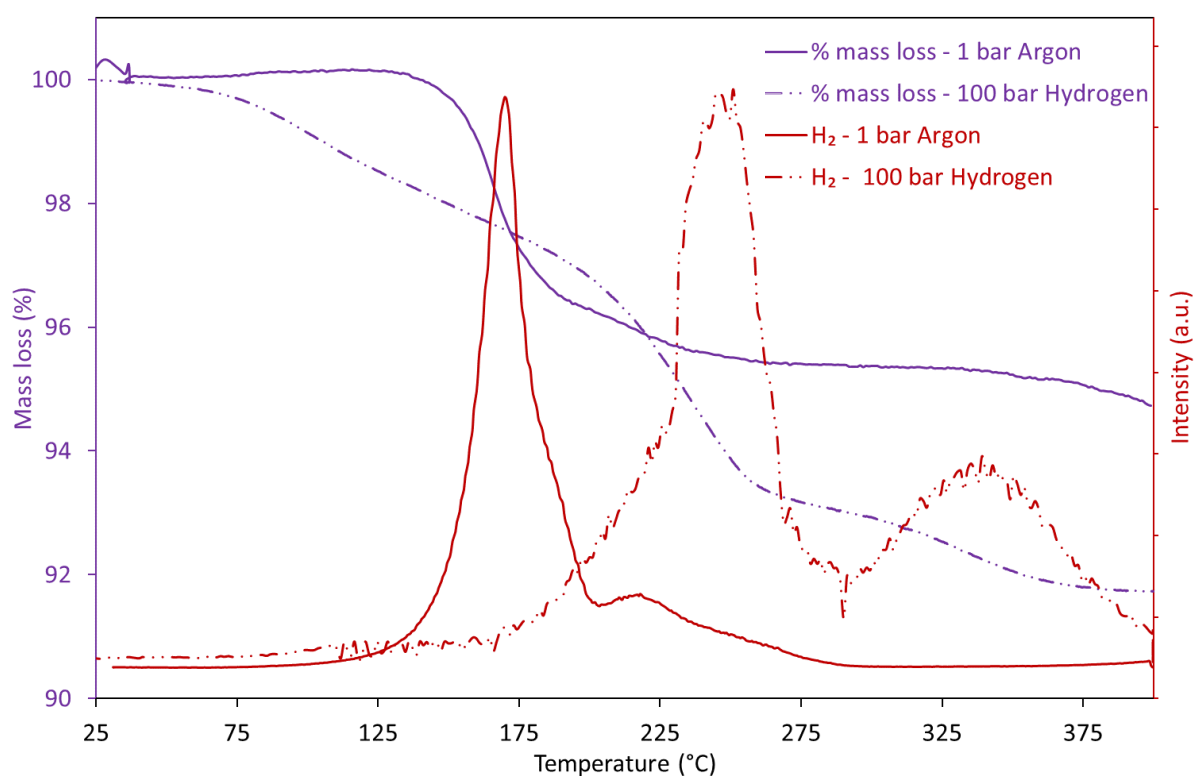


Figure 3-5: Mass loss and MS traces of the two ball-milled 2LiNH₂ + MgH₂ samples, (preparation as described), heated at 2°C min⁻¹, showing hydrogen release (red) and % mass loss (purple) against temperature.

Figure 3-5 shows mass loss and mass spectrometry traces of two ball-milled samples. The hydrogen desorption profiles of the samples were different: desorption from sample ball-milled under 100 bar hydrogen pressure occurred at higher temperatures and the second feature was more pronounced. The onset temperature of rapid hydrogen release (according to mass

spectrometry data), from the sample in which the reagents were ball-milled under 1 bar argon pressure, was significantly reduced compared to those seen in Figure 3-4. The peak hydrogen desorption temperature of the sample ball-milled under 1 bar argon was around 160°C, a reduction of 200°C relative to the hand-ground sample.

This peak value was in good agreement with work carried out by Xiong *et al.*⁵¹ who found peak desorption from a ball-milled sample based on 2LiNH_2 and MgH_2 was reached at 166°C. Although the sample that was ball-milled under pressure began to lose mass steadily from temperatures as low as 75°C, from the mass spectrometry profile it was possibly due to ammonia. Mass loss from the sample milled under atmospheric pressure did not begin until nearly 150°C, almost 75°C higher, but the rapid initial mass loss was in good agreement with a sharp hydrogen peak. The majority of the mass loss from the sample ball-milled under 1 bar argon occurred within a narrow temperature range, around 40°C indicating that a single reaction dominated, unlike the samples shown in Figure 3-4.

These results confirm that reduced particle size alone was not enough to reduce desorption temperature and ammonia release dramatically. Complete dispersion of the reacting species was a critically important factor. By ball-milling the starting materials together the mixing of the sample and homogeneity of the reactants throughout the sample should be greatly increased. This should enable fast diffusion of cations throughout the medium. Increased homogeneity across the sample explains why a single reaction was observed in Figure 3-4 after ball-milling together, rather than multiple gas release reactions from poorly mixed starting materials. Mass transport across grain boundaries^{66,28} and the diffusion of Li^+ ²⁹ have both previously been identified as rate-limiting steps in hydrogen desorption. According to Dunst *et al.*¹²⁹ ball-milling can be used to improve the lithium ion diffusion properties thus reducing the Li^+ ion conductivity of a sample. High energy ball-milling can generate local defects such as crystal

dislocations, and structural vacancies within the sample which mediate Li^+ diffusion across the tetrahedral and octahedral sites through the bulk structure with a lower energy barrier^{130, 131}.

Hydrogen desorption peaked at the lowest temperature when the sample was ball-milled under 1 bar argon. The gradient of the peak was smooth and steep, showing steady hydrogen release, indicating good homogeneity of the sample. From the hydrogen desorption profiles observed for the ball-milled samples, milling the starting reagents under 1 bar argon would be preferred to maximise low temperature hydrogen desorption and minimise ammonia release. Subsequently, all other samples were ball-milled together.

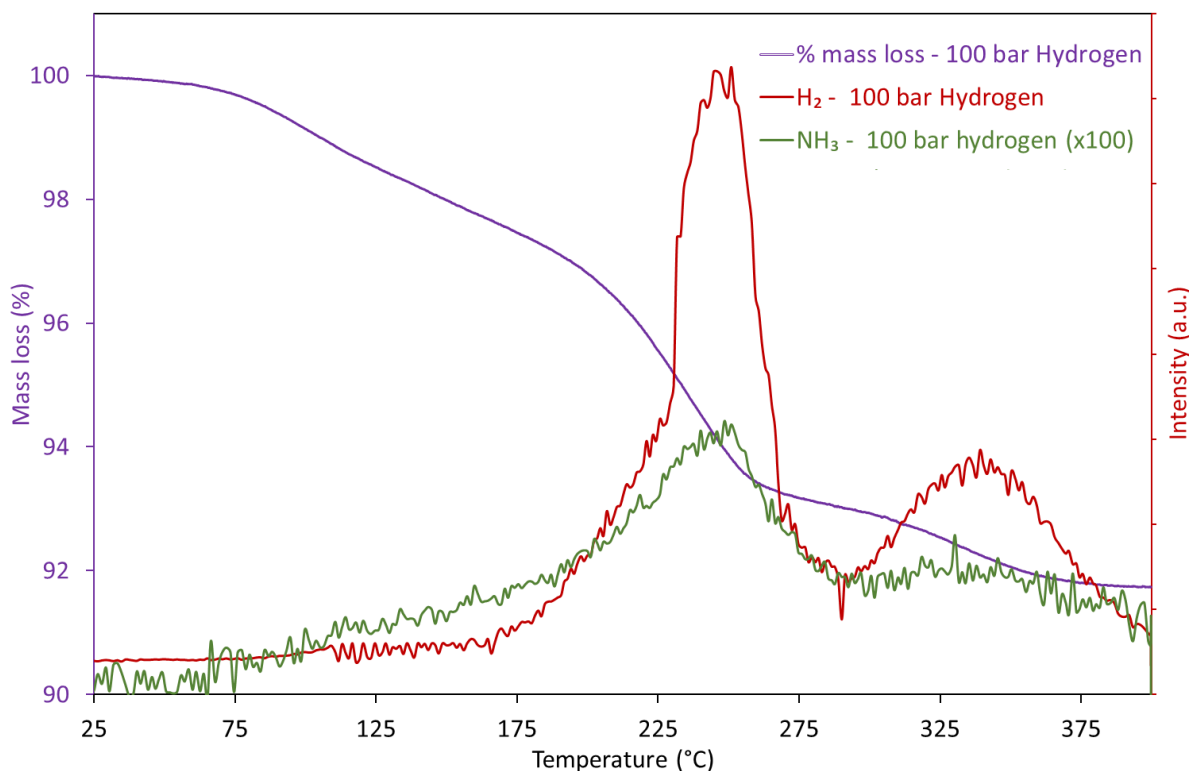
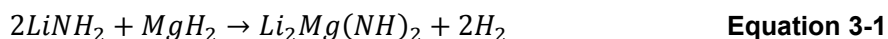


Figure 3-6: Mass loss and MS trace of $2\text{LiNH}_2 + \text{MgH}_2$ sample ball-milled under 100 bar hydrogen pressure, heated at 2°C min^{-1} , showing hydrogen (red) and ammonia (green) release and % mass loss (purple) against temperature.

In order to ascertain where the low temperature mass loss from the sample ball-milled under 100 bar hydrogen originated from, ammonia release from this sample was also considered and is shown in Figure 3-6. Although it was necessary to multiply the ammonia release trace by a factor of 100, ammonia release from this sample began around 75°C , similar to when the mass loss began, and peaked around the same temperature as hydrogen release. Even when the

ammonia release from the sample ball-milled under 1 bar argon was multiplied by 100 times, no peaks were observed.

It seems likely that mass loss observed from the sample that was ball milled under 1 bar argon may be solely due to hydrogen. In this system, the readily reversible hydrogen releasing reaction is from amide to a mixed cation imide according to Equation 3-1.



If hydrogen was released according to Equation 3-1, it would account for 5.54 wt% of the sample, close to the experimentally determined total mass loss of 5.30 wt% up to temperatures of 400°C. The reduction in ammonia release achieved compared to the hand-ground sample may be due to a partial metathesis reaction of LiNH_2 and MgH_2 to form $\text{Mg}(\text{NH}_2)_2$ and LiH , which are the thermodynamic products⁵¹. LiH has been shown to react more quickly with ammonia than MgH_2 , hence the ability to reduce the amount of the ammonia observed in the output gas stream⁵⁰. The powder XRD patterns of the ball milled samples after TPD-MS were very similar to those observed after heating the samples for 12 hours at 400°C described in Sections 3.4.4.2 and 3.4.4.3.

Pottmaier *et al.*¹³² studied a ball-milled $2\text{LiNH}_2 + \text{MgH}_2$ system prepared under 1 bar argon and found that a partial reactant conversion induced by ball-milling (evidenced by powder XRD) of the reactants to $\text{Mg}(\text{NH}_2)_2$ and LiH ¹³² occurred. It was shown that $\text{Mg}(\text{NH}_2)_2$ was a precursor to the formation of $\text{Li}_2\text{Mg}(\text{NH})_2$, so the production of a small amount of $\text{Mg}(\text{NH}_2)_2$ effectively changed the original desorption pathway. The formation of $\text{Mg}(\text{NH}_2)_2$ could also seed the desorption reaction; seeding has previously been shown to lower the kinetic barrier (activation energy) of hydrogen release¹³³. A study carried out by Barison *et al.*⁵⁸ considered the effects of varying the length of time ball-milling was carried out for. It was found that milling for 24 hours or longer was required to produce $\text{Mg}(\text{NH}_2)_2$, even though LiNH_2 was still observed. Varin *et al.*¹²³ investigated

the milling energy input during milling and found that high energy input was required to induce the formation of $\text{Mg}(\text{NH}_2)_2$ but this could conversion was found to occur without the loss of H_2 .

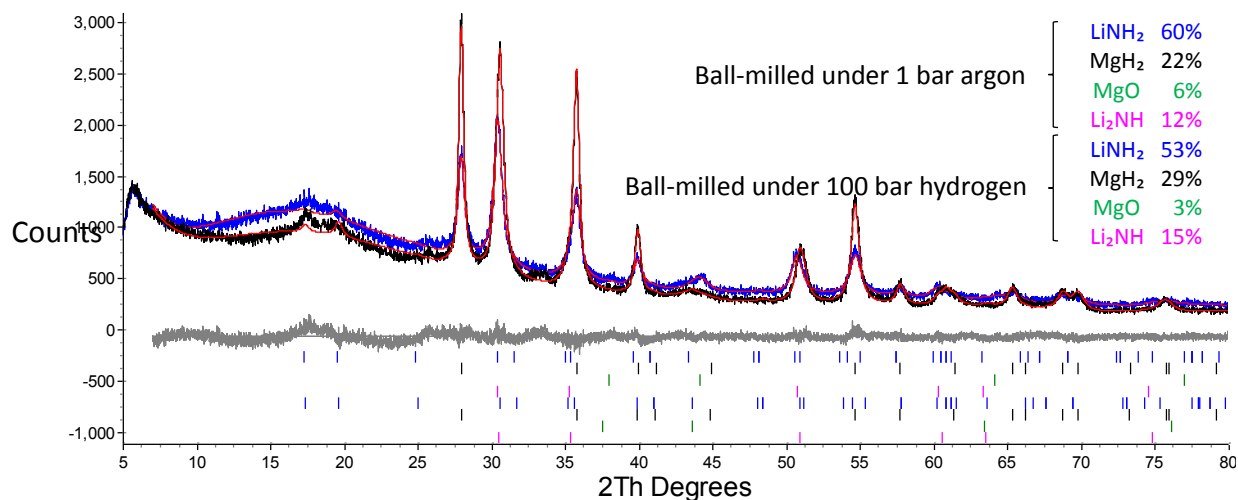


Figure 3-7: Powder XRD pattern of two of the prepared $2\text{LiNH}_2 + \text{MgH}_2$ samples, with Rietveld fit showing the difference (grey), calculated (red) and observed (blue, ball-milled under 1 bar argon; and black, ball-milled under 100 bar hydrogen) with the peak positions indicated for LiNH_2 (blue) and MgH_2 (black), MgO (green) and Li_2NH (pink).

Powder XRD data (Figure 3-7) were recorded after ball-milling preparation to compare the phases present. Powder XRD data recorded of both samples ball-milled together did not show any evidence of LiH or $\text{Mg}(\text{NH}_2)_2$. From this data, it was concluded that a metathesis reaction was not observed after milling under the conditions used in this work.

Although LiNH_2 and Li_2NH have been identified in the data shown in Figure 3-7, it is likely there is some ambiguity in the existence of these as distinct phases. David *et al.*²⁰ highlighted the importance of non-stoichiometry in these phases as well as the similarities in their main peak positions. As some intensity was observed at low angles (peaks at $\sim 18^\circ$ and 20°), this is a clear indication of the presence of the lithium amide structure which has lower symmetry than Li_2NH . However, the absence of these low angle peaks does not mean that the sample is compositionally lithium imide as its structure can accommodate large quantities of amide anions. It was felt that fitting both LiNH_2 and Li_2NH was the best way of modelling the distribution of the phases in the sample with the data quality available.

Sample preparation	LiNH ₂ lattice parameters (Å) and cell volume (Å ³)	Li ₂ NH lattice parameters (Å) and cell volume (Å ³)
Reference lattice parameters ^{20, 134-136}	$a = b = 5.04309$ $c = 10.2262$ Volume = 260.08	$a = b = c = 5.0769$ Volume = 130.86
	$a = b = 5.037$ $c = 10.278$ Volume = 260.77	$a = b = c = 5.0479$ Volume = 128.56
Ball-milled under 1 bar argon	$a = b = 5.048$ (6) $c = 10.21$ (2) Volume = 260.2 (6)	$a = b = c = 5.090$ (3) Volume = 131.9 (3)
Ball-milled under 100 bar hydrogen	$a = b = 5.070$ (9) $c = 10.25$ (3) Volume = 263.6 (9)	$a = b = c = 5.065$ (3) Volume = 129.9 (3)

Table 3-1: Cell parameter comparison of LiNH₂ and Li₂NH from as milled samples under 1 bar argon and 100 bar hydrogen pressure

A comparison of the refined cell parameters has been made in Table 3-1. Two different sets of cell parameters have been included for LiNH₂ and Li₂NH which show the potential variation from different published sources. David *et al.*²⁰ have refined over 20 variations to the lithium imide basic structure, demonstrating the large range of non-stoichiometry this phase can accommodate. For Li_(2-x)NH_(1+x) x can range from 0.30 to 0.98, with a cell volume variation of 124.97 Å³ to 131.03 Å³ for $x = 0.30$ and $x = 0.98$ respectively. From cell volumes calculated in Table 3-1, a value of 131.9 Å³ for a Li₂NH cell seems quite high, considering that the Li₂NH structure does not have any vacancies. This would suggest that the identification of Li₂NH in this pattern may be incorrect, likely due to ambiguity in phase identification between LiNH₂ and Li₂NH, but the pattern was not well modelled with just LiNH₂.

Based on David *et al.*'s²⁰ work, a cell volume of 129.9 Å³ would suggest a stoichiometry of around Li_{1.30}NH_{1.70} which would represent a phase with more amide-type anions than imide-type anions. A high proportion of amide anions would be in good agreement with the suppression of hydrogen release during ball-milling under 100 bar hydrogen. The cell volume of lithium amide

for this sample was also greater than previously determined for stoichiometric lithium amide. Unfortunately, due to the quality of the data presented here these values should be considered as more of an indication of how the cells have varied, rather than absolute values.

The peak broadening observed in Figure 3-7 was thought to be caused by small particle sizes as well as by the introduction of strain and disorder into the sample by ball-milling. The full-width at half maximum (FWHM) was greater for the sample milled under 1 bar argon pressure indicating this sample had a higher degree of disorder and strain as the milling regime was the same for both samples (i.e. the particle size was lower), although this has not been experimentally proven. Although the composition of both samples was similar, variations in peak broadening indicate subtle differences between the two samples. One hypothesis is that ball-milling under 100 bar hydrogen pressure maintains a higher hydrogen content in the compounds and so the local defects generated are less significant, leading to narrower peaks. This would be in agreement with the greater temperatures required to release hydrogen from this sample (Figure 3-5).

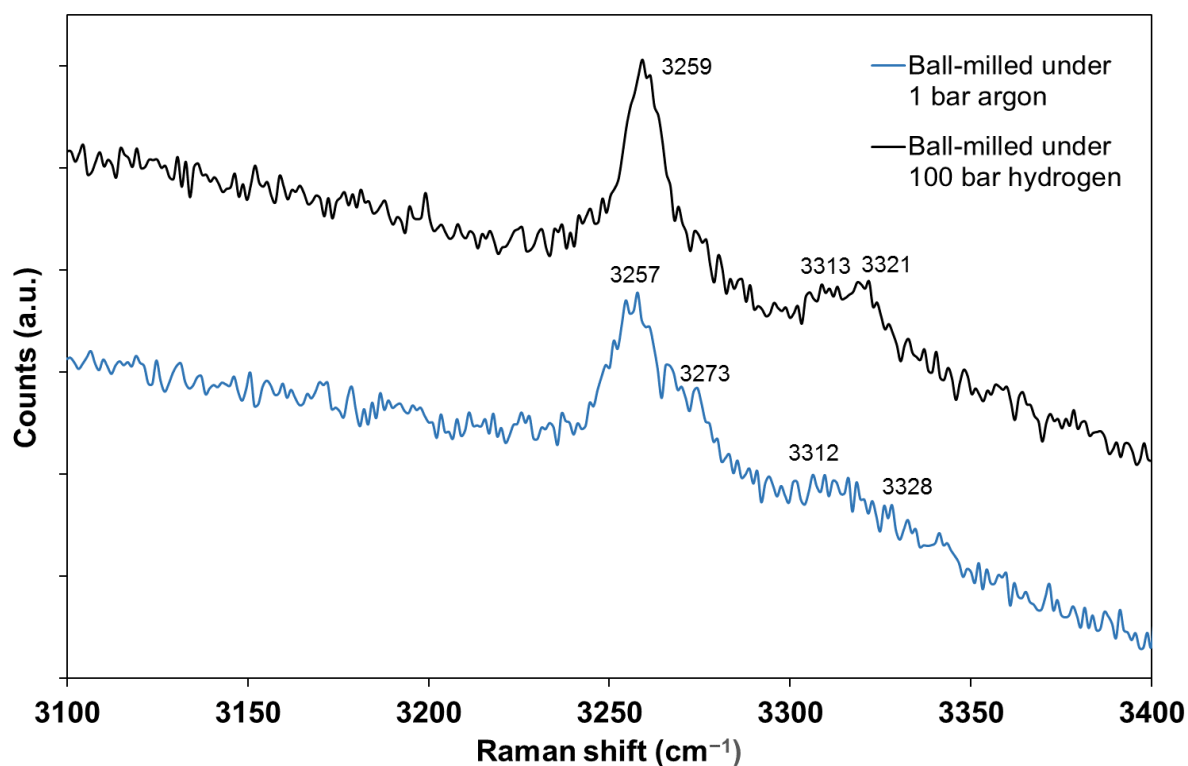


Figure 3-8: Raman spectra recorded after milling of two of the prepared $2\text{LiNH}_2 + \text{MgH}_2$ samples, (blue, ball-milled under 1 bar argon; and black ball-milled under 100 bar hydrogen) with key peaks labelled.

However, Raman spectra recorded after ball-milling preparation, shown in Figure 3-8, indicated that the samples were not exactly the same. Lithium amide was clearly observed in both spectra, whereas no evidence of any imide phases (peaks expected around 3150-3200 cm^{-1}) could be seen from either Raman spectrum. There were some features observed in both Raman spectra in the regions which could be caused by $\text{Mg}(\text{NH}_2)_2$, (around 3273 and 3328 cm^{-1})¹³⁷. Peaks observed around 3260, 3313 and 3320 cm^{-1} were attributed to LiNH_2 ^{138, 139}. Although clear differentiation of the samples may not be possible by powder XRD due to poor crystallinity, Raman spectra also indicate subtle differences between the two samples. The data shown in Figure 3-5 proves that the samples react differently under desorption conditions.

As discussed briefly in Section 3.1, starting from $\text{Mg}(\text{NH}_2)_2$ may improve the properties of this system. The powder XRD pattern in Figure 3-9 was recorded after the synthesis of $\text{Mg}(\text{NH}_2)_2$. Unfortunately, the sample was not pure: a small amount of magnesium oxide was formed and some MgH_2 remained. Unfortunately, the starting materials used in these reactions were not pure (~95%) so it is possible that small amounts of Mg metal or MgO were in the starting materials, even if they were not clearly detected by Powder XRD. This was taken into account when calculating the amount of LiH required for desorption reactions and sample mass losses.

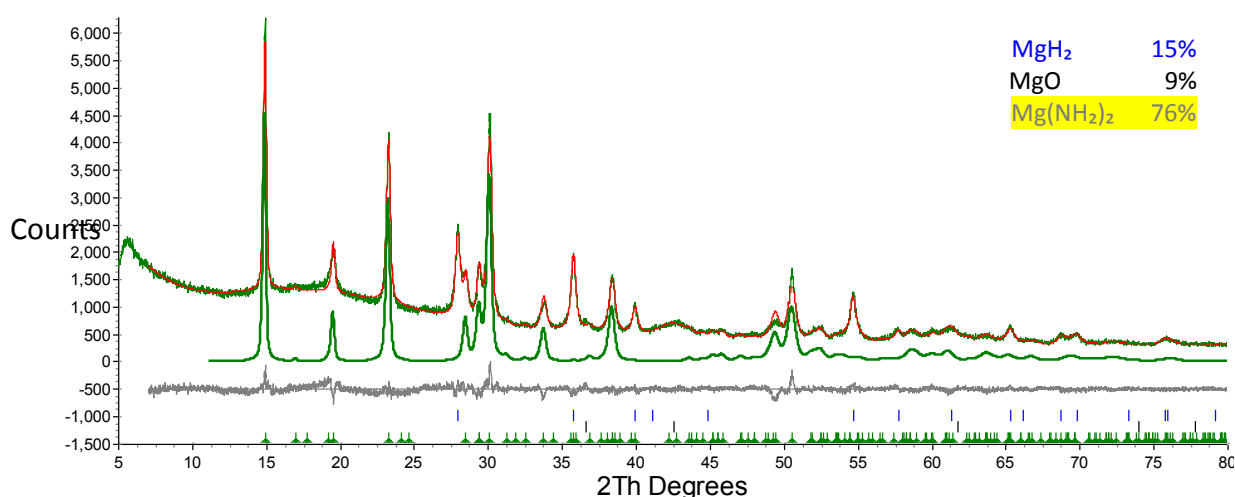


Figure 3-9: Powder XRD pattern of synthesised $\text{Mg}(\text{NH}_2)_2$, with Rietveld fit showing the difference (grey), calculated (red) and observed (green) with the peak positions indicated for MgH_2 (blue), MgO (black), and $\text{Mg}(\text{NH}_2)_2$ (green and highlighted).

An alternative way of ‘starting’ from $\text{Mg}(\text{NH}_2)_2$ and 2LiH would be by cycling the sample made from LiNH_2 and MgH_2 to produce the alternative reactants via re-hydrogenation. Following hydrogenation, the phases produced are $\text{Mg}(\text{NH}_2)_2$ and LiH , which should allow the comparison of these samples. A powder XRD pattern of the sample that was used for this experiment is shown in Figure 3-10.

Similarly to Figure 3-7, both LiNH_2 and Li_2NH have been identified in the pattern shown in Figure 3-10. Removing either of these phases led to intensity mismatches on several peaks. The refined lattice parameters of both phases were compared to the literature values. The cell volume of LiNH_2 was slightly lower than expected and that of Li_2NH was slightly higher; this indicated it was possible both phases were non-stoichiometric. It can be seen that, although the sample was repeatedly cycled, a small amount of the original starting materials remained, but magnesium amide and lithium hydride were the main components.

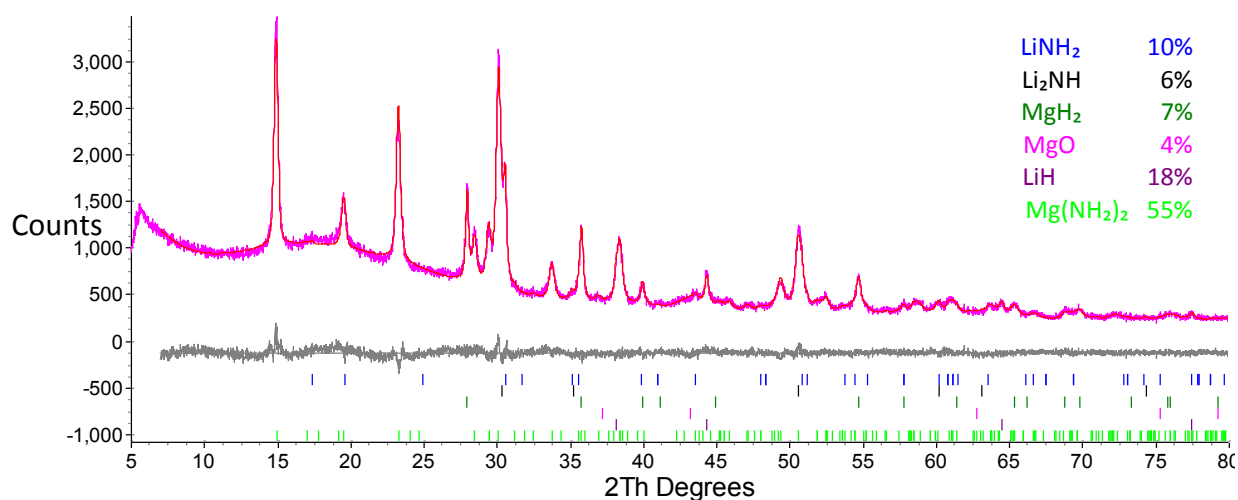


Figure 3-10: Powder XRD pattern of cycled sample before the desorption experiment, with Rietveld fit showing the difference (grey), calculated (red) and observed (pink) with the peak positions indicated for LiNH_2 (blue), Li_2NH (black), MgH_2 (green), LiH (purple) and $\text{Mg}(\text{NH}_2)_2$ (light green).

The mass loss and mass spectrometry traces from a ball-milled sample starting from $\text{Mg}(\text{NH}_2)_2$ and a re-hydrogenated sample which had been cycled 3 times after ball-milling are shown in Figure 3-11. By cycling the sample, because the products after hydrogenation are $\text{Mg}(\text{NH}_2)_2$ and LiH , the starting materials of these samples should show similar characteristics.

Figure 3-11 shows mass losses and mass spectrometry traces of the two samples starting from $\text{Mg}(\text{NH}_2)_2$ and LiH described above.

The hydrogen desorption profile of the sample that was prepared from $\text{Mg}(\text{NH}_2)_2$ was similar to that from the sample ball-milled under 1 bar argon prepared from LiNH_2 shown in Figure 3-5. The first hydrogen feature was the largest peak in the magnesium amide based sample, unlike the cycled sample whose hydrogen desorption was transferred more towards higher temperatures. The occurrence of two hydrogen desorption peaks in the mass spectrometry trace from the cycled sample is good agreement with desorption from a more complex mixture of phases, (identified in Figure 3-10), compared to the samples ball milled under 1 bar argon or 100 bar hydrogen pressure. Increasing the number of phases in a sample promotes the possibility of more hydrogen releasing pathways occurring. According to bailawa *et al.*³⁵ a peak in the hydrogen desorption trace around 225-250°C would be in good agreement with hydrogen release caused by a reaction of LiNH_2 with LiH.

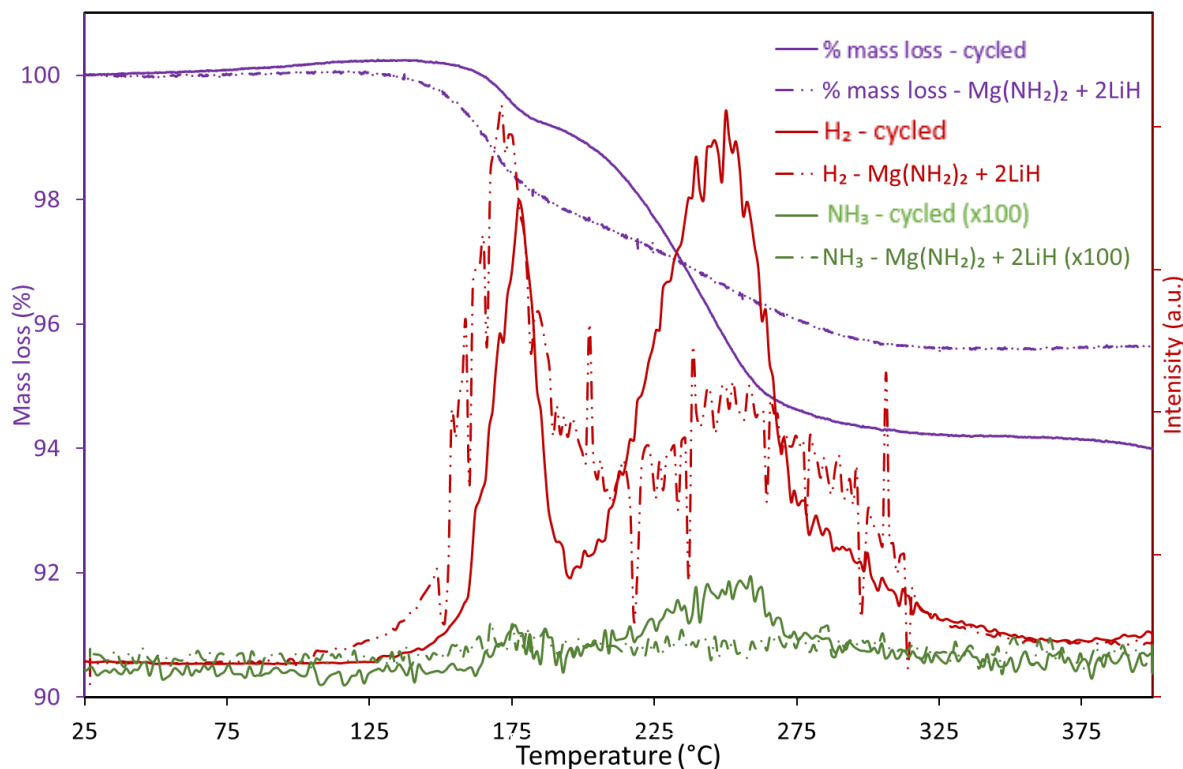


Figure 3-11: Mass loss and MS traces of the two ball-milled samples, one made from $\text{Mg}(\text{NH}_2)_2 + 2\text{LiH}$ and the other after 3 cycles of de- and re-hydrogenation, showing hydrogen (red) and ammonia (green) release and % mass loss (purple) against temperature.

The onset temperatures of mass loss and hydrogen release for both samples were similar to those from $2\text{LiNH}_2 + \text{MgH}_2$. The onset temperature of the cycled sample had increased by 10°C , indicating that the sample had degraded slightly with respect to the initial desorption step of the sample. Slight ammonia release was observed from both samples, but more from the cycled sample at higher temperatures.

The results from TGA-MS experiments are summarised in Table 3-2. The overall mass loss (wt%) as well as mass loss up to 220°C are included for comparison. The sample ball-milled under 1 bar argon was found to maximise low temperature hydrogen desorption. If the mass loss observed from this sample, up to ~ 5.5 wt%, was attributed to hydrogen, around 80% of the available hydrogen has been desorbed before 225°C .

Sample preparation	Onset mass loss temperature ($^\circ\text{C}$)	Peak hydrogen desorption temperature ($^\circ\text{C}$)	Comments	Total Mass loss [up to 220°C] (%)
Hand-ground	195	350	Significant ammonia release was observed.	18.05
Ball-milled separately under 1 bar argon	195	240	Ammonia release was observed.	13.30
Ball-milled under 1 bar argon	145	170	No ammonia release was observed.	5.30 [4.2]
Ball-milled under 100 bar hydrogen	75 (~ 160)	245, 340	A small amount of ammonia was released.	8.30 [4.5]
$\text{Mg}(\text{NH}_2)_2 + 2\text{LiH}$	150	170, 250	Similar profile to that of ball milled samples. Minimal ammonia release.	4.4 [2.8]
Ball-milled cycled	160	180, 250	Hydrogen release shifter to higher temperatures. Some ammonia release.	5.6 [2.4]

Table 3-2: Summary of the key features from the mass spectrometry and mass losses of the samples tested to show the effects of preparation on the samples in this section.

Closer examination of the mass spectrometry data recorded during desorption from the sample ball-milled under 100 bar hydrogen would suggest that hydrogen desorption did not begin until 160°C, which would be more comparable to other samples. Significant mass loss in other samples correlates well to the beginning of hydrogen release. The implication of this observation is that the mass loss observed before 160°C is likely to be ammonia in amounts below the detection limits of the equipment used, so the total mass loss is reduced to 5.3 wt% and the mass loss before 220°C is reduced to around 2 wt%. These approximations mean the behaviour of the sample ball-milled under 100 bar hydrogen was more comparable to the samples starting from, or thought to start from $\text{Mg}(\text{NH}_2)_2 + 2\text{LiH}$ (in the case of the cycled sample). Behaviour that was similar to samples known to start from $\text{Mg}(\text{NH}_2)_2$ would be in good agreement with the observation of some $\text{Mg}(\text{NH}_2)_2$ from Raman data recorded of the sample ball-milled under 100 bar hydrogen after preparation.

Desorption from samples whose reagents were $\text{Mg}(\text{NH}_2)_2 + 2\text{LiH}$ (or cycled) was shifted towards higher temperatures; less than 50% of the hydrogen (from hydrogenated to imide state) was lost below 220°C. The hydrogen desorption temperatures were consistent across the samples where the reagents had been ball-milled together, with the exception of the sample that was ball-milled under 100 bar hydrogen pressure. The reason for this exception is slightly unclear, as previous studies have not observed any anomalies following this method of preparation. The visual appearance of this sample was not different to any the other ball-milled samples and the powder XRD pattern after milling was very similar to the sample milled under 1 bar argon, with broad peaks, indicating that ball-milling was successful. It is possible that the broadness of these peaks had masked any small changes to the sample, that were observed by Raman data which could be responsible for the variation. If both LiNH_2 and $\text{Mg}(\text{NH}_2)_2$ were present as starting materials, then this could change the desorption mechanism. Paik *et al.*¹⁴⁰ examined a system starting from both LiNH_2 , $\text{Mg}(\text{NH}_2)_2$ and LiH where they did not observe large amounts of

ammonia release, but imide product from the system was Li_2NH not $\text{Li}_2\text{Mg}(\text{NH})_2$ as perhaps expected from a mixed cation system.

The cycled sample displayed a slight increase in peak desorption temperature, which could have been caused by agglomeration of particles. A significant increase in the desorption temperatures occurred when the samples were hand ground or the components were ball-milled separately. The improved desorption temperatures are likely accounted for by a combination of factors. Reducing the particle size alone by ball-milling was not enough to reduce dramatically the desorption temperature. The hydrogen desorption temperatures were decreased from three ball-milled samples (described in Table 3-1). It was thought that a higher degree of disorder (i.e. defects) had been introduced into the phases in these samples and they may also have a larger range of phase compositions. If different thermodynamic pathways were available due to slight compositional variances or additional phases in the samples then the desorption temperatures could change. A reduction in particle size would also cause kinetic improvements due to increased contact between phases, resulting in more potential sites for hydrogen desorption. This would shorten the distances of ion diffusion required within the samples.

The only previous study where the conditions of sample preparation were varied was carried out by Chen *et al.*²⁸ starting from $\text{Mg}(\text{NH}_2)_2$ and 2LiH . The peak hydrogen desorption temperatures observed from the $\text{Mg}(\text{NH}_2)_2$ and 2LiH samples prepared by Chen²⁸ were approximately 175°C and 350°C , when they were ball milled and ground by hand, respectively. These are identical to the temperature ranges observed in this work. Ball-milling can influence the kinetics of a reaction by; encouraging the formation of new phases, improving dispersion, decreasing diffusion lengths and crystallite sizes, and consequently contact of the reactive starting materials would be greatly improved. It is known that agglomeration of particles can occur when samples are cycled¹⁴¹ through the growth of crystallite grains. This accounts for the slight increase in peak desorption temperature shown by the cycled sample and suggests that crystallite size and

the effects of increasing it were contributing factors in determining the desorption peak temperature.

Ball-milling can change the thermodynamic pathways of a reaction by generating by-products, that may stabilise or seed products, changing the enthalpy of the overall desorption pathway, but also through reducing the kinetic barrier to the formation of intermediates and products, increasing the rate of the reaction. This underlines the need to understand not only the desorption properties but also the potential change of desorption mechanism post ball-milling by changing the reactants.

Improved mixing of the samples can also account for the decrease in ammonia release. The easier it is for the reaction between amide and hydride to occur in order to liberate hydrogen, the less likely it is that ammonia will be released through decomposition of the amide. If the mutual dispersion of both phases within each other is high, then the reaction between the two phases is more facile. It is important to note that the hydrogen desorption temperatures of this system were mainly independent of the method of milling used, when ball-milling was employed. This would suggest that the properties that are being measured in most samples (excluding the sample ball-milled under 100 bar hydrogen) are of the intrinsic system, but also demonstrates how sensitive the system response is the method of preparation used.

3.4.2 Activation energies

TGA-MS data can be used in order to carry out kinetic calculations to estimate the activation energies (E_a) of first hydrogen release step from different samples. By varying the ramp rates used in the TGA experiments, kinetic calculations to estimate the activation energy could be carried out according to Kissinger's method¹⁴² (Equation 1-7), and the results are shown in Table 3-2. Figure 3-12 shows Kissinger's plots from five samples prepared using various methods. LiNH_2 and MgH_2 samples were prepared by, (1) ball-milling separately and subsequently

combining by hand, (2) ball-milling together under a 1 bar argon atmosphere and (3) ball-milling together under 100 bar hydrogen atmosphere. Two further samples were also prepared, (4) LiNH₂ and MgH₂ cycled 3 times after initial preparation according to (2), and (5) a sample prepared from previously synthesised Mg(NH₂)₂ (described in Section 3.2) and LiH. The activation energies were calculated through the relationship described in Equation 1-7 and are shown in Table 3-3.

As the starting materials for 4 of 5 samples were the same and the activation energy values calculated from these samples varied, this data does not fit the classical explanation of activation energy. This implies that the estimated activation energy was a measure of the reduction of the energy required to overcome the rate determining step produced by varying the preparation.

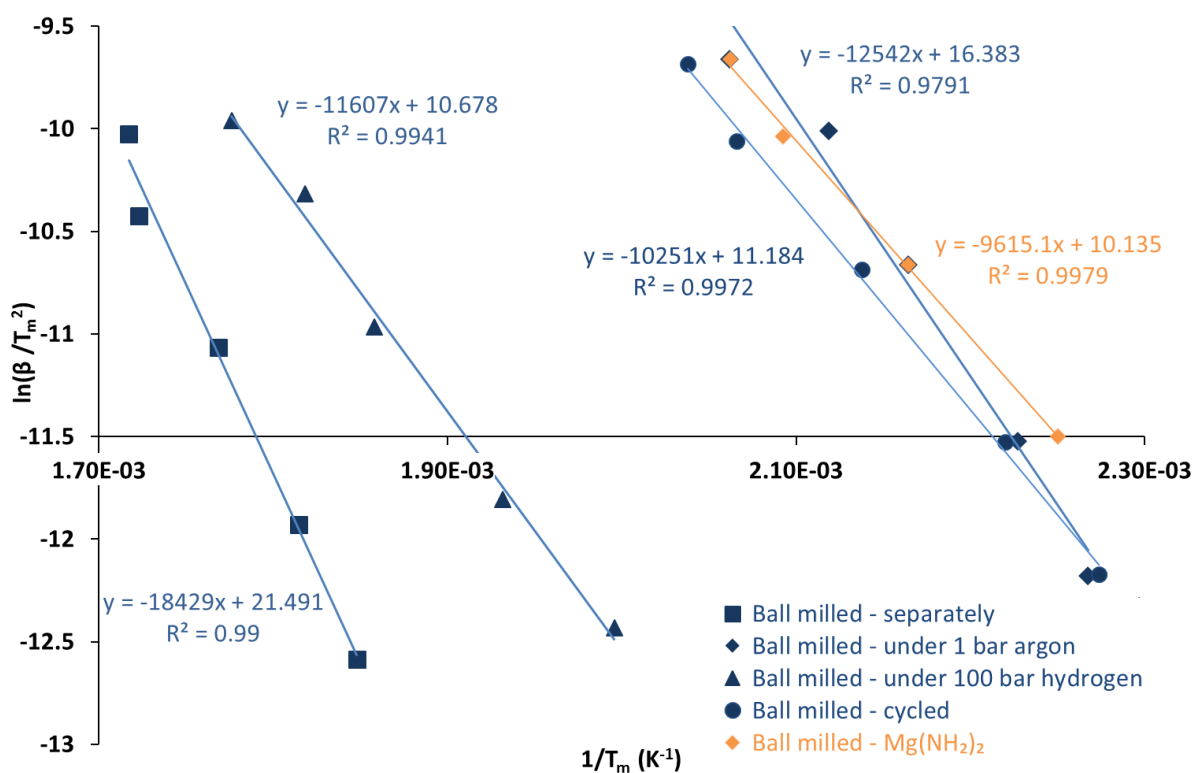


Figure 3-12: Kissinger's plot showing five samples prepared in different ways (described in text), prepared from 2LiNH₂ and MgH₂ (blue) and from Mg(NH₂)₂ and 2LiH (orange).

As shown in Figure 3-12, samples that were ball-milled together (Samples 2, 3, 4 and 5) displayed a considerable reduction in E_a compared to the one that was ball-milled separately (Sample 1). The degree of uncertainty was estimated by considering the sampling rate of the mass

spectrometer and heating rate of the TGA. A single scan of all the mass channels selected takes around 30-40 seconds, so when the sample heating rate is $10^{\circ}\text{C min}^{-1}$, the peak temperature determined could be within the time from one data point to another, approximately $\pm 5^{\circ}\text{C}$ for a

sample ramped at $10^{\circ}\text{C min}^{-1}$. This allows for a calculation of the potential error in the measured peak temperature. This can then be plotted as a possible variation in gradient of the line of best fit, which was used to estimate the activation energy. The estimated uncertainty in the activation energy value was calculated to be $\pm 6 \text{ kJ mol}^{-1}$.

Sample preparation	Estimated activation energy (kJ mol^{-1})
Components ball-milled separately (1)	153
Components ball-milled under 1 bar Ar (2)	104
Components ball-milled under 100 bar H_2 (3)	97
Ball-milled cycled (4)	85
$\text{Mg}(\text{NH}_2)_2 + 2\text{LiH}$ (5)	80

Table 3-3: Estimated values of activation energies for various samples.

The lowest activation energies came from samples which had previously been reacted, i.e. sample starting from $\text{Mg}(\text{NH}_2)_2$ and the cycled sample. This finding was in contrast to research by Qin *et al.*⁶⁴ who compared starting from LiNH_2 and MgH_2 to $\text{Mg}(\text{NH}_2)_2$ and LiH and suggested that the activation energy starting from the former reagents was lower. Research by Xie *et al.*¹⁴¹ illustrated the importance of particle size of the amide. Magnesium amide was manufactured into particle sizes of 100, 500 and 2000 nm and heated with LiH . The activation energies of the respective samples were found to be 122, 134 and 182 kJ mol^{-1} . Using powder XRD data recorded from hand-ground and ball-milled samples after preparation, a rough estimate of particle sizes can be made *via* the Scherrer Equation.

$$\tau = \frac{K\lambda}{\beta \cos\theta}$$

Equation 3-2: Scherrer Equation

where;

τ : crystallite size (nm)

K : shape factor

λ : X-ray wavelength (nm)

β : line broadening at full width at half maximum (radians)

θ : Bragg angle (°)

The values are only a rough estimate as both the instrument and other sample factors, apart from crystallite size, can contribute to peak broadening. The estimated crystallite size in a sample which was hand ground was ~2000 nm while those that were ball-milled were found to be ~250 nm. The crystallite size across all ball-milled samples was consistent regardless of the milling conditions. If reduced crystallite sizes were the most important factor for facilitating low activation energies, then these two samples, because of their preparation, would have been thought to have the highest level of agglomeration and hence higher activation energy. However, these two samples were also made up of the largest number of phases; the sample that started from $\text{Mg}(\text{NH}_2)_2$ also included MgH_2 as a starting material due to impurities in the synthesised amide.

The presence of several phases, including some which may not have been in a fully hydrogenated state, could seed the products and destabilise the reactants which might contribute to a lower effective energy barrier. The activation energy of the hand-ground sample was calculated to be $207.5 \text{ kJ mol}^{-1}$. As expected, this was considerably larger than that of the ball-milled samples. Several other groups have determined activation energies for the Li-Mg-N-H system, mostly via Kissinger's method, some of which are listed in Table 3-3. There is considerable variation in the calculated values of the activation energies, but the values estimated in this work are comparable to similar samples.

Sample preparation	Starting materials	Estimated activation energy (kJ mol ⁻¹)
12 hours of ball milling	Mg(NH ₂) ₂ + 2LiH	111 ⁶²
36 hours of ball milling	Mg(NH ₂) ₂ + 2LiH	105 ⁵⁷
36 hours of ball milling under 50 bar H ₂ pressure	Mg(NH ₂) ₂ + 2LiH	104 ¹⁰⁴
20 hours of ball milling	Mg(NH ₂) ₂ + 2LiH	88.1 ²⁸
1 hour of ball milling	Mg(NH ₂) ₂ + 2LiH	134 ¹⁴³
2 hours of ball milling	2LiNH ₂ + MgH ₂	119 ⁸⁴
24 hours of ball milling under 50 bar H ₂ pressure	2LiNH ₂ + MgH ₂	135 ⁹⁰
24 hours of ball milling	2LiNH ₂ + MgH ₂	85 ⁶⁴

Table 3-4: Estimated values of activation energies reported in the literature.

3.4.3 Differential scanning calorimetry

DSC measurements of the samples were carried out. When solely hydrogen is released from a sample it is possible to evaluate the enthalpy changes corresponding to hydrogen desorption reactions using DSC. A more traditional way of determining the enthalpy change of a system would be using volumetric methods to find equilibrium plateau pressures to produce a Van't Hoff plot. However, these measurements require significant amounts of equipment time that unfortunately were not available for this work.

Although most samples desorbed a mixture of hydrogen and ammonia, the first step of hydrogen release was not normally accompanied by a considerable amount of ammonia, thus the energy changes from this step could be compared. Further analysis of the DSC data was carried out in Section 4.4.

The heating segments of several DSC experiments carried out of the samples described above in the TGA experiments are shown in Figure 3-13. The related cooling segments of the DSC experiments were flat and no features were observed. Up to temperatures of ~300°C, the behaviour of three samples as shown in the DSC traces that were prepared by ball-milling, (1 bar

argon, cycled and $\text{Mg}(\text{NH}_2)_2$ and LiH) were very similar. The peak temperatures and areas under the peaks are shown in Table 3-5.

Sample preparation	Temperature of 1 st peak (°C)	Area of peak (J/g)	Temperature of 2 nd peak (°C)	Area of peak (J/g)
Ball-milled under 1 bar argon	182	-387	240	-56
Ball-milled under 100 bar hydrogen	-	-	257	-50
$\text{Mg}(\text{NH}_2)_2 + 2\text{LiH}$	176	-289	255	-28
Ball-milled cycled	180	-146	255	-164

Table 3-5: Peak temperatures and areas underneath the two main peaks from DSC data.

The peak temperatures and number of the endothermic events observed in the DSC traces correlate very closely with the desorption behaviour and hydrogen desorption peak temperatures shown in the TGA experiments for all samples. The area of the peak is directly related to the amount (mass) of gas released during that event. The increased area of the 2nd peak for the cycled samples is in good agreement with TGA-MS data which showed a large 2nd hydrogen peak in contrast to the other samples.

The sample ball-milled under pressure showed a significantly different DSC trace. This was the only sample, where the mass loss was greater than 5.6 wt% in total, and which displayed an exothermic peak in the heating segment. The estimated activation energy of this sample was not largely different to any of the other samples. The reason for the difference in behaviour from this sample compared to the other samples was not immediately obvious and will be further discussed in Section 3.5. There was little difference in the powder XRD patterns of the samples ball-milled under 1 bar argon and 100 bar hydrogen after milling. However, the total mass loss and DSC traces showed these two samples were different. The hydrogen desorption traces from both samples were different and the endothermic peak observed around 250 °C in Figure 3-13 from the sample ball-milled under 100 bar hydrogen corresponds well to the hydrogen desorption peak from this sample.

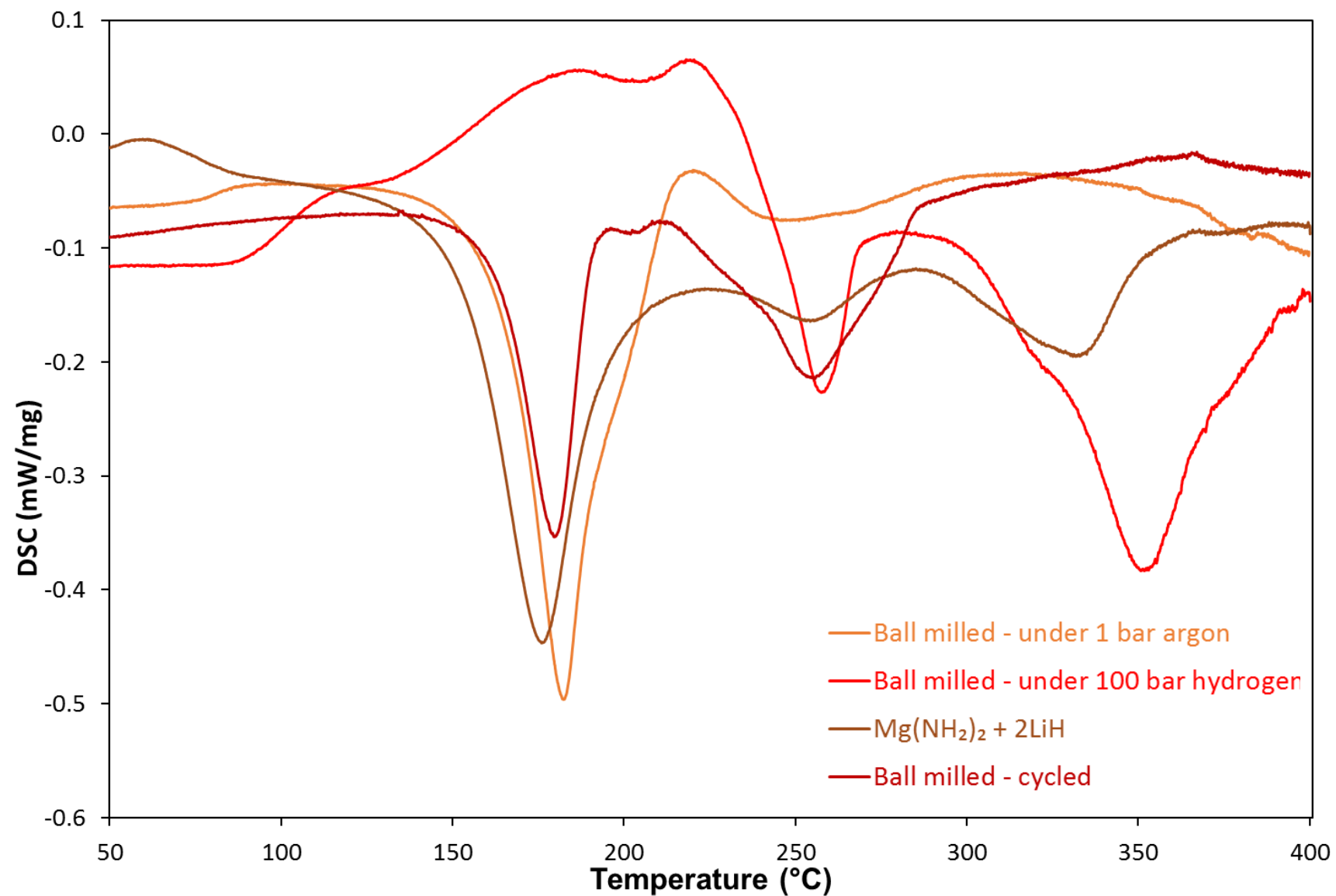


Figure 3-13: DSC heating segment of $2\text{LiNH}_2 + \text{MgH}_2$ and $\text{Mg}(\text{NH}_2)_2 + 2\text{LiH}$ samples prepared by previously described methods.

3.4.4 Powder XRD

Flowing argon experiments were carried out at various temperatures on samples prepared by hand grinding, and ball-milling under 1 bar argon and 100 bar hydrogen to examine the intermediate phases formed by ambient temperature powder XRD after the experiments. Hydrogenations and desorption under vacuum were also carried out to understand how preparation and cycling affects the phases formed in the system.

3.4.4.1 Hand-ground

Samples were hand-ground and heated for 12 hours at various temperatures and the products were analysed using powder XRD data. Structural work in the area of solid-state chemistry is often carried out using hand preparation of samples. Hand preparation is a useful technique as the decrease in grain size induced by ball-milling can make the peaks in the powder XRD patterns of ball-milled samples difficult to identify clearly. However, as discussed previously, it is possible that the reaction pathway may not be the same as that taken by samples which are ball-milled.

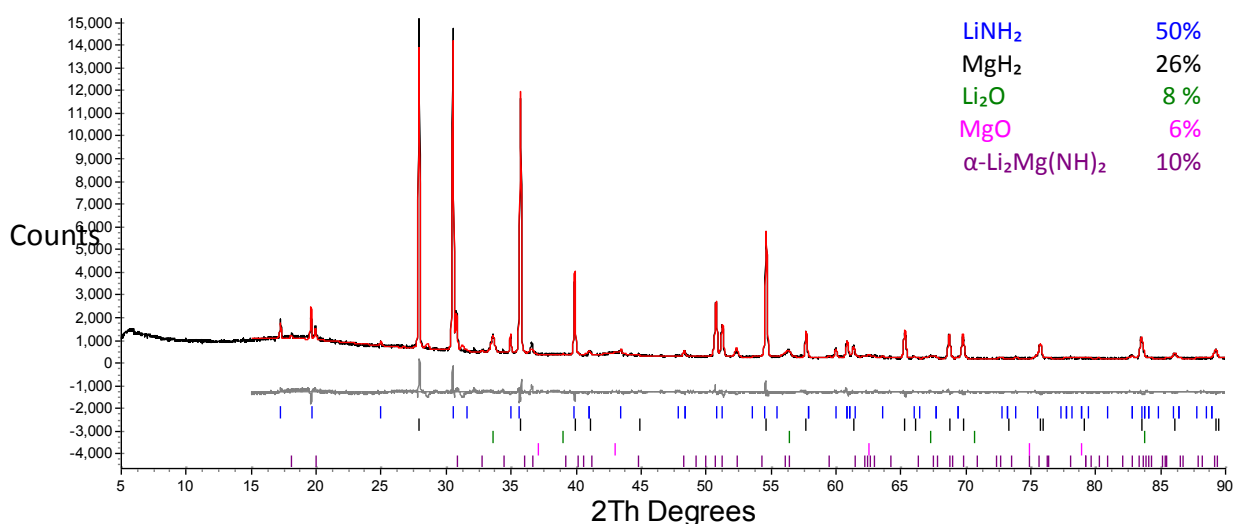


Figure 3-14: Powder XRD pattern of 2LiNH₂ + MgH₂ sample heated at 275°C for 12 hours, with Rietveld fit showing the difference (grey), calculated (red) and observed (black) traces with the peak positions indicated for LiNH₂ (blue), MgH₂ (black), Li₂O (green), MgO (pink) and α-Li₂Mg(NH)₂ (purple).

Samples were prepared from 2LiNH₂ and MgH₂ and no reactions between the starting materials were observed below 275°C. A degree of oxidation of the samples was observed at most

temperatures. At 275°C, the peaks assigned to α - $\text{Li}_2\text{Mg}(\text{NH})_2$ were first observed in the powder XRD pattern (Figure 3-14), while β - $\text{Li}_2\text{Mg}(\text{NH})_2$ was first observed at temperatures of 325°C. Intermediates, such as $\text{Li}_2\text{Mg}_2(\text{NH})_3$ ⁶⁹ were not observed in these powder XRD patterns recorded *ex-situ*.

A large reduction in the amount of starting materials remaining was seen between 300°C and 325°C. The amount of α - $\text{Li}_2\text{Mg}(\text{NH})_2$ fluctuated as the temperature of the experiments was increased. The highest amount was observed at 325°C and this phase was no longer observed after the reaction was carried out at 375°C. At 375°C the maximum amount of β - $\text{Li}_2\text{Mg}(\text{NH})_2$ was observed and the powder XRD pattern from this temperature is shown in Figure 3-15. The total amount of $\text{Li}_2\text{Mg}(\text{NH})_2$ remained constant between 325°C and 375°C.

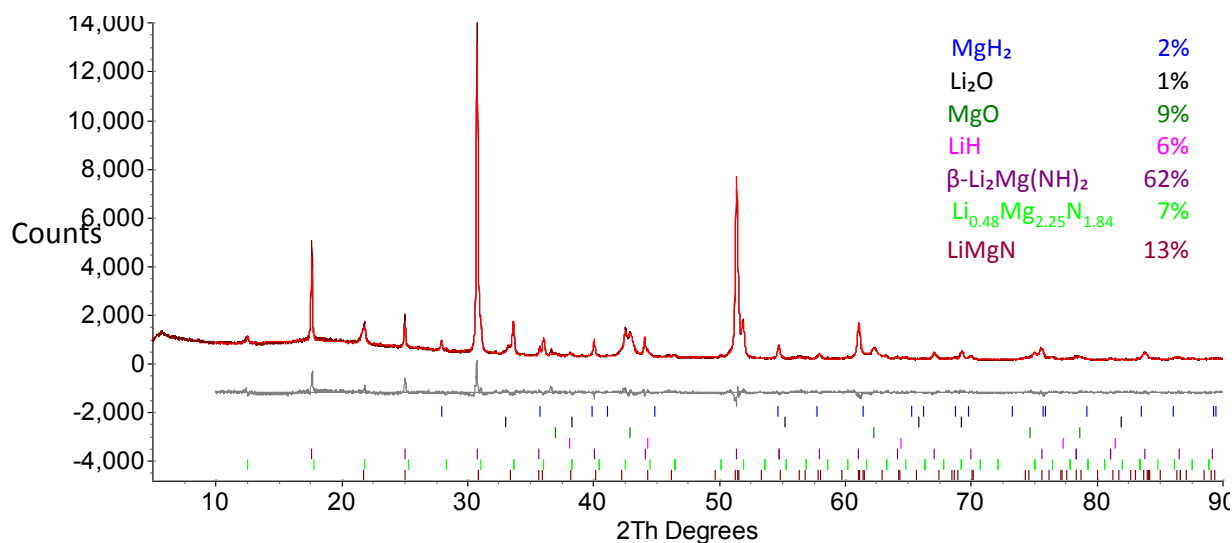


Figure 3-15: Powder XRD pattern of $2\text{LiNH}_2 + \text{MgH}_2$ sample heated at 375°C for 12 hours, with Rietveld fit showing the difference (grey), calculated (red) and observed (black) traces with the peak positions indicated for MgH_2 (blue), Li_2O (black), MgO (green), MgO (pink), β - $\text{Li}_2\text{Mg}(\text{NH})_2$ (purple), $\text{Li}_{0.48}\text{Mg}_{2.52}\text{N}_{1.84}$ (light green) and LiMgN (brown).

The wt% of both phases of $\text{Li}_2\text{Mg}(\text{NH})_2$ and the nitride phases against temperature are compared in Table 3-6. There was a small unidentified peak which appeared in several patterns around 11-13° (indicated in Figure 3-19 but first observed in Figure 3-15). Literature searches for peaks in this area indicated that peaks in this range observed at elevated reaction temperatures could be indicative of lithium magnesium nitrides¹⁴⁴. These nitride type phases were observed at

all the starred temperatures in Table 3-6, Table 3-7 and Table 3-8. The peak positions for Mg_3N_2 and $\text{Li}_{0.24}\text{Mg}_{2.76}\text{N}_{1.92}$, space group $I2_13$ (No. 199), an isostructural, nitrogen-deficient, magnesium-rich phase of LiMgN are very similar.

Bailey *et al.*¹⁴⁴ explored the 'structure stability field' of variable cation and nitrogen ratios within LiMgN beyond the stoichiometric phase. They published structural data for five variations of a LiMgN-type phase solved to space group $I2_13$ which are all strongly magnesium-rich and nitrogen-deficient, as well as other variations with different space groups. Several structures of stoichiometric phases of LiMgN belonging to space group $Pnma$ (No. 62) were also published, some formed at temperatures as low as 200°C. A slightly Li-rich phase of LiMgN was also found and the structure solved in space group $Fm\bar{3}m$ (No. 225).

Given the range of stoichiometries 'LiMgN' can accommodate, a different approach was used in Topas to assess these phases. Instead of using structural data, a pawley fit was first performed using each possible space group to ascertain if any of the three structure types detailed above were likely to be found in the patterns. Using the as-determined lattice parameters, modelling was attempted with the relevant structural data available for that space group. In the case of Figure 3-15, it was thought that two phases of LiMgN were present, a stoichiometric phase, and $\text{Li}_{0.48}\text{Mg}_{2.25}\text{N}_{1.84}$.

All the possible structural variants solved by Bailey *et al.*¹⁴⁴, five for the cubic phase, and four for the orthorhombic phase were compared, and the most similar models taken forwards. As the structural variants for the cubic phase have varying stoichiometry, the best fit was found with the structure previously solved¹⁴⁴ for $\text{Li}_{0.48}\text{Mg}_{2.52}\text{N}_{1.84}$ but the lattice parameter determined in this work was found to be slightly smaller, 9.966(3) Å compared to a published value 9.9909(3) Å. As the fit using modelled data was close, a refinement of the occupancies of the cations and nitrogen atoms was attempted. Unfortunately, without occupancy constraints a full refinement could not

be achieved and the model fitted to the data in Figure 3-15 includes restraints. Difficulties in fully modelling LiMgN were also encountered with other patterns in this chapter.

Temperature (°C)	Amount of α -Li ₂ Mg(NH) ₂ (wt%)	Amount of β -Li ₂ Mg(NH) ₂ (wt%)	Total amount of Li ₂ Mg(NH) ₂ (wt%)	Nitride phases (wt%)
275	10	-	10	-
300	19	1	20	-
325	56	9	65	-
350*	15	49	64	9
375*	-	62	62	20
400	-	50	50	17

Table 3-6: Estimated wt% by quantitative phase analysis of two phases of Li₂Mg(NH)₂ and all nitride phases prepared from 2LiNH₂ + MgH₂ hand ground samples.

The structural conversion from α - to β -Li₂Mg(NH)₂ only occurs after a high-energy input into the system due to the energy required to overcome the large kinetic barrier to formation of the β -Li₂Mg(NH)₂ phase. This can be achieved by increased reaction temperatures or high energy ball-milling. It has previously been found to occur at temperatures around 350°C⁴ - 400°C⁷¹. As the powder X-ray diffraction pattern analysed in Figure 3-15 was recorded after the sample was heated at 375°C for 12 hours, these reaction conditions could account for the phase transition observed.

The structure of β -Li₂Mg(NH)₂ has a more ordered distribution of Li and Mg atoms than α -Li₂Mg(NH)₂⁷³. Studies on ball-milled samples found both these phases could be formed below 280°C. The formation of β -Li₂Mg(NH)₂ at higher temperatures in this work is likely accounted for by poor contact and mixing of the two starting ingredients, resulting in large Li⁺ ion diffusion distances and few low energy routes for diffusion to occur available. This generates a large kinetic barrier for a process that may otherwise be thermodynamically possible. The diffusion of Li⁺ has previously been determined to be the rate-limiting step in the 2LiNH₂ and MgH₂ system²⁹.

As discussed in Section 1.6.2 and shown in Scheme 1-2, the formation of the mixed cation imide is the most important route to reversible hydrogen storage. Hence, how preparation of samples affects the temperature at which these phases are formed and the type and amount of the phase is of interest. Clearly, the apparatus available has resulted in a certain degree of oxidation of samples, which has been unavoidable. The amount of oxidation observed appeared to be largely independent of preparation. The desorption and absorption properties of the two accessible phases of $\text{Li}_2\text{Mg}(\text{NH})_2$ are slightly different. Desorption under vacuum to form $\beta\text{-Li}_2\text{Mg}(\text{NH})_2$ could occur at lower temperatures and more rapidly than when desorption conditions were used to force the formation of $\alpha\text{-Li}_2\text{Mg}(\text{NH})_2$. Hydrogenation of the β -phase was also faster and successful at lower temperatures.

In addition to the major product, $\text{Li}_2\text{Mg}(\text{NH})_2$, Li_2NH and a nitride phase were also formed in these reactions indicating that competing reactions were consuming the starting materials. This was not unexpected due to the poor homogeneity of the sample through hand mixing. If MgH_2 was not available then LiNH_2 could decompose⁴⁵, through the formation of Li_2NH (Equation 3-3), which would also explain why ammonia release was observed in the TPD-MS experiment (Figure 3-1) peaking at around 375°C.



In Figure 3-15, lithium hydride was observed as a product; although the wt% is very small, due to the mass of LiH, the mol% is much higher, ~20%. The presence of LiH would imply that a metathesis reaction was occurring, however, powder XRD evidence for $\text{Mg}(\text{NH}_2)_2$ was not observed. A possible explanation for the lack of powder XRD evidence for $\text{Mg}(\text{NH}_2)_2$ may be given by considering the total scattering intensity of the phase and number of peaks produced by that phase. As a significant number of peaks are observed for $\text{Mg}(\text{NH}_2)_2$, unless it is present in large amounts the intensity of the peaks for this phase may be indistinguishable even if there is some

Mg(NH₂)₂ present. The formation of either Mg₃N₂ or LiMgN could indicate that non-stoichiometric reactions were taking place (Equations 3-4 or 3-5) and the homogeneity of samples was poor.

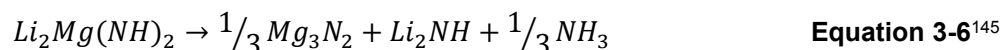


The formation of Li₂NH in some of these samples would be unsurprising if a magnesium-rich nitride phase was also formed. The formation of a magnesium deficient nitride phase could indicate that non-stoichiometric reactions were taking place (Equations 3-4 and/or 3-5) and the contact of the two reacting phases was poor. The formation of both Li₂NH and Mg₃N₂ could also be consistent with Equation 3-5, and with the observation of LiH in the powder XRD patterns⁵⁴.



This reaction could also explain the lack of Mg(NH₂)₂ observed in the powder XRD patterns, as they were not recorded in-situ but after samples had cooled down. If the reaction proceeded according to Equation 3-5, and the equilibria lay to the right (products) and the formation of Mg(NH₂)₂ was the rate limiting step in this reaction, then excess LiH could be observed. When the product wt% of Mg₃N₂ and Li₂NH from Figure 3-15 were converted to mol%, the ratio was approximately 1:4, close to that of the products in Equation 3-5.

An alternative reaction, which could explain both the formation of Mg₃N₂ and Li₂NH at higher temperatures (Figure 3-15) and some of the observed ammonia release from this sample during TGA experiments, (Figure 3-4) would be a reaction where Li₂Mg(NH)₂ decomposes into multiple products. Such a reaction was suggested by Isobe *et al.*¹⁴⁵ and is shown in Equation 3-6.



3.4.4.2 Ball-milled under 1 bar argon

A similar powder XRD study to the one described in Section 3.4.4.1 was carried out on two ball-milled samples of 2LiNH₂ and MgH₂: one milled under atmospheric argon and the other under

100 bar H_2 . As shown in Section 3.3.1 ball-milling dramatically reduced hydrogen desorption temperatures. The results presented in this section are from samples that were ball milled under atmospheric argon pressure. The literature on reactions under milling reports varied results with some observing metathesis reactions occur under milling whilst others observed no changes to the materials other than particle size and improvements in the degree of dispersion.

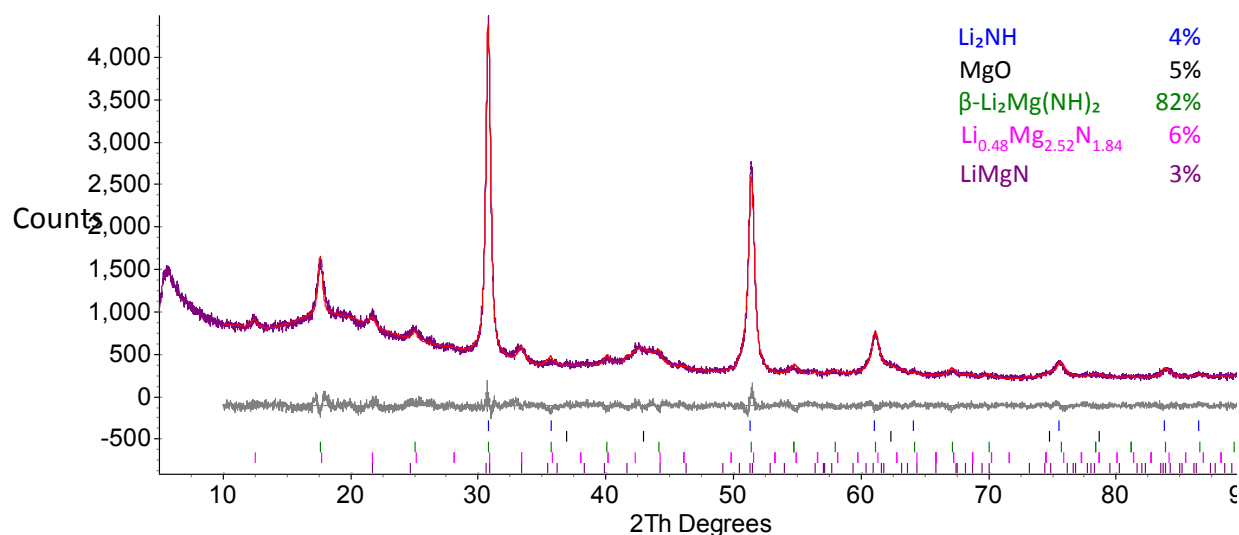


Figure 3-16: Powder XRD pattern of $2LiNH_2 \cdot MgH_2$ sample ball-milled under 1 bar argon heated at $200^\circ C$ for 12 hours, with Rietveld fit showing the difference (grey), calculated (red) and observed (purple) traces with the peak positions indicated for Li_2NH (blue), MgO (black), $\beta-Li_2Mg(NH)_2$ (green), $Li_{0.48}Mg_{2.52}N_{1.84}$ (pink), and $LiMgN$ (purple).

As discussed previously, the powder XRD pattern after milling did not show evidence of any metathesis reactions, only the formation of Li_2NH (Figure 3-7). A large amount of $\beta-Li_2Mg(NH)_2$ was observed in samples at all temperatures, from temperatures as low as $150^\circ C$. This was in contrast to the hand-ground sample where significant amounts of $\beta-Li_2Mg(NH)_2$ were not observed until $75^\circ C$ after the α -phase was first seen. The amount of $\alpha-Li_2Mg(NH)_2$ peaked after heating at $225^\circ C$ and it was no longer observed after heating at $300^\circ C$. In the reactions of samples milled under 1 bar argon, a magnesium-rich mixed cation nitride phase and $LiMgN$ were observed at temperatures as low as $200^\circ C$ (Figure 3-16). Low temperature formation may be influenced by the introduction of strain and vacancies during high energy ball milling. In contrast to the hand-

ground system, where mainly magnesium nitride was observed, mainly lithium nitride was found in this ball-milled system.

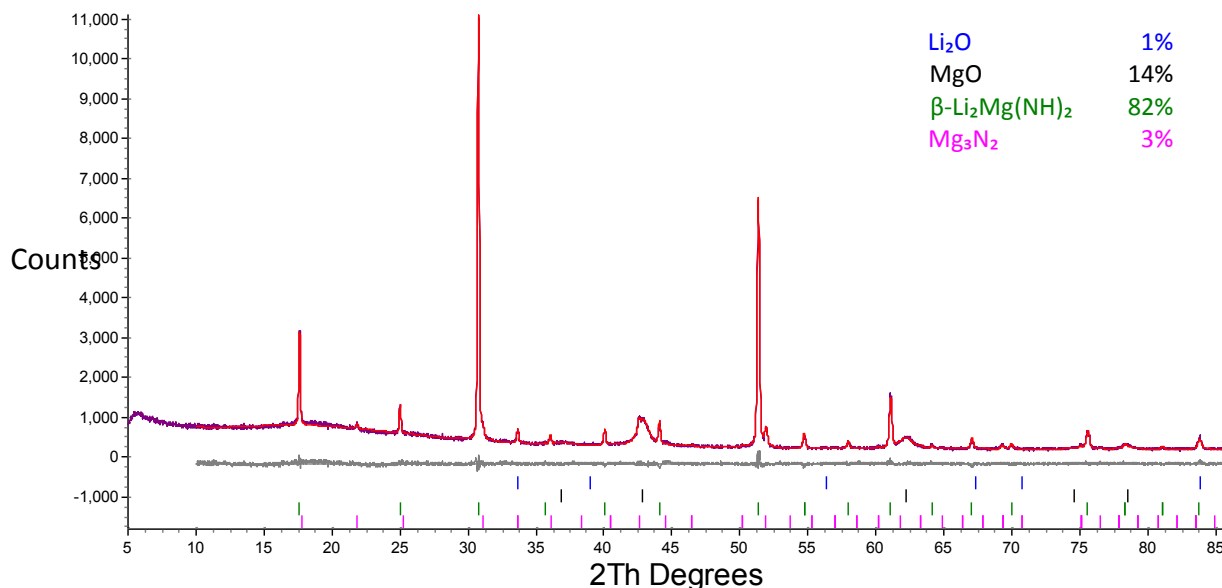


Figure 3-17: Powder XRD pattern of 2LiNH₂ + MgH₂ sample ball-milled under 1 bar argon, heated at 400°C for 12 hours, with Rietveld fit showing the difference (grey), calculated (red) and observed (purple) traces with the peak positions indicated for Li₂O (blue), MgO (black), β-Li₂Mg(NH)₂ (green) and Mg₃N₂ (pink).

The powder XRD pattern in Figure 3-17 shows the composition of the sample heated for 12 hours at 400°C. It was slightly surprising that the amount of β-Li₂Mg(NH)₂ observed was similar, whether the sample was heated at 200°C (Figure 3-15) or 400°C (Figure 3-17). Interestingly, there was no evidence of LiMgN in Figure 3-17, after the sample had been heated to 400°C. Compared to the pattern shown in Figure 3-15, the peaks in Figure 3-17 are sharp and well defined. This is likely due to the sintering and annealing effects of heating the sample at 400°C which will remove many of the structural vacancies and encourage agglomeration of small particles produced by high energy ball-milling.

Formation of the β-phase at 150°C proves that although the α-phase may be favoured by low temperature, Li₂Mg(NH)₂ formation was not completely temperature controlled. As evidenced by powder XRD patterns, a large amount of β-Li₂Mg(NH)₂ was converted to α-Li₂Mg(NH)₂ (mid-range temperature experiments ~225 – 275°C) and then reverted to back to β-

$\text{Li}_2\text{Mg}(\text{NH})_2$ as the heating temperatures were increased (Figure 3-17). According to Liang *et al.*⁷³ the β -phase is more highly ordered than the α -phase and is the ground energy state structure above 52°C. The former has 3 different tetrahedral interstitial sites, 2 of which are only occupied by Li, whereas the α -phase has 2 different cation sites which are both occupied by disordered Li and Mg. As the β -phase has been reported⁷³ to be kinetically unfavourable, a large energy input during milling may have allowed the phase to overcome its kinetic limitations and form directly upon hydrogen release.

At moderate temperatures, such as the mid-range temperatures in this work, this means that the transformation from β -phase to α -phase observed would not be a thermodynamically favourable process⁷³. As gas back-pressure was found to be a dominant factor in determining the phase structure⁷¹, an explanation for this transformation might be that increased pressure within the experimental setup during desorption had caused the β - to α -phase transition. However, pressures of around 9 bar were thought to be required to cause this transformation⁷¹ and it seems unlikely that a pressure this high would have been reached, especially in a flowing system.

Temperature (°C)	Amount of $\alpha\text{-Li}_2\text{Mg}(\text{NH})_2$ (wt%)	Amount of $\beta\text{-Li}_2\text{Mg}(\text{NH})_2$ (wt%)	Total amount of $\text{Li}_2\text{Mg}(\text{NH})_2$ (wt%)	Nitride phases (wt%)
150	-	59	59	-
200	-	82	82	9
225	21	50	71	2
250*	39	35	74	4
275*	41	28	71	5
300*	-	67	67	6
350	-	72	72	4
400	-	82	82	3

Table 3-7: Estimated wt% by quantitative phase analysis of two phases of $\text{Li}_2\text{Mg}(\text{NH})_2$ and all nitride phases prepared from $2\text{LiNH}_2 + \text{MgH}_2$ samples ball-milled under 1 bar argon.

The amounts of α - and β - $\text{Li}_2\text{Mg}(\text{NH})_2$ as well as the total amount of nitride phases are compared in Table 3-7. A larger proportion of the mixed imide was formed at lower temperatures in the system ball-milled under 1 bar argon than in the hand-ground system. The formation of the nitride phases began at much lower temperatures but the amount formed did not change significantly between reactions at 200°C and 400°C.

3.4.4.3 Ball-milled under 100 bar hydrogen

The results presented in this section are from samples which were milled under 100 bar H_2 pressure. Unfortunately, there were no methods available to analyse any gas release that may or may not have occurred during ball-milling. As this sample was milled under hydrogen pressure, hydrogen release during milling should be less likely due to equilibrium constraints for further hydrogen release. However, from the powder XRD recorded after milling was presented in Figure 3-7, in addition to the starting materials, MgO and Li_2NH were also identified after milling. Raman spectrum indicated the presence of $\text{Mg}(\text{NH}_2)_2$ after milling preparation. The presence of Li_2NH suggested that pressurising the pot had not suppressed the gas release during milling.

The peak profiles in the powder XRD patterns after heating the samples ball-milled under 100 bar hydrogen (*i.e.* Figure 3-18) were mostly sharper at lower temperature than those observed in the corresponding powder XRD patterns in the samples milled under 1 bar argon. $\text{Li}_2\text{Mg}(\text{NH})_2$ (α -phase) was first observed in the powder XRD patterns at 200°C, 75°C lower than compared to hand ground samples and 50°C higher than the sample ball-milled under 1 bar argon, (but similar to formation temperatures observed by Rijssenbeek *et al.*⁴). The temperatures at which α - $\text{Li}_2\text{Mg}(\text{NH})_2$ appeared and peaked, were very similar in both ball-milled samples.

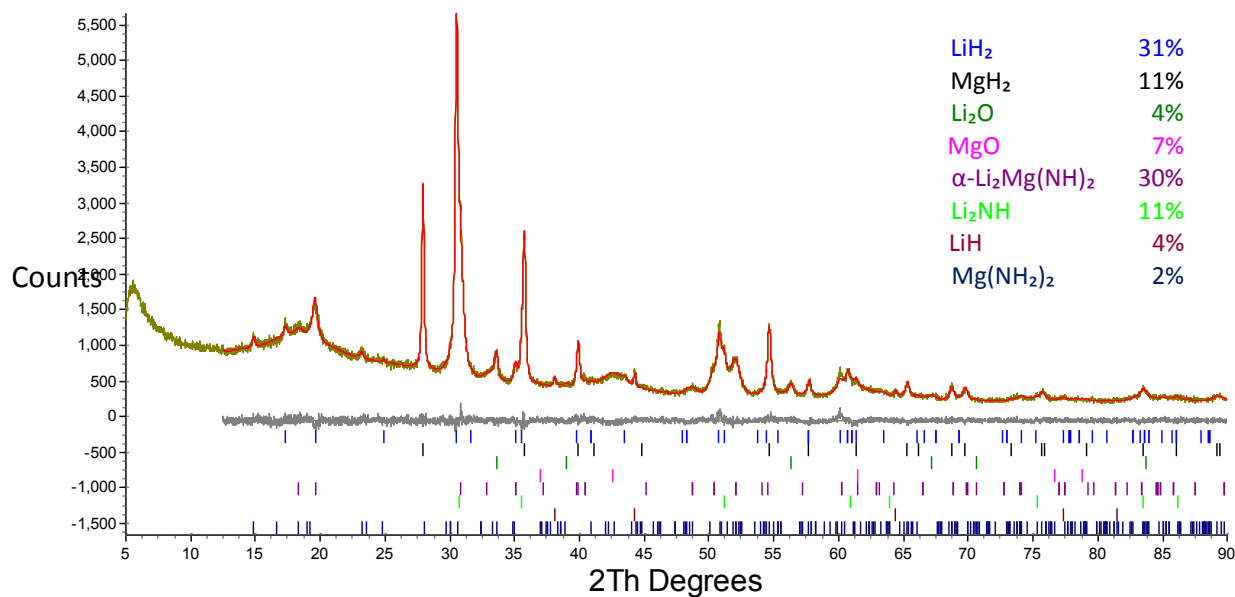


Figure 3-18: Powder XRD pattern of 2LiNH₂ + MgH₂ sample ball-milled under 100 bar hydrogen, heated at 200°C for 12 hours, with Rietveld fit showing the difference (grey), calculated (red) and observed (black) traces with the peak positions indicated for LiNH₂ (blue), MgH₂ (black), Li₂O (green), MgO (pink), α-Li₂Mg(NH)₂ (purple), Li₂NH (light green) and LiH (brown) and Mg(NH₂)₂ (dark blue).

Initial formation of the β-phase when milling was carried out under 1 bar argon proves that although the samples appeared to be the same (initial powder XRD characterisation), there are some fundamental differences in how they react which could be attributed to the altered particle level interactions caused by the conditions during ball-milling. This could indicate that less disorder had been introduced into the sample ball-milled under 100 bar hydrogen pressure. As the formation of Li₂Mg(NH)₂ was thought to be the main phase for facilitating hydrogen release, this temperature was in good agreement with the peak of hydrogen desorption which occurred at 185°C (Figure 3-4).

Unlike the hand-ground sample and sample milled under 1 bar argon, both Mg(NH₂)₂ and LiH were observed in the powder XRD pattern at 200°C. These were not observed directly after milling in powder XRD data, but only after heating at 200°C. It is likely that Mg(NH₂)₂ was not visible due to poor crystallinity and the peaks caused by LiH were obscured due to broad peaks from other phases and the fact that the X-ray scattering strength of LiH is very low. Heating the

sample at 200°C has acted as an annealing process which has made $\text{Mg}(\text{NH}_2)_2$ visible on the powder XRD pattern.

The presence of these two phases confirms that a metathesis reaction had occurred in this sample. This was unsurprising, as the mixing of the sample during ball-milling would decrease the particle sizes and increase the contact between the two starting materials, allowing more facile reactions between LiNH_2 and MgH_2 . The formation of fully hydrogenated metathesis products during milling and under heating suggests that hydrogen release during milling was inhibited under pressure. After heating at 225°C for 12 hours, neither $\text{Mg}(\text{NH}_2)_2$ and LiH were observed in the powder XRD pattern and the amount of $\alpha\text{-Li}_2\text{Mg}(\text{NH}_2)_2$ had increased.

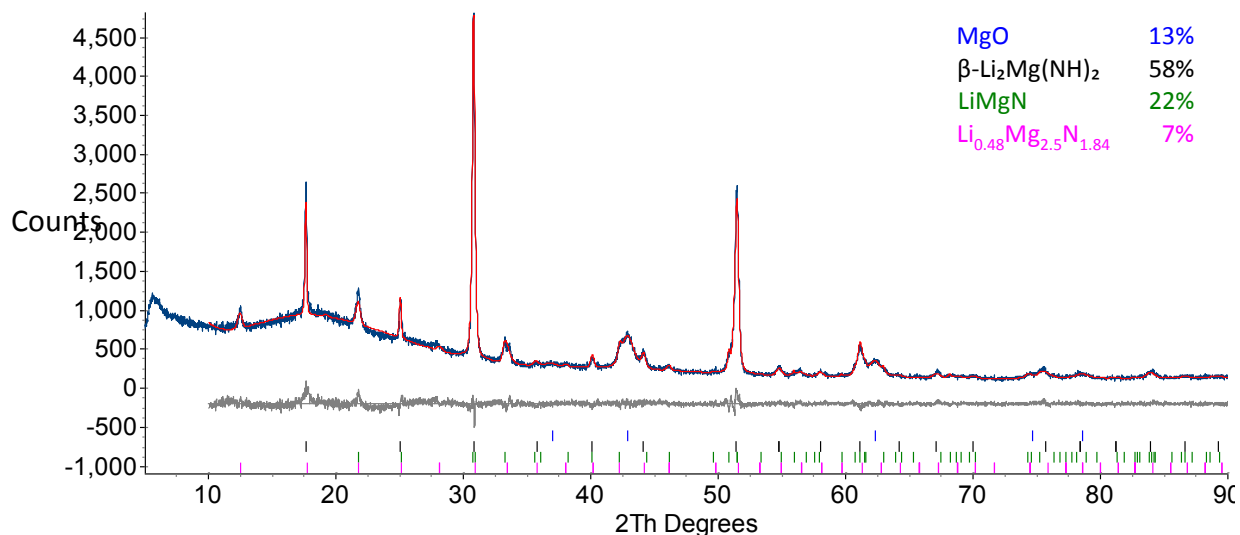


Figure 3-19: Powder XRD pattern of $2\text{LiNH}_2 + \text{MgH}_2$ sample ball-milled under 100 bar hydrogen, heated at 350°C for 12 hours, with Rietveld fit showing the difference (grey), calculated (red) and observed (dark blue) traces with the peak positions indicated for MgO (blue), $\beta\text{-Li}_2\text{Mg}(\text{NH})_2$ (black), LiMgN (green), $\text{Li}_{0.48}\text{Mg}_{2.52}\text{N}_{1.84}$ (pink).

A significant amount of $\beta\text{-Li}_2\text{Mg}(\text{NH})_2$ was observed at 250°C in this ball-milled sample, around 100°C lower than in the hand-ground sample. The powder XRD pattern displayed in Figure 3-19 was recorded after heating at 350°C for 12 hours. $\beta\text{-Li}_2\text{Mg}(\text{NH})_2$ was the majority phase in this sample and two phases of LiMgN were also observed.

Temperature (°C)	Amount of α - $\text{Li}_2\text{Mg}(\text{NH})_2$ (wt%)	Amount of β - $\text{Li}_2\text{Mg}(\text{NH})_2$ (wt%)	Total amount of $\text{Li}_2\text{Mg}(\text{NH})_2$ (wt%)	Nitride phases (wt%)
200	30	-	30	-
225	78	-	78	-
250	29	50	79	-
300*	7	65	72	9
350*	-	58	58	29
400*	-	65	65	18

Table 3-8: Estimated wt% by quantitative phase analysis of two phases of $\text{Li}_2\text{Mg}(\text{NH})_2$ and all nitride phases prepared from $2\text{LiNH}_2 + \text{MgH}_2$ samples ball-milled under 100 bar H_2 pressure.

The wt% of the $\text{Li}_2\text{Mg}(\text{NH})_2$ and nitride phases are compared in Table 3-8. The total amount of $\text{Li}_2\text{Mg}(\text{NH})_2$ produced from both ball-milled samples was greater than the hand-ground samples and was consistent over a larger temperature range than the hand-ground samples. The temperature at which the formation of β - $\text{Li}_2\text{Mg}(\text{NH})_2$ was first observed was the same as the hydrogen desorption peak.

The products observed after heating all three systems to temperatures of around 350-400°C were dominated by β - $\text{Li}_2\text{Mg}(\text{NH})_2$. The amount of nitride phases observed in the hand-ground and ball-milled systems was mostly comparable. The hand-ground system included lithium- and magnesium-rich phases as well as a mixed cation nitride phase. These phases suggest a range of reactions were occurring which were not according to the 2: 1 Li to Mg reactant stoichiometry. At similar temperatures, the samples ball-milled under 1 bar argon favoured the formation of Mg_3N_2 , whereas the samples ball-milled under 100 bar hydrogen favoured the formation of LiMgN phases.

As discussed in Section 3.4.4.1 the peak positions of Mg_3N_2 and a magnesium-rich LiMgN phase are very similar. There are several examples of slight intensity mismatches in the patterns presented in Sections 3.4.4.2 and 3.4.4.3 which could indicate variations in cation occupancies but

very little variation was observed in the calculated lattice parameters (<0.01% by cell volume) and the data quality was not sufficient to differentiate clearly and determine the compositions in these nitride phases. As Li is the lighter element it would be more difficult to determine accurately in powder XRD patterns and further work would include neutron diffraction on deuterated samples. The lowest amount of nitrides was observed in the samples ball-milled under 1 bar argon pressure, but they began to appear at lower temperatures than in the samples milled under 100 bar hydrogen pressure. The mixed-cation imide phases were observed at lower, more accessible temperatures after ball-milling. At reaction temperatures of 200°C the samples milled under 1 bar argon pressure yielded a large proportion of β -Li₂Mg(NH)₂, (greater than 80wt%). This suggests that milling under these conditions is favourable for inducing low temperature desorption and possible alternative reaction pathways are facilitated involving reactions occurring during milling.

Several groups^{40, 80, 145} have used MgH₂ excess when preparing ball-milled samples to prevent ammonia loss. To investigate the requirement for excess hydride, a hand-ground sample containing 10% excess MgH₂ was prepared and the amounts of LiNH₂ and MgH₂ were compared after heating to 325°C for 12 hours to a sample without MgH₂ excess. The ratio of remaining LiNH₂ and MgH₂ remained unchanged regardless of the excess, so during these experiments an excess of MgH₂ was not used.

3.4.4.4 Cycling experiments

To further understand how the two ball-milled samples behaved under cyclic conditions, isothermal desorption experiments under vacuum, flowing argon and 10 bar argon pressure were carried out. Due to the augmented temperatures, slow rates and large ammonia release seen in TGA-MS experiments, hand-prepared samples were not included in these experiments.

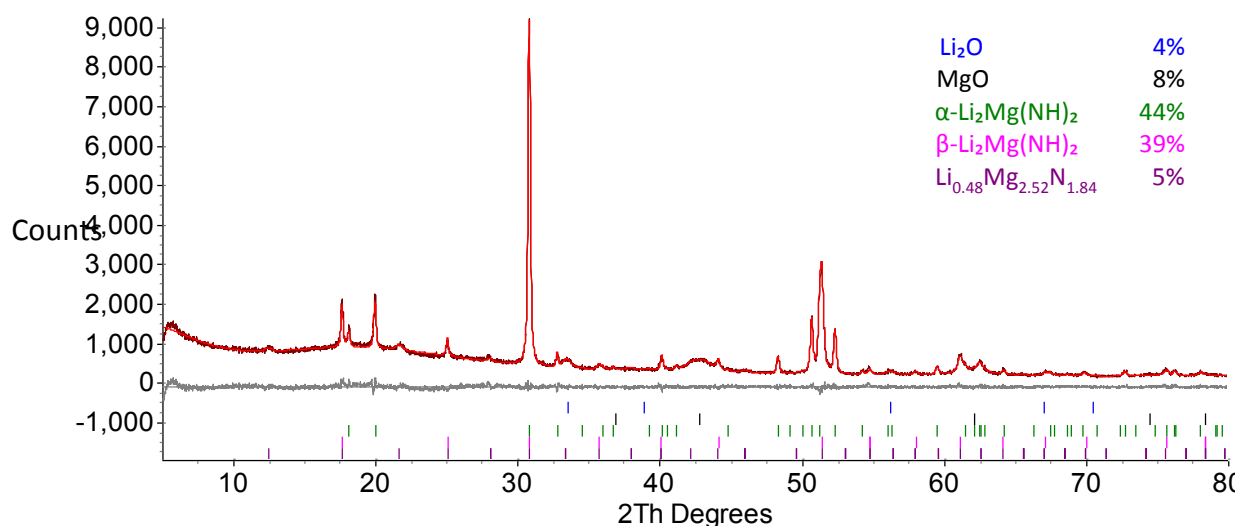


Figure 3-20: Powder XRD pattern of 2LiNH₂ + MgH₂ sample ball-milled under 100 bar hydrogen, heated at 220°C under flowing argon for 50 hours, with Rietveld fit showing the difference (grey), calculated (red) and observed (black) traces with the peak positions indicated for Li₂O (blue), MgO (black), α-Li₂Mg(NH)₂ (green), β-Li₂Mg(NH)₂ (pink) and Li_{0.48}Mg_{2.52}N_{1.84} (purple).

As previous work on the LiNH₂-MgH₂ system had selected 220°C as an ideal temperature for isothermal desorption^{26, 42, 141}, this was employed for the desorption experiments described below. This temperature (close to 225°C) was also where the largest portion of Li₂Mg(NH)₂ was observed (Table 3-7 and Table 3-8). The extended duration was chosen to ensure dehydrogenation was complete so that the effects of conditions and preparation could be accurately assessed.

The powder XRD patterns of the two ball-milled samples after desorption under flowing argon are shown in Figure 3-20 and Figure 3-21. According to Liang *et al.*⁷¹ the phase of Li₂Mg(NH)₂ formed is independent of temperature under 280°C, but governed by gas back pressure. A low pressure (< 3 bar) should favour the formation of β-Li₂Mg(NH)₂, while a higher pressure (>9 bar) should mean α-Li₂Mg(NH)₂ would dominate. Unfortunately, Liang *et al.*⁷³ could not offer an explanation for why the gas back pressure should influence which phase of Li₂Mg(NH)₂ was formed. Additional factors which may also contribute to controlling the phase produced are further discussed in Section 3.5. The phase transitions observed during work carried out within this chapter on various samples would indicate that the stoichiometry of the

reactants (i.e. cation availability and hydrogen deficiency) is an important factor in controlling the phase of $\text{Li}_2\text{Mg}(\text{NH})_2$ produced.

The appearance of a large amount of $\alpha\text{-Li}_2\text{Mg}(\text{NH})_2$ in these two samples heated under flowing argon, especially in Figure 3-21, based on recent findings of phase controlling-factors would be unusual. From these results, it would appear there are likely to be other contributing factors which control the phase of $\text{Li}_2\text{Mg}(\text{NH})_2$ produced.

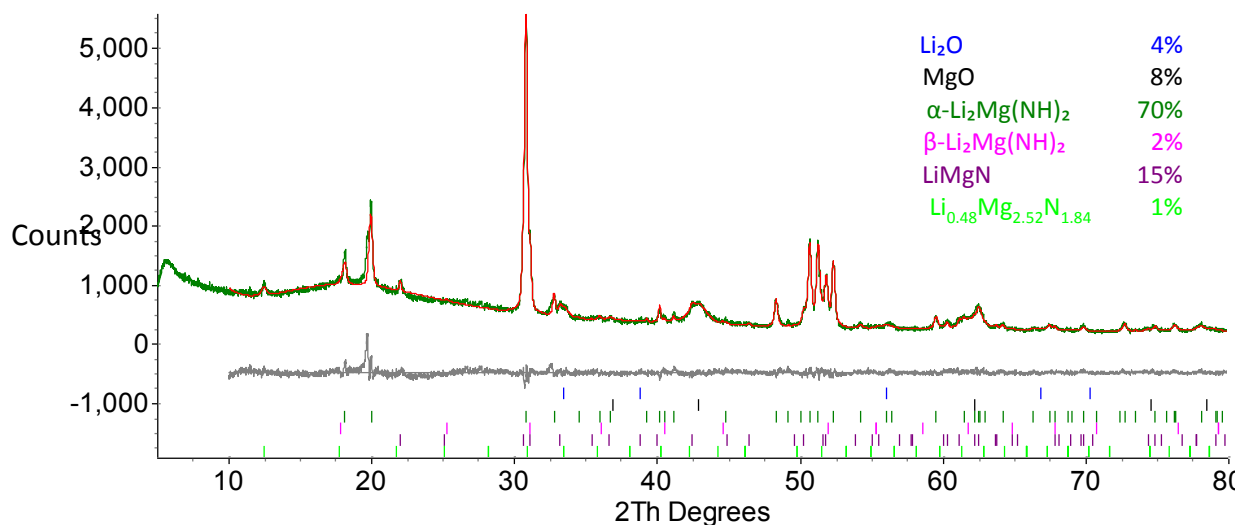


Figure 3-21: Powder XRD pattern of $2\text{LiNH}_2 + \text{MgH}_2$ sample ball-milled under 1 bar argon, heated at 220°C under flowing argon for 50 hours, with Rietveld fit showing the difference (grey), calculated (red) and observed (green) traces with the peak positions indicated for Li_2O (blue), MgO (black), $\alpha\text{-Li}_2\text{Mg}(\text{NH})_2$ (green), $\beta\text{-Li}_2\text{Mg}(\text{NH})_2$ (pink), LiMgN (purple) and $\text{Li}_{0.48}\text{Mg}_{2.52}\text{N}_{1.84}$ (light green).

The amounts of the α - and β -phases in the sample that was initially milled under pressure were very similar. When the TGA-MS trace shown in Figure 3-5 is considered in correlation to these samples, the mass loss from the samples milled under 100 bar hydrogen was more gradual whereas the gradient of mass loss from the sample milled under 1 bar argon was sharp indicating the amount of gas during the desorption peak might have been higher, which could lead to a different reaction. This deduction would be in a good agreement with the powder XRD results of these samples. The variation between the formation of the α - and β -phases of $\text{Li}_2\text{Mg}(\text{NH})_2$, and causes will be discussed in more detail in Section 3.5.

A small amount of lithium amide was also observed after desorption from the sample ball-milled under 1 bar argon, indicating that desorption from this sample (around 220°C) was not complete. This was unsurprising as decomposition of pure LiNH_2 does not occur until temperatures over 300°C⁴⁵. As neither phase was used in excess and MgH_2 did not also remain, this could have been caused by reactions occurring at a stoichiometry of 1MgH_2 to 1LiNH_2 .

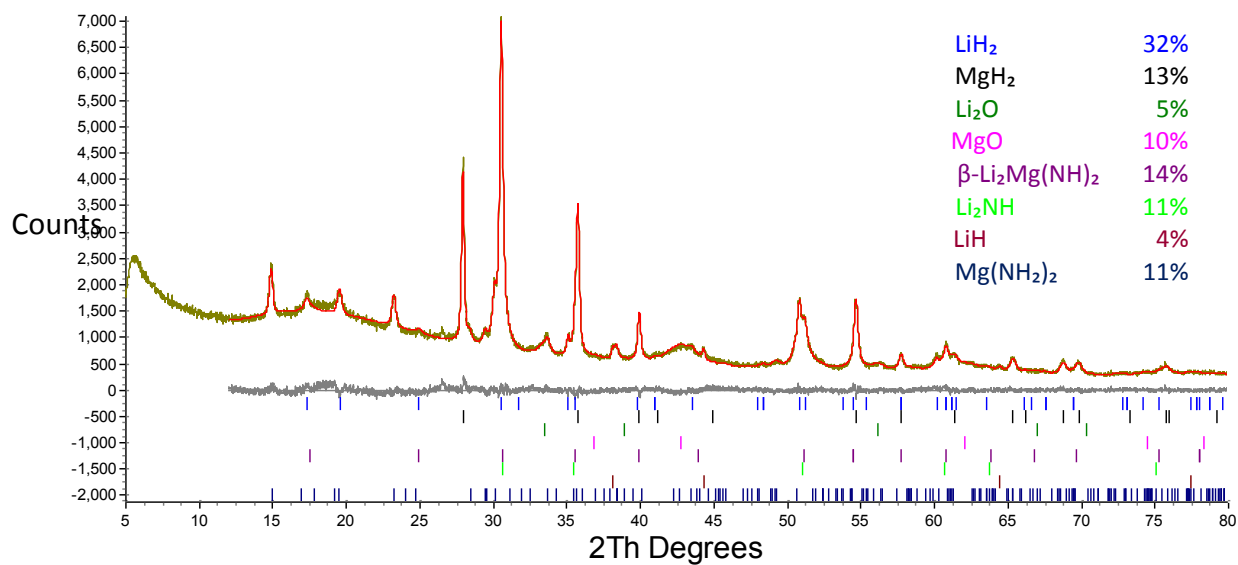
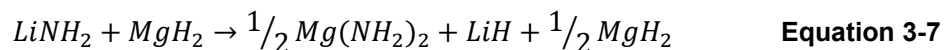


Figure 3-22: Powder XRD pattern of $2\text{LiNH}_2 + \text{MgH}_2$ sample ball-milled under 100 bar hydrogen, heated at 220°C under vacuum for 50 hours, with Rietveld fit showing the difference (grey), calculated (red) and observed (green) traces with the peak positions indicated for LiNH_2 (blue), MgH_2 (black), Li_2O (green), MgO (pink), $\beta\text{-Li}_2\text{Mg}(\text{NH})_2$ (purple), Li_2NH (light green), LiH (brown) and $\text{Mg}(\text{NH}_2)_2$ (dark blue).

The powder XRD in Figure 3-22 showed that the sample ball-milled under 100 bar hydrogen behaved very differently under vacuum desorption conditions to desorption under flowing argon. In this sample, a large proportion of the sample was made up of hydrogenated phases: the starting materials of lithium amide and magnesium hydride remained, as well as metathesis products, lithium hydride and magnesium amide. This was surprising as desorption from samples heated under dynamic vacuum would have been expected to be more complete than under flowing argon conditions. The observed differences from the same sample under different desorption conditions may indicate that additional gases, such as ammonia, are an important part of the desorption pathway, and by removing NH_3 more successfully under vacuum, the amount of imide phases produced was reduced.

The powder XRD pattern in Figure 3-22 is very similar to that shown in Figure 3-18. This was surprising as by heating the sample for 50 hours at 220°C, especially under vacuum, this would have been expected to encourage the sample to reach complete desorption. One explanation for the production of $Mg(NH_2)_2$ and LiH could be the first stage of a desorption pathway that produced LiMgN discussed by Liu *et al.*¹⁴⁶ and is shown in Equation 3-7.



As expected, with a low gas back-pressure (vacuum) only β - $Li_2Mg(NH_2)_2$ was formed. Desorption under vacuum for the sample ball-milled under 100 bar hydrogen would not be a chosen condition to maximise the potential hydrogen storage capacity of this sample because a lot of fully hydrogenated phases remained. The desorption products observed in the powder XRD pattern shown in Figure 3-24 were more similar to those observed from the samples heated under flowing argon. Desorption under vacuum had promoted the formation of the β -phase over the α -phase. However, the presence of LiH indicates that a metathesis reaction had previously occurred within this sample.

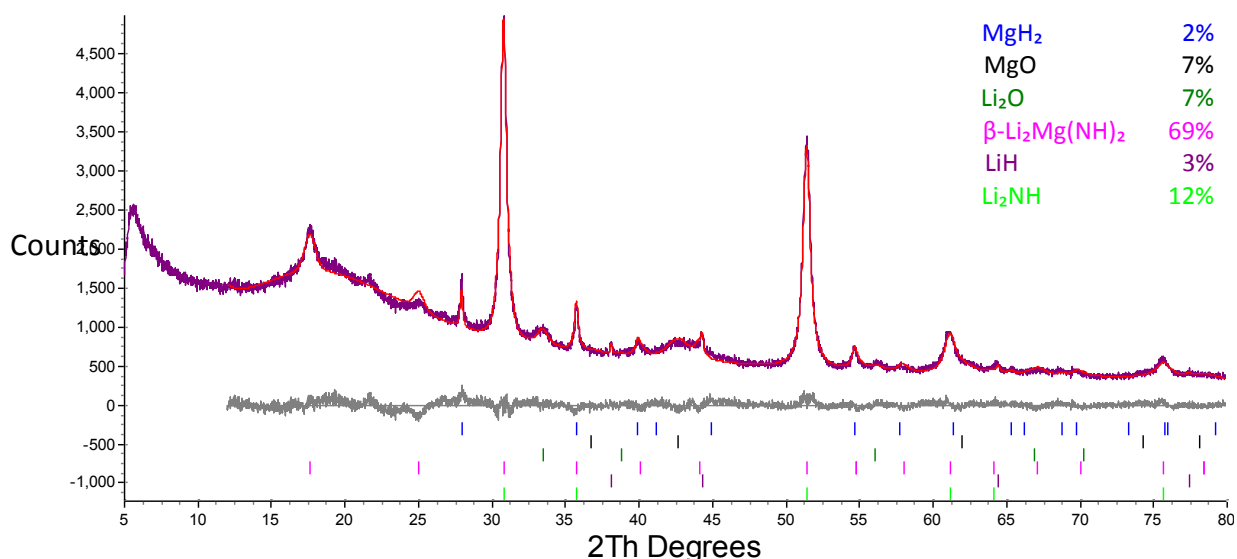


Figure 3-23: Powder XRD pattern of $2LiNH_2 + MgH_2$ sample ball-milled under 1 bar argon, heated at 220°C under vacuum for 50 hours, with Rietveld fit showing the difference (grey), calculated (red) and observed (purple) traces with the peak positions indicated for MgH_2 (blue), MgO (black), Li_2O (green), β - $Li_2Mg(NH_2)_2$ (pink), LiH (purple) and Li_2NH (light green).

From the powder XRD results of desorption under vacuum and flowing argon, as predicted the α -phase of $\text{Li}_2\text{Mg}(\text{NH})_2$ was not formed under low or no gas back-pressure, but formation of both phases under flowing argon suggested that the pressure distinction for formation of $\text{Li}_2\text{Mg}(\text{NH})_2$ made by Liang *et al.*⁷¹ may not be as clear as expected.

The amount of oxides observed in all samples after desorption (Figure 3-20 and Figure 3-24) was very similar, around 15%, indicating that changing the desorption or preparation method had no effect on the degree of oxidation. As shown in Table 3-9, the total amount of $\text{Li}_2\text{Mg}(\text{NH})_2$ observed in three samples after desorption was similar. Apart from oxides and very small amount of lithium nitride, $\text{Li}_2\text{Mg}(\text{NH})_2$ was the major product in both the samples heated under flowing argon, and the formation of the α -phase was favoured. The result from the sample milled under 100 bar hydrogen desorbed under vacuum stands out from the other three.

Sample preparation (desorption conditions)	Amount of $\alpha\text{-Li}_2\text{Mg}(\text{NH})_2$ (wt %)	Amount of $\beta\text{-Li}_2\text{Mg}(\text{NH})_2$ (wt %)	Total amount of $\text{Li}_2\text{Mg}(\text{NH})_2$ (wt%)	Nitride phases (wt%)
100 bar hydrogen (argon)	44	39	83	5
1 bar argon (argon)	70	2	72	16
100 bar hydrogen (vacuum)	-	14	14	-
1 bar argon (vacuum)	-	69	69	-

Table 3-9: Estimated wt% by quantitative phase analysis of two phases of $\text{Li}_2\text{Mg}(\text{NH})_2$ and nitride phases prepared from ball-milled $2\text{LiNH}_2 + \text{MgH}_2$ samples after thermal reaction at 220°C for 50 hours.

Rehydrogenation of both the samples heated under flowing argon was carried out for 24 hours at 200°C under 100 bar H₂. The powder XRD patterns in Figure 3-24 showed that Li₂Mg(NH)₂ was not observed after rehydrogenation of the ball-milled samples. A large amount of LiNH₂ and also some MgH₂ were observed in this pattern which was surprising as it was not thought possible to re-produce either phase after rehydrogenation as they were not the thermodynamic products of this reaction⁶⁵. Neither phase was identified in the powder XRD pattern after desorption. However, according to the hydrogenation path suggested by Weidner *et al.*⁶⁹, the presence of LiNH₂ would indicate that the rehydrogenation pathway had not been completed (Equation 1-16).

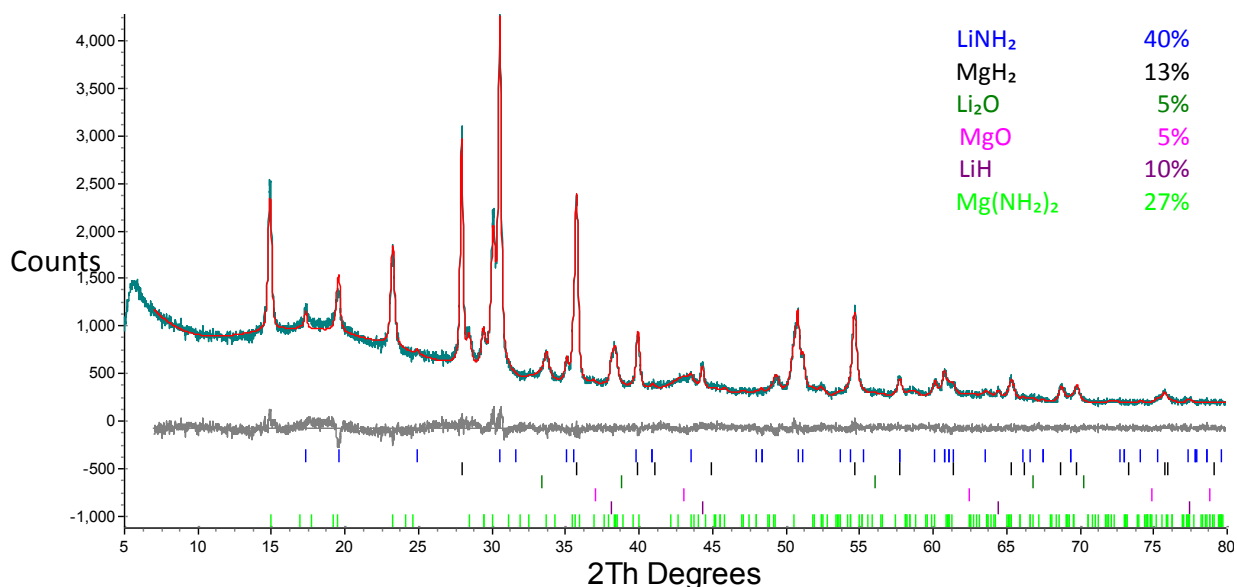


Figure 3-24: Powder XRD pattern of 2LiNH₂ + MgH₂ sample ball-milled under 100 bar hydrogen, after rehydrogenation at 200°C for 24 hours at 100 bar H₂ of sample shown in Figure 3-20 with Rietveld fit showing the difference (grey), calculated (red) and observed (turquoise) traces with the peak positions indicated for LiNH₂ (blue), MgH₂ (black), Li₂O (green), MgO (pink), LiH (purple), and Mg(NH₂)₂ (light green).

The more typically expected products of rehydrogenation, LiH and $\text{Mg}(\text{NH}_2)_2$ were also observed indicating successful rehydrogenation had occurred. When the wt% values were converted into mol% numbers, the lithium-containing phases were much higher than the magnesium containing phases, $4\text{LiNH}_2 + \text{MgH}_2$ and $3\text{LiH} + \text{Mg}(\text{NH}_2)_2$. This would indicate that magnesium had been lost from the desorption-absorption cycle at some point. A small amount of Li_2NH was observed in the powder XRD pattern of the sample ball-milled under 1 bar argon. In contrast to the sample milled under 100 bar hydrogen, the mol% ratio of lithium- to magnesium-containing phases was very similar to that of the initial reactants *i.e.* $2\text{LiNH}_2 + \text{MgH}_2$ and $2\text{LiH} + \text{Mg}(\text{NH}_2)_2$. In this sample the expected products, LiH and $\text{Mg}(\text{NH}_2)_2$ dominated the sample, accounting for more than 75 mol%. Before hydrogenation the sample ball-milled under 1 bar argon consisted of mainly $\alpha\text{-Li}_2\text{Mg}(\text{NH})_2$, whereas the sample milled under 100 bar hydrogen consisted of almost 50:50 mix of α - and $\beta\text{-Li}_2\text{Mg}(\text{NH})_2$.

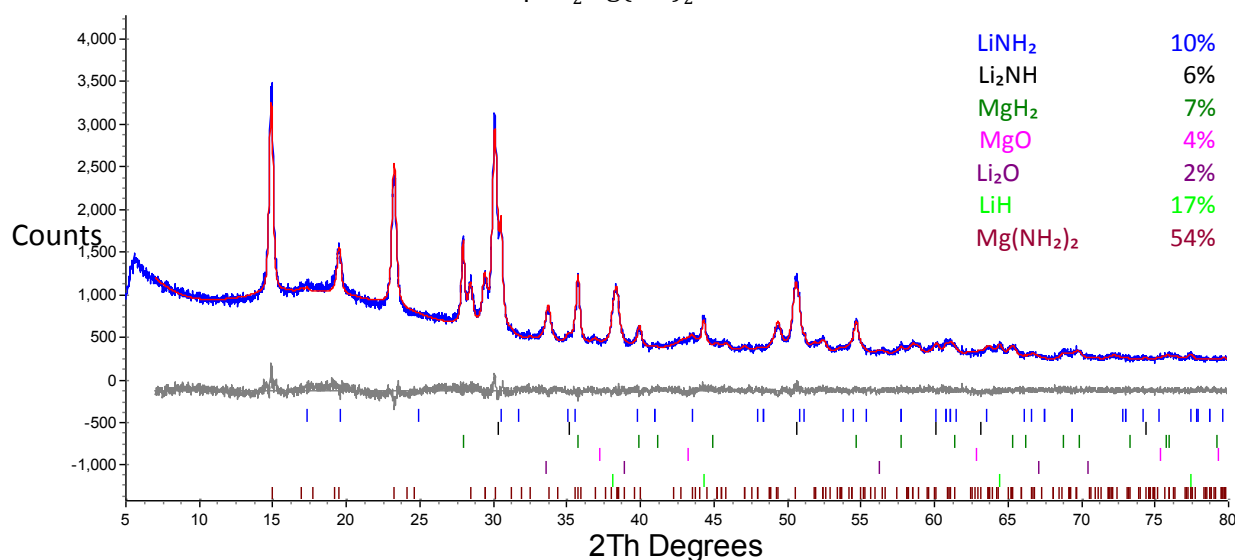


Figure 3-25: Powder XRD pattern of $2\text{LiNH}_2 + \text{MgH}_2$ sample ball-milled under 1 bar argon, after rehydrogenation at 200°C for 24 hours at 100 bar H_2 of sample shown in Figure 3-21, with Rietveld fit showing the difference (grey), calculated (red) and observed (blue) traces with the peak positions indicated for LiNH_2 (blue), Li_2NH (black), MgH_2 (green), MgO (pink), Li_2O (purple), LiH (light green) and $\text{Mg}(\text{NH}_2)_2$ (brown).

It was thought that the sample milled under 100 bar hydrogen, which contained more $\beta\text{-Li}_2\text{Mg}(\text{NH})_2$ would have been the easiest to re-hydrogenate, but the amount of LiH and $\text{Mg}(\text{NH}_2)_2$ was greater in the sample ball-milled under 1 bar argon.

3.4.5 Raman spectra

Raman spectra were recorded from selected samples after key reactions. The results of some of the spectra provide a different perspective to the findings of the powder XRD patterns. This can be accounted for by the fact that Raman spectroscopy is a local technique, coupled with poor homogeneity within some samples. The ability of several phases in these processes to accommodate both amide- and imide-type anions simultaneously whilst maintaining the original structure provides further explanation for the inconsistencies between Raman and powder XRD data. Interestingly, cubic Li_2NH can be formed from LiNH_2 when only 15% of the hydrogen has been desorbed, and accommodate up to 85% amide-type anions within its structure¹⁴⁷. Even though multiple locations in all samples were tested, the results in this work were mainly used to confirm the level of hydrogenation within the sample from powder XRD. Raman was also found to be a useful technique for identifying between LiNH_2 and $\text{Mg}(\text{NH}_2)_2$ in this work.

Determination between imides and amides was clear due to peak locations (around 3170 cm^{-1} for imide and $>3250\text{ cm}^{-1}$ for amide). However, due to imide peaks being characteristically broad, lithium imide as well as mixed cation imides peaks often overlapped. The resolution of the peaks was often found not to be sufficient in order to differentiate clearly between phases (i.e. between α - or β - $\text{Li}_2\text{Mg}(\text{NH})_2$) in many samples apart from to identify the state of hydrogenation.

The Raman data collected from most samples after most desorption experiments described in Section 3.4.4.3, displayed intensity in the area between 3150 and 3200 cm^{-1} that was mostly poorly defined. A spectrum where these peaks can be distinguished clearly is displayed in Figure 3-26. Liang *et al.*⁷¹ identified peaks in the FTIR at 3182 cm^{-1} and 3161 cm^{-1} from α - $\text{Li}_2\text{Mg}(\text{NH})_2$ and a peak at 3173 – 3179 cm^{-1} corresponding to the β -phase. Li_2NH ⁴⁵ would be

identified in Raman/FTIR spectra with a peak occurring around 3160 cm^{-1} , while peaks at 3250, 3240 and 3198 cm^{-1} would indicate the presence of MgNH^{148} .

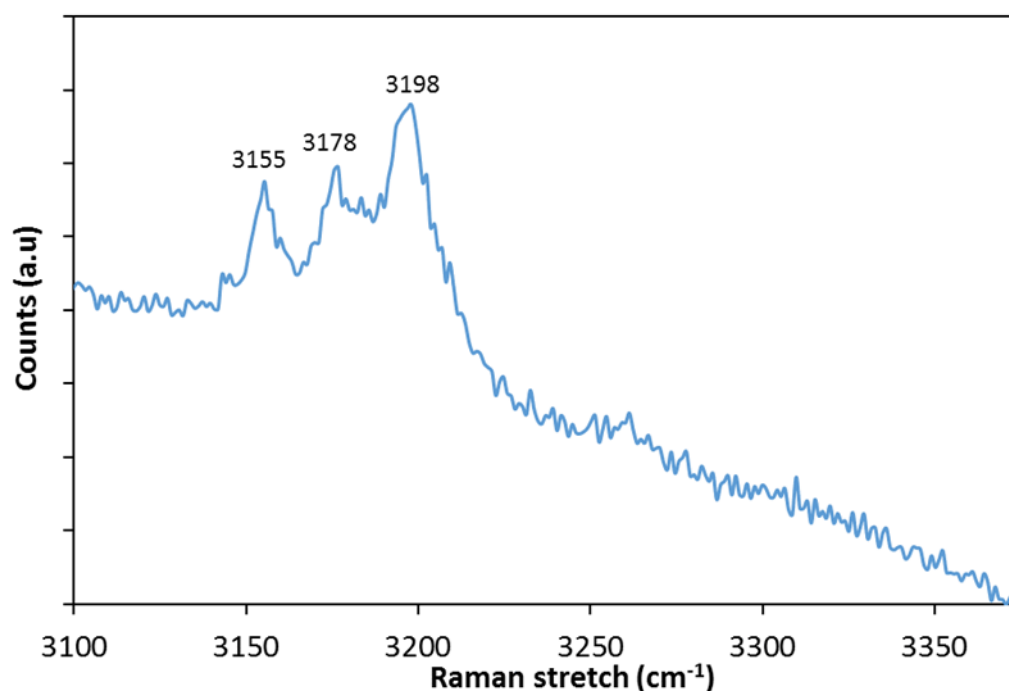


Figure 3-26: Raman spectrum of $2\text{LiNH}_2 + \text{MgH}_2$ sample ball-milled under 1 bar argon, heated at 220°C for 50 hours recorded at room temperature.

Previously, $\text{Li}_2\text{Mg}_2(\text{NH})_3$, a phase first seen by Juza¹⁴⁹ was identified by Hu *et al.*¹⁵⁰ as an intermediate in a desorption reaction in the Li–Mg–N–H system. It was also identified as a key intermediate at temperatures below 220°C in the desorption reaction¹⁵¹ between $\text{LiNH}_2 + \text{MgH}_2$ which would be in good agreement with previous suggestions of reactions at a 1 to 1 reagent ratio occurring. The corresponding Raman stretches for $\text{Li}_{4/3}\text{Mg}_{4/3}(\text{NH})_3$ were 3198 cm^{-1} and 3164 cm^{-1} , which closely correlate to peaks identified in spectra from this work.

This phase, $\text{Li}_{4/3}\text{Mg}_{4/3}(\text{NH})_3$, was previously assigned to a tetragonal space group¹⁴⁹, $I-4$, but this was reassessed and the structure solved using simultaneous refinements of X-ray and neutron diffraction data and assigned to space group $I\bar{4}2m$, with lattice parameters $a = 5.130 \text{ \AA}$ and $c = 9.619 \text{ \AA}$ ⁶⁹. This phase is based on the anti-fluorite structure, with a nitrogen lattice on the fcc positions and the cations in tetrahedral sites, similar to in LiNH_2 and $\text{Li}_2\text{Mg}(\text{NH})_2$. The lattice

parameters and structure of $\alpha\text{-Li}_2\text{Mg}(\text{NH})_2$ ($a = 9.7837 \text{ \AA}$, $b = 4.9893 \text{ \AA}$ and $c = 5.1984 \text{ \AA}$ as solved by synchrotron powder XRD) indicate that $\text{Li}_{4/3}\text{Mg}_{4/3}(\text{NH})_3$ is similar in structure. The cubic phase, $\beta\text{-Li}_2\text{Mg}(\text{NH})_2$ also has lattice parameters in the same region, $a = 5.0268 \text{ \AA}$.

Although the peaks in the powder XRD patterns were identified to belong to $\alpha\text{-Li}_2\text{Mg}(\text{NH})_2$, Raman data suggested that imide anions in three environments were present. One third of the tetrahedral sites in $\alpha\text{-Li}_2\text{Mg}(\text{NH})_2$ are vacant so it possible that this phase could accommodate further magnesium cations, making the imide anion sites more similar to in $\text{Li}_{4/3}\text{Mg}_{4/3}(\text{NH})_3$, resulting in slight shifts in the Raman data. However, the $\alpha\text{-Li}_2\text{Mg}(\text{NH})_2$ lattice parameters determined by powder XRD for both samples heated under flowing argon did not show any variation from the published values⁴ (to 3 dp).

The peaks identified in Figure 3-26 would indicate that $\beta\text{-Li}_2\text{Mg}(\text{NH})_2$, a $\text{Li}_{4/3}\text{Mg}_{4/3}(\text{NH})_3$ type phase and/or Li_2NH were present in this sample. Although peak(s) were not observed there was intensity around 3182 cm^{-1} and 3161 cm^{-1} , strongly suggesting $\alpha\text{-Li}_2\text{Mg}(\text{NH})_2$ was also present. As so many of the peaks corresponding to the phases in this work overlapped and peak-resolving software was not available to fit the Raman spectra, it was felt that unfortunately this technique was limited in usefulness for conclusively determining different imide phases.

3.5 Overall discussion

For a system to be developed as a hydrogen store, several properties of the material need to be measured, understood and optimized. The peak hydrogen desorption temperatures and rates of hydrogen release are often the properties that are assessed first to determine the initial parameters of the behaviour of a material. TGA-MS experiments showed that particle size reduction alone was not enough to reduce the reaction temperature of LiNH_2 and MgH_2 but a high degree of mixing was also required. The peak hydrogen desorption temperatures observed from LiNH_2 - or $\text{Mg}(\text{NH}_2)_2$ -based samples ball-milled under 1 bar argon were similar, and when the

samples were hand-ground, ball-milled separately or under pressure (100 bar H₂) the peak desorption temperature observed was higher. This would suggest that hydrogen desorption temperatures were influenced strongly by kinetic factors such as the diffusion rate of Li⁺.

Sample factors	Ball-milled separately	Ball-milled under 1 bar argon	Ball-milled under 100 bar hydrogen
Dispersion	x	✓	✓
Particle size	✓	✓	✓
In-situ reactions	x	✓	✓
Desorption during milling	✓	✓	x

Table 3-10: Summary of the effects of different conditions applied during ball milling.

The results presented in this chapter show that the preparation method can largely account for kinetic performance of the samples during the initial desorption and rehydrogenation steps. Although assessment of the first hydrogen cycle does not necessarily provide all the important information about how a sample might behave under cycling conditions, it allows an preliminary assessment of the viability of desorption and hydrogenation to be carried out. By assessing the first step of the hydrogen cycle this offers the best-case scenario for the properties of the sample in question before any detrimental effects such as ammonia release or increase in grain sizes occur. In addition, much of the literature on these types of systems focusses on the initial hydrogen release steps so this allows direct comparisons to be made. A summary of the factors thought to affect the samples and changes that happen during ball-milling has been made in Table 3-10.

The behaviour of the sample milled under 100 bar H₂ was quite different to the other samples where the reagents were ball-milled. Looking at the behaviour of the samples under desorption testing, a simple explanation considering the findings published in the literature, would be that samples ball-milled under 1 bar argon would undergo a complete metathesis

reaction (to $\text{Mg}(\text{NH}_2)_2$ and LiH) during milling and so the desorption temperatures at should be the same as those seen from the $\text{Mg}(\text{NH}_2)_2$ -based and cycled sample, (that had been converted to $\text{Mg}(\text{NH}_2)_2$ and LiH through hydrogenation), which was not the case. The application of pressure during ball-milling was thought to stop desorption and further reactions, so the components of the sample ball-milled under 100 bar hydrogen would be the same as when the reagents were ball-milled separately. The total mass loss from the sample milled under 100 bar hydrogen was higher than could solely be attributed to hydrogen, indicating that reasonably large amounts of ammonia were also desorbed. However, as little evidence of differences between the samples ball-milled under 1 bar argon or 100 bar hydrogen could be seen directly after milling, this explanation cannot be true; instead a more complicated scenario is proposed.

From the data recorded, the justification for the variation in behaviour between the samples milled under 1 bar argon and 100 bar hydrogen appears to be a combination of factors. Ball-milling under 100 bar hydrogen facilitates the metathesis conversion reaction more than milling under 1 bar argon. As the rate of conversion (metathesis reaction) was thought to be reasonably slow, suppression of gas release during milling was an important factor in maintaining the hydrogenated state of the reactants to allow the formation of $\text{Mg}(\text{NH}_2)_2$ in-particular. This would indicate that some desorption did occur during milling when the sample was milled under 1 bar argon.

The large exothermic peak observed in the heating segment of the DSC trace from the sample ball-milled under 100 bar hydrogen can be attributed to the crystallisation of $\text{Mg}(\text{NH}_2)_2$ and LiH . This would be a reasonable assumption as $\text{Mg}(\text{NH}_2)_2$ and LiH are the thermodynamic products. Heating the sample at low temperature seems to have acted as an annealing reaction for these phases. The peak hydrogen desorption temperatures from the samples ball milled under 1 bar argon and 100 bar hydrogen from TGA-MS (Figure 3-5) and amounts of $\text{Li}_2\text{Mg}(\text{NH}_2)_2$

observed at comparable temperatures in powder XRD were in good agreement, but this does not provide a complete explanation for the variation in desorption temperatures.

When the phases of $\text{Li}_2\text{Mg}(\text{NH})_2$ initially produced from the two samples, were considered, $\beta\text{-Li}_2\text{Mg}(\text{NH})_2$ was first seen from the sample ball-milled under 1 bar argon whereas $\alpha\text{-Li}_2\text{Mg}(\text{NH})_2$ was the phase identified first from the sample ball-milled under 100 bar hydrogen. The cubic β -phase of $\text{Li}_2\text{Mg}(\text{NH})_2$ was found to be the thermodynamic product, whereas the α -phase was determined to be the kinetic phase⁷³. A schematic illustration of the energy changes for the formation of the α and β phases of $\text{Li}_2\text{Mg}(\text{NH})_2$ is shown in Figure 3-27.

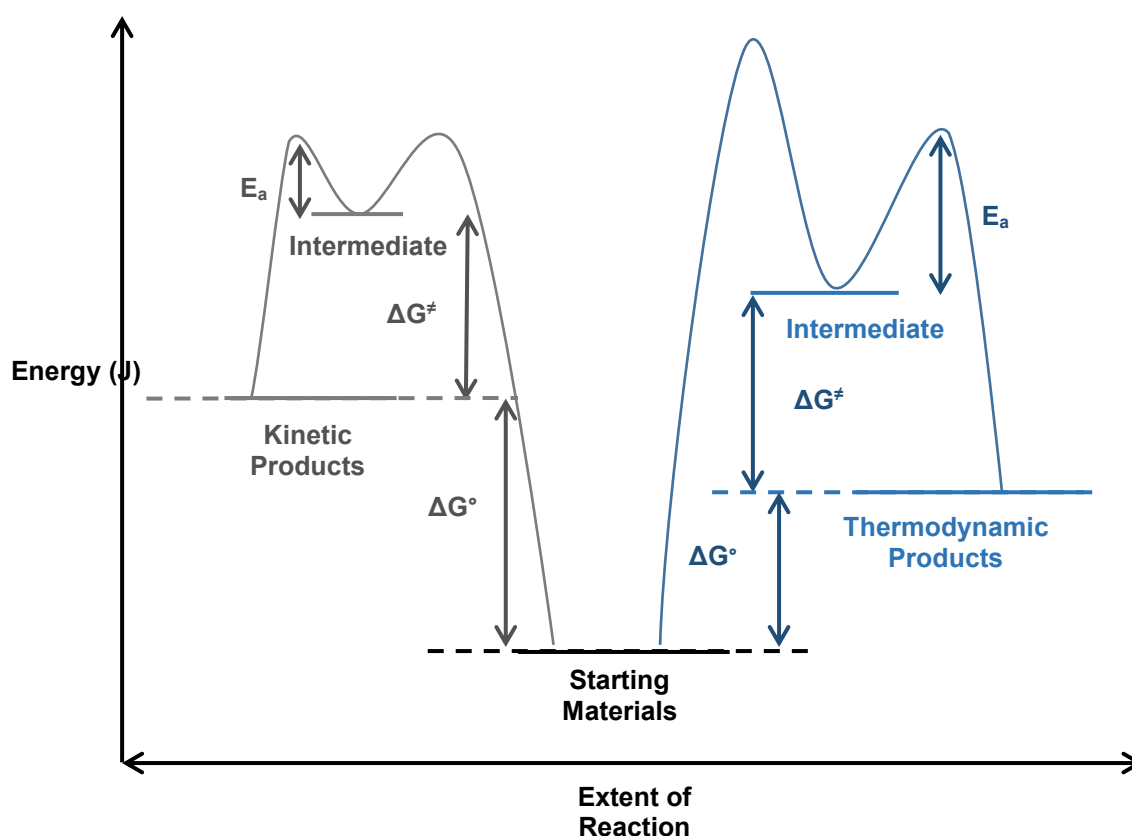


Figure 3-27: Schematic diagram of reaction pathway energy changes when a reaction is under kinetic or thermodynamic control.

Interestingly, changing the desorption conditions *i.e.* under flowing argon or under vacuum, seemed to control the phase of $\text{Li}_2\text{Mg}(\text{NH})_2$ produced. Isothermal reactions carried out under vacuum favoured $\beta\text{-Li}_2\text{Mg}(\text{NH})_2$ regardless of the preparation method. This was in good

agreement with the findings of Liang *et al.*⁷¹. The reason for this phase preference is unclear. Liang *et al.*⁷¹ suggested that the activation energy to form β - $\text{Li}_2\text{Mg}(\text{NH})_2$ was lower than to form α - $\text{Li}_2\text{Mg}(\text{NH})_2$ which may account for this effect.

Although the phase formed can be controlled by temperature⁴ or gas back-pressure⁷¹, it can also be influenced by the ball-milling preparation; high energy milling was thought to facilitate the formation of the β - $\text{Li}_2\text{Mg}(\text{NH})_2$ ⁷³. This could indicate that the sample ball-milled under 1 bar argon was able to absorb more energy during milling and this resulted in the inclusion of defects and higher strain in the sample, as well the possibility of a higher degree of non-stoichiometry. The combined effects of these factors led to the formation of the thermodynamic product. As desorption was thought to occur during milling of the sample milled under 1 bar argon, this may also indicate that the α and β phases of $\text{Li}_2\text{Mg}(\text{NH})_2$ have a preferred hydrogen content range which can influence the phase formed. It's also possible that the variation in starting materials before thermal reactions, the composition of the intermediates formed in each system could be slightly different, which could contribute to the controlling factors for the formation of α - or β - $\text{Li}_2\text{Mg}(\text{NH})_2$ from the two samples.

As pressurised milling conditions were thought to suppress hydrogen release, and the structure of α - $\text{Li}_2\text{Mg}(\text{NH})_2$ was very similar to $\text{Li}_{4/3}\text{Mg}_{4/3}(\text{NH})_2$, an intermediate in the desorption mechanism¹⁵², the cell volume of α - $\text{Li}_2\text{Mg}(\text{NH})_2$ was carefully scrutinised over the temperature range to check for increases which might suggest that additional cations or anion groups were being accommodated in the α - $\text{Li}_2\text{Mg}(\text{NH})_2$ structure. Non-stoichiometry within this structure could account for the perceived formation of α - $\text{Li}_2\text{Mg}(\text{NH})_2$ from β - $\text{Li}_2\text{Mg}(\text{NH})_2$ during the change in degree of hydrogenation, and also why the sample ball-milled under 100 bar hydrogen went through an α - $\text{Li}_2\text{Mg}(\text{NH})_2$ type structure first. Unfortunately, the maximum variation observed in the α - $\text{Li}_2\text{Mg}(\text{NH})_2$ cell volume was less than 0.1%.

Juza *et al.*¹⁵³ reported significant work on the alkali and alkaline earth metal amides, imides and nitrides. As well as the formation of LiNH_2 and $\text{Mg}(\text{NH}_2)_2$, the formation of $\text{LiMg}(\text{NH}_2)_3$ was also observed. The resulting XRD of this phase was 'identical' to that of $\text{Mg}(\text{NH}_2)_2$ if a few 'slight differences' in intensity were disregarded. In this case, distinction of the lattice parameters of $\text{LiMg}(\text{NH}_2)_3$ from and $\text{Mg}(\text{NH}_2)_2$ was not possible. This was attributed to the closeness of atomic radii of Li^+ and Mg^{2+} , 0.73 Å and 0.71 Å respectively¹⁵⁴. In the context of this work, the above finding may go some way to explaining the lack of variation in lattice parameters observed, even when possible cation substitution may be suspected.

If the factors which can control the phases produced can be understood, this also has implications for the cycling ability of the system as it was thought that $\beta\text{-Li}_2\text{Mg}(\text{NH}_2)_2$ can be rehydrogenated more rapidly and at lower temperatures⁷¹. However, the β -phase was not observed to be the most favourable to rehydrogenate in this study, but more work will be required to confirm this.

Unfortunately, in-depth temperature studies were not carried out on the $\text{Mg}(\text{NH}_2)_2 + 2\text{LiH}$ or cycled samples so a comparison of the phase preference for $\text{Li}_2\text{Mg}(\text{NH}_2)_2$ cannot be made. It was suggested that the mechanism of desorption from $\text{Mg}(\text{NH}_2)_2 + 2\text{LiH}$ to form $\text{Li}_2\text{Mg}(\text{NH}_2)_2$ was a two-stage reaction and could proceed through the formation of LiNH_2 and $\text{Li}_2\text{Mg}_2(\text{NH}_2)_3$. As these samples were not milled under pressure, if the degree of hydrogenation of the reagents was important, these samples would be expected to follow the behaviour of the sample milled under 1 bar argon, as they do in TGA-MS and DSC experiments as the sample ball-milled under 1 bar argon was found to be a mixture of $\text{Mg}(\text{NH}_2)_2$ and LiNH_2 after milling.

Although it is difficult to present conclusive evidence for these hypotheses, it is widely accepted that many of these phases are close in structure (evidenced in Figure 1-2) and are also easily able to accommodate a range of stoichiometries and cations. This means that high quality,

well resolved, *in-situ* data would be required to fully characterise this system, and the phases produced in its hydrogen cycle.

3.6 Conclusions

The results in this chapter have compared the reactions of the Li–Mg–N–H system, when prepared by ball milling or hand grinding, from lithium amide and magnesium hydride in addition to magnesium amide and lithium hydride. Experiments included desorption and hydrogenation reactions, differential scanning calorimetry, Raman spectroscopy and powder XRD experiments.

Hydrogen desorption from the hand-ground sample began slowly around 195°C and peaked at 350°C. It was also accompanied by a large amount of ammonia which was attributed to the decomposition of LiNH_2 (Equation 3-4) caused by poor mixing and large grain sizes of the starting materials. When samples were prepared by ball-milling, the desorption temperatures dropped dramatically and hydrogen release was prevalent. The peak hydrogen desorption temperatures of all ball-milled samples were reduced by around 170°C. The desorption behaviour of the sample milled under 100 bar H_2 pressure was different to other samples from varying starting materials which were milled under atmospheric argon pressure. A larger amount of the hydrogen release was shifted to higher temperatures (2nd peak) and ammonia was also observed in the gas flow.

No changes in the powder XRD patterns for hand-ground samples were observed until they were heated at temperatures of 275°C or more. The α -phase of $\text{Li}_2\text{Mg}(\text{NH})_2$ dominated the powder XRD patterns up to temperatures of 350°C after which the β -phase was observed. The powder XRD patterns from reactions of the sample milled under 100 bar hydrogen followed a similar reaction outline, albeit at lower temperatures, to the hand ground samples. However, the powder XRD patterns recorded across a temperature range of the $2\text{LiNH}_2 + \text{MgH}_2$ sample ball-

milled under 1 bar argon showed the conversion of $\beta\text{-Li}_2\text{Mg}(\text{NH})_2$ to $\alpha\text{-Li}_2\text{Mg}(\text{NH})_2$ which was not thought to be possible due to thermodynamic preferences.

The activation energies of the four ball-milled samples were all comparable to previous work on this system. The lowest activation energy was observed from the sample prepared from $\text{Mg}(\text{NH}_2)_2$ and 2LiH . DSC results showed that the samples which were not milled under pressure all behaved similarly and the peak temperatures of the endothermic event, linked to the first step of hydrogen desorption meant those samples behaved in a similar manner. A larger change in enthalpy was observed for the second endothermic peak compared to the first endothermic event in the cycled sample. This was in good agreement with the TGA-MS data where a larger peak and mass loss was observed at corresponding temperatures ($\sim 250^\circ\text{C}$) than the low temperature peak ($\sim 180^\circ\text{C}$).

The sample milled under 100 bar hydrogen behaved differently to the other samples and was the only sample to display an exothermic area during the heating segment of the experiment. It was thought that this was caused by the crystallisation of $\text{Mg}(\text{NH}_2)_2$ and LiH which were initially identified by Raman spectroscopy directly after milling and then by powder XRD after heating at low temperatures. The differences in behaviour were thought to be routed in the amount of hydrogen contained within the sample after milling and the phases produced during milling.

Rehydrogenation of ball milled samples starting from 2LiNH_2 and MgH_2 was successful, regardless of their preparation method. The formation of LiNH_2 and MgH_2 after rehydrogenation was surprising as it was thought that $\text{Mg}(\text{NH}_2)_2$ and LiH were the thermodynamic products of this reaction. The powder XRD pattern in Figure 3-10 shows that even after 3 cycles of desorption and hydrogenation reactions, LiNH_2 and MgH_2 were still observed.

3.7 Further work

To improve the quality of the starting materials, especially from $\text{Mg}(\text{NH}_2)_2$ and LiH , alternative experiments to produce $\text{Mg}(\text{NH}_2)_2$ without the presence of unreacted MgH_2 or Mg could be carried out, perhaps starting from Mg metal instead and milling under ammonia pressure rather than argon. Monitoring any gaseous products by mass spectrometry or chromatography during or after ball milling of the mixtures would also be beneficial for this work. Exploration into whether the amount of oxide observed in these samples could be reduced would also be useful, as this could ensure that uneven formation of oxides did not disturb the stoichiometry of the reactants.

Further work could be carried out on the four ball-milled samples described in this work to ascertain enthalpy and entropy values for hydrogen desorption from a Van't Hoff plot using a manometric hydrogen gas sorption analyser. It was planned that this work would have been carried out during this study so that kinetic and thermodynamic values could have been compared; unfortunately, sufficient equipment time was not available. Further investigations into the differences between the samples ball-milled under 1 bar argon and 100 bar hydrogen pressures would be carried out. In-situ powder XRD data collected from the beginning of the heating reactions should show how the initial reactions vary before desorption occurs.

Desorption–absorption cycles could also be carried out and investigations into the plateau hydrogen pressures that could be achieved from different samples at various temperatures. Isothermal experiments for desorption and absorption segments could be carried out so that calculations could be made to ascertain the rates of hydrogen release and also compare the extent of reaction between differently prepared samples at similar temperatures. Scanning electron microscopy could also be used to look at the samples to examine how the mixing of reactants, particle sizes and grain sizes varied after preparation and also after different stages in the

hydrogen cycle. It would be interesting to assess how agglomeration of the samples after a single hydrogen cycle and after three or five cycles changed.

4 Storage properties of the Li–N–H and Li–Mg–N–H system doped with CaBr₂ or CaCl₂

4.1 Introduction

The Li-Mg-N-H system has undergone numerous in-depth experiments, so efforts are now concentrated on the improvement of this system as a hydrogen store, with specific attention on low temperature hydrogen cycling. To improve the system, changes must be made either to the thermodynamics—how favourable the reaction is—or kinetics, which control the rate of the reaction or both. Nayeboossadri *et al.*²⁹ identified the rate-limiting step of hydrogen desorption from the bulk material of the Li-Mg-N-H system as the ability of Li⁺ to diffuse within the material²⁹. Diffusion can be controlled by bulk and grain effects. The rate of diffusion through the bulk of the material can be affected by factors such as distance travelled, due to the formation of a product layer, and available pathways through site vacancies or interstitial positions for Li⁺ hopping. When smaller grain size particles are introduced, the number of grain boundaries within the microstructure of a material is increased and hence the atomic mobility is less hindered due to the increased number of grain boundary pathways. If lithium ions have the ability to migrate more freely within the system, then the rate of desorption should be increased.

Several groups have looked at doping the Li–Mg–N–H system with borohydride compounds such as NaBH₄¹⁰⁷, and LiBH₄ in catalytic and stoichiometric amounts^{96, 97}. LiBH₄ provided an alternative route for dehydrogenation through the in-situ formation of Li₄BH₄(NH₂)₃, which weakened the N–H bond in the amide ion and subsequently helped to seed the Li₂Mg(NH)₂ product⁵⁶. Earlier work on replacing LiH in the 2LiH–Mg(NH₂)₂ system with CaH₂ suggested that, via thermodynamic destabilisation, the heat of hydrogen desorption could be reduced¹⁵⁵ by the inclusion of calcium. A more recent publication examined the effects of adding CaH₂ in ‘catalytic’

amounts, 0.08 mole fraction, and found the activation energy of the first hydrogen desorption step could be reduced¹⁴³.

Li *et al.*^{90, 108} investigated the benefits of combining Ca^{2+} and $[\text{BH}_4]^-$ ions by doping the Li-Mg-N-H system with 0.1–0.3 mole fraction of $\text{Ca}(\text{BH}_4)_2$. It was proposed that simultaneous thermodynamic and kinetic improvements could be made by introducing calcium borohydride into the system due to Ca^{2+} and $[\text{BH}_4]^-$ ions, respectively^{107, 155}. It was concluded that optimum performance of the doped system was achieved by adding 0.1 mole fraction $\text{Ca}(\text{BH}_4)_2$. The onset temperature of dehydrogenation was lowered and the rates of de- and rehydriding were vastly improved. $\text{Li}_4(\text{NH}_2)_3\text{BH}_4$ was identified as a key intermediate in the desorption process from the borohydride-based systems.

It was found that the addition of halides to the Li-N-H or Li-Mg-N-H systems among others, produced a kinetic improvement by improving lithium ion mobility^{47, 156}. A phase that contains chlorine, $\text{Li}_4(\text{NH}_2)_3\text{Cl}$, which is an isostructural equivalent to $\text{Li}_4\text{BH}_4(\text{NH}_2)_3$, could provide a similar route to system improvement. This could be achieved through the addition of calcium chloride instead of calcium borohydride and would remove the possibility of desorption from the borohydride anion which could then produce Li_3BN_2 , a phase which has shown limited reversibility¹⁰⁹. A similar lithium amide bromide phase, with the composition $\text{Li}_7(\text{NH}_2)_6\text{Cl}$ also exists⁴⁷. In a KF-doped Li-Mg-N-H system, a metathesis reaction was also observed whose product were KH and LiF. However, instead of proposing the improvement in desorption temperature had been generated by the inclusion of an alternative anion into a phase, a mechanistic pathway change was suggested. This was caused by the formation of $\text{Li}_3\text{K}(\text{NH}_2)_4$ as an intermediate which lowered the reaction enthalpy of the second dehydrogenation step¹⁵⁷.

Research in this chapter will compare the effects of doping, mainly the Li–Mg–N–H system, with various amounts of CaCl_2 and CaBr_2 against the pristine undoped systems and those doped with $\text{Ca}(\text{BH}_4)_2$, using several techniques.

4.2 Experimental

The doped Li–Mg–N–H systems were made from either LiNH_2 (Sigma–Aldrich, 95%) and MgH_2 (Alfa Aesar, 98%) used in a 2:1 ratio or $\text{Mg}(\text{NH}_2)_2$ (prepared ‘in-house’) and LiH (Sigma–Aldrich, 95%) used in a 1:2 ratio, and anhydrous CaCl_2 (Sigma–Aldrich, >96%), anhydrous CaBr_2 (Alfa Aesar, 99.5%) or CaBH_4 (Sigma–Aldrich), which were used in sub-stoichiometric amounts between 0.05 and 0.20 mole fraction. The samples were used for a selection of experiments, some with different preparation conditions, such as hand-grinding or ball-milling as described below.

Samples were ball-milled in 250 ml stainless steel milling pots in a Retsch PM400 planetary ball-mill at 300 rpm for 24 hours with a ball to sample mass ratio of 40:1. To prevent excessive temperature rises in the milling vessel, 2 minutes of milling were followed by 2 minutes paused. Samples were run under one of two conditions: argon at atmospheric pressure or under 100 bar hydrogen pressure. Some samples were heated under flowing argon to temperatures between 150°C and 400°C for up to 72 hours (preparation according to chapter 2.1.1). Magnesium amide was synthesised from a ball-milled sample of MgH_2 . MgH_2 was heated under flowing ammonia gas at 300°C for 24 hours, reground by hand and re-heated for a further 24 hours under the same conditions. *Ex-situ* powder XRD data were recorded using a Siemens D5005 instrument in capillary mode with a wavelength of 1.5406 Å (Section 2.7.6).

TPD–MS samples were heated at a ramp rate of 2°C min⁻¹ to 400°C and held for a short time before the power was cut. Samples were reground before powder XRD measurements were collected. TGA–MS samples were heated at various ramp rates (1, 2, 5, 10 and 15°C min⁻¹) to 400°C and cooled to room temperature. DSC samples were heated at a ramp rate of 2°C min⁻¹ to 400°C

and subsequently cooled to 25°C under 3 bar argon. Raman spectra were collected on a Renishaw inVia Raman microscope operating with a 633 nm laser using a cell sealed under an argon atmosphere.

Samples selected for rehydrogenation were re-ground, sealed in an airtight steel reactor and pressurised to 100 bar H₂ before being heated at a ramp rate of 2°C min⁻¹ to 200°C and held for 24 hours. When post rehydrogenation PXRD data were required, samples were re-ground before PRXD measurements were collected.

4.3 Thermal desorption

4.3.1 TPD-MS

4.3.1.1 Li-N-H hand-ground samples

Initial investigations into the effect of using calcium dopants on desorption were carried out on the single cation LiNH₂ + 2LiH system. Samples were prepared via hand grinding using a pestle and mortar. The hydrogen profile of the control sample (LiNH₂ + 2LiH) and those of the doped samples are all shown in Figure 4-1 to make a relative comparison between all samples. Dopants were added in a molar ratio of 0.1:1 LiNH₂ as this amount was found to be enough to show whether a positive effect on the desorption properties would be observed. The hydrogen release profiles were normalised to allow a comparison of the temperatures and profile shapes; as the masses of samples prepared varied, quantitative comparisons using mass spectrometry data from these samples were not carried out.

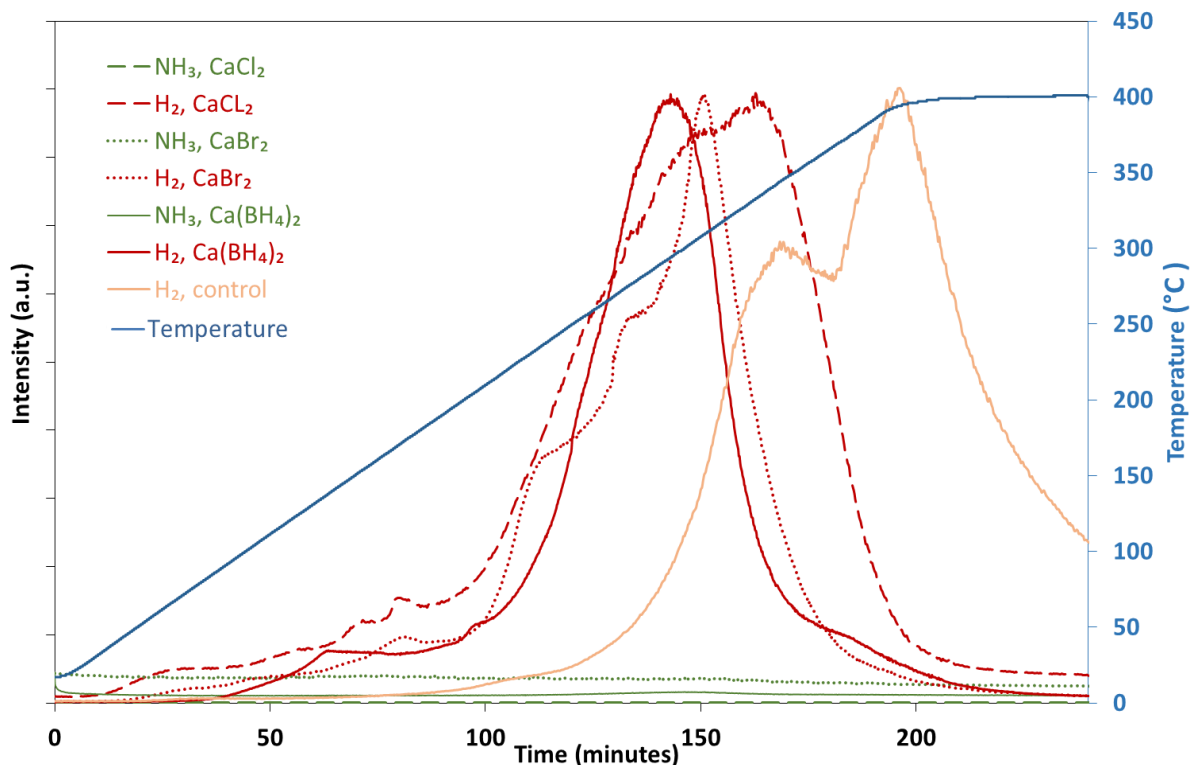


Figure 4-1: TPD-MS trace of the control sample ($\text{LiNH}_2 + 2\text{LiH}$) and $\text{LiNH}_2 + 2\text{LiH} + 0.1\text{CaX}_2$, samples heated at 2°C min^{-1} , showing gas release against time, H_2 (red), NH_3 (green) and temperature (blue).

Two hydrogen desorption events were observed in the control sample which peaked at 350°C and 395°C . The ammonia trace did not show any observable features so it was not included in Figure 4-1. The hydrogen profile recorded when the CaCl_2 -doped sample was heated to 400°C displayed a broad desorption similar to the control, but desorption peaked at a lower temperature, $\sim 335^\circ\text{C}$, and was not split into two resolved peaks. Hydrogen release from the CaBr_2 -doped sample occurred in three clear steps, and peaked at 310°C . The gradient of hydrogen release shown by the calcium bromide doped sample was the steepest of all the samples in the system, indicating that the reaction rate of this sample was the fastest. Both calcium halide doped samples displayed small desorption features below temperatures of 200°C . A sample doped with 0.1 mole fraction $\text{Ca}(\text{BH}_4)_2$ was also prepared; the hydrogen release observed from this sample was smooth and peaked at 300°C .

Dopant identity	Hydrogen peak temperature (°C)	Approximate onset temperature (°C)
Control	388	225
CaCl ₂	328	75
CaBr ₂	301	85
Ca(BH ₄) ₂	282	100

Table 4-1: Hydrogen peak temperatures for different types of calcium dopant added to the LiNH₂ + 2LiH system at mole ratio of x = 0.1.

Significant desorption for all the doped samples began at around 200°C, while substantial hydrogen release from the control sample did not begin until 60°C higher. In contrast to the control sample, where no hydrogen was observed below 210°C, all doped samples displayed small events in the hydrogen desorption profile below this temperature. This could indicate that the kinetics of hydrogen desorption for the doped samples were more rapid than the undoped sample. The addition of dopants could provide the formation of an alternative phase, such as an imide halide, which could have a lower reaction enthalpy. The formation of a small amount of a phase with a similar structure (in this case to Li₂NH) will lower the activation energy of main product, Li₂NH by helping to nucleate it. Rearrangement of a similar phase can be achieved with a lower energy input, hence desorption and the desorption product is observed at lower temperatures. The hydrogen desorption characteristics of the doped samples based on the LiNH₂ + 2LiH system are summarised in Table 4-1.

The approximate onset temperature for each sample was estimated from where rapid and significant hydrogen desorption was first observed in the trace. A reduction of over 100°C in the hydrogen evolution onset temperatures was observed for all doped samples with respect to the control. The calcium halide doped samples began to desorb hydrogen at a lower temperature although the calcium borohydride sample peaked at a lower temperature. This showed that the halides were effective at lowering the initial temperature of desorption, even though hydrogen desorption was slow. An early hypothesis from these results might be that the inclusion of the

halides reduced the enthalpy of desorption, but did not increase the rate of desorption, indicating that reaction kinetics at low temperatures were poor.

The largest difference between the halide and borohydride dopants was that desorption from samples doped with halides displayed several hydrogen features steps, most noticeably in the CaBr_2 sample, whereas desorption from the $\text{Ca}(\text{BH}_4)_2$ was smooth throughout. This indicates that the desorption mechanisms of the halide-doped samples may be more complicated than those of the borohydride-doped samples. Possibilities will be discussed in Section 4.7.

4.3.1.2 Li–Mg–N–H hand-ground samples

As previously discussed in the introduction, it is well known that the addition of Mg into the Li–N–H system means the properties become more favourable for hydrogen storage and as such provide a better starting platform.

The importance of preparation methods within this system has already been identified and discussed in Chapter 3. Different sample preparation methods will also be used in this chapter, which ultimately may help to understand the mechanisms that control dehydrogenation. In this section, the effects on the TPD–MS desorption profiles of doping hand-ground samples with calcium halides are compared. In this case, the $2\text{LiNH}_2 + \text{MgH}_2$ sample was deemed the ‘control’. The desorption profile from the control sample was included for ease of comparison to the CaCl_2 - and CaBr_2 -doped samples. The desorption profiles of samples doped with various amounts of CaCl_2 and CaBr_2 were investigated. A sample containing $\text{Ca}(\text{BH}_4)_2$ was also tested in order to make a comparison to the work carried out on the lithium-only system.

Initially samples doped with $x = 0.1, 0.15$ and 0.2 mole fraction of CaCl_2 (*i.e.* 0.1: 2 LiNH_2) were compared to the control and the resulting TPD–MS traces are displayed in Figure 4-2. The amounts added were kept low to balance the effect of the dopant without compromising the gravimetric content of the material.

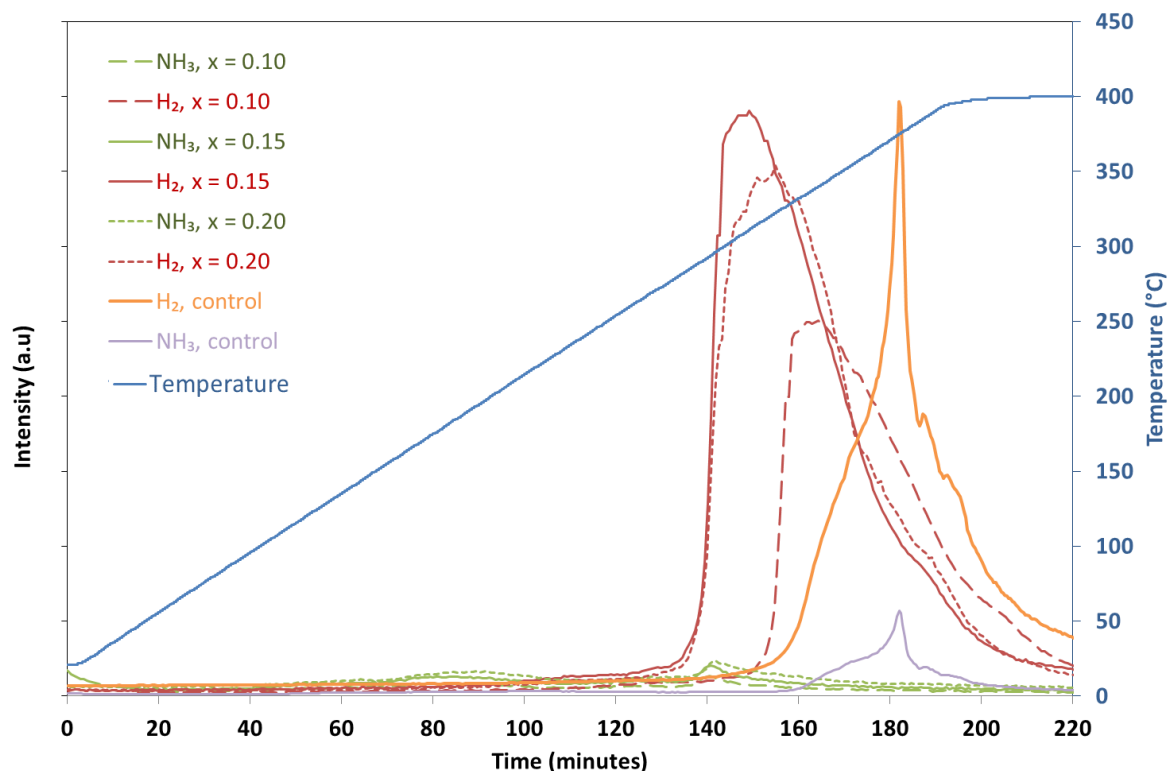


Figure 4-2: TPD–MS trace of $2\text{LiNH}_2 + \text{MgH}_2 + x\text{CaCl}_2$ samples heated at 2°C min^{-1} , showing gas release against time, H_2 (red), NH_3 (green) and temperature (blue).

The hydrogen release profiles in Figure 4-2 have broad peak shapes, which was in contrast to the control sample, which was reasonably sharp at the peak, although the onset of dehydrogenation was more rapid than the control. When $x = 0.15$ and 0.20 , the peak desorption temperatures were lowered by approximately 50°C compared to the control to 315°C and 325°C , respectively. It is noteworthy that by 400°C hydrogen release appeared to have significantly slowed in all the doped samples. The relative ammonia release from all samples doped with CaCl_2 was suppressed with respect to the control sample. The dopant amount of $x = 0.15$ was apparently the most effective in lowering the desorption temperature. Although this is one important factor,

the overall effectiveness of the dopant is based on all the requirements of a reversible storage material.

The asymmetric shape of the peak (shoulder at around $\sim 385^{\circ}\text{C}$) indicates that desorption temperature was above that needed to satisfy thermodynamic parameters (i.e. the hydrogen-releasing reaction was thermodynamically favourable) and began rapidly when the kinetic barrier to hydrogen release was overcome, subsequently slowing as poor kinetics dominated the gas release. The slowing of the reaction as it proceeds is in good agreement with a diffusion controlled solid-state reaction. A product layer (imide) is formed at the amide/hydride interfaces and then as the reaction proceeds, the amount of product layer increases, and so does the diffusion distance for Li^+ , hence the rate of reaction slows as the product layer grows. Chen *et al.*²⁸ identified the 'resistance to mass transport', i.e. the diffusion of Li^+ through the product layer, as the rate-determining step.

An alternative explanation for the presence of a shoulder in the desorption profile, was that multiple reactions which peaked at different temperatures may occur. The temperature of the shoulder observed in the doped samples was close to the peak desorption temperature of the control sample. This would suggest that the same reaction was producing hydrogen in all samples, just in lower amounts from the doped samples. It was thought that calcium chloride was likely to be providing an alternative lower temperature reaction route.

The latter explanation was based on the assumption that for a hand-ground sample there is a reasonable chance that dopant dispersion throughout the sample is poor. This means that an inhomogeneous sample has been produced, resulting in undoped areas within the sample following the original desorption pathway. The lack of contact between sample components and large grain sizes resulting from hand-ground samples will also contribute to slow kinetics. If a larger amount of the catalyst was used to force only the lower temperature hydrogen forming

reaction to proceed, the gravimetric capacity of the material would be more heavily compromised and the reagent would no longer be present in a catalytic role.

The TPD-MS profiles of the CaBr_2 -doped samples are shown in Figure 4-3. In the system doped with CaBr_2 the amounts were restricted to $x = 0.10$ and 0.15 due to the molecular weight of bromine, which results in a much higher gravimetric penalty. The profile of hydrogen desorption when using CaBr_2 as a dopant was quite different from that observed from the control or any of the chloride-doped samples. The main hydrogen desorption peak was sharp and a well-defined second peak was also observed. A sharp desorption peak is indicative of fast reaction kinetics once the reaction has overcome the activation energy barrier under reaction conditions which are thermodynamically favourable. Ammonia release was also suppressed relative to the control or chloride-doped samples.

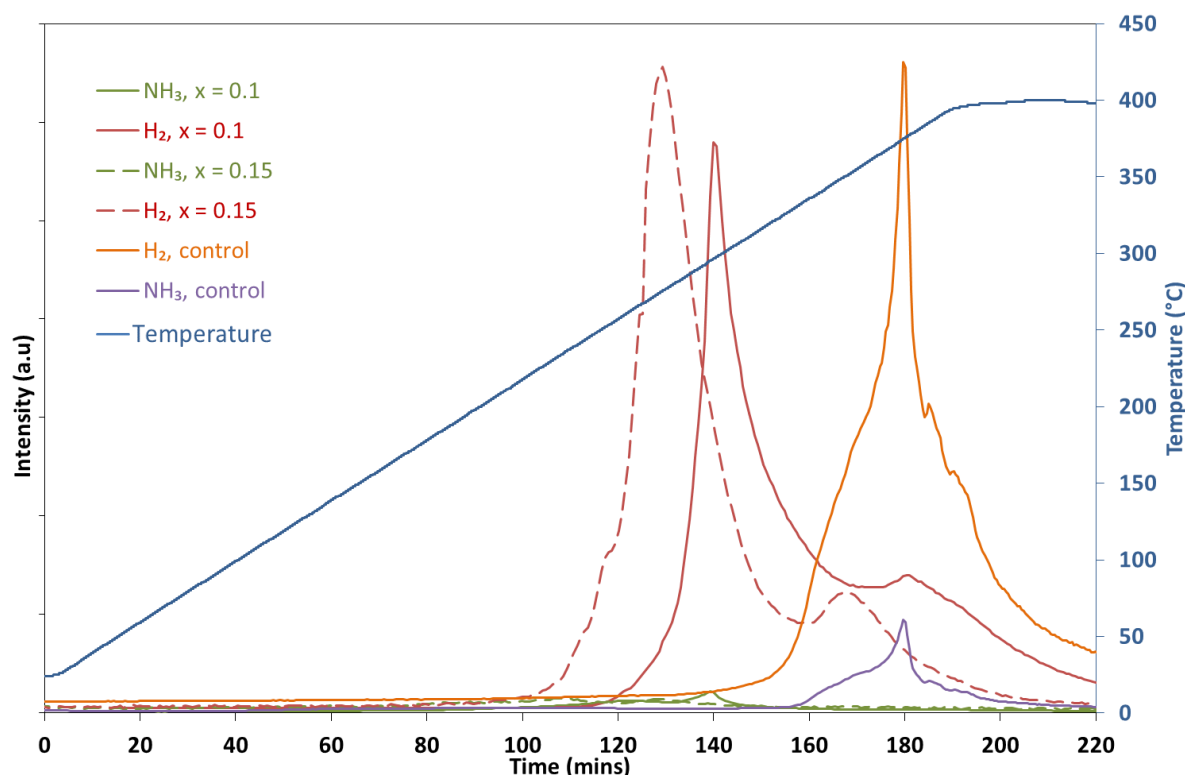


Figure 4-3: TPD-MS trace of $2\text{LiNH}_2 + \text{MgH}_2 + x\text{CaBr}_2$ samples heated at 2°C min^{-1} , showing gas release against time, H_2 (red), NH_3 (green) and temperature (blue).

Increasing the content of CaBr_2 in the sample lowered the temperature of the desorption peak; doping with 0.15 CaBr_2 lowered the peak temperature by $\sim 100^\circ\text{C}$ with respect to the

control, and almost 50°C when compared to similarly doped CaCl_2 samples. When $x = 0.15$, hydrogen release had finished by 400°C.

As illustrated in Figure 4-3, the temperature of the second peak when $x = 0.10$ was close to temperature of the original desorption peak (control) and shoulder in the CaCl_2 -doped samples. However, unlike the shoulder identified in the CaCl_2 -doped samples whose temperature was reasonably independent of dopant amount, the second desorption peak in the CaBr_2 -doped samples shifted to a lower temperature as the amount of dopant was increased. It was found that the addition of CaBr_2 was more effective than CaCl_2 at increasing the amount of low temperature hydrogen desorption.

In order to make a relative desorption comparison to the calcium halide dopants discussed previously, a sample of $2\text{LiNH}_2 + \text{MgH}_2$ doped with 0.1 mole fraction $\text{Ca}(\text{BH}_4)_2$ was prepared and tested under the same conditions as the calcium halide doped samples. The TPD-MS trace of the

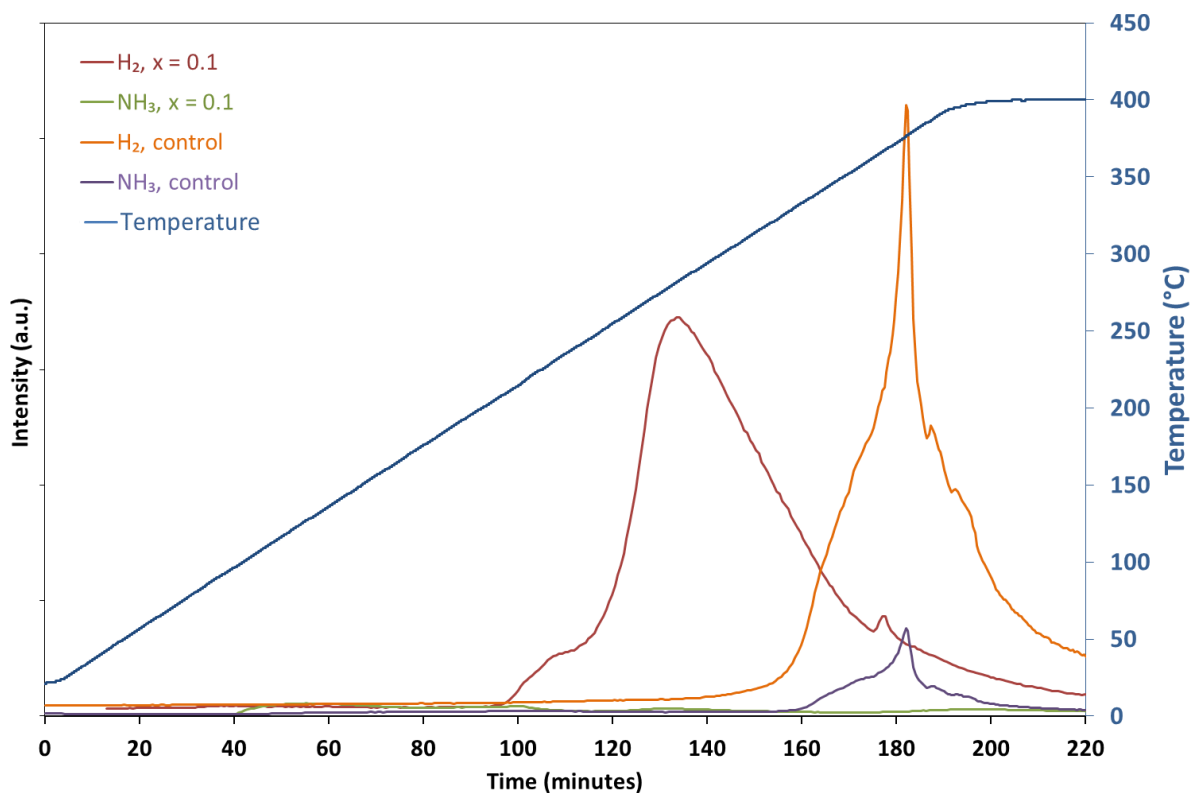


Figure 4-4: TPD-MS trace of $2\text{LiNH}_2 + \text{MgH}_2 + 0.1\text{Ca}(\text{BH}_4)_2$ sample heated at 2°C min^{-1} , showing gas release against time, H_2 (red), NH_3 (green) and temperature (blue).

calcium borohydride doped sample is shown in Figure 4-4. Hydrogen evolution began at roughly 210°C and peaked at 285°C, an improvement of almost 100°C when compared to the control. Ammonia release was minimal. The shape of the main desorption peak was broad, and a second small peak was observed at a comparable temperature to previous experiments.

4.3.1.3 TPD–MS hand-ground sample summary

Desorption characteristics of both systems were directly compared and key information is summarised in Table 4-2. There were several similarities between both doped systems: ammonia release in all doped samples was minimal, and all observed peak hydrogen temperatures of doped samples were reduced with respect to the control samples. Through doping the samples, the reduction in peak temperature observed was similar for the same dopant in both systems, *ca.* 60–90°C as seen in Table 4-2. The trend in effectiveness of reducing the peak desorption temperature of the dopants was the same in both systems. There were also a number of significant differences between the desorption profiles from Li–N–H and Li–Mg–N–H doped samples. No desorption was observed below temperatures of 200°C in the Li–Mg–N–H system, whereas the doped samples in the Li–N–H system displayed small hydrogen release events, which began around 100°C and increased in rate at approximately 200°C.

Sample	Peak temperature (°C)		Features	
	Li	Li–Mg	Li	Li–Mg
Control	388	374	Two peaks, smaller at 341°C	Single peak, slight NH ₃ release
0.1 CaCl ₂	328	332	Very broad main peak	Broad asymmetric peak
0.1 CaBr ₂	301	297	Two distinct shoulders at low temperatures and sharp main peak	Sharp main peak, smaller additional peak at higher temperature
0.1 Ca(BH ₄) ₂	282	285	Smooth peak	Smooth peak

Table 4-2: Comparison of the desorption temperatures and notable features, where Li represents the Li–N–H and Li–Mg represents the Li–Mg–N–H systems.

The gradient of all the hydrogen desorption peaks in this section was sharp at the beginning, indicating that once the reaction began (overcame the activation energy) the rate of desorption was reasonably rapid. Hydrogen desorption was observed over a much larger temperature range in the Li-N-H system. It is notable that although the pristine Li-Mg-N-H system has been shown to desorb at lower temperatures, here the onset temperatures of the doped Li-N-H system were much more favourable. As the preparation of all samples was the same, and rate of desorption was rapid around the peaks, it was thought lower initial onset temperatures were likely to be accounted for by thermodynamic preferences.

When considering the amount and type of dopant added to a sample, it is important to balance the loss of hydrogen capacity in the system and whether the improvement generated still makes the material viable in terms of overall gravimetric capacity. A summary of the key desorption temperatures of hand-ground Li-Mg-N-H doped samples tested is presented in Table 4-3 along with the theoretical hydrogen wt% which can be accessed when the sample undergoes the first, most accessible, amide to imide desorption step.

Dopant content (x) and identity	Theoretical H ₂ wt% (amide to imide step)	Hydrogen Peak Temperature (°C)	Approximate onset temperature (°C)
Control	5.54	374	325
0.10 CaCl ₂	4.80	332	310
0.15 CaCl ₂	4.50	310	290
0.20 CaCl ₂	4.24	322	290
0.10 CaBr ₂	4.33	297	275
0.15 CaBr ₂	3.91	275	250
0.20 CaBr ₂	3.56	-	-
0.10 Ca(BH ₄) ₂	5.05	275	210

Table 4-3: Comparison of dopant content and type to the theoretical gravimetric H₂ capacity and the measured peak desorption temperatures of the corresponding sample.

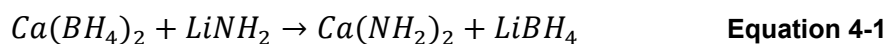
In conclusion, it can be seen that the calcium dopants tried here were successful in reducing the hydrogen peak temperatures compared to the control system and followed the trend: $\text{Ca}(\text{BH}_4)_2 < \text{CaBr}_2 < \text{CaCl}_2 < \text{Control}$. Figure 4-2 and Figure 4-3 show that ammonia emissions from doped samples were suppressed when compared to the control. TPD-MS results show that significant improvement can be made to the pristine lithium amide based system when both LiH and MgH_2 are used.

4.3.2 TGA-MS

4.3.2.1 Li-Mg-N-H ball-milled samples

To investigate the effects of ball milling conditions on desorption from the Li-Mg-N-H system, several ball milling regimes, the same as employed in Chapter 3 and described in Section 4.2, were carried out. TGA-MS was used to assess the behaviour of such samples and to enable an accurate comparison of the mass losses from samples prepared under various regimes.

Powder XRD patterns of the ball-milled undoped samples after milling (Figure 3-5) did not show any evidence of metathesis but during ball-milling of samples prepared by Li *et al.*⁹⁰ a mechano-chemical reaction occurred (Equation 4-1).



By the production of LiBH_4 during milling, this allowed for low temperature reactions with LiNH_2 to produce $\text{Li}_4(\text{NH}_2)_3\text{BH}_4$ as an intermediate. By altering the intermediates in the desorption mechanism, the reaction pathway would be changed, which could change reaction thermodynamics and account for a decrease in the temperature of desorption.

Powder XRD patterns of the ball-milled samples doped with 0.1 mole fraction of CaCl_2 in this work were recorded. The powder XRD pattern after 24 hours of ball-milling under 100 bar hydrogen is shown in Figure 4-5. Due to poor resolution and broad peaks it was difficult to discern accurately the respective amounts of lithium and calcium imides. Due to the close similarities between the structures of $\text{Li}_2\text{NH}^{134}$ and CaNH^{158} , (both space group No. 225, $Fm\bar{3}m$) and lattice parameters (5.0769 Å and 5.143 Å), respectively, when the lattice parameters of both phases were allowed to freely refine they were found to be 5.104(3) Å and 5.110(3) Å, respectively. The deviation of the lattice parameters from the ideal values to a central area could suggest cross substitution of either cation into the other phase, or, the formation of a single phase containing both Ca^{2+} and Li^+ cations has been formed. The resolution of the peaks was not clear enough to determine whether two sets of peaks or one larger asymmetric peak was present in this case so both Li_2NH and CaNH have been modelled in Figure 4-5.

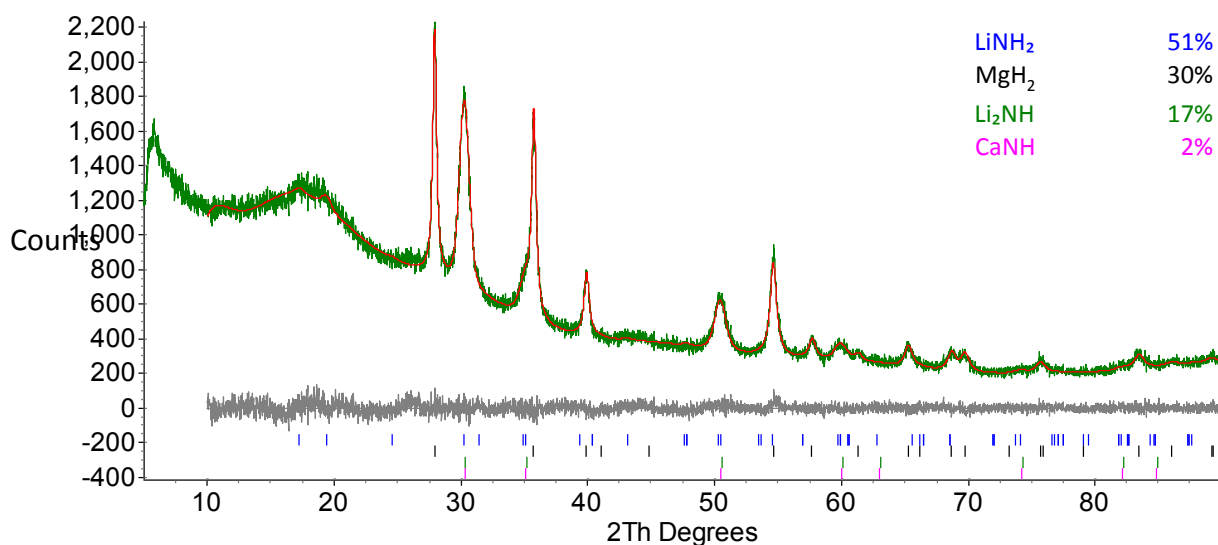


Figure 4-5: PXRD pattern of the $2\text{LiNH}_2 + \text{MgH}_2$ CaCl_2 -doped sample ball-milled under 100 bar hydrogen, when $x = 0.1$ directly after milling with Rietveld fit showing the difference (grey), calculated (red) and observed (green) with the peak positions indicated for LiNH_2 (blue), MgH_2 (black), Li_2NH (green) and CaNH (pink).

The other product of the metathesis reaction, if it followed that suggested in Equation 4-1, for the addition of CaCl_2 instead of $\text{Ca}(\text{BH}_4)_2$, LiCl , was not observed. However, neither was the dopant, CaCl_2 . The peaks in the powder XRD pattern recorded of the sample doped with CaCl_2 , after milling under 1 bar argon were very broad and quantitative identification of the phases was

not attempted. The peak positions were comparable to the CaCl_2 -doped sample ball-milled under 100 bar hydrogen, suggesting a similar composition.

Similarly, to Raman data recorded of the undoped samples in Chapter 3 directly after milling, Raman data (Figure 4-6) recorded directly after ball-milling the CaCl_2 -doped samples also showed there were differences between the samples milled under 1 bar argon and 100 bar hydrogen. Only LiNH_2 was identified after milling under 100 bar hydrogen. After milling under 1 bar argon, intensity was observed in the imide region, (below 3200 cm^{-1}) indicating that some desorption had occurred during milling. In the amide region of the spectrum, peaks relating to both LiNH_2 and $\text{Mg}(\text{NH}_2)_2$ were observed, although the LiNH_2 peaks were found to be at slightly lower wavenumbers than previously observed (Figure 3-8).

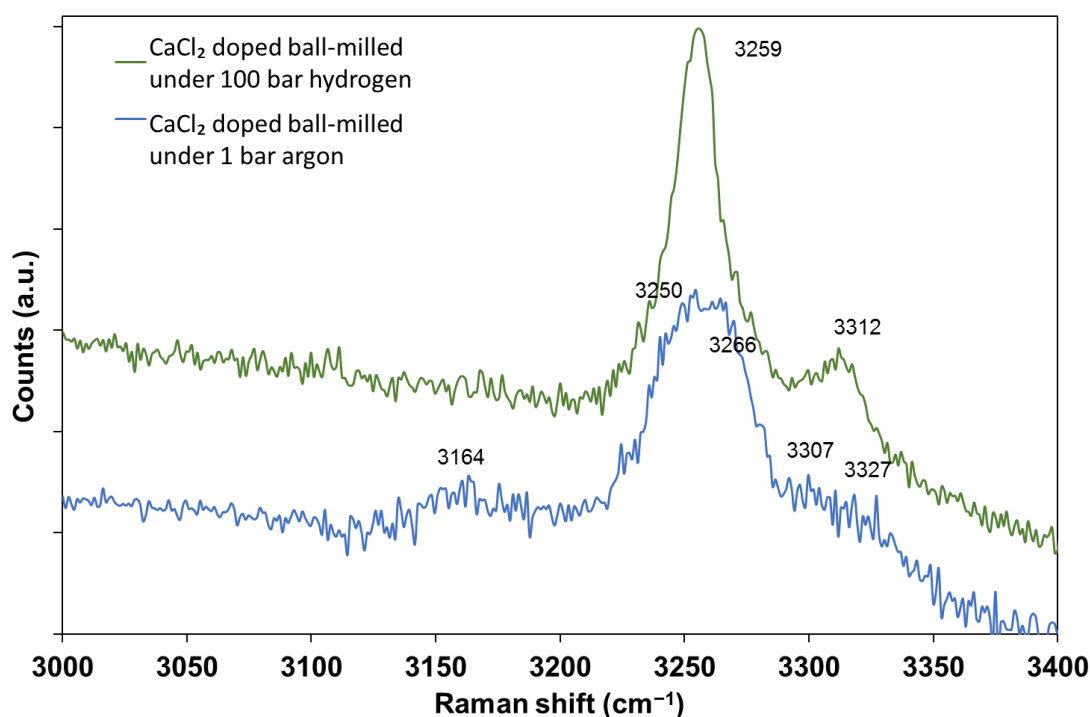


Figure 4-6: Raman spectra recorder after milling of two $\text{LiNH}_2 + \text{MgH}_2$ CaCl_2 -doped samples when $x = 0.1$ (green, ball-milled under 100 bar hydrogen; and blue ball-milled under 1 bar argon) with key peaks labelled.

Research carried out into the formation of lithium amide halides by Davies¹³⁹ showed that the Raman peaks recorded of amide halide phases were shifted to slightly lower wavenumbers than lithium amide. The data in Figure 4-6 would suggest that a structure incorporating some

chloride had been formed as the Raman peaks were lower than expected, indicating a weakening of the N-H bond, caused by the inclusion of chloride anions¹³⁹.

After consideration of the desorption data recorded from hand-ground samples, which was summarised in Table 4-3, the doped ball-milled samples discussed and analysed in this section were prepared with either 0.1 mole fraction of CaCl_2 or CaBr_2 . Although the samples doped with 0.15 mole fraction of the respective calcium halides displayed lower onset and peak desorption temperatures, ball-milling the samples should improve the dispersion of the dopant throughout the sample. This should mean lower amounts of dopant should be more effective and this will also reduce the gravimetric penalty of including these compounds, especially in the case of CaBr_2 . A comparison of the mass spectrometry and mass loss traces from thermogravimetric experiments of samples ball-milled under atmospheric pressure and under 100 bar hydrogen pressure are shown in Figure 4-7 respectively.

The intensity of the hydrogen peaks has been normalised. The ammonia traces for the ball-milled samples in Figure 4-7 and Figure 4-8 were not shown. It was previously discussed in Section 3.4.1 that a multiplication factor of around 100 times was required to view the ammonia peaks which makes it difficult to compare relative intensities to the hydrogen peaks, and in some samples where mass loss exceeded that possible by solely hydrogen, no peaks were observed. The total theoretical hydrogen content of the doped samples is shown in Table 4-3.

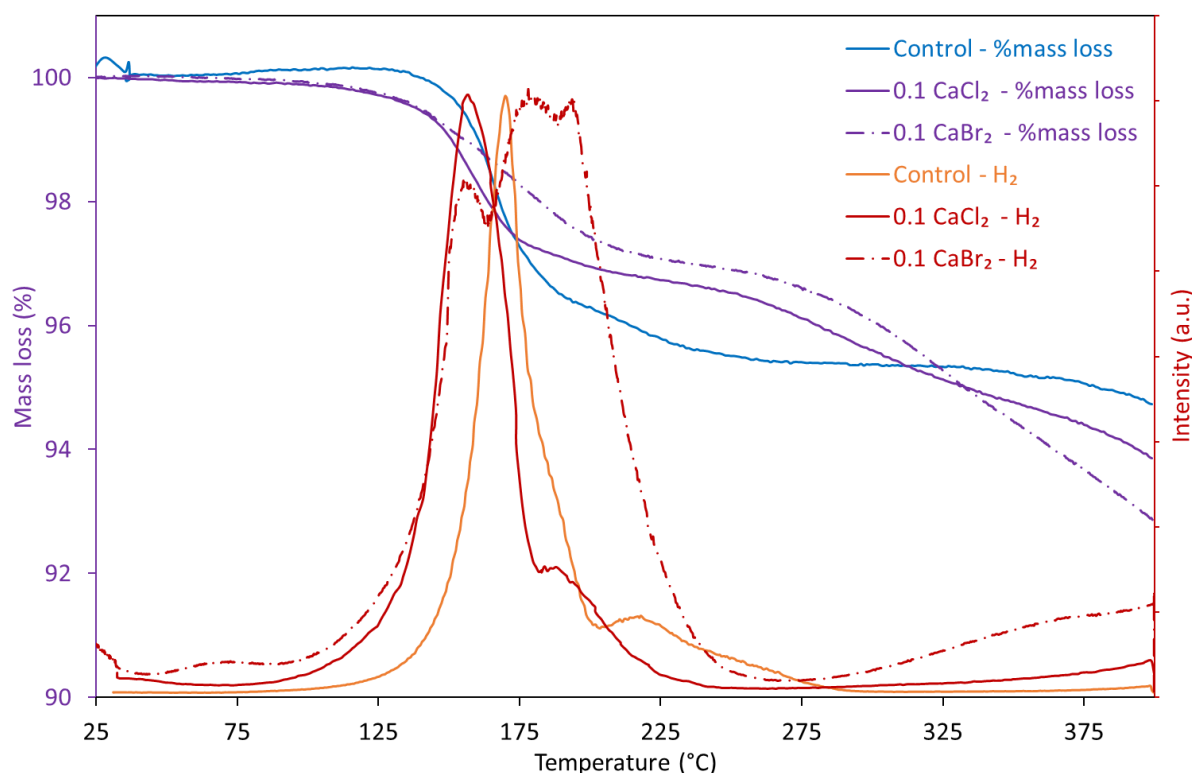


Figure 4-7: Mass loss and mass spectrometry traces of doped samples ball-milled under 1 bar argon (control, $2\text{LiNH}_2 + \text{MgH}_2$ sample for reference) where 0.1 mole fraction of CaCl_2 or CaBr_2 was added, heated at 2°C min^{-1} , showing hydrogen release (red) and % mass loss (purple) against temperature.

Apart from a significant drop in the desorption temperatures observed from the ball-milled samples, which was expected due to the increased homogeneity, reduced particle sizes and diffusion lengths, the biggest variation between hydrogen desorption profiles of the doped hand-ground and ball-milled samples were the shapes of the peaks (Figure 4-2 and Figure 4-3). The onset, peak and peak temperatures of additional features are compared in Table 4-4.

In contrast to the broad hydrogen release profiles observed from the CaCl_2 -doped hand-ground samples, the hydrogen profile after milling was more similar to the control sample; a large sharp main peak and a smaller second shoulder. The profile from the CaBr_2 -doped sample, although it began steeply was broad and displayed three smaller peak features. Unlike the control sample, hydrogen release began again from both CaCl_2 - and CaBr_2 -doped samples in the range of

275°C–400°C. This was more significant from the CaBr_2 -doped sample, in good agreement with a larger dip in mass from the mass loss profile of this sample.

To explain these phenomena, the as-received chemicals were examined. The grain size of the as-received CaCl_2 was larger than CaBr_2 , which after preparation by hand may not have been significantly altered, leading to poor dispersion and a lower accessible surface area for reaction. After ball-milling, any inconsistent grain sizes should have been removed and dispersion of the dopant should be improved and consistent across the whole sample. The desorption profiles observed from the ball-milled samples should present a more accurate view of the true effects that the dopants have.

To compare the rate of hydrogen release, the mass spectrometry traces were normalised and integrated. The gradients from the linear regions of hydrogen release, *i.e.* the peaks from the mass spectrometry traces from the samples ball-milled under 1 bar argon, which correspond to

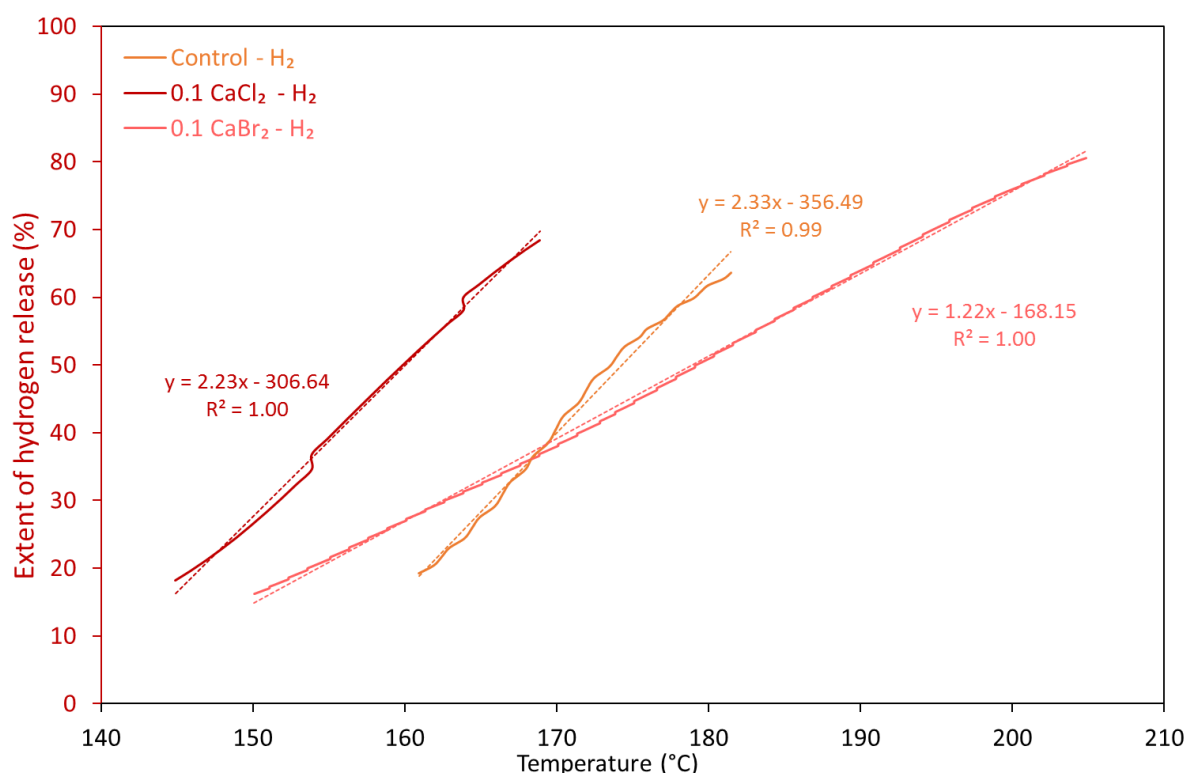


Figure 4-8: Normalised integrated hydrogen mass spectrometry profiles from doped samples ball-milled under 1 bar argon (control, $2\text{LiNH}_2 + \text{MgH}_2$ sample for reference) where 0.1 mole fraction of CaCl_2 or CaBr_2 was added, showing the linear regions of the hydrogen release against temperature.

the rate of release are shown in Figure 4-8. The rate of hydrogen release from the much smaller second peak observed from these samples was not evaluated. It can be seen that the rate of hydrogen release from the control was similar to the sample doped with 0.1 mole fraction CaCl_2 , though the temperature range of hydrogen release from the doped sample was lower.

Although the temperature range of hydrogen release from the CaBr_2 -doped sample was larger than the other two samples, the rate of hydrogen release was slower. The control sample and the 0.1 mole fraction CaCl_2 -doped sample lost around 60% of their hydrogen during this linear region where the rate was reasonably constant, whereas approximately 70% of hydrogen released was lost in the linear region of the CaBr_2 -doped sample.

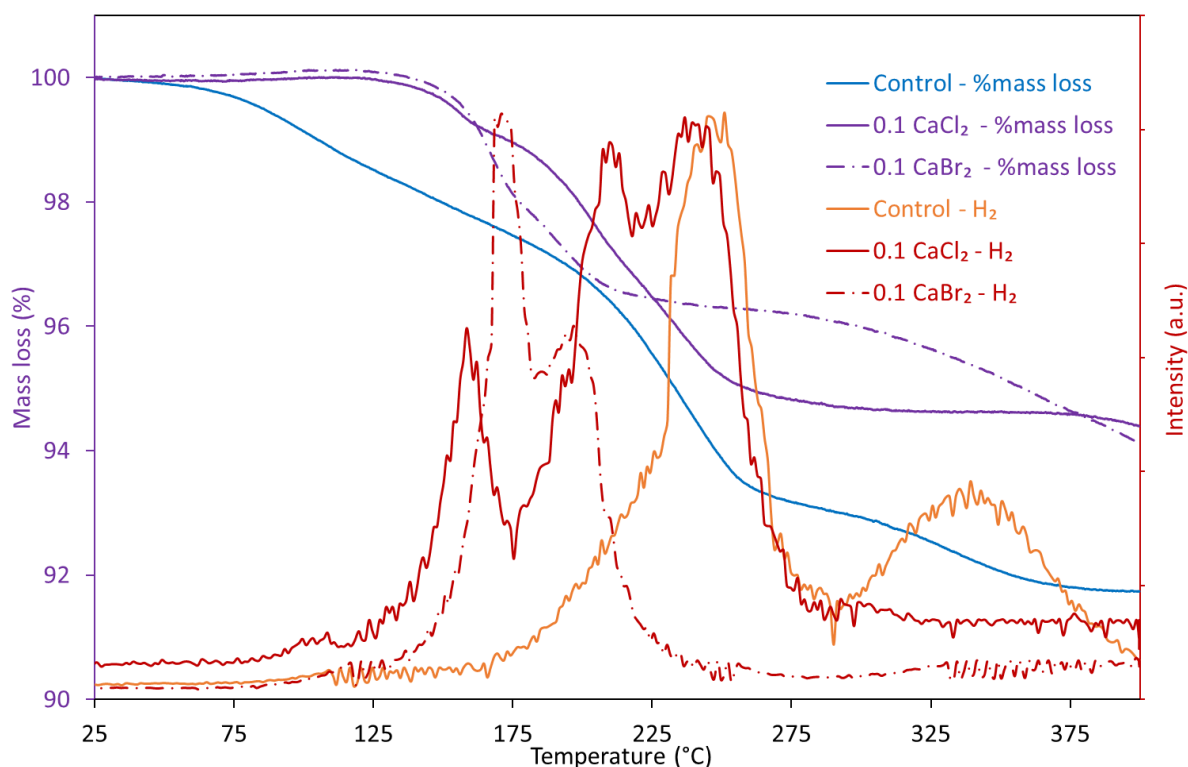


Figure 4-9: Mass loss and mass spectrometry traces of doped samples (control - $2\text{LiNH}_2 + \text{MgH}_2$ sample for reference) ball milled under 100 bar hydrogen where 0.1 mole fraction of CaCl_2 or CaBr_2 was added, heated at 2°C min^{-1} , showing hydrogen release (red) and % mass loss (purple) against temperature.

As previously discussed in Section 3.4.1 the control sample, which was ball-milled under hydrogen pressure, displayed two clear hydrogen desorption peaks at higher temperatures. The formation of two more distinct peaks from the samples ball-milled under 100 bar hydrogen

compared to the samples milled under 1 bar argon, indicates that the conditions of milling change the reaction that occurred.

The two doped samples in Figure 4-9 showed quite different desorption trends to the control. Most of the hydrogen from the CaCl_2 -doped sample was desorbed at lower temperatures than the control and the first hydrogen peak was observed at 160°C . Hydrogen desorption occurred over quite a large temperature range, with the largest peak across a temperature range of $210\text{--}240^\circ\text{C}$. In contrast to the control and CaCl_2 -doped sample, the temperature range of desorption from the CaBr_2 -doped sample was narrow and the temperature of the largest peak considerably lower, at 170°C . As shown in Table 4-4, the temperature of the main desorption peak decreased significantly (around 15°C), but the temperature of the 2nd peak was lowered by 60°C upon the addition of 0.1 mole fraction of CaBr_2 . The peak hydrogen desorption temperatures of all the respective ball-milled samples (apart from the control sample milled under 100 bar

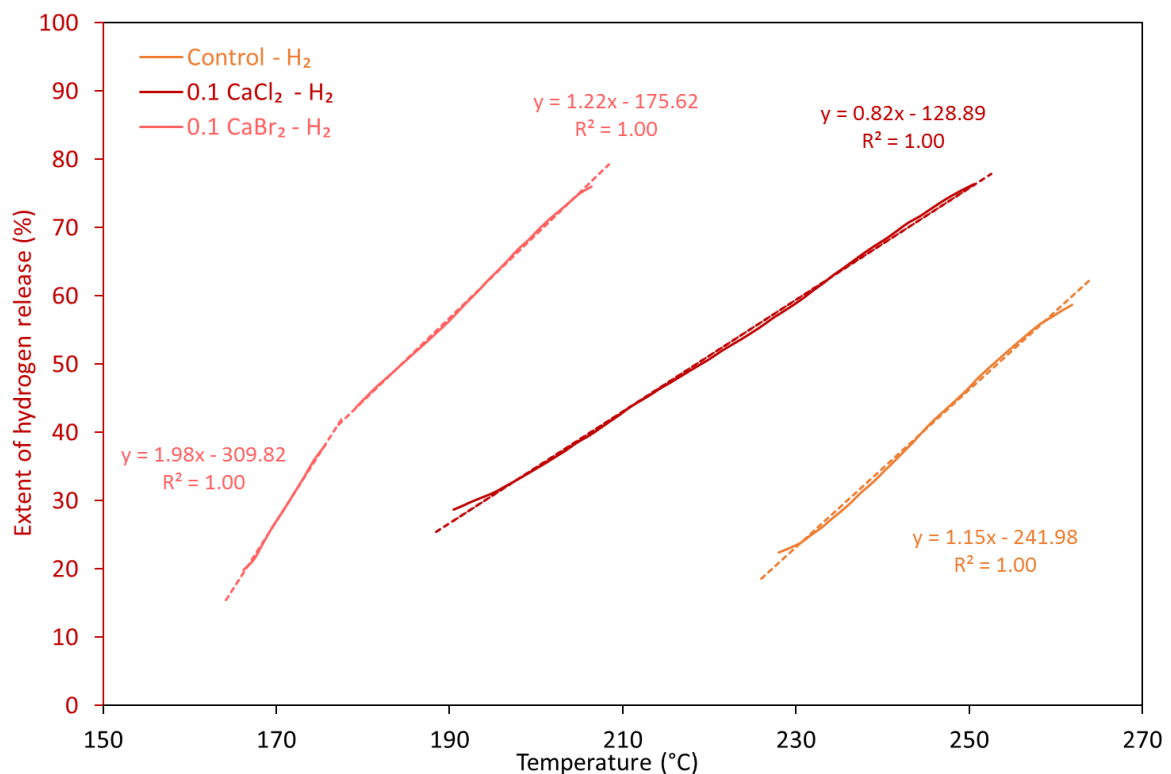


Figure 4-10: Normalised integrated hydrogen mass spectrometry profiles from doped samples ball-milled under 100 bar hydrogen (control, $2\text{LiNH}_2 + \text{MgH}_2$ sample for reference) where 0.1 mole fraction of CaCl_2 or CaBr_2 was added showing the linear regions of the 1st step of hydrogen release against temperature.

hydrogen) were similar, but adding a dopant to the samples milled under 100 bar hydrogen showed the largest reduction in peak temperatures.

In order to compare the rates of reaction of the doped samples ball-milled under 100 bar hydrogen, the same comparison as shown in Figure 4-8 was made. The gradient(s) from the linear areas corresponding to hydrogen release (Figure 4-9) were analysed and are shown in Figure 4-10. It can be seen that a very limited amount of hydrogen was actually desorbed from the control sample below temperatures of 230°C. In combination with the mass loss trace from this sample displayed in Chapter 3, (Figure 3-5) the early mass loss from the sample was a combination of ammonia and hydrogen, as less than 10% (up to 200°C) of the total theoretical hydrogen content, even if all the hydrogen contained in this sample was lost, cannot account for over 2 wt% mass loss from the sample.

In the samples ball-milled under 100 bar hydrogen, the addition of calcium halide dopants shifted more of the hydrogen release to lower temperatures. The addition of CaBr_2 almost doubled the initial rate of hydrogen desorption compared to the control. Almost 80% of hydrogen had already been lost from the CaBr_2 -doped sample before the control had desorbed 10%. The CaBr_2 -doped sample showed two clear linear areas of hydrogen desorption. Interestingly, the rate of hydrogen release from the CaCl_2 -doped sample was slower than the control, even though hydrogen desorption began at much lower temperatures.

Due to time constraints, it was only possible run a TGA-MS experiment on a 0.1 mole fraction CaCl_2 -doped sample starting from $\text{Mg}(\text{NH}_2)_2 + 2\text{LiH}$. The CaCl_2 dopant was chosen as when added to the $2\text{LiNH}_2 + \text{MgH}_2$ control sample ball-milled under 1 bar argon, this dopant had displayed good rates of reaction and low desorption temperatures.

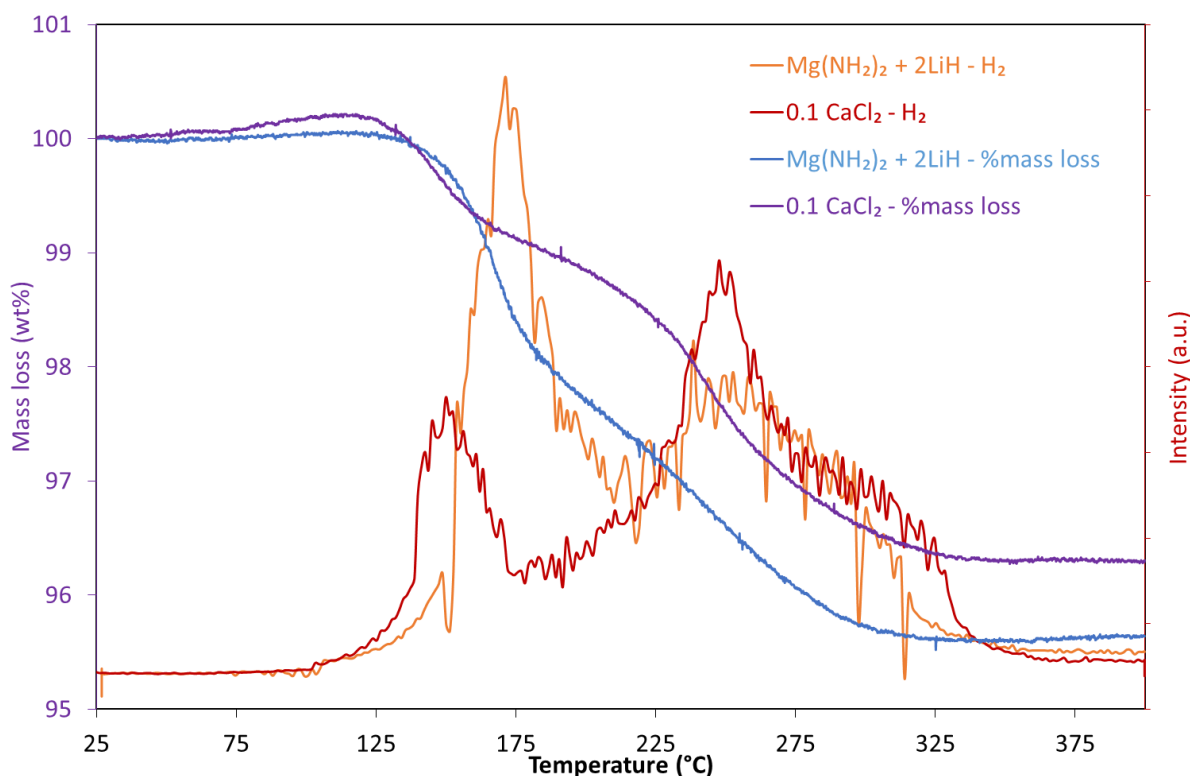


Figure 4-11: Mass loss and mass spectrometry traces of ball-milled (control, $\text{Mg}(\text{NH}_2)_2 + 2\text{LiH}$ sample for reference) doped sample where 0.1 mole fraction of CaCl_2 was added, heated at 2°C min^{-1} , showing hydrogen release (red) and % mass loss (purple) against temperature.

Both samples displayed two hydrogen peaks and the CaCl_2 -doped sample reduced the initial peak temperature of hydrogen release to 150°C , an improvement of 20°C compared to the $\text{Mg}(\text{NH}_2)_2$ control sample. The total wt% lost from these samples was less than all of the samples based on LiNH_2 ; this may be due to some hydrogen release during the synthesis of $\text{Mg}(\text{NH}_2)_2$. Unfortunately, the inclusion of the halide dopant shifted more of the hydrogen release to higher temperatures. In both cases, the wt% of mass loss remained stable from temperatures of around 300°C .

When the rates of hydrogen release were considered, the rate of hydrogen release from the control sample was more rapid at lower temperatures, but the rate increased from the doped sample during the second stage of hydrogen release. The rates observed from these samples (starting from $\text{Mg}(\text{NH}_2)_2$) were lower than the majority of hydrogen releasing events from samples starting from LiNH_2 .

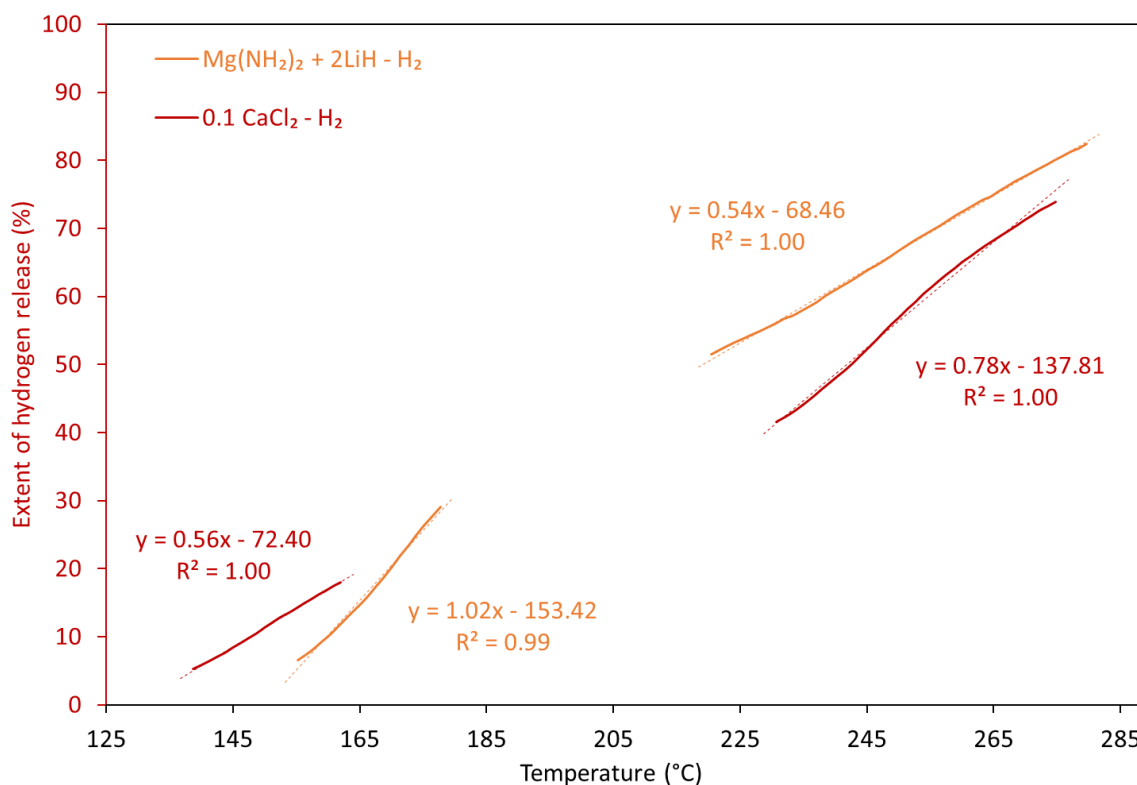


Figure 4-12: Normalised integrated hydrogen mass spectrometry profiles from ball-milled (control, $\text{Mg}(\text{NH}_2)_2 + 2\text{LiH} - \text{H}_2$ sample for reference) doped sample where 0.1 mole fraction of CaCl_2 was added, showing the linear areas of the hydrogen release against temperature.

4.3.2.2 TGA-MS ball-milled summary

The tables presented in this section are a summary of the graphical data presented in 4.3.2. The data collected in TGA-MS experiments has allowed a comparison of the peak hydrogen desorption temperatures as well as a comparison of temperature resolved-data on the rates of hydrogen release.

Table 4-4 shows a comparison of the peak hydrogen desorption temperatures observed from the control Li-Mg-N-H sample and doped samples. The inclusion of calcium halide dopants decreased the onset and peak desorption temperature of the first peak in all samples, with respect to the control which was prepared in the same way. There did not seem to be much difference in the peak temperatures whether CaCl_2 or CaBr_2 was added. Preparation by milling under 1 bar argon would be favourable to ensure the lowest desorption temperatures possible.

Sample	Hydrogen (Onset) and 1 st Peak Temperature (°C)			2 nd (3 rd) Hydrogen Peak Temperature (°C)	
	1 bar argon	100 bar hydrogen	Mg(NH ₂) ₂	1 bar argon	100 bar hydrogen
Control	(145) 170	(170) 250	(120) 170	220	340
0.1 CaCl ₂	(100) 155	(130) 160	(120) 150	190	210–240
0.1 CaBr ₂	(100) 155	(140) 170	-	180 (195)	200

Table 4-4: Comparison of the hydrogen desorption temperatures of the doped samples ball-milled under 1 bar argon and 100 bar hydrogen.

The calculated rates of hydrogen release are shown in Table 4-6. The rates were calculated from the integrated mass spectrometry traces for hydrogen release. The fastest rate was observed from the sample doped with 0.1 mole fraction CaCl₂ which was ball-milled under atmospheric argon conditions. In contrast, the fastest rate from samples milled under 100 bar hydrogen was observed after the addition of 0.1 mole fraction CaBr₂. From comparison of these rates, there did not appear to be a trend between the type of dopant and effect on the rate of hydrogen release. The rate of hydrogen release from the CaCl₂-doped samples was similar to that of the respective controls, regardless of the milling conditions, whereas the hydrogen release rate from the CaBr₂-doped samples was more dependent on the milling conditions.

Sample	Gradient of hydrogen release (Further steps)		
	1 bar argon	100 bar hydrogen	Mg(NH ₂) ₂ + 2LiH
Control	2.23	1.15	1.02 (0.54)
0.1 CaCl ₂	2.23	0.82	0.56 (0.78)
0.1 CaBr ₂	1.21	1.98 (1.22)	-

Table 4-5: Comparison of the gradients of the linear areas (peaks observed in the mass spectrometry traces) of integrated hydrogen release.

The inclusion of CaCl₂ into the Mg(NH₂)₂ did not improve the initial rate of desorption observed from the low temperature peak. A notable observation from the samples milled under

100 bar hydrogen, with the exception of the CaBr_2 -doped sample, was that the initial rate of reaction was poor. This was surprising as it was thought that milling under 100 bar hydrogen should suppress any hydrogen release during milling, thus this portion would readily desorb at low temperatures instead. In contrast to the release rates, the temperature at which 80% of the hydrogen from the CaBr_2 -doped samples appeared to be mostly independent of the ball-milling preparation.

The data in Table 4-6 indicates the temperature at which 80% of the hydrogen release for that sample had occurred. It can be seen that the hydrogen release reactions for the doped sample ball-milled under 1 bar argon proceeded rapidly, in particular desorption from the 0.1 mole fraction CaCl_2 -doped sample ensued more quickly than any other sample. As confirmed by the gradients shown in Table 4-5, the rate of hydrogen release from the control sample milled under 100 bar hydrogen was slow and 80% of hydrogen release was not completed until 330°C , almost 100°C higher than any competing sample.

Sample	Temperature ($^\circ\text{C}$) at which 80% hydrogen had been released		
	1 bar argon	100 bar hydrogen	$\text{Mg}(\text{NH}_2)_2 + 2\text{LiH}$
Control	205	330	275
0.1 CaCl_2	183	255	287
0.1 CaBr_2	205	215	-

Table 4-6: Comparison of the temperatures at which 80% of the respective hydrogen amounts (mass spec) were released from the samples.

A comparison using 100% of hydrogen release was not made as due to the tail off of hydrogen release this would be the end of the experiment. As each sample released a different amount of hydrogen, the overall wt% of 100% of hydrogen from one sample does not equal the same wt% from other samples. Difficulties with resolving the mass loss into hydrogen and ammonia release were encountered because the ammonia signal was so weak. Table 4-7 gives an

indication of the varying amounts of mass loss (wt%) for each sample when 80% of hydrogen release was reached. It can be seen that although the samples milled under 100 bar hydrogen required higher temperatures in order to desorb 80% of the hydrogen release, it was likely that this accounted for a greater overall wt% of the sample. However, as the amount of ammonia desorption could not be completely accounted for, to use these values as a more than a rough comparison, some experimental adjustments and further calculations would be needed.

Sample	Approximate mass loss (wt%) when 80% of hydrogen had been released from respective samples		
	1 bar argon	100 bar hydrogen	Mg(NH ₂) ₂ + 2LiH
Control	3.8	7.6	4.0
0.1 CaCl ₂	2.8	4.9	3.3
0.1 CaBr ₂	2.7	3.4	-

Table 4-7: Comparison of the mass loss (wt%) from samples at the respective temperatures (taken from Table 4-6) when 80% of hydrogen had been released from the samples.

A comparison of the gravimetric capacities and total mass losses recorded was made in Table 4-8. As the total mass loss from one doped sample exceeded the total theoretical hydrogen content in the sample, further gaseous decomposition products must have been formed. For the samples where 80% of hydrogen had already been released by lower temperatures (~250°C), by considering the mass loss values at this point, it was concluded that the majority of additional decomposition products were formed after the 1st step of hydrogen desorption.

The mass losses from the samples starting from Mg(NH₂)₂ were lower than the other samples. From looking at the mass loss traces, the mass of these samples remained steady after 275°C, perhaps indicating that the hydrogenation state of the sample had reached imides and that these samples did not further dehydrogenate to nitrides. The total mass loss from all the doped samples starting from 2LiNH₂ and MgH₂ was greater than that corresponding to the amide to imide step. This could have two implications, either that the addition of the dopant makes the transition

from amide nitride more accessible, or the doped samples desorb up to their amide imide capacity but this is accompanied by further gas release, likely ammonia.

Sample	Total potential H ₂ gravimetric capacity (%)	H ₂ capacity from amide to imide (wt%)	Total mass loss (wt%)		
			1 bar argon	100 bar hydrogen	Mg(NH ₂) ₂
Control	8.31	5.54	5.26	8.27	4.37
0.1 CaCl ₂	7.20	4.80	6.15	5.60	3.71
0.1 CaBr ₂	6.51	4.35	7.15	5.90	-

Table 4-8: Comparison of gravimetric hydrogen capacities and the approximate mass losses recorded by TGA–MS experiments after the 1st hydrogen desorption.

It was also possible that a small proportion of the halide could have been lost, either as HCl or HBr or chlorine or bromine gas. Due to the relative mass of hydrogen compared to bromine (or chlorine), if only a very small amount of a halide was lost, it could have accounted for a reasonably large mass loss. All these gases were scanned for in the outlet gas stream by mass spectrometry, but if released, they were below the detection limits of the instruments used. Unfortunately, based on the data available it is difficult to conclude the exact desorption products from these samples and which dopants were more efficient in terms of suppressing ammonia release and maximising the rate of hydrogen desorption at low temperatures.

In the samples milled under 100 bar hydrogen, the dopants were more effective: a large decrease in desorption temperatures from both samples occurred and large increase in the reaction rate of the CaBr₂-doped sample was observed. In contrast to the release rates, the temperature at which 80% of the hydrogen from the CaBr₂-doped samples appeared to be independent of the ball-milling preparation. The CaCl₂-doped sample prepared from Mg(NH₂)₂ was the only doped sample which did not display an improvement in temperature.

4.3.3 Kinetic calculations

Mass loss profiles and corresponding mass spectrometry traces can be used to calculate the activation energy of the hydrogen releasing reaction. The calculations were previously described and carried out in Section 3.4.2. The results in this section were calculated from the first hydrogen desorption step in all cases.

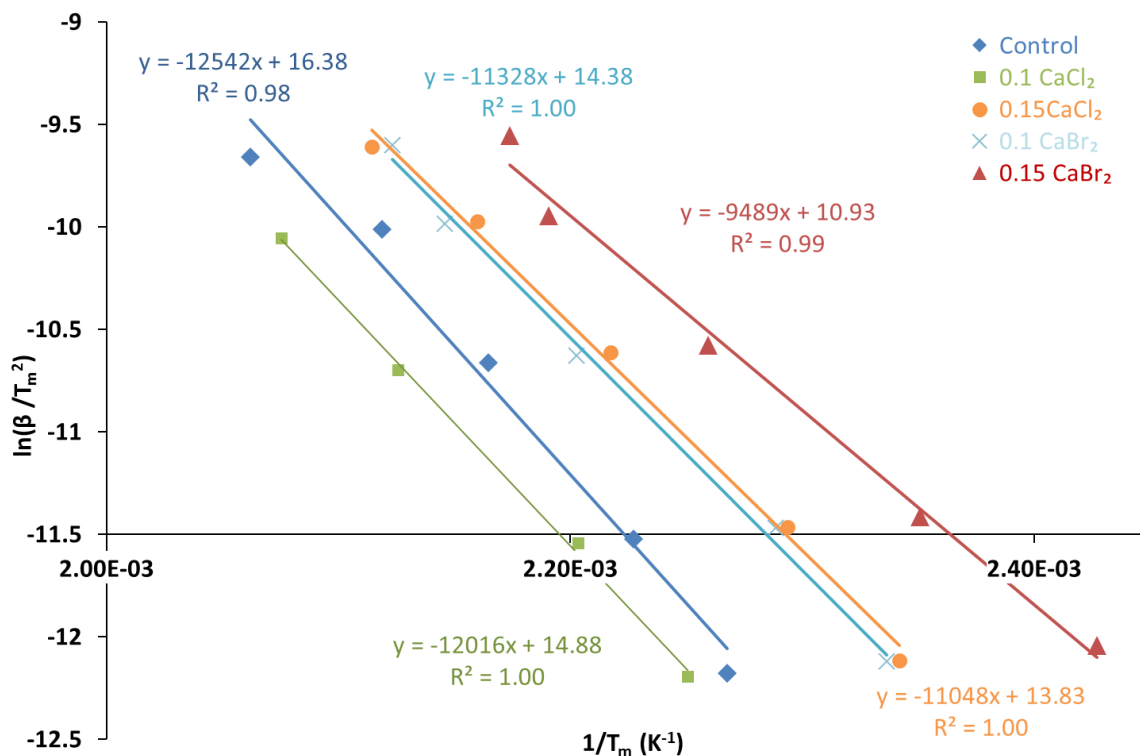


Figure 4-13: Kissinger's plot showing five samples which were all ball-milled under 1 bar argon, all starting from $2\text{LiNH}_2 + \text{MgH}_2$ (dark blue) including samples doped with various amounts of CaCl_2 or CaBr_2 (as stated).

The Kissinger's plot of the samples ball-milled under 1 bar argon is shown in Figure 4-13. Samples with varying amounts of dopant were tested. As expected, the activation energy of the control sample was the highest measured and increasing the amount of dopant included decreased the effective activation energy of these samples. The CaBr_2 -doped samples displayed the lowest activation energies. The Kissinger's plot of the samples ball-milled under 100 bar hydrogen is shown in Figure 4-14. Only samples with 0.1 mole fraction of dopant added were

available to test after ball-milling under 100 bar hydrogen. The activation energies of these samples were comparable to the samples ball-milled under 1 bar argon.

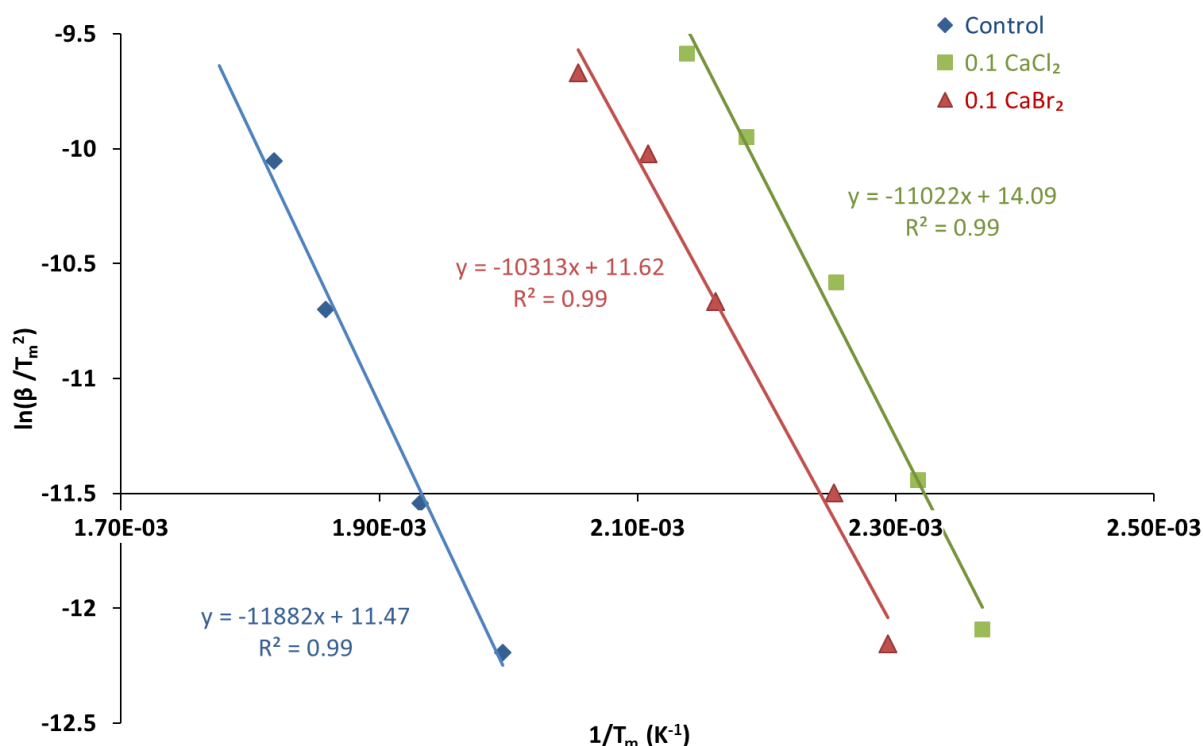


Figure 4-14: Kissinger's plot showing three samples which were all ball-milled under 100 bar H₂ pressure, all starting from 2LiNH₂ + MgH₂ (dark blue) including samples doped with 0.1 mole fraction of CaCl₂ or CaBr₂ (as stated).

From the changes in the estimated activation energies in Table 4-9, the relative changes for the doped samples do not correlate with the degree of reduction in the peak temperatures for the doped samples. The desorption temperature of the control sample milled under 100 bar hydrogen was considerably higher than the corresponding sample milled under 1 bar argon and yet the activation energy of the later sample was higher. These results indicate that the variation in peak hydrogen desorption temperatures is not solely due to kinetic improvements through the addition of dopants but the preparation method and dopant also change the thermodynamics of the samples.

Sample	Estimated activation energy (kJ mol ⁻¹)		Percentage reduction (%)	
	1 bar argon	100 bar hydrogen	1 bar argon	100 bar hydrogen
Control	104	97	-	-
0.1 CaCl ₂	99	92	5	5
0.1 CaBr ₂	94	86	10	11
0.15 CaCl ₂	92	-	12	-
0.15 CaBr ₂	79	-	25	-

Table 4-9: Estimated values of activation energies (error ± 6 kJ mol⁻¹) for various samples where the control was 2LiNH₂ + MgH₂.

According to the estimated values in Table 4-9 the improvement relative to the respective control samples was similar regardless of the conditions under which the samples were ball milled. Increasing the amount of dopant to 0.15 mole fraction did decrease the activation energies of those samples further, but carries an associated gravimetric loss of capacity. The values presented in Table 4-9 show that although the method of preparation changed the rate of reaction (Table 4-5), the activation energy required for the reaction to proceed was quite similar regardless of preparation conditions. The Kissinger's plot of the 0.1 mole fraction CaCl₂ doped sample starting from Mg(NH₂)₂ and 2LiH is shown in Figure 4-15. The estimated activation energies for the first step of hydrogen desorption are shown in Table 4-10. The improvement compared to the control sample made by doping the sample with CaCl₂ was more notable than when starting from 2LiNH₂ and MgH₂.

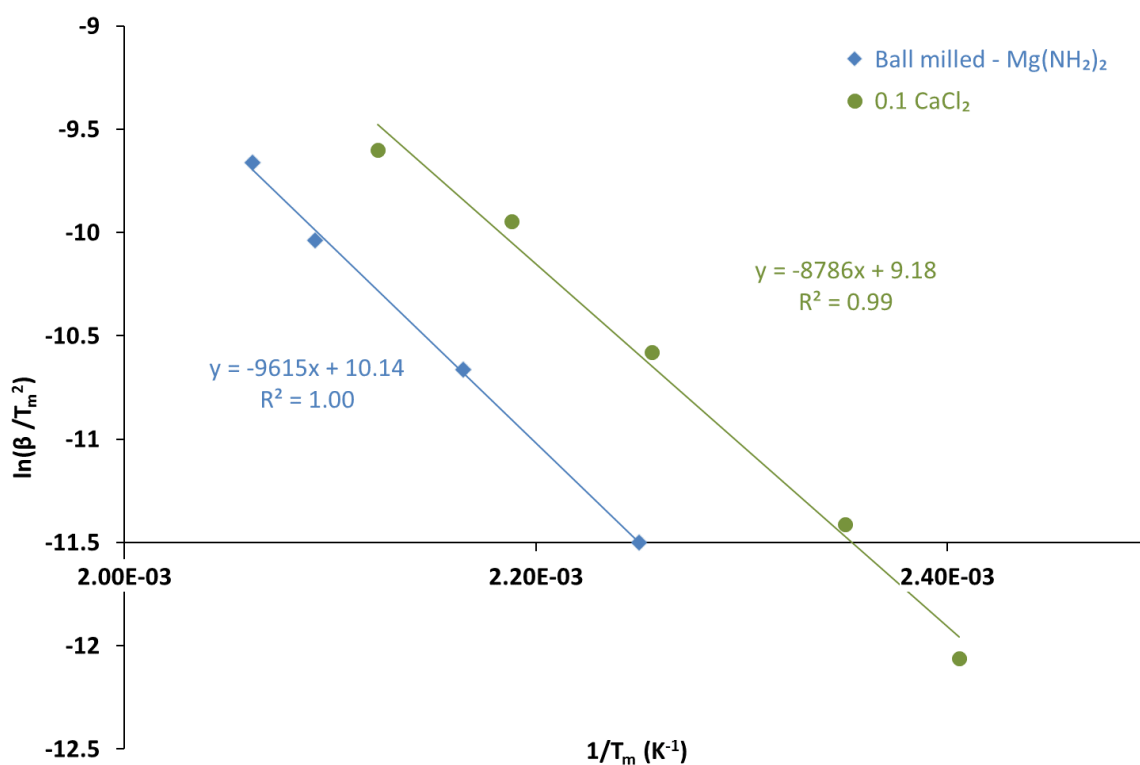


Figure 4-15: Kissinger's plot showing two samples which were all ball-milled under atmospheric argon pressure, starting from $Mg(NH_2)_2 + 2LiH$ (dark blue) including a sample doped with 0.1 mole fraction $CaCl_2$.

The activation energies of these samples (Table 4-10) were lower than those from the $LiNH_2$ (Table 4-9) samples. Although the values were slightly higher, a lower activation energy from the $Mg(NH_2)_2$ based sample would be similar to the observations of Li et al.^{90, 108} However, it is also possible that this could be due to the mixture of components helping to provide alternative pathways, due to incomplete synthesis of $Mg(NH_2)_2$.

Sample	Estimated activation energy ($kJ\ mol^{-1}$)	Percentage reduction (%)
Control	80	-
0.1 $CaCl_2$	73	9

Table 4-10: Estimated values of activation energies (error $\pm 6\ kJ\ mol^{-1}$) for two samples where the control was $Mg(NH_2)_2$ and $2LiH$.

4.4 Differential scanning calorimetry

DSC measurements of several doped samples were carried out. Due to time restraints on this equipment only the CaCl_2 -doped samples were selected to undergo DSC experiments. Similar to the undoped Li-Mg-N-H samples, only the heating segments of these experiments showed any features and as such are displayed in Figure 4-16, Figure 4-17 and Figure 4-19.

The DSC from the samples ball-milled under 1 bar argon showed a clear endothermic event which was dominated by a desorption event, seen in TGA experiments, when the sample transformed from amide to imide. The peak temperature of the doped sample was slightly lower than the undoped sample, which was in good agreement with the TGA-MS data. The rest of the trace only displayed small features indicating there were few competing reactions and the amide-imide reaction likely dominated in these samples.

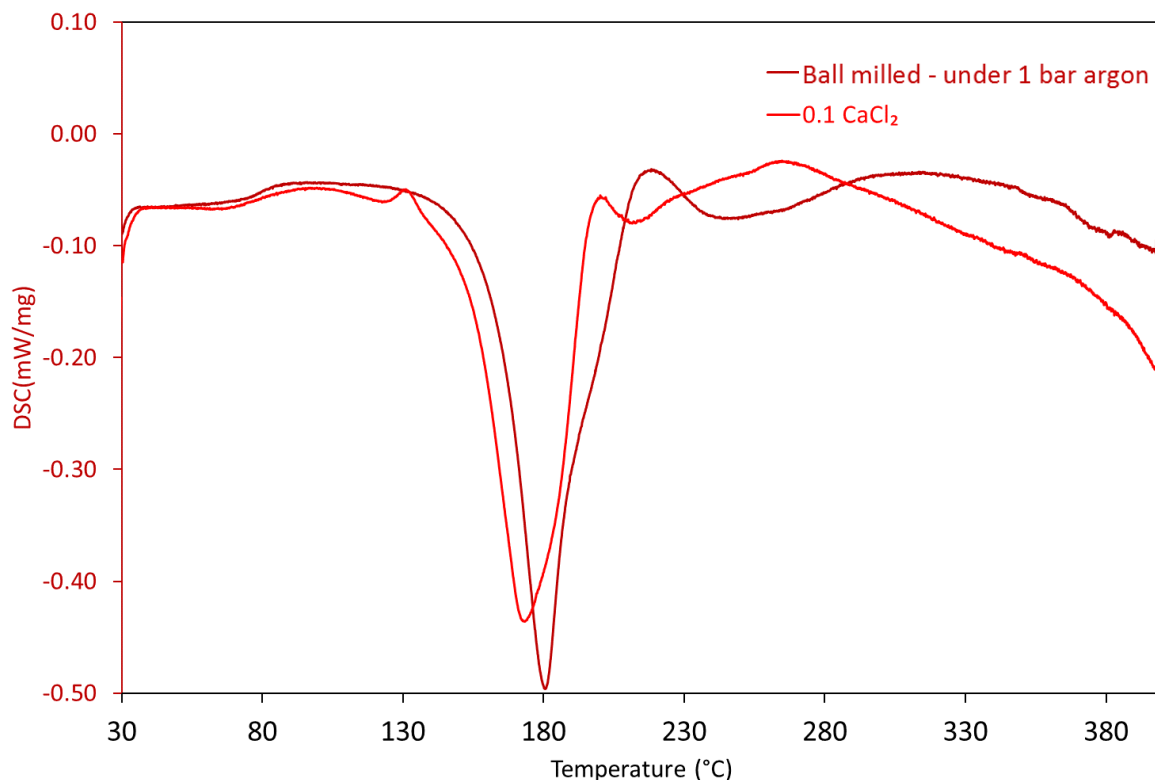


Figure 4-16: DSC heating segment of control ($2\text{LiNH}_2 + \text{MgH}_2$ ball-milled under 1 bar argon) and 0.1 mole fraction CaCl_2 doped sample.

Similarly, the features observed in the DSC traces from the samples milled under 100 bar hydrogen (Figure 4-17) closely mirror the features in the hydrogen desorption profiles observed

from these samples (Figure 4-9). As shown by the number of DSC peaks, several competing reactions were occurring in these samples. This might suggest, either an inhomogeneous sample was produced during the milling, or several distinct reactions were occurring. As an additional component, CaCl_2 , was added to the samples, it would seem likely that the variation in behaviour between the doped and control samples was due to additional reactions occurring involving calcium and chlorine. The exothermic area in the undoped sample ball-milled under 100 bar hydrogen was attributed the crystallisation of $\text{Mg}(\text{NH}_2)_2$ and 2LiH and the Raman data recorded of the CaCl_2 -doped sample milled under 100 bar hydrogen also indicated the presence of $\text{Mg}(\text{NH}_2)_2$ after ball-milling preparation. However, the CaCl_2 -doped sample also released hydrogen during low temperature range between $135\text{--}250^\circ\text{C}$, which accounts for the endothermic areas within this range and results in traces which have several apparent peaks. Although the traces in Figure 4-17 look quite different, when the subtle changes in gradient of the undoped sample milled under 100

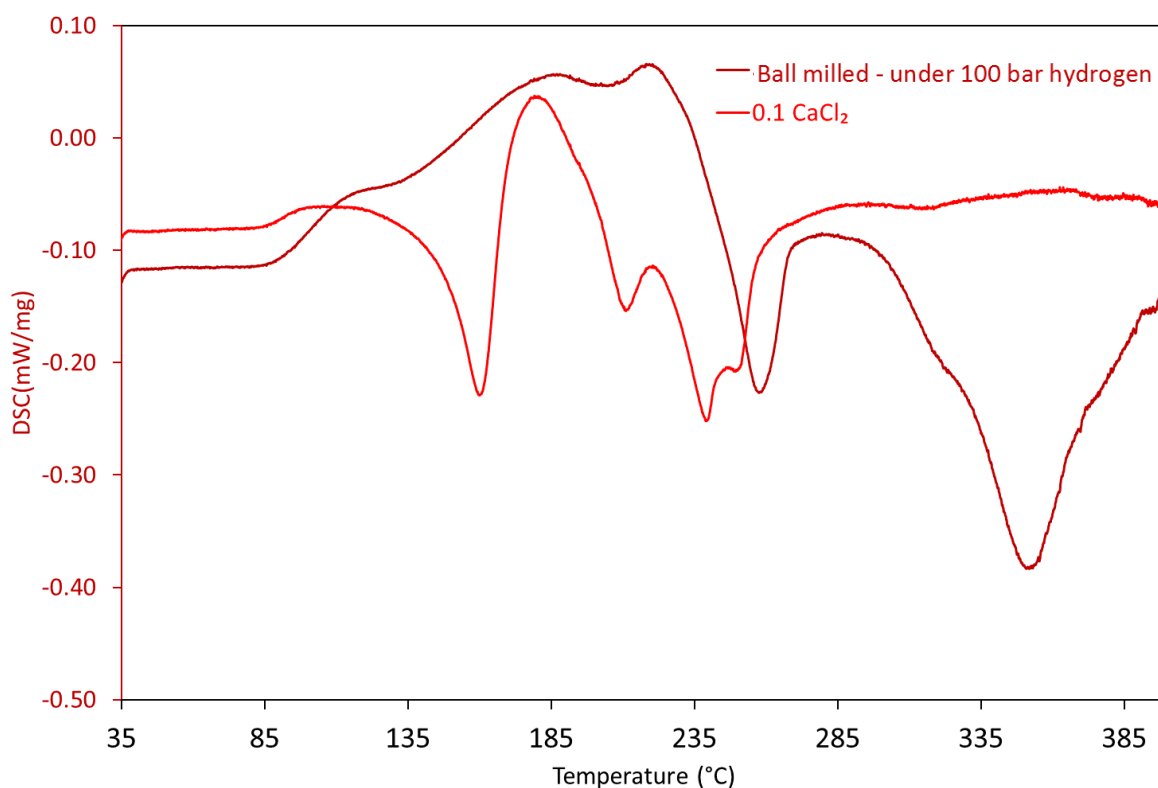


Figure 4-17: DSC heating segment of control ($2\text{LiNH}_2 + \text{MgH}_2$ ball-milled under 100 bar hydrogen) and 0.1 mole fraction CaCl_2 doped sample.

bar hydrogen are considered, the peaks in the doped sample do broadly mirror the behaviour of the undoped sample.

The DSC traces from the samples starting from $\text{Mg}(\text{NH}_2)_2$ and 2LiH (Figure 4-18) were similar to the samples ball-milled under 1 bar argon. The three endothermic peaks observed were in good correlation with the hydrogen release peaks from both these samples in the TGA-MS. The decreased area of the first peak for the doped samples is in good agreement with TGA-MS data which showed a smaller hydrogen peak compared to the control. No exothermic areas were observed. A numerical summary of the data presented in these figures is shown Table 4-11.

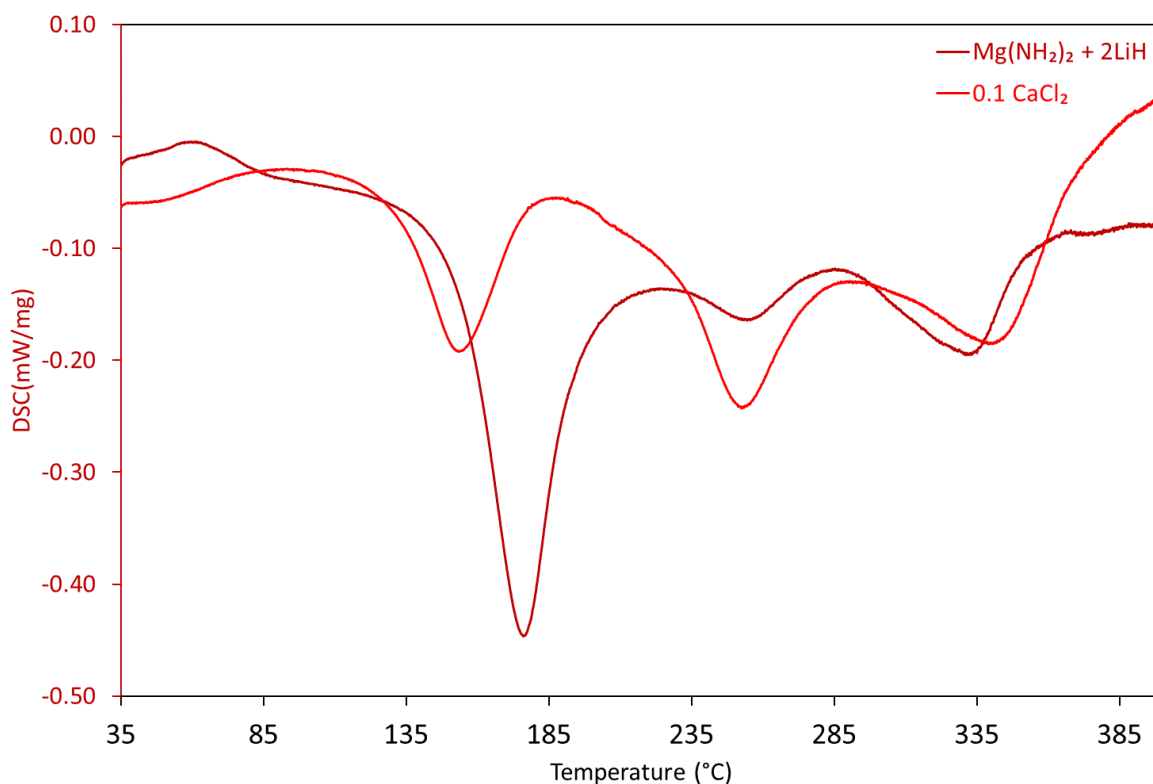


Figure 4-18: DSC heating segment of control ($\text{Mg}(\text{NH}_2)_2 + 2\text{LiH}$ ball-milled) and 0.1 mole fraction CaCl_2 -doped sample.

As the areas of these peaks are proportional to the amount of hydrogen released in that step, and the starting masses of the samples varied, the magnitude of the areas under the peaks cannot be directly compared across different samples. To complicate these calculations, the mass loss was thought to be composed of both hydrogen and ammonia in most samples. In order to

attempt to account for both of these factors, calculations to estimate the enthalpy change associated with the first step of desorption from the samples in Figure 4-16, Figure 4-17 and Figure 4-18 were carried out and the values are displayed in Table 4-11

Sample preparation	Temperature of 1 st peak (°C)	Estimated Enthalpy change (kJ mol ⁻¹ H ₂)
Ball-milled under 1 bar argon	182	22.1
Ball-milled under 1 bar argon + 0.1 CaCl ₂	174	25.2
Ball-milled under 100 bar hydrogen	-	-
Ball-milled under 100 bar hydrogen + 0.1 CaCl ₂	160	25.8
Mg(NH ₂) ₂ + 2LiH	176	26.2
Mg(NH ₂) ₂ + 2LiH + 0.1 CaCl ₂	154	25.0

Table 4-11: Peak temperatures and areas underneath the largest low temperature peak from DSC data for several samples (estimated error was calculated to be 0.4 kJ mol⁻¹).

In order to calculate the values in Table 4-11, the mass loss (in mg) associated with the DSC peak was calculated from gravimetric data for the respective samples and this was then converted into moles. The area under the peaks (J/g) was then multiplied by the original sample mass, and divided by the number of moles of H₂ to estimate the enthalpy change in kJ mol⁻¹ of H₂. Like the calculation for the TGA uncertainty value, the sampling rates of the mass spectrometer and DSC, as well as heating rate of the DSC were considered. As the enthalpy calculation is made per unit mass (which is converted into mol) the error in the balance used to record to sample mass must also be included.

The values for the undoped samples calculated in Table 4-11 are in a lower region than expected. However, the enthalpy values calculated for the low temperature desorption step from DSC measurements by Hu *et al.*¹³⁷ and Liu *et al.*¹⁵⁵ from systems based on Mg(NH₂)₂ and CaH₂ were found to be 21.4 kJ mol⁻¹ H₂ and 28.2 kJ mol⁻¹ H₂, respectively. Tokoyada *et al.*¹⁵⁹ calculated the

enthalpy values of several well-known systems using DSC and found that the results were comparable to the values calculated from Van't Hoff plots which are more traditionally employed for this calculation.

This calculation has been based on several assumptions; first that the mass loss from pseudo-gravimetric calculations to calculate the mass of hydrogen released during TGA experiments were accurate. Pseudo-gravimetric calculations were carried out based on calibrated mass spectrometry data from TGA experiments to estimate the proportion of hydrogen and ammonia during the release events for the DSC peaks. The corrected masses of hydrogen were used in the enthalpy calculations, but as shown in Figure 3-5, the relative ammonia signal was low, which may mean these figures are slightly lower than they should be.

The other assumption made was that the change in the sample mass at any given point was small in comparison to the starting mass. This meant that the enthalpy change (mW/mg) was calculated against the starting mass of the sample, not the mass at that point in the experiment. As the total mass change was not greater than 5 wt% at any given time the effect should not be significant.

The final assumption was that the sample behaved as a perfectly conductive sample, *i.e.* that the contact of the sample to the pan was good and the DSC sensor detected 100% of the heat effects from the sample. Although a calibration was done using metals, these are good conductors and, during the measured melting events used for the calibration, spread out completely within the pan, ensuring good heat flow. However, the samples used in this work are powders and it is likely they are less conductive of heat and have an uneven contact with the pan, which would result in a lower amount of heat transfer. These effects can be accounted for by a process used by Isobe *et al.*¹⁶⁰ to calculate a cell constant but unfortunately due to material constraints this was not carried out.

Although the values in this work may not be comparable to other results from the Li-Mg-N-H system, they can still be used to compare the effectiveness of the dopants against the respective controls. Unfortunately, as an exothermic peak was observed in the undoped sample ball-milled under 100 bar hydrogen, the enthalpy could not be calculated for comparison to the doped sample prepared under the same conditions. The calculated enthalpy of all the doped systems was similar whereas more variation was observed in the undoped samples. The enthalpy of the sample ball-milled under 1 bar argon was the lowest observed.

4.5 Powder XRD

Due to the similarities in desorption behaviour between the control samples and the CaCl_2 -doped samples, a systematic powder XRD study under flowing argon conditions was carried out to compare the intermediates and products formed after various preparation methods with and without the addition of CaCl_2 . From desorption data, it appeared that doping the samples with CaBr_2 affected the samples differently and, due to the complex nature of analysing a system with three cations it was decided to concentrate on the CaCl_2 -doped samples. However, cycling work was carried out on the CaBr_2 -doped samples to examine the effects of the preparation and dopants on rehydrogenation.

4.5.1 Hand-ground

Although hand-ground samples were not tested in TGA or DSC experiments, due to the complication of this system by adding in an additional cation and anion, and the broadening of peaks in the powder XRD patterns caused by ball-milling, it was decided also to collect powder XRD data from doped hand-ground samples. As discussed in Section 3.4.4.1, the desorption mechanism and products may not be with the same as those observed from ball-milled samples. The samples were heated for 12 hours at varying temperatures and once cooled, powder XRD data were collected at room temperature.

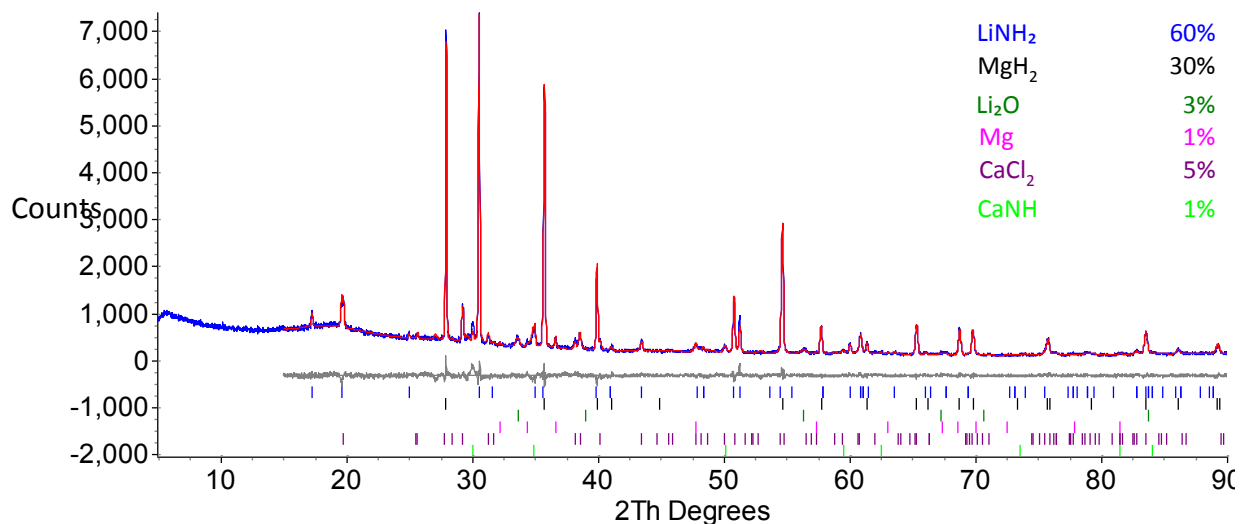


Figure 4-19: Powder XRD pattern of 0.1 mole fraction CaCl₂-doped (2LiNH₂ + MgH₂) hand-ground sample heated at 200°C for 12 hours, with Rietveld fit showing the difference (grey), calculated (red) and observed (purple) traces with the peak positions indicated for LiNH₂ (blue), MgH₂ (black), Li₂O (green), Mg (pink), CaCl₂ (purple) and CaNH (light green).

The powder XRD pattern shown in Figure 4-20 shows that even at 200°C, a small amount of oxidation had occurred (Li₂O and MgO) and, interestingly, a very small amount of CaNH was identified. Mg metal was also identified and its peaks were not overlapped. The formation of CaNH, and a reduction of the starting amount of CaCl₂ would imply that CaCl₂ facilitated a low temperature partial desorption–metathesis reaction. The suggested metathesis reaction for CaCl₂ is shown in Equation 4-2, which would produce LiCl. As discussed previously⁹³, at accessible temperatures, LiCl has been seen to react with LiNH₂ to produce Li₄(NH₂)₃Cl. However, neither LiCl nor Li₄(NH₂)₃Cl could be unambiguously identified in the powder XRD patterns of these doped hand-ground samples.

The formation of CaNH occurred around 75°C lower than any imide phase was observed in the control hand-ground sample. This would be in good agreement with the literature which suggests that the decomposition of Ca(NH₂)₂ begins around 60°C^{161, 162} lower than either LiNH₂ or Mg(NH₂)₂. It was found that Ca(NH₂)₂ could then react with MgH₂ to form a magnesium calcium imide phase⁹⁰ (Equation 4-3). This phase is similar to the cubic structure of CaNH with partial substitution of the Ca²⁺ cations for Mg²⁺. A full structure solution is not available for MgCa(NH)₂.

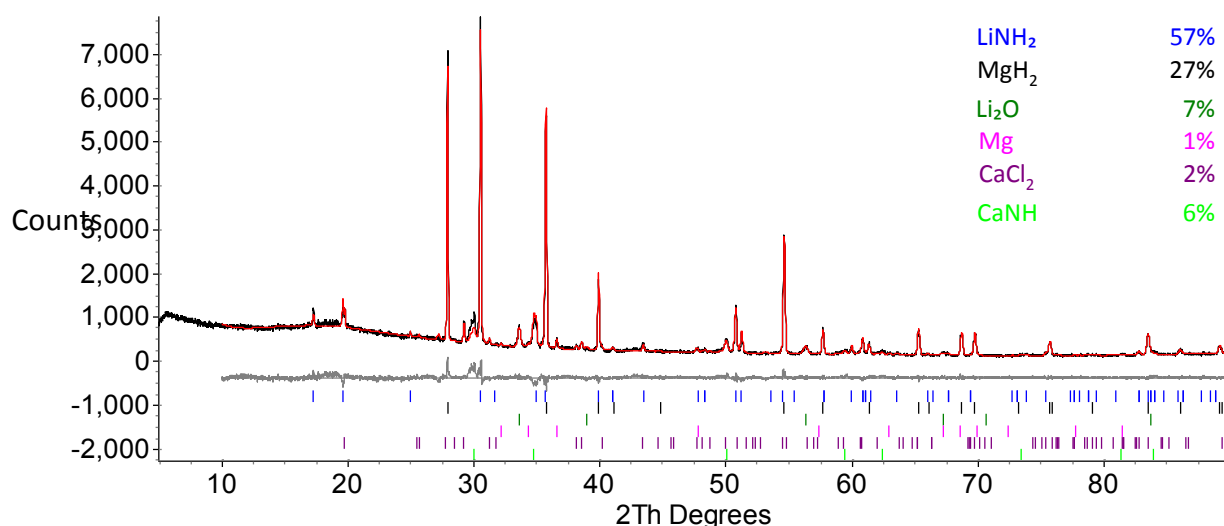
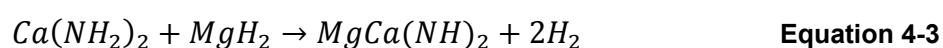
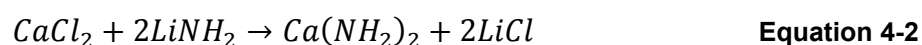


Figure 4-20: Powder XRD pattern of 0.1 mole fraction CaCl₂-doped (2LiNH₂ + MgH₂) sample heated at 275°C for 12 hours, with Rietveld fit showing the difference (grey), calculated (red) and observed (green) traces with the peak positions indicated for LiNH₂ (blue), MgH₂ (black), Li₂O (green), Mg (pink), CaCl₂ (purple) and CaNH (light green).

The presence of CaNH in these samples indicates that the decomposition of calcium amide (Equation 4-4) had been the dominant reaction of Ca(NH₂)₂ that was formed from metathesis (Equation 4-2). The low temperature of Ca(NH₂)₂ decomposition may explain why the fully hydrogenated phase was not observed (potentially formed and decomposed *in situ*) in the powder XRD patterns and could explain ammonia release (Figure 4-2) from these samples.



It can be seen from Figure 4-20 that introducing an additional compound (the dopant) into the Li-Mg-N-H system, even in small amounts, increases the number of phases formed. Although the doped sample in Figure 4-20 was heated at 275°C, the same temperature at which Li₂Mg(NH)₂ was first observed in the control sample, only a small amount of Li₂NH rather than Li₂Mg(NH)₂ was observed. This was unexpected as desorption began at a lower temperature (Table 4-2) from the

doped sample. Interestingly, apart from the formation of CaNH, metathesis products such as phases like LiCl or MgCl₂ were not identified from these powder XRD patterns.

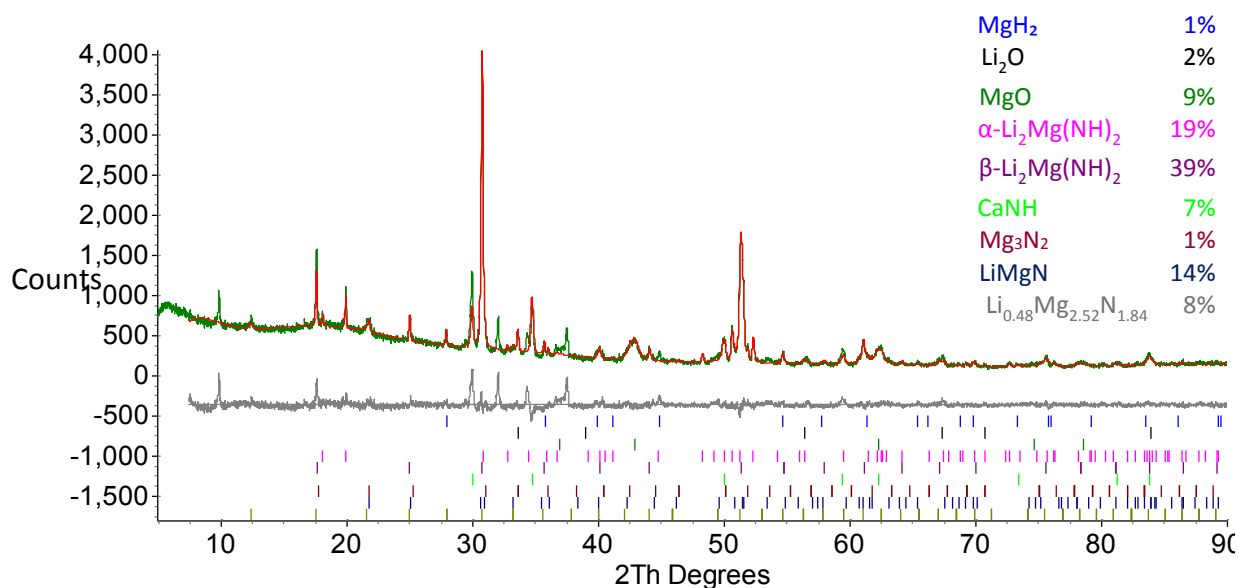


Figure 4-21: Powder XRD pattern of 0.1 mole fraction CaCl₂-doped (2LiNH₂ + MgH₂) hand-ground sample heated at 350°C for 12 hours, with Rietveld fit showing the difference (grey), calculated (red) and observed (green) traces with the peak positions indicated for MgH₂ (blue), Li₂O (black), MgO (green), α-Li₂Mg(NH)₂ (pink), β-Li₂Mg(NH)₂ (purple), CaNH (light green), Mg₃N₂ (brown), LiMgN (dark blue) and Li_{0.48}Mg_{2.52}N_{1.84} (grey).

From previous work on incorporating halides into this Li–Mg–N–H system^{89, 92, 93}, quite often a lithium or lithium magnesium amide halide phase is formed as an intermediary, either as a single or mixed cation phase. These phases were characterised by Davies *et al.*^{163, 164} but the characteristic low angle peaks of the cubic and hexagonal phases were not observed in these powder XRD patterns. It is also possible that an imide halide phase could be formed. Interestingly, Li₇(NH)₃Cl⁴⁷ and CaNH¹⁵⁸ (and MgCa(NH)₂) share the same space group (*Fm* $\bar{3}$ *m*), and the lattice parameters are also very similar, *a* = 5.157(3) Å compared to *a* = 5.143 Å, respectively. The similarities in the structures may mean that there is a chance of cross-substitution across these phases.

The lattice parameters from across the temperature range of the ‘as-fitted’ CaNH are compared in Figure 4-22. They are all slightly larger than the published values for CaNH, and increase up to reaction temperatures of 300°C and then stabilise around 5.157 Å. Anderson *et al.*⁴⁷

identified a large solid solution range that exists for $\text{Li}_7(\text{NH})_3\text{Cl}$, ($5.13 \text{ \AA} \geq a \geq 5.21 \text{ \AA}$) so it is unsurprising to see variation in the cell parameters in this case. A larger than expected lattice parameter could be a result of the replacement of a small number of imide anions with Cl^- anions.

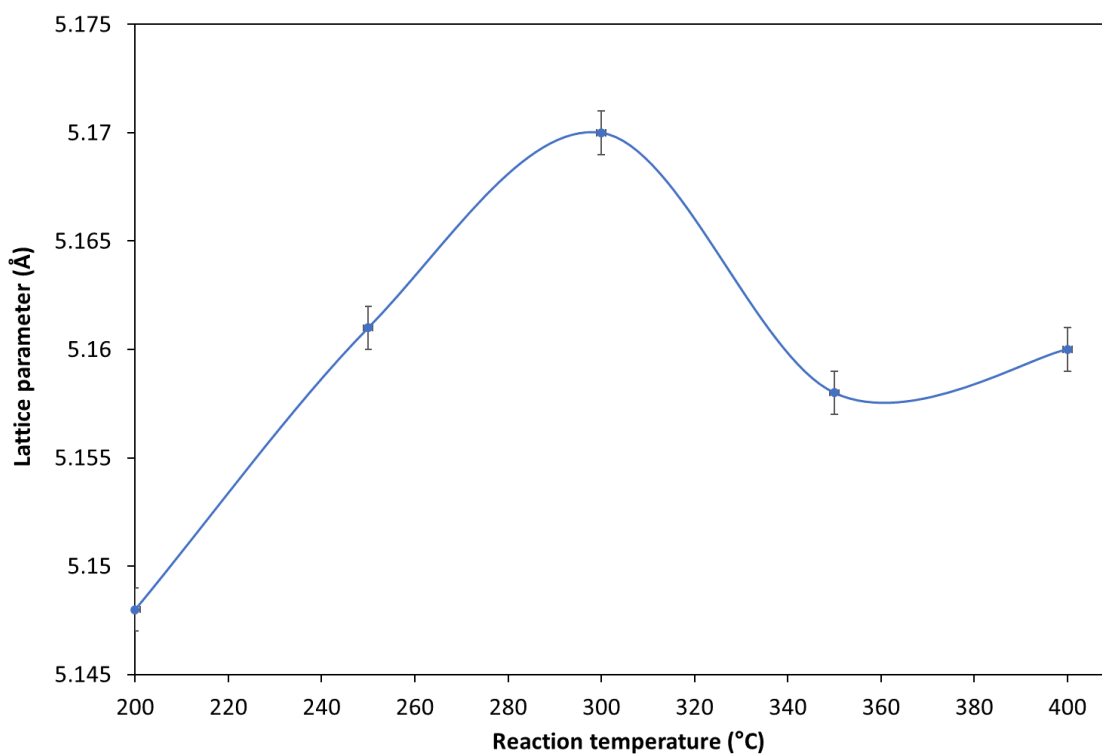


Figure 4-22: Variation in lattice parameter (a) of CaNH identified in 0.1 mole fraction CaCl_2 -doped ($2\text{LiNH}_2 + \text{MgH}_2$) hand-ground samples heated for 12 hours at varying temperatures.

As the heating temperature was increased, $\text{Li}_2\text{Mg}(\text{NH})_2$ was first observed after heating at 300°C. A small amount of $\text{Li}_{0.48}\text{Mg}_{2.52}\text{N}_{1.78}$ was also observed in these patterns. A number of unfitted peaks were observed after heating at 350°C (Figure 4-21). By 350°C the peaks assigned to the initial dopant, CaCl_2 were no longer observed, but nor could any other known stoichiometric chlorine-containing phases be identified. However, due to the ability of the many phases in this system to accommodate a range of stoichiometries and alternative ions, and the low amounts of dopants added (0.1 mole fraction), it is possible that chlorine anions could easily be incorporated into the phases with little variation in lattice parameters, as shown in Figure 4-22. There is some intensity mismatch in some of the peaks observed in Figure 4-21 which could be evidence of the

inclusion of a small amount of halide anions into some of the structures. Unfortunately, the quality of the powder XRD data is not sufficient to analyse these slight variations in detail.

Temperature (°C)	Amount of α - $\text{Li}_2\text{Mg}(\text{NH})_2$ (wt%)	Amount of β - $\text{Li}_2\text{Mg}(\text{NH})_2$ (wt%)	Total amount of $\text{Li}_2\text{Mg}(\text{NH})_2$ (wt%)	Nitride phases (wt%)
300	62	13	75	-
325	37	30	67	14
350	19	39	58	23
400	-	69	69	8

Table 4-12: Estimated wt% by quantitative phase analysis of two phases of $\text{Li}_2\text{Mg}(\text{NH})_2$ and all nitride phases prepared from 0.1 mole fraction CaCl_2 -doped $2\text{LiNH}_2 + \text{MgH}_2$ hand-ground samples.

A significant peak, indicated (in Figure 4-21) at 10° was observed with no overlap to other phases and could not be fitted to a known phase. It was observed around mid-range temperatures for this sample, first appearing at 300°C . From inspection of the difference trace in Figure 4-21 it was accompanied by several other peaks. Recent literature on the addition of halides into this system,^{89, 93, 101, 128, 165} and older literature^{77, 144, 150, 166} looking more at the fundamental structural work on this system from both nitride and hydrogenated starting materials was searched and found no previous evidence for this low angle peak. This and the other unidentified peaks were found in several other patterns in this chapter but were not observed in powder XRD patterns from samples that did not include calcium dopants. This will be discussed further discussion will after Figure 4-23 (sample ball-milled under 1 bar argon was heated at 400°C for 12 hours) where the peaks are clearer.

The wt% of the respective phases of $\text{Li}_2\text{Mg}(\text{NH})_2$ are compared in Table 4-12. Although $\text{Li}_2\text{Mg}(\text{NH})_2$ was not identified until 300°C , 25°C higher than the control sample, the proportion was much higher. The addition of 0.1 mole fraction of CaCl_2 does not appear to have been detrimental to the amount of mixed cation imide produced. In fact, the total wt% after reaction at 325°C was higher than observed for any hand-ground control sample (Table 3-6). Unfortunately,

the addition of CaCl_2 has not reduced the quantity of nitride-type phases formed in the hand-ground system compared to the undoped samples, but no Li_2NH was observed.

4.5.2 Ball-milled under 1 bar argon pressure

To complement the data collected from hand-ground doped samples in Section 4.5.1, the same experiments were carried out on doped samples ball-milled under 1 bar argon. These results can then be compared to those presented in Section 3.4.4.2. Unfortunately, the peaks observed in the powder XRD pattern recorded after heating at 150°C for 12 hours were too broad to allow accurate analysis of this sample.

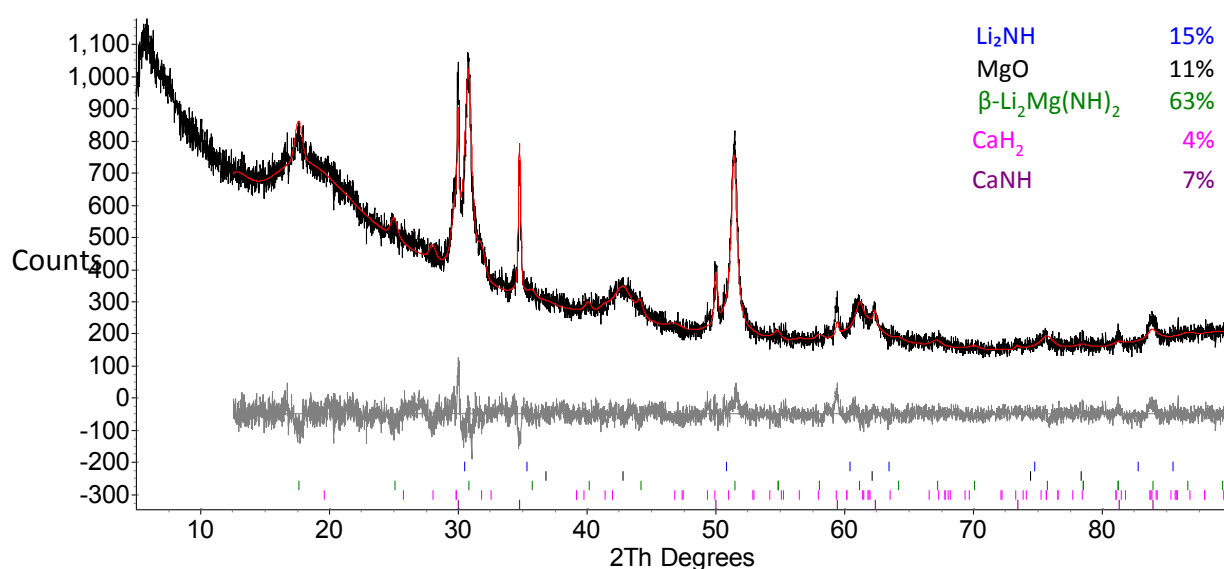


Figure 4-23: Powder XRD pattern of 0.1 mole fraction CaCl_2 -doped sample ($2\text{LiNH}_2 + \text{MgH}_2$) ball-milled under 1 bar argon heated at 200°C for 12 hours, with Rietveld fit showing the difference (grey), calculated (red) and observed (black) traces with the peak positions indicated for Li_2NH (blue), MgO (black), $\beta\text{-Li}_2\text{Mg}(\text{NH})_2$ (green), CaH_2 (pink) and CaNH (purple).

Both Li_2NH and $\beta\text{-Li}_2\text{Mg}(\text{NH})_2$ were observed after heating at 200°C for 12 hours in Figure 4-24 and the β -phase of $\text{Li}_2\text{Mg}(\text{NH})_2$ was again seen at a lower temperature than the α -phase of $\text{Li}_2\text{Mg}(\text{NH})_2$ (observed only after reaction at 250°C). CaCl_2 was not observed in any doped ball-milled samples, instead CaNH and CaH_2 were identified.

Apart from oxides, only $\beta\text{-Li}_2\text{Mg}(\text{NH})_2$ and CaNH were observed in Figure 4-21. A rationale for the production of CaNH was discussed in Section 4.5.1. The production of CaH_2 is more likely to have been caused by a metathesis reaction which was not accompanied by desorption. The powder XRD pattern displayed in Figure 4-25 was recorded after reaction at 400°C . Several peaks, in the same positions as those seen in Figure 4-21 (and Figure 4-27), sample that was ball-milled under 100 bar hydrogen after heating at 400°C for 12 hours), were not fitted. Some of these peaks overlap with those identified for CaNH (at 30.0 , 34.8 and 50.1°). The peak positions of CaNH are similar to those observed from MgNH according to the structure published by Dolci *et al.*¹⁶⁷ in 2011, but the structural information does not account for all the unidentified peaks observed in these patterns.

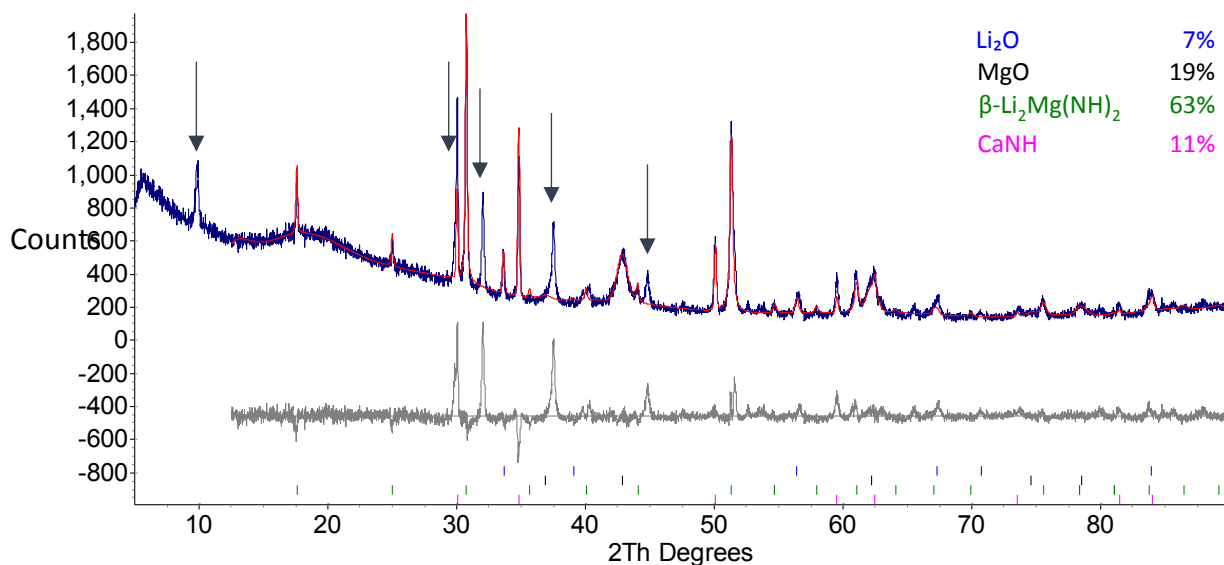


Figure 4-24: Powder XRD pattern of CaCl_2 -doped sample ($2\text{LiNH}_2 + \text{MgH}_2$) ball-milled under 1 bar argon, heated at 400°C for 12 hours, with Rietveld fit showing the difference (grey), calculated (red) and observed (dark blue) traces with the peak positions indicated for Li_2O (blue), MgO (black), $\beta\text{-Li}_2\text{Mg}(\text{NH})_2$ (green) and CaNH (pink). Unfitted peaks indicated.

These peaks were compared to known phases, particularly chlorine-containing compounds, as none had been identified in these samples and some, such as $\text{Li}_4(\text{NH}_2)_3\text{Cl}$, $\text{Li}_{3.5}\text{Mg}_{0.5}(\text{NH}_2)_3\text{Cl}$ and $\text{Li}_7(\text{NH}_2)_6\text{Cl}$ ^{159, 160, 164} and their respective imides as well as a spinel-type Li_2MgCl_4 , also have comparable low angle peaks, but could not be assigned to these.

In an attempt to identify what phase these peaks might belong to, the possible peak positions and intensities were refined using a peak fitting regime in Topas¹¹⁹. The systematic reflection absences in the diffraction pattern suggested that the phase was face-centred. Indexing the peak positions in Topas suggested the most likely space groups were orthorhombic.

Space Group	Number of unindexed peaks	Cell Volume (Å ³)	a Lattice parameter (Å)	b Lattice parameter (Å)	c Lattice parameter (Å)
<i>F222</i>	1	1596.138	17.8180	8.9259	10.0359
<i>F222</i>	1	532.046	17.8180	10.0359	2.9753
<i>F222</i>	1	366.510	17.8180	5.1428	3.9997
<i>F222</i>	1	1362.990	17.8180	12.1458	6.2981
<i>F222</i>	0	1064.453	17.8154	9.4776	6.3028

Table 4-13: Top indexing results from Topas, all to space group *F222* (no. 22)

The most likely space group appeared to be *F222* (space group No. 22) which has the same unique *hkl* reflections as *Fmm2* and *Fmmm*. Various lattice parameters were tried, but to include the low angle peak (around 10°) a large *a* lattice parameter was required. All the solutions in Table 4-13 were investigated using a model-independent Pawley fit. Using the quality of fit factors calculated in Topas and visual inspection of the fit of the solutions, the most favourable lattice parameters were $a = 17.8180 \text{ \AA}$, $b = 12.1458 \text{ \AA}$ and $c = 6.2981 \text{ \AA}$. The lattice parameters were then refined to $a = 17.838(6) \text{ \AA}$, $b = 12.097(3) \text{ \AA}$ and $c = 6.292(2) \text{ \AA}$. Unfortunately, as this data was laboratory data the error on the lattice parameter is quite high. The only discrepancy between the modelled and observed data appeared to be at 20°, where no clear peak was observed in the data, but a small peak had been modelled. A peak may have modelled to a peak of noise seem at the same 2theta value. CaNH had been previously modelled in the powder XRD pattern, but was removed from the refinement shown in Figure 4-25 to consider the peaks that could not be fully described by this phase in the Pawley fit for the unknown phase.

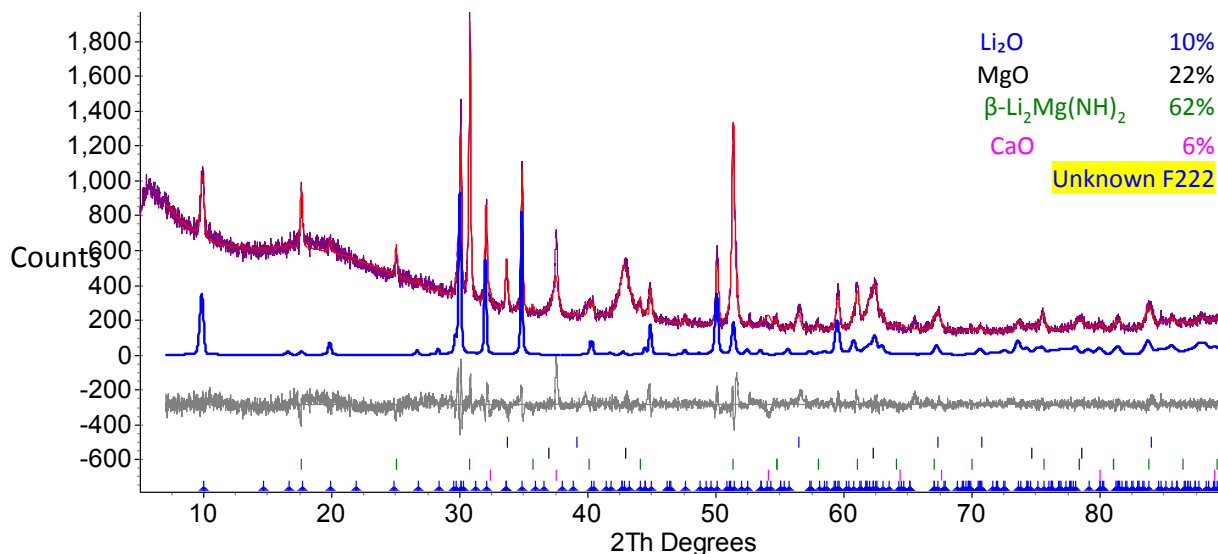


Figure 4-25: Powder XRD pattern of CaCl₂-doped sample (2LiNH₂ + MgH₂) ball-milled under 1 bar argon, heated at 400°C for 12 hours, with Rietveld fit showing the difference (grey), calculated (red) and observed (dark blue) traces with the peak positions indicated for Li₂O (blue), MgO (black), β-Li₂Mg(NH)₂ (green), CaO (pink) and Pawley fit with peak positions indicated for unknown F222 phase (blue and highlighted).

The similarity in some of the peak positions to CaNH might suggest that this phase may be a supercell of CaNH with the possibility of some cation and/or anion substitution, although no previous evidence for such a phase could be found. The amount of β-Li₂Mg(NH)₂ observed from the doped sample was lower than the undoped sample. As detailed in Table 4-14, unlike the control sample, the reactions carried out at 300°C and higher resulted in similar proportions of the products. Similar amounts of CaNH were observed across the temperature range of the reactions, showing that this phase was formed at low temperatures (>200°C) and appears to be unreactive, effectively blocking these components from participating in further reactions. Inspection of the CaNH cell volume across the temperature range did not show much variation, indicating it was unlikely that the composition had changed significantly. This would suggest that the active phase in the reaction from the addition of CaCl₂ was in-fact LiCl which was formed through Equation 4-2.

Temperature (°C)	Amount of α - $\text{Li}_2\text{Mg}(\text{NH})_2$ (wt%)	Amount of β - $\text{Li}_2\text{Mg}(\text{NH})_2$ (wt%)	Total amount of $\text{Li}_2\text{Mg}(\text{NH})_2$ (wt%)	Nitride phases (wt%)
200	-	63	63	-
250	14	58	72	-
300	-	70	70	-
350	-	69	69	-
400	-	62	62	-

Table 4-14: Estimated wt% by quantitative phase analysis of two phases of $\text{Li}_2\text{Mg}(\text{NH})_2$ and nitride phases prepared from 0.1 mole fraction CaCl_2 -doped $2\text{LiNH}_2 + \text{MgH}_2$ samples ball-milled under 1 bar argon.

Interestingly in the samples ball-milled under 1 bar argon, the addition of CaCl_2 seems to have arrested the formation of nitride phases at higher temperatures. However, it is likely that the operating temperatures of this storage medium would be around 200°C, so the effects at higher temperatures would not be so important as the nitride phases are not favourable for reversible hydrogen storage. Comparing the phases observed from the doped sample shown in Table 4-14 to those in Table 3-6, the behaviour of the 0.1 mole fraction CaCl_2 -doped sample was very similar to the control sample ball-milled under 1 bar argon.

The transition from β - $\text{Li}_2\text{Mg}(\text{NH})_2$ to α - $\text{Li}_2\text{Mg}(\text{NH})_2$ and back was seen in both undoped and doped samples, even though experiments heating at 225°C and 275°C were not carried out in this case. The oxide content increased with higher reaction temperatures, but more markedly in the doped system.

4.5.3 Ball-milled under 100 bar hydrogen

Samples from the 0.1 mole fraction CaCl_2 -doped mixture ball-milled under 100 bar hydrogen were taken and heated at various temperatures. As in Sections 4.5.1 and 4.5.2 the products were analysed using powder XRD. In the undoped system, the behaviour of the samples ball-milled under 100 bar hydrogen was different to those which were milled under 1 bar argon. The biggest variations between milling conditions were the formation temperatures and order in which the respective phases of $\text{Li}_2\text{Mg}(\text{NH})_2$ were observed.

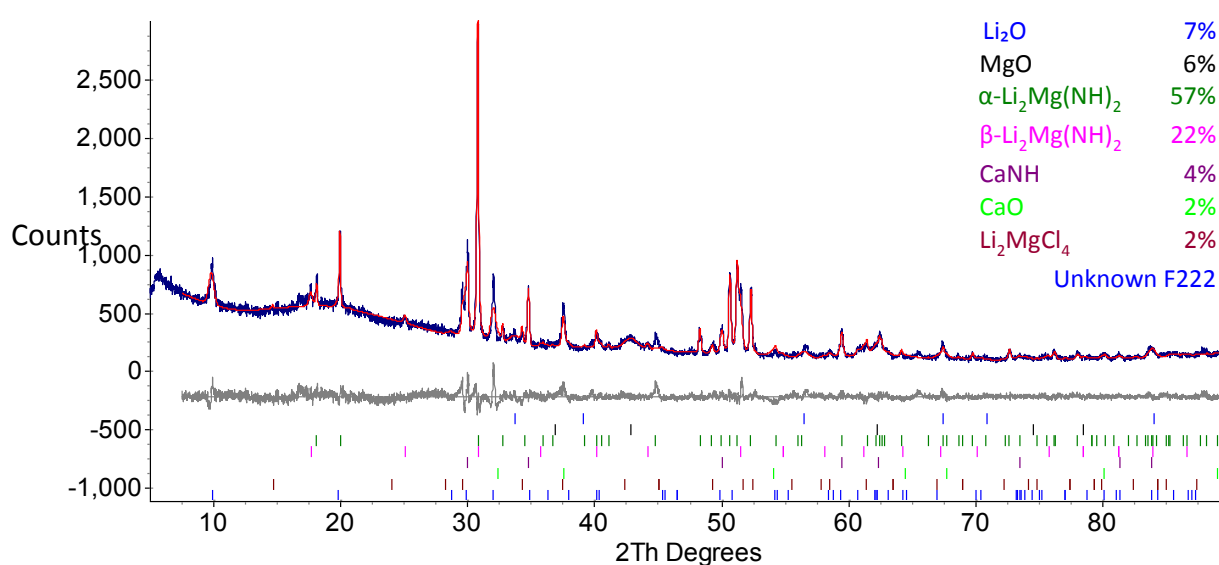
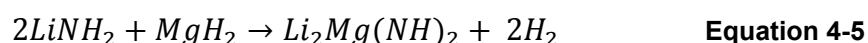


Figure 4-26: Powder XRD pattern of CaCl_2 -doped ($2\text{LiNH}_2 + \text{MgH}_2$) sample ball-milled under 100 bar hydrogen, heated at 250°C for 12 hours, with Rietveld fit showing the difference (grey), calculated (red) and observed (dark blue) traces with the peak positions indicated of Li_2O (blue), MgO (black), $\alpha\text{-Li}_2\text{Mg}(\text{NH})_2$ (green), $\beta\text{-Li}_2\text{Mg}(\text{NH})_2$ (pink), CaNH (purple), CaO (green) and Li_2MgCl_4 (brown) and Pawley fit with peak positions indicated for unknown F222 phase (blue).

The powder XRD after heating to 250°C is shown in Figure 4-26, the lowest temperature at which CaNH was observed after ball-milling under 100 bar hydrogen. CaCl_2 was not observed in any samples after heating and, in contrast to the comparable undoped sample, both $\alpha\text{-Li}_2\text{Mg}(\text{NH})_2$ and $\beta\text{-Li}_2\text{Mg}(\text{NH})_2$ were observed after reactions at 200°C .

A small amount of a chloride-containing phase Li_2MgCl_4 was observed in this sample. This ternary lithium magnesium chloride has an inverse spinel-type structure, can crystallize under ambient conditions and, most interestingly, displays rapid lithium ion conductivity¹⁶⁸. As high

lithium ion conduction is thought to be an important property to lower the temperatures and improve rates of de- and re-hydrogenations, the formation of this phase could be an indication of how this dopant benefits the system. A route for the formation of this phase is suggested through the formation and reaction of $\text{Li}_2\text{Mg}(\text{NH})_2$ in Equations 4-5 and 4-5a and would compete with Equation 4-2 for the consumption of CaCl_2 but Equation 4-5a would also produce CaNH , as observed in Figure 4-27 and explain the absence of $\text{Ca}(\text{NH}_2)_2$.



A similar powder XRD pattern was observed after heating the sample ball milled under 100 bar hydrogen pressure (Figure 4-27) to 400°C as the sample ball milled under 1 bar argon (Figure 4-24). Similarly, to the samples ball-milled under 1 bar argon, CaNH was observed across the temperature range, and remained after heating at 400°C. The amounts of $\text{Li}_2\text{Mg}(\text{NH})_2$ after heating at various temperatures are shown in Table 4-15. Unlike the undoped samples, the total amount of $\text{Li}_2\text{Mg}(\text{NH})_2$ observed after heating at 400°C was the same as that at 200°C or 250°C. The total amount of $\text{Li}_2\text{Mg}(\text{NH})_2$ was reasonably consistent across a wide temperature range of the doped samples regardless of ball-milling conditions. Apart from the order of the formation of the α - and β -phases of $\text{Li}_2\text{Mg}(\text{NH})_2$, the dehydrogenation pathways of the doped samples seem to be more similar regardless of ball-milling regime.

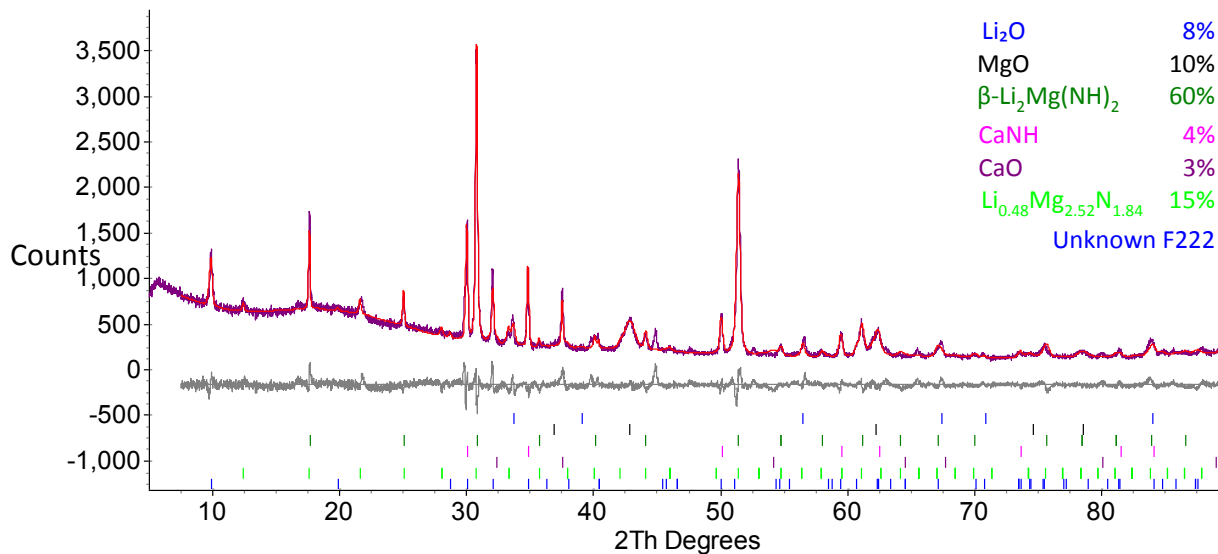


Figure 4-27: Powder XRD pattern of CaCl₂-doped sample (2LiNH₂ + MgH₂) ball-milled under 100 bar hydrogen, heated at 400°C for 12 hours, with Rietveld fit showing the difference (grey), calculated (red) and observed (blue) traces with the peak positions indicated of Li₂O (blue), MgO (black), β-Li₂Mg(NH)₂ (green), CaNH (pink) CaO (purple), Li_{0.48}Mg_{2.52}N_{1.84} (light green) and Pawley fit with peak positions indicated for unknown F222 phase (blue).

The amount of Li₂Mg(NH)₂ observed after reaction at low temperatures was higher in the doped samples than the undoped samples (Table 3-8). This shows the reaction can proceed at lower temperatures, implying a thermodynamic improvement to dehydrogenation temperatures has been made through the addition of 0.1 mole fraction CaCl₂, but this limited hydrogen desorption capacity. As the samples were heated isothermally for a long duration of 12 hours, the effect from differing rates of the reaction should be minimised as all reactions should be mostly complete after 12 hours. In contrast to the samples which were ball-milled under 1 bar argon, after reactions at higher reaction temperatures, samples ball-milled under 100 bar hydrogen did promote the formation of nitride phase(s). The reasons for this are unclear. Interestingly, the Li₂Mg(NH)₂ content in the two samples after reaction at 400°C was similar, so it seems unlikely further desorption had occurred from Li₂Mg(NH)₂ but more likely a direct reaction forming lithium-magnesium nitride (Equation 3-4).

Temperature (°C)	Amount of α - $\text{Li}_2\text{Mg}(\text{NH})_2$ (wt%)	Amount of β - $\text{Li}_2\text{Mg}(\text{NH})_2$ (wt%)	Total amount of $\text{Li}_2\text{Mg}(\text{NH})_2$ (wt%)	Nitride phases (wt%)
200	53	21	74	-
250	57	22	79	-
300	7	55	62	8
350	4	57	62	5
400	-	60	60	15

Table 4-15: Estimated wt% by quantitative phase analysis of two phases of $\text{Li}_2\text{Mg}(\text{NH})_2$ and nitride phases prepared from 0.1 mole fraction CaCl_2 -doped $2\text{LiNH}_2 + \text{MgH}_2$ samples ball-milled under 100 bar hydrogen.

4.5.4 Cycling experiments

To understand how the doped ball-milled samples behaved compared to the control samples, isothermal desorption experiments under flowing argon were carried out on the ball-milled samples, (1 bar argon and 100 bar hydrogen), the same as those in discussed Section 3.4.4.3. The powder XRD pattern of the 0.1 mole fraction CaCl_2 -doped sample ball-milled under 1 bar argon after desorption into flowing argon at 220°C for 50 hours is displayed in Figure 4-28.

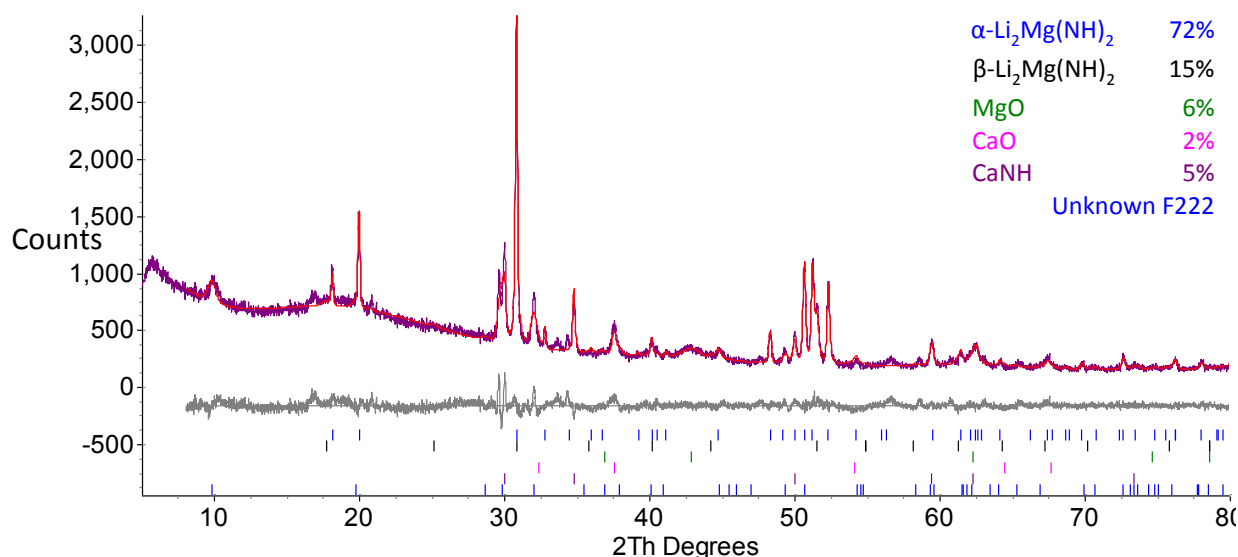


Figure 4-28: Powder XRD pattern CaCl_2 -doped sample ($2\text{LiNH}_2 + \text{MgH}_2$) ball-milled under 1 bar argon, heated at 220°C under flowing argon for 50 hours, with Rietveld fit showing the difference (grey), calculated (red) and observed (purple) traces with the peak positions indicated for α - $\text{Li}_2\text{Mg}(\text{NH})_2$ (blue), β - $\text{Li}_2\text{Mg}(\text{NH})_2$ (black) and MgO (green), CaO (pink) and CaNH (purple) and Pawley fit with peak positions indicated for unknown F222 phase (blue).

Although there are multiple small peaks which could not be fitted (discussed in Section 4.5.1), the major product of this experiment was $\alpha\text{-Li}_2\text{Mg}(\text{NH}_2)_2$ like the control sample ball-milled under 1 bar argon. However, in contrast to the control samples, the powder XRD patterns from the two CaCl_2 -doped ball-milled samples were almost the same. The only slight difference is shown in Figure 4-29.

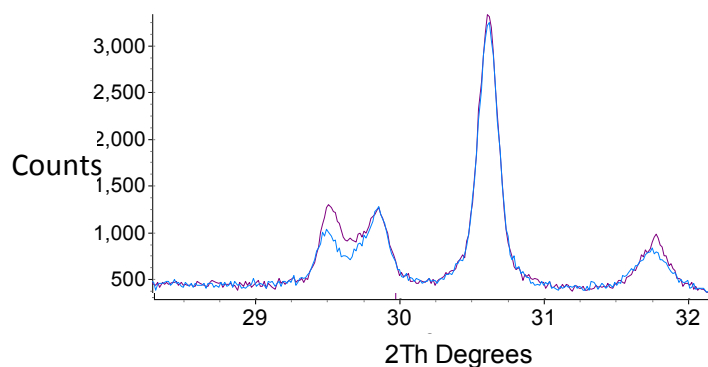


Figure 4-29: Comparison of powder XRD patterns of CaCl_2 -doped samples ($2\text{LiNH}_2 + \text{MgH}_2$) ball milled under 1 bar argon (blue) and 100 bar hydrogen (purple).

Unfortunately, the peaks ($\sim 29.5^\circ$ and 32°) where the difference was observed were assigned to the unknown F222 phase (Figure 4-28) so it was not possible to identify exactly how the different preparation methods had affected the phases formed, but differences in intensity would suggest that the occupancy or type of ion was different. As the CaCl_2 - and CaBr_2 -doped samples behaved differently under desorption testing, powder XRD patterns were recorded of the CaBr_2 -doped samples after cycling. Unlike the CaCl_2 -doped samples, the resulting powder XRD patterns from the two milled CaBr_2 -doped samples after desorption under flowing argon were different. The significant factors for the system i.e. the phases of $\text{Li}_2\text{Mg}(\text{NH}_2)_2$ were similar, but the side products from competing reactions were different.

The CaBr_2 -doped samples produced more complicated powder XRD patterns than the CaCl_2 -doped samples. The resulting powder XRD patterns after milling of the CaBr_2 -doped samples were very similar. After desorption of the CaBr_2 -doped sample ball-milled under 100 bar hydrogen under flowing argon, a previously reported bromide-containing phase¹⁶⁴ was identified

in the resulting powder XRD pattern as well as peaks which were typical of the unknown F222 phase, (discussed in Section 4.5.2). A Pawley fit was used to describe $\text{Li}_7(\text{NH}_2)_6\text{Br}$ in Figure 4-30 as the observed intensities and positioning of some peaks did not fit exactly to the crystallographic data file published⁴⁷. $\text{Li}_7(\text{NH}_2)_6\text{Br}$ has previously been synthesised at 250°C under flowing argon, conditions, close to those used in the sample preparation before Figure 4-30 was recorded.

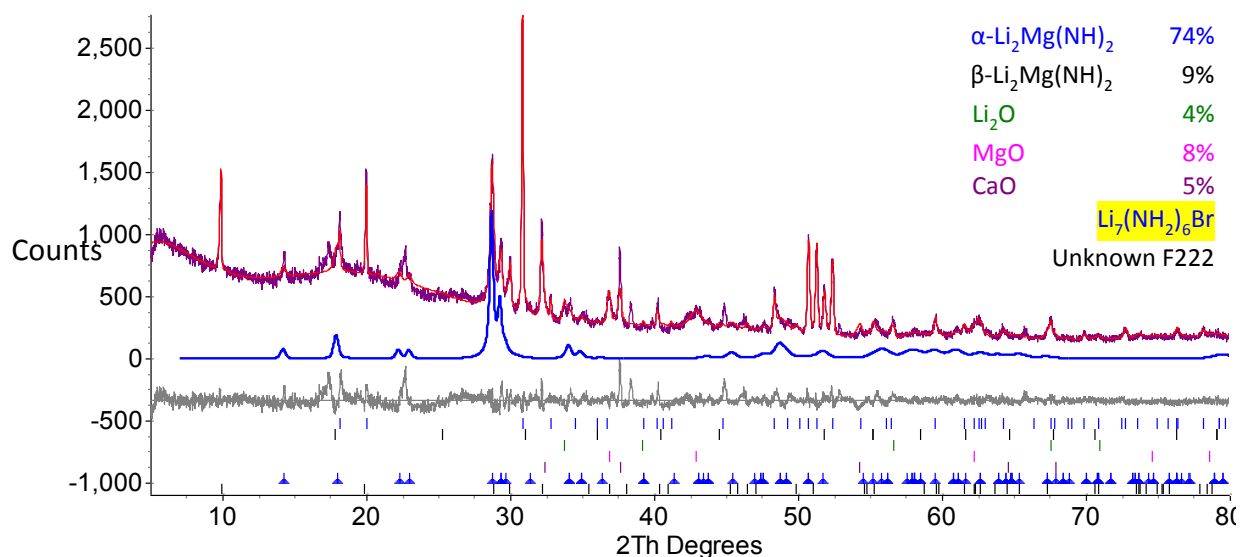


Figure 4-30: Powder XRD pattern of CaBr_2 -doped sample ($2\text{LiNH}_2 + \text{MgH}_2$) ball-milled under 100 bar hydrogen, heated at 220°C under flowing argon for 50 hours, with Rietveld fits showing the difference (grey), calculated (red) and observed (blue) traces with the peak positions indicated for $\alpha\text{-Li}_2\text{Mg}(\text{NH})_2$ (blue), $\beta\text{-Li}_2\text{Mg}(\text{NH})_2$ (black) and MgO (green), CaO (pink) and Pawley fits with peak positions indicated for $\text{Li}_7(\text{NH}_2)_6\text{Br}$ (blue and highlighted) and unknown F222 phase (black).

Unfortunately, several of the small peaks observed (Figure 4-31) could not be unambiguously assigned to a known phase. The intensity of the peak around 10° in the powder XRD pattern in Figure 4-30 was in a similar position and higher in intensity than seen in many of the patterns from CaCl_2 -doped samples in this chapter. If this unknown phase contained halide anions, an increase in intensity and lattice parameters could be in good agreement with the replacement of the chloride anion with the bromide anion.

After desorption from doped samples, the α -phase of $\text{Li}_2\text{Mg}(\text{NH})_2$ dominated as a main desorption product. Unfortunately, the desorption properties of the doped samples were not

tested under vacuum, so the effect of the dopants on the phase dependence under desorption conditions could not further be explored in this case.

As the resulting powder XRD patterns after dehydrogenation and hydrogenation of doped samples were complicated, and it had not been possible to fit multiple peaks in the patterns, Raman spectra of these samples were also recorded to assist with assessment of the hydrogenation states after respective treatments. The Raman spectra recorded after desorption in Figure 4-30 did not show any evidence of amide-type compounds, indicating the conversion of amide to imide for samples doped with CaCl_2 or CaBr_2 appeared to be complete as indicated by analysis of powder XRD patterns.

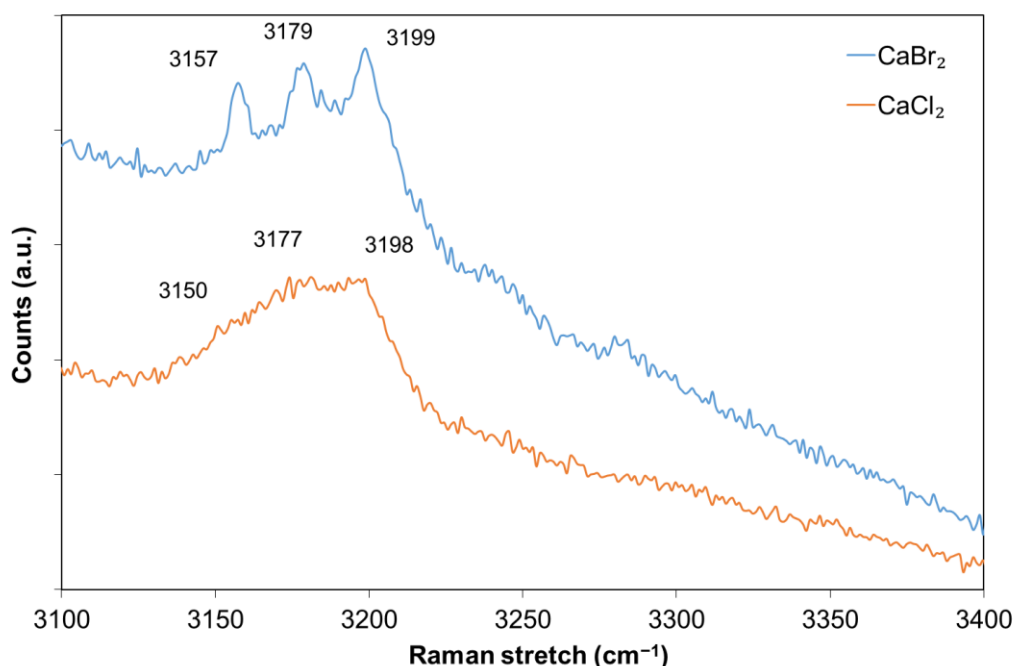


Figure 4-31: Typical Raman spectra of CaCl_2 - and CaBr_2 -doped ($2\text{LiNH}_2 + \text{MgH}_2$) ball-milled samples heated at 220°C under flowing argon for 50 hours.

The powder XRD pattern in Figure 4-32 was recorded after attempted hydrogenation of the CaCl_2 -doped sample milled under 1 bar argon after desorption into flowing argon. After hydrogenation of the desorbed samples it was not possible to fit several of the peaks observed in powder XRD patterns. Most phases observed in this sample were imide-type phases and a small amount of $\text{Mg}(\text{NH}_2)_2$ was also identified as well as peaks corresponding to the F222 phase. The

lattice parameter values of several key phases, Li_2NH and $\alpha\text{-Li}_2\text{Mg}(\text{NH})_2$ were compared and there was little variation from the published values. The reversibility of this doped sample was considerably worse than either of the undoped samples tested in Chapter 3.

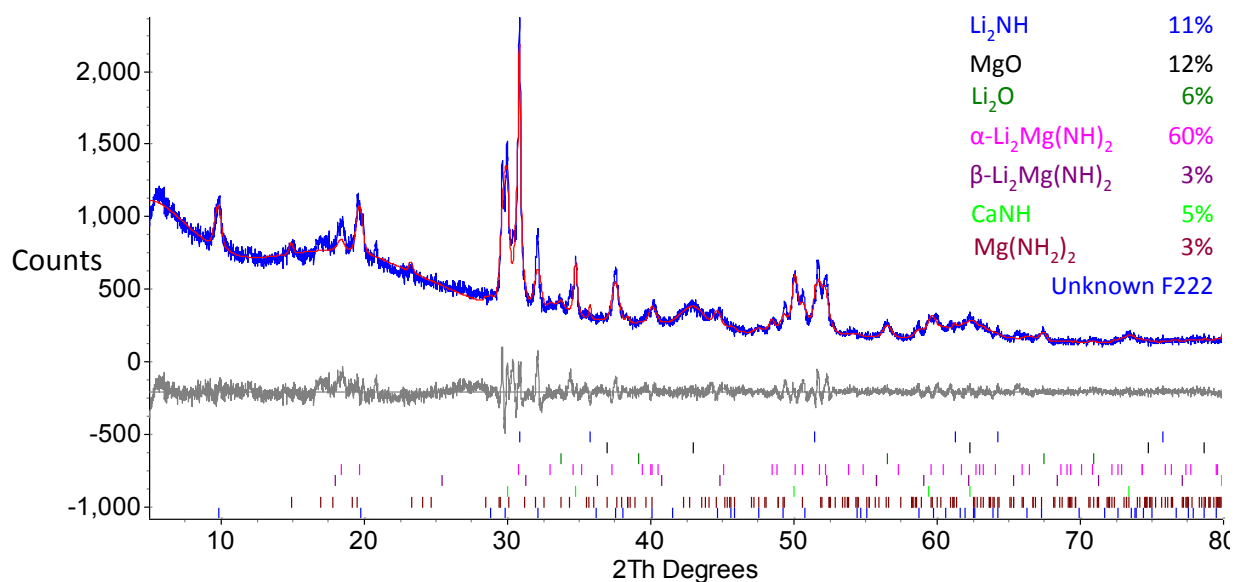


Figure 4-32: Powder XRD pattern of CaCl_2 -doped sample ($2\text{LiNH}_2 + \text{MgH}_2$) ball-milled under 1 bar argon after rehydrogenation at 200°C for 24 hours at 100 bar H_2 of sample in Figure 4-29 with Rietveld fits showing the difference (grey), calculated (red) and observed (blue) traces with the peak positions indicated for Li_2NH (blue), MgO (black), Li_2O (green), $\alpha\text{-Li}_2\text{Mg}(\text{NH})_2$ (pink), $\beta\text{-Li}_2\text{Mg}(\text{NH})_2$ (purple), CaNH (light green), $\text{Mg}(\text{NH}_2)_2$ (brown) and Pawley fits with peak positions indicated for unknown F222 phase (blue).

The powder XRD pattern in Figure 4-33 showed that hydrogenation of the CaBr_2 -doped sample was more successful than the CaCl_2 -doped sample. LiNH_2 , MgH_2 and $\text{Mg}(\text{NH}_2)_2$ were observed in this sample and, in contrast to the CaCl_2 -doped sample, $\beta\text{-Li}_2\text{Mg}(\text{NH})_2$ instead of $\alpha\text{-Li}_2\text{Mg}(\text{NH})_2$ was observed. After desorption from both halide-doped samples the proportion of $\alpha\text{-Li}_2\text{Mg}(\text{NH})_2$ was very similar. After attempted hydrogenation of the CaBr_2 -doped sample, $\alpha\text{-Li}_2\text{Mg}(\text{NH})_2$ was no longer observed. This could suggest that the β -phase of $\text{Li}_2\text{Mg}(\text{NH})_2$ has a higher hydrogen content, so conversion was achieved under hydrogenation conditions, or, the formation of $\text{Li}_7(\text{NH}_2)_6\text{Br}$ under flowing argon conditions subsequently seeded formation of $\beta\text{-Li}_2\text{Mg}(\text{NH})_2$, overcoming the kinetic barrier to this phase. Analysis of the system thermodynamics,

considering the formation of $\beta\text{-Li}_2\text{Mg}(\text{NH})_2$, could have suggested that the hydrogenation conditions chosen may not have been optimised i.e. the temperature was too high.

The amide bromide identified after desorption was also observed after hydrogenation although the peak positions and intensities were slightly different to those seen in Figure 4-30. Unfortunately, as the structure of this phase has not been solved, a Pawley fit was used, which allows for quite a lot of variation within the fit. The cell volume of $\text{Li}_7(\text{NH}_2)_6\text{Br}$ varied quite a lot across Figure 4-30 and Figure 4-33 but unexpectedly the largest cell volume was observed before hydrogenation. The diffraction patterns recorded by Davies¹³⁹ and Anderson *et al.*⁴⁷ were more similar to those observed after attempted hydrogenation (Figure 4-33). The cell volume of the identified phase in this case was around 2% lower than the published figure⁴⁷, likely indicating a slight non-stoichiometry between the lithium and bromide ions.

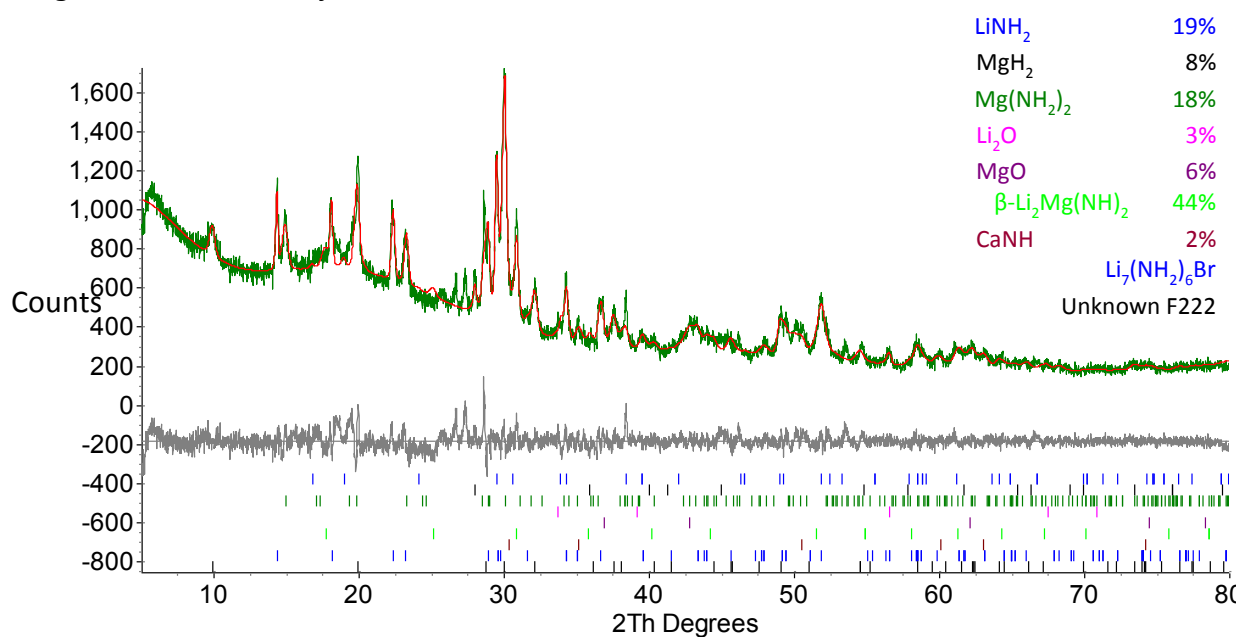


Figure 4-33: Powder XRD pattern of CaBr_2 -doped sample ($2\text{LiNH}_2 + \text{MgH}_2$) ball-milled under 100 bar hydrogen after rehydrogenation at 200°C for 24 hours at 100 bar H_2 of sample in Figure 4-29 with Rietveld fits showing the difference (grey), calculated (red) and observed (green) traces with the peak positions indicated for LiNH_2 (blue), MgH_2 (black), $\text{Mg}(\text{NH}_2)_2$ (green), Li_2O (pink), MgO (purple), $\beta\text{-Li}_2\text{Mg}(\text{NH})_2$ (light green), CaNH (brown) and Pawley fits with peak positions indicated for $\text{Li}_7(\text{NH}_2)_6\text{Br}$ (blue) and unknown F222 phase (black).

Analysis of the Raman spectra recorded after hydrogenation of the two doped samples (Figure 4-34) showed that the phases suggested from the peaks observed were in reasonable

agreement with those identified by powder XRD. The peaks from both doped samples did indicate that amide component of the phase was $\text{Mg}(\text{NH}_2)_2$ rather than LiNH_2 . However, the signal-to-noise ratio in this samples was quite low, so this was likely to be obscuring some fine detail in the spectra. It's possible that crystalline $\text{Mg}(\text{NH}_2)_2$ was not present, which is why it was not observed in the powder XRD patterns. The peaks observed for both samples in the imide region were in good agreement with the phases of α - and β - $\text{Li}_2\text{Mg}(\text{NH})_2$ observed in powder XRD. No clear peaks were observed in Figure 4-34 for the CaBr_2 -doped sample that would indicate the presence of $\text{Li}_7(\text{NH}_2)_6\text{Br}$.

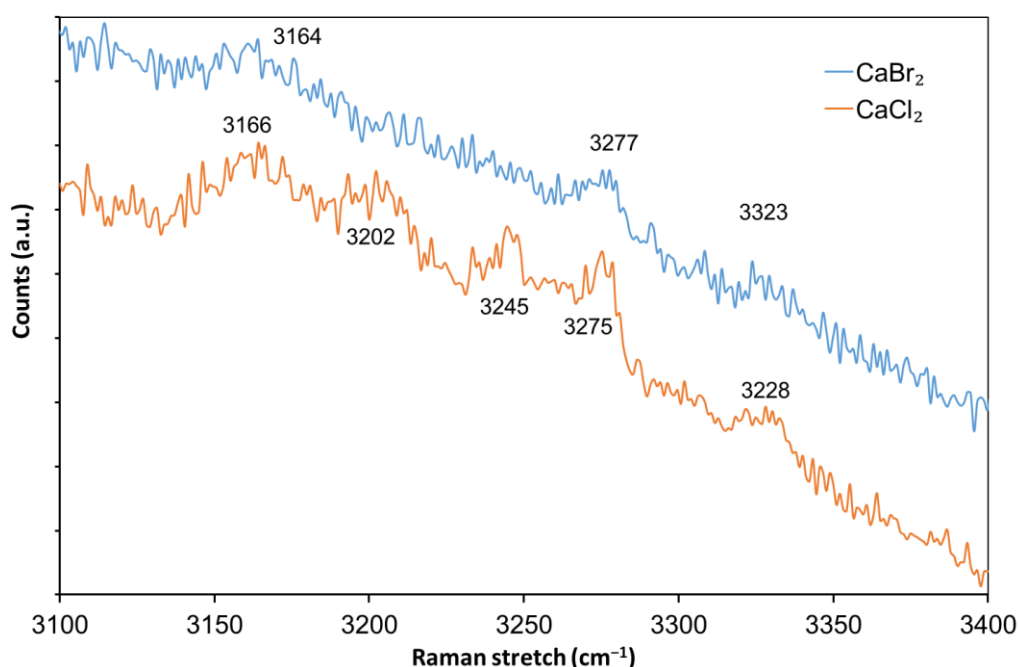


Figure 4-34: Typical Raman spectra of CaCl_2 - and CaBr_2 -doped ($2\text{LiNH}_2 + \text{MgH}_2$) ball-milled samples after rehydrogenation at 200°C under 100 bar H_2 for 24 hours.

The peak observed at 3245 cm^{-1} could have two origins. The peak was seen by Liang *et al.*⁷³ after heating the same Li-Mg-N-H system up to 400°C . It was thought to have resulted from the partial decomposition of $\text{Li}_2\text{Mg}(\text{NH})_2$. The peak was also seen by Gamba *et al.*¹⁶⁹ (along with a peak at 3303 cm^{-1}) and was assigned to a cubic phase of $\text{Li}_4(\text{NH}_2)_3\text{Cl}$, although an amide chloride phase was not seen in powder XRD data. Powder XRD and Raman data presented in this section would suggest that the ability of the doped samples to undergo hydrogenation was not as

Figufigood as the undoped samples. Rehydrogenation of the CaBr_2 -doped sample was more successful than of the CaCl_2 -doped sample.

4.6 Raman spectroscopy

As discussed in Section 3.4.5 the Raman spectra recorded often provide a different outlook of the sample in question. Several spectra have been provided and discussed in support of specific areas in the course of this chapter. The Raman stretches of several different phases are compared in Table 4-16.

Phase	Raman stretch (cm^{-1})
$\text{Ca}(\text{NH}_2)_2$ ¹⁷⁰	3228, 3290
$\text{Mg}(\text{NH}_2)_2$ ¹⁷¹	3273, 3328
LiNH_2 ¹³⁸	3260, 3315
CaNH ¹⁷²	3178
MgNH ¹⁴⁸	3198, 3251
Li_2NH ⁴⁵	3160
$\text{MgCa}(\text{NH})_2$ ¹⁷²	3151
$\text{Li}_2\text{Ca}(\text{NH})_2$ ¹⁷³	3143
$\alpha\text{-Li}_2\text{Mg}(\text{NH})_2$ ¹⁷⁴	3182, 3161
$\beta\text{-Li}_2\text{Mg}(\text{NH})_2$ ¹⁵⁰	3174
$\text{Li}_2\text{Mg}_2(\text{NH})_3$ ¹⁵⁰	3198, 3165

Table 4-16: List of Raman/FTIR stretches from several amide and imide phases that might be expected to be identified in this work.

It can be seen that many of the Raman stretches corresponding to key phases involved in this work are very close together, especially when the calcium containing phases are also considered. This increases the possibility of phase mis-identification if Raman spectroscopy was used exclusively. A combination of powder XRD and Raman data was found to be more useful in

this work. It is thought that as the inclusion of halides into the structures weakens the N-H bond, so the Raman stretches of a phase which has accommodated a small amount of halide might be expected to be shifted to a slightly lower wavenumber. No evidence of $\text{Ca}(\text{NH}_2)_2$ could be found in Raman spectra of any of these doped samples, although it is possible the peaks were obscured by more prominent amides or imides.

4.7 Overall discussion

Powder XRD and Raman data suggested that major *in-situ* reactions were not observed after preparation of the CaCl_2 -doped sample ball-milled under 100 bar hydrogen, similar to the undoped system. A small amount of $\text{Ca}(\text{NH}_2)_2$ was observed in the powder XRD pattern. The peak hydrogen desorption temperature of the doped sample ball-milled under 100 bar hydrogen compared to the undoped sample was considerably reduced and the exothermic area observed in DSC which was attributed to the crystallisation of $\text{Mg}(\text{NH}_2)_2$ was not as dominant.

The intensity observed in the Raman spectra of the doped sample milled under 1 bar argon indicated that imide-type phases were present. As the peak was quite broad, from ~ 3130 – 3190 cm^{-1} , identification of the phase was difficult. Close examination of the fine detail in the Raman spectrum of this sample (Figure 4-6) also suggested that $\text{Ca}(\text{NH}_2)_2$ was present as well. No evidence of $\text{Mg}(\text{NH}_2)_2$ was found. These results show that the introduction of CaCl_2 allowed partial desorption, likely to $\text{Li}_2\text{Mg}(\text{NH})_2$, and a metathesis reaction to occur in which $\text{Ca}(\text{NH}_2)_2$ rather than $\text{Mg}(\text{NH}_2)_2$ was produced.

In both samples, the addition of CaCl_2 has disrupted the formation of $\text{Mg}(\text{NH}_2)_2$, either during ball-milling or under heating at low temperatures. This suggests the dopant has provided an alternative reaction pathway (such as in Equations 4-2 and 4-4), that has a lower energy requirement than the metathesis reaction of $\text{LiNH}_2/\text{MgH}_2$ to form $\text{Mg}(\text{NH}_2)_2/\text{LiH}$ which occurred preferentially before desorption in the undoped samples. If the metathesis reaction was no longer

observed, this could help to explain the considerable drop in desorption temperature. $\text{Mg}(\text{NH}_2)_2$ was not observed after heating the doped sample milled under 100 bar hydrogen at low temperatures (Figure 4-26) whereas evidence of this phase was seen (Figure 3-18) after heating the undoped sample milled under 100 bar hydrogen at comparable temperatures.

Initial data recorded by TPD-MS suggested that reductions in the peak hydrogen desorption temperature could be made through the addition of calcium halide dopants. The addition of both dopants in low quantities (0.1 mole fraction) to ball-milled samples reduced peak hydrogen desorption temperatures. They also changed the profile of mass loss recorded. The mass loss 'plateau' of the undoped sample (seen in Figure 4-7), where it was thought the sample remained mainly as imide (Table 3-6), was observed at a higher temperature and the mass of the sample was stable over a larger range of temperatures. The masses of the doped samples reached a plateau at lower temperatures, but a second desorption step began to occur once temperatures reached 275°C , whereas the control did not begin further significant desorption until after reacting at 375°C .

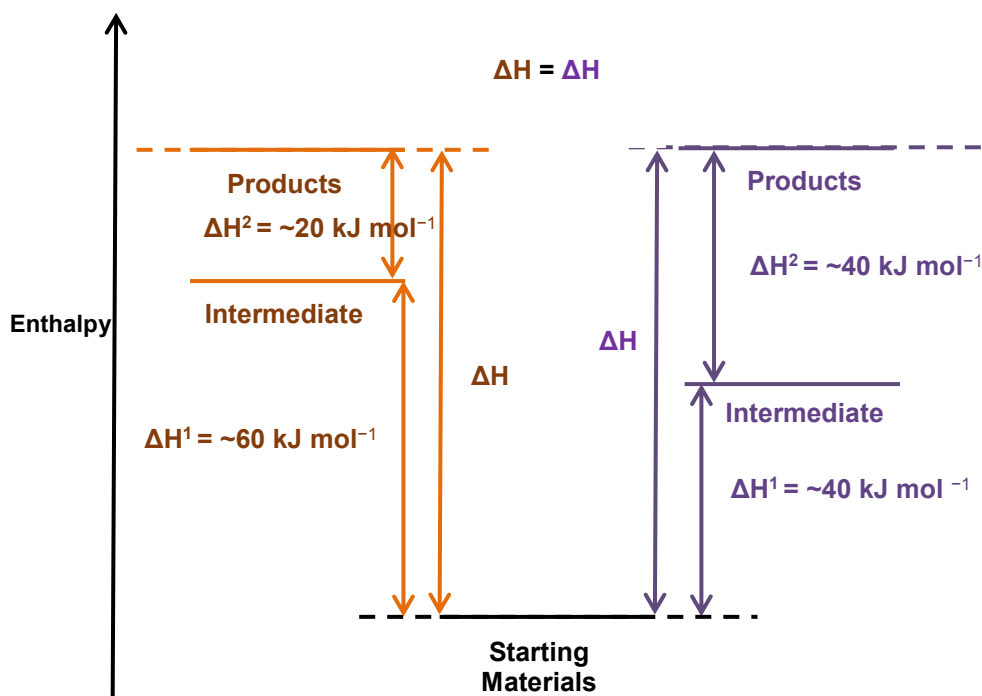


Figure 4-35: Illustration of how the thermodynamics can be changed by the formation of alternative intermediates.

The variation in desorption temperatures between doped and undoped samples, especially in the samples milled under 100 bar hydrogen, which would be thought to be more hydrogenated after ball-milling could be explained in part by the schematic in Figure 3-27. If lithium amide or imide halides are produced as intermediate phases, (or seed the formation of $\text{Li}_2\text{Mg}(\text{NH})_2$) then they could lower the energy required to form the final products (in this case $\text{Li}_2\text{Mg}(\text{NH})_2$). For example, if the sample is heated at a temperature that is high enough to allow a reaction whose enthalpy is 40 kJ mol^{-1} , then the products on the right-hand side in Figure 3-27 will be reached, but the products on the left-hand side will not be formed at the same temperature. To overcome the higher enthalpy, a higher temperature will be required, resulting in a higher desorption temperature. Clearly, the activation energies of these phases, as well as the temperatures at which they can be formed need to be considered, but this simplistic approach demonstrates that although the energy of the product is not different, the reaction pathway can be tailored to change the thermodynamic limitations of the system to reduce the temperature at which the whole reaction can proceed.

Although the introduction of halides into this system may be able to reduce the enthalpy of the reaction within the system, recent work⁹³ on the inclusion of LiCl into the Li-Mg-N-H system, albeit in stoichiometric amounts, revealed that competing reactions for LiNH_2 can lead to a situation where preferential reaction paths upon cycling were established.

In this case, the formation of unfavourable side products produced an increase in the activation energy after cycling⁹³. Even though the initial effects on the storage properties were only slight by introducing 0.1 mole fraction of dopant, if an unreactive phase was formed, low dopant amounts should minimise the impact on system capacity and performance. When doped samples were analysed by powder XRD after crude cycling attempts, evidence of a previously identified amide halide phase was found, but only in the CaBr_2 -doped sample. A variation of this

phase was seen after desorption and attempted rehydrogenation, which could suggest that this phase could be unreactive once formed.

When the rates of hydrogen release from both the control and doped ball-milled samples, (1 bar argon and 100 bar hydrogen) were considered, an interesting phenomenon was observed. The rate of desorption from the 0.1 mole fraction CaBr_2 -doped sample milled under 100 bar hydrogen was more rapid than the other samples milled under 100 bar hydrogen, whereas the desorption rate observed from the 0.1 mole fraction CaBr_2 -doped sample milled under 1 bar argon was significantly slower than other similarly prepared samples. This implied that the doped samples behaved differently after preparation under different milling conditions.

TGA-MS and DSC data were used to calculate quantitative values for kinetic (activation energy) and thermodynamic (enthalpy of hydrogen desorption) parameters. The estimated activation energies of the undoped samples varied according to preparation, the reasons for which were previously discussed in Section 3.4.2 and 3.5. It should be noted that even though the desorption temperatures of the first peak from the undoped sample ball-milled under 100 bar hydrogen were much higher those milled under 1 bar argon; the activation energies were very similar. This shows the method is robust and activation energy calculated is independent of the peak desorption temperature. This would indicate that desorption from the undoped sample ball-milled under 100 bar hydrogen is governed by thermodynamics or slow reaction rate (kinetics) because the activation energy is comparable to other samples, so cannot be responsible for the higher desorption temperature. Around a 10% relative reduction in effective E_a for samples doped with 0.1 mole fraction CaCl_2 compared to their respective controls, was achieved regardless of preparation and starting materials.

DSC data were used for estimating the hydrogen desorption enthalpy, and although the calculated values were below the figures previously observed for this system (which were discussed in Section 4.4), they provide a useful comparison across various samples in this work.

Unfortunately, as a clear endothermic area was not observed, an enthalpy value was not calculated for the sample ball-milled under 100 bar hydrogen. The lowest enthalpy of hydrogen desorption was observed from the sample ball-milled under 1 bar argon, which would suggest that the addition of these dopants in small amounts had not reduced the overall enthalpy of hydrogen desorption.

Interestingly, the estimated enthalpy changes of the 0.1 mole fraction CaCl_2 -doped samples were all very similar as were the desorption temperatures. As the activation energies were found to vary, this could indicate that the desorption temperatures observed from the doped samples were dominated by the thermodynamic parameters, resulting in little variation. Similar values for all the CaCl_2 -doped samples indicated that desorption from these samples was more consistent than from the undoped samples and preparation of these samples was not as important. Although a correction was made to attempt to account for mass loss by ammonia, it was difficult to quantify how accurate these values were.

The calculated enthalpy values followed the opposite trend to activation energies. The undoped sample based on $\text{Mg}(\text{NH}_2)_2$ had been found to have the highest enthalpy requirement of all samples calculated, but its peak desorption temperature was the same as the sample starting from LiNH_2 . This would suggest that the desorption temperature of the $\text{Mg}(\text{NH}_2)_2$ -based sample was strongly influenced by the reduction in activation energy.

Ultimately, the cyclic function of a material is one of the most important properties to understand and one of the most difficult and time-consuming to measure. The working nature of the sample is considerably complicated on the addition of further compounds which are included to 'dope' or 'catalyse' the sample. Determining whether the addition of such compounds, on the face of it, improves the apparent desorption properties but actually produces effects, such as inactive or preferentially active phases that would rapidly deteriorate under cycling conditions is

important. Hydrogenation of the doped samples did not appear to be as successful as that of the undoped samples.

An amide chloride phase was not observed in the powder XRD patterns of the cycled samples, but Raman data recorded could indicate the presence of cubic-Li₄(NH₂)₃Cl. Lithium amide bromide was likely detected by powder XRD. Although lithium amide bromide has been shown to be reversible¹³⁹, as it was observed after desorption and remained after hydrogenation, the hydrogen storage capacity of this phase has not been assessed during these experiments. It's likely a higher desorption temperature would have been required.

Although cycling work was undertaken in this study, an interrupted method was used; transference of a sample from flowing argon or vacuum line to hydrogenation vessel with the chance of atmospheric exposure is not truly representative of the 'ideal' cycling conditions a sample would experience. This was evidenced by the relatively high level of oxidation observed by powder XRD in many samples, which could have compromised the samples, even with best practice procedures employed.

The addition of an additional cation and anion into this system, especially in small amounts, has added further complexity to an already complicated system. The structural similarities, particularly in cubic phases, the ability to accommodate a range a hydrogenated states and various cations/anions mean careful examination of peak intensities and very slight variations in lattice parameters could indicate that the phase identified is not the exact stoichiometric phase presumed. Work by Makepeace *et al.*¹⁷⁵ indicated that due to the structural similarities of Ca(NH₂)₂ and CaNH, like LiNH₂ and Li₂NH, the calcium system was likely to be able to accommodate a degree of non-stoichiometry within both amide and imide phases.

The calculated sizes of the cations Li⁺, Mg²⁺ and Ca²⁺ are 0.73, 0.71 and 1.01 Å respectively¹⁵⁴. The closeness of the ionic radii of Li⁺ and Mg²⁺ shows why they are easily

interchangeable within the imide system. This work has looked at the addition of 0.1 mole fraction CaX_2 . Although the Ca^{2+} cation is $\sim 30\%$ larger than the $\text{Li}^+/\text{Mg}^{2+}$ cations, only $\sim 5\%$ of the cations in the doped systems are Ca^{2+} . Even if all the Ca^{2+} cations available were substituted into a single phase containing $\text{Li}^+/\text{Mg}^{2+}$ cations, the change in cell volume would be very small.

The calculated anion sizes of Cl^- and Br^- are 1.67 and 1.82 Å respectively¹⁵⁴. In amide halides of the same structure, $\text{Li}_7(\text{NH}_2)_6\text{Cl}$ ¹⁶³ and $\text{Li}_7(\text{NH}_2)_6\text{Br}$ ⁴⁷, where the only difference was the halide anion, a 2% increase in cell volume was observed. The Cl^- anion is also smaller than the NH_2^- anion⁴⁷. The combination of varying cations and anions means that without high quality data the determination of the exact composition of phases in this system by powder XRD can be extremely difficult. There were several powder XRD patterns recorded during this work where the outline peak positions showed similarities to known amide/imide halide phases, but the intensities and exact positions could not be fitted with available structural data.

4.8 Conclusions

The initial investigations into the addition of calcium dopants into the Li–N–H and Li–Mg–N–H systems showed that they successfully reduced the peak temperature of hydrogen desorption. The lowest hydrogen desorption temperatures were observed upon the addition of CaBr_2 . Increasing the amount of dopant reduced the peak desorption temperature in the initial work, but as these comparisons were carried out on hand-ground samples and ball-milling should improve the dispersion, it was decided to maintain a low level of dopant to maximise the gravimetric content of hydrogen in the samples.

The lowest hydrogen desorption temperatures after ball-milling were observed from CaCl_2 -doped samples, although the performance of the CaBr_2 -doped samples in this respect was similar. Unlike the undoped samples, where ball-milling under 100 bar hydrogen increased the peak desorption temperature, the conditions of milling or the chosen starting materials (LiNH_2 or

Mg(NH₂)₂) did not significantly alter the peak temperatures observed of hydrogen desorption. When samples were ball-milled under atmospheric argon pressure, the improvement made through the addition of 0.1 mole fraction of CaCl₂ was similar regardless of the starting materials.

The fastest rate of desorption was observed from a sample doped with 0.1 mole fraction of CaCl₂ ball-milled under 1 bar argon. For both ball-milled systems, the behaviour of the undoped and CaCl₂-doped samples was similar and the CaBr₂-doped samples did not appear to follow the same trend. Although the addition of 0.1 mole fraction CaCl₂ to the Mg(NH₂)₂-based system did not improve the initial rate of hydrogen release, the rate of the second, larger desorption stage was increased.

The activation energy of all the calcium halide containing samples was reduced relative to the respective controls. The largest reduction in activation energy was observed when 0.15 mole fraction CaBr₂ was added to the sample. Although the activation energies from the samples ball-milled under 100 bar hydrogen were lower, the relative decrease compared to the control was very similar for both 0.1 mole fraction CaCl₂- and CaBr₂-doped samples. Increasing the content of the halide dopant from 0.1 mole fraction to 0.15 resulted in a further decrease in activation energy for both CaCl₂- and CaBr₂-doped samples. The lowest activation energy was observed from a 0.1 mole fraction CaCl₂-doped sample whose initial reagents were Mg(NH₂)₂ and 2LiH.

It was previously seen that the DSC trace recorded from the sample ball-milled under 100 bar hydrogen was quite different from the other samples and unfortunately an enthalpy calculation could not be completed for this sample. Compared to the expected values for desorption enthalpy from this system, the values were low, but possible causes for this were previously discussed in detail. There was little variation in the calculated enthalpies of hydrogen desorption across the 0.1 mole fraction CaCl₂-doped samples, where an enthalpy of around 25 kJ mol⁻¹ H₂ was achieved. The lowest desorption enthalpy was actually observed from the undoped

sample ball-milled under 1 bar argon. From the data recorded, the addition of CaCl_2 did not make an improvement to the thermodynamic properties of this system.

Assessment of the powder XRD patterns showed that the total amount of $\text{Li}_2\text{Mg}(\text{NH})_2$ formed across the temperature range of these reactions was reasonably consistent and largely independent of preparation. Unfortunately, the broadness of the peaks in samples reacted at 150°C for 12 hours meant quantitative analysis was not accurate, however, the amount of $\text{Li}_2\text{Mg}(\text{NH})_2$ observed after reactions at 200°C would suggest that the imide was likely to have been formed at lower temperatures. The CaCl_2 -doped sample milled under 1 bar argon displayed the same transition from $\beta\text{-Li}_2\text{Mg}(\text{NH})_2$ to $\alpha\text{-Li}_2\text{Mg}(\text{NH})_2$ and back to $\beta\text{-Li}_2\text{Mg}(\text{NH})_2$ at similar temperatures as observed in the undoped sample milled under 1 bar argon. Formation of $\beta\text{-Li}_2\text{Mg}(\text{NH})_2$ was favoured from the CaCl_2 -doped sample milled under 1 bar argon in the low temperature range (less than 250°C) where the doped sample milled under 100 bar hydrogen favoured $\alpha\text{-Li}_2\text{Mg}(\text{NH})_2$ in this temperature range. This phenomenon was thought to be preparation rather than dopant controlled.

Nitride phases were not identified by powder XRD in the samples ball-milled under 1 bar argon, but were observed after reaction at temperatures above 300°C in the samples ball-milled under 100 bar hydrogen. The absence of nitride phases implies that samples only dehydrogenated to imide and that where the mass loss recorded during the desorption experiments was larger than the amide to imide step, a mixture of hydrogen and ammonia was released. Additional peaks were observed in several of the patterns after reactions above 250°C . These peaks could not be assigned to a known phase, but were indexed to a F222 unit cell (space group no. 22) which appeared to have some overlap with some of the CaNH peaks. It was possible that this may be a related 'supercell' of an calcium imide-type phase containing some chloride (bromide) ions.

The ability of the calcium halide-doped samples to rehydrogenate under the same conditions as the undoped samples was poor. Hydrogenation of the CaBr_2 -doped samples was more successful than the CaCl_2 -doped samples. From the summary of desorption data in Tables 4-4, 4-5 and 4-7, the most favourable sample for balancing the favourable desorption properties—low temperature, extent of reaction and overall rate of hydrogen release with gravimetric capacity—would be a sample doped with 0.1 mole fraction CaCl_2 ball-milled under 1 bar argon. Clearly the same sort of in-depth studies looking at the hydrogenation properties of these samples, such as varying reaction temperatures and applied hydrogen pressures, whilst monitoring the mass change are required to understand which sample would be the most favourable as an all-round hydrogen store.

4.9 Further work

Further work would be focussed on trying to understand how the calcium dopants interact with the samples, both from a structural and physical point of view. This could include mapping the dispersion of the calcium dopants in the samples, using a technique such as using EDX and looking at whether the dopants agglomerate during cycling. More structural work into both systems containing calcium dopants is required to understand the phases formed during desorption and hydrogenation in order to elucidate the mechanisms of hydrogen storage in these materials. Temperature and time resolved *in-situ* powder XRD and Raman experiments would be useful to ascertain when phases were formed and consumed as the duration and temperature of the experiment was varied.

Further work would involve the assessment of CaBr_2 -doped samples by DSC for comparison to the CaCl_2 -doped samples. As in Chapter 3, volumetric methods would be used in order to calculate the enthalpy and entropy values for hydrogen desorption. Perhaps most crucially, when considering the role of the dopants in this system, hydrogenation and cycling work on the doped systems would help to ascertain if a long term positive effect on this system could

be caused by the addition of these dopants or whether inactive phases were formed within the first few cycles which neutralised the effects of these materials on the storage properties of this system. Isothermal experiments on the various systems would also provide a better comparison of the variation in reaction rates than non-isothermal experiments.

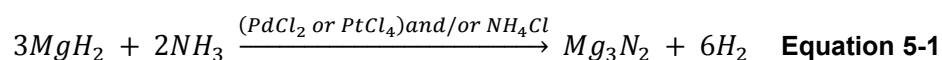
Work has already been carried out on systems containing some other halide phases at stoichiometric levels, such as LiCl^{37} , but further work investigating the effects of small amounts of lithium and magnesium halides should help to ascertain if cation and anion both affected the system or not. Further series of work could investigate changing the cation of the dopant compound to potassium or sodium through the inclusion of KCl , KBr , NaCl or NaBr into the Li-Mg-N-H system.

5 Reactions of Magnesium Hydride and Ammonium Chloride

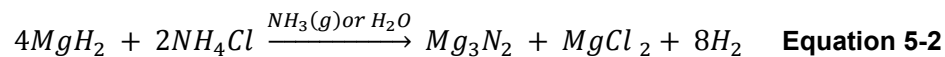
5.1 Introduction

Magnesium hydride possesses some good potential properties for hydrogen storage; it is a low cost material which has a high hydrogen gravimetric capacity (7.6 wt%)¹⁷⁶. However, slow kinetics and a reasonably high desorption temperature limit the use of pristine MgH₂ as a real contender for hydrogen storage¹⁷⁷. Research into improvement of this medium has considered conventional catalysts such as palladium¹¹⁶ and alloying with transition metals such as vanadium, manganese¹²² and nickel¹⁷⁸ to increase the activity of the compound with respect to hydrogen desorption and uptake. Unorthodox methods include the addition of graphite¹⁷⁹ and metal oxide nanoparticles¹¹⁵.

Most commonly, magnesium hydride is now used as a component in more complex systems such as the LiNH₂-MgH₂ system⁴⁰. By the addition of an alternative cation, due to the differences in electronegativity, the bonding of the hydrogen atom can be weakened and the accessibility of hydrogen improved in a complex system⁴⁸. In this work, we are considering a new system which looks at combining MgH₂ with ammonium chloride NH₄Cl. The hydrogen-releasing reaction between MgH₂ and NH₃ is a fundamental step in the Li-Mg-N-H system which has been discussed in chapters 3 and 4. Studies into the reaction of ammonia gas and MgH₂ have shown hydrogen production can be achieved. Li *et al.*¹⁸⁰ investigated traditional catalysts such as PdCl₂ and PtCl₂ to dope MgH₂ (Equation 5-1) in combination with the use of NH₄Cl as a promoter in that reaction¹⁸⁰.



Although the above reaction was successful with NH_4Cl as a promoter, a side reaction is also possible, as shown in eqn. 6-2, and could provide 7.54 wt% H_2 .



Li *et al.*¹⁸⁰ found that Equation 5-2 was dependent on the presence of water or gaseous ammonia to react with NH_4Cl to produce HCl to react with MgH_2 . The role of NH_4Cl in the reaction was uncertain. Some of the methods used to carry out these experiments were based on wet chemistry, which is quite different to approaches normally used in solid-state complex hydride chemistry. Data collection used to prove this hypothesis was limited to gas chromatography on the reaction headspace and no component analysis (X-ray diffraction) was used to determine the reaction products. Techniques such as ball milling, heating under an inert atmosphere (mainly argon) and temperature-programmed desorption coupled with mass spectrometry to analyse exhaust products are normally used in solid-state chemistry. In this work, experiments based on solid-state techniques under inert conditions will be carried out on the reactions of MgH_2 and NH_4Cl .

5.2 Experimental

Ammonium chloride and magnesium hydride (Alfa-Aesar, 98%) were hand ground together in the desired molar ratios of in an argon-filled glove box (<10ppm O_2 , 1 ppm H_2O). The samples were then heated under flowing argon or ammonia to temperatures between 150°C and 350°C for up to 72 hours (preparation according to chapter 2.1.1). Ex-situ powder X-ray diffraction data were recorded using a Siemens D5005 instrument in capillary mode with a wavelength of 1.5406 Å (chapter 2.7.6). Powder synchrotron X-ray diffraction data were collected at Diamond Light Source, UK on I11 beamline. Samples were measured using a wavelength of 0.826205 Å. Ground samples were prepared and sealed into 0.5 mm borosilicate capillaries in an

argon filled glovebox using resin and rotated in the X-ray beam during measurement at ambient temperatures.

Raman spectra were collected on a Renishaw inVia Raman microscope operating with a 633 nm laser using a cell sealed under an argon atmosphere. TPD-MS samples were heated at a ramp rate of $2^{\circ}\text{C min}^{-1}$ to 400°C and held for an hour before uncontrolled cooling back to room temperature. TGA-MS samples were heated at a ramp rate of $2^{\circ}\text{C min}^{-1}$ to 400°C and cooled to room temperature. Samples selected for rehydrogenation were reground, sealed in an airtight steel reactor and pressurised to 100 bar H_2 before being heated at a ramp rate of $2^{\circ}\text{C min}^{-1}$ to 200°C and held for 24 hours. DSC samples were heated at a ramp rate of $2^{\circ}\text{C min}^{-1}$ to 400°C and subsequently cooled to 25°C under 3 bar argon.

5.3 Reactions of NH_4Cl with MgH_2

5.3.1 Powder X-ray diffraction

There is no previously published work concerning the reactions of ammonium chloride with magnesium hydride in the solid-state under an inert atmosphere. Initial investigations considered the potential formation of new phases. It has been shown previously in the synthesis of $\text{Li}_4(\text{NH}_2)_3\text{Cl}$ that lithium amide and lithium chloride powders can be combined to form new solid-state compounds at temperatures below some of their constituent melting points, (i.e. lithium chloride melts at 605°C) but $\text{Li}_4(\text{NH}_2)_3\text{Cl}$ is formed at temperatures around 400°C ^{47, 164}. Therefore, although the melting points of NH_4Cl and MgH_2 are 338°C and 327°C respectively, initial reactions were investigated from temperatures around 200°C .

5.3.1.1 *Ex Situ* under flowing argon

Investigations into the reactions between ammonium chloride and magnesium hydride at the fixed stoichiometric value of 1: 1 were first carried out across a range of temperatures and times. These reactions were carried out on a flowing argon line and all powder XRD data were recorded at room temperature after cooling. No reaction between the two compounds was observed below 175°C after any heating duration. When heated at 175°C for 12 hours the starting materials remained in the approximate weight percentages expected from a starting ratio of 1:1.

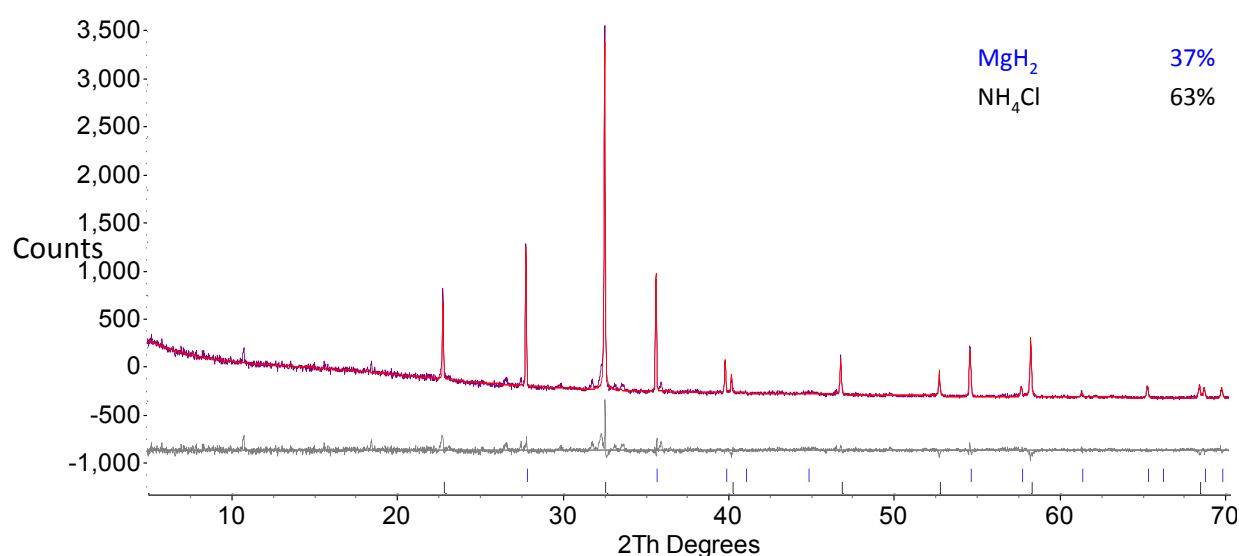


Figure 5-1: Powder XRD pattern of NH₄Cl + MgH₂ sample after heating at 175°C for 12 hours, with Rietveld fit showing the difference (grey), calculated (red) and observed (purple) traces with the peak positions indicated for MgH₂ (blue) and NH₄Cl (black).

The appearance of a few small peaks, most noticeable at ~11° and 18° (starred) in Figure 5-3 indicated the formation of a small amount of an additional phase. In order to isolate this unknown phase and remove the remaining starting materials, the heating temperature was increased. As can be seen from Figure 5-3 as the temperature was increased, the relative intensity of the unknown phase increased, the overall intensities of the starting materials decreased. This phase was observed in powder XRD data recorded after heating for 12 hours at temperatures up to 215°C before the peak intensities began to drop; the reduction in intensity of these peaks could also be achieved by heating for a longer duration at temperatures below 215°C or higher temperatures.

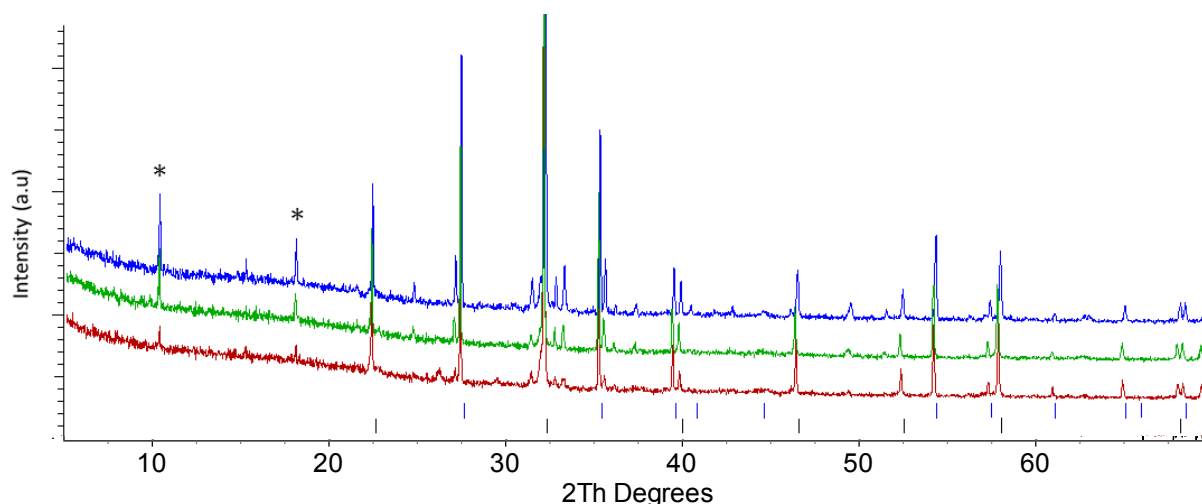


Figure 5-2: Stacked PXRd powder XRD traces of $\text{NH}_4\text{Cl} + \text{MgH}_2$ samples heated for 12 hours at 175°C (red), 185°C (green) and 195°C (blue) with the appearance of new small peaks indicated (starred) with peak positions indicated for MgH_2 (blue) and NH_4Cl (black).

The set of peaks identified here (in Figure 5-1 and Figure 5-2) are later discussed in Section 5.11. The unassigned peaks identified in the lower temperature reactions were strongly observed in the pattern recorded after heating to 215°C, but numerous additional peaks also appeared as well as the starting materials (Figure 5-2). These peaks were identified as a side product, $\text{Mg}(\text{NH}_3)_2\text{Cl}_2$ (space group *Cmmm*), but difficulty with severely overlapping peaks in the region of 31–34° still left some peaks unassigned. A possible route for the formation of $\text{Mg}(\text{NH}_3)_2\text{Cl}_2$ from the starting materials has been suggested in Equation 5-3.

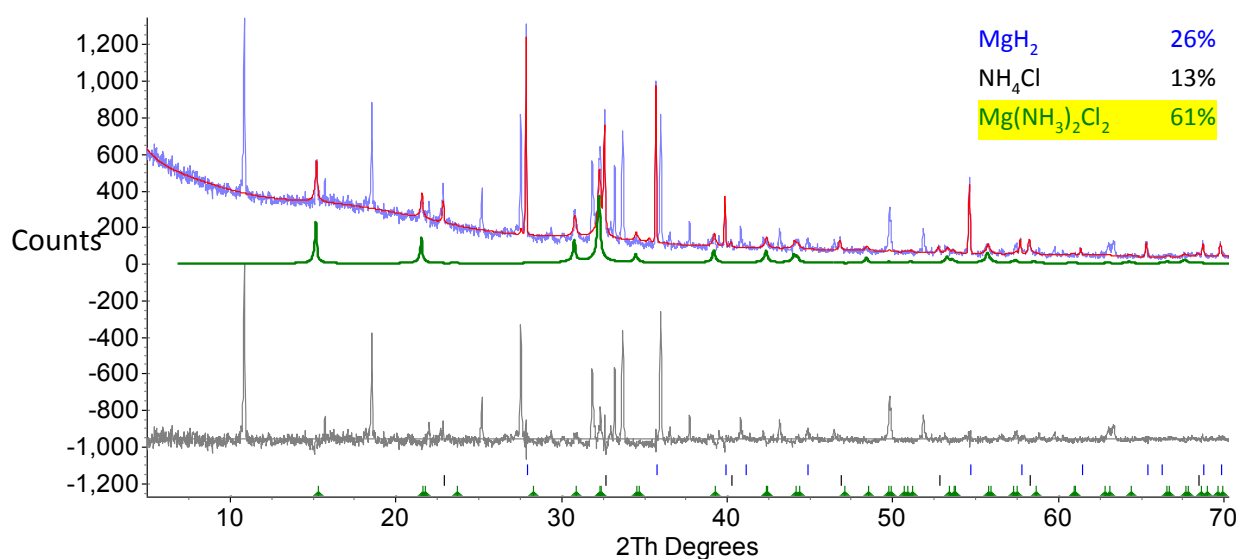
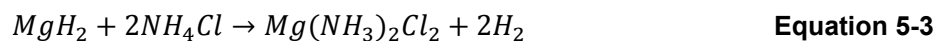


Figure 5-3: Powder XRD pattern of $\text{NH}_4\text{Cl} + \text{MgH}_2$ sample heated at 215°C for 12 hours, with Rietveld fit showing the difference (grey), calculated (red) and observed (blue) traces with the peak positions indicated for MgH_2 (blue), NH_4Cl (black) and $\text{Mg}(\text{NH}_3)_2\text{Cl}_2$ (green highlighted trace).

However, the reaction shown in Equation 5-3 was unlikely to be the only one proceeding as when the remaining mol% of the compounds were considered, rather than the wt% displayed, more MgH₂ remained than NH₄Cl. If Equation 5-3 was taken into account this would be expected.

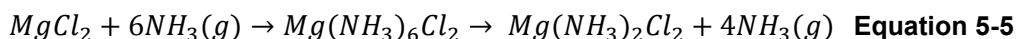
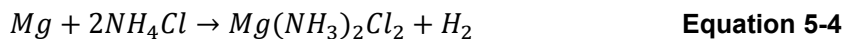


The formation reactions will be considered in more detail after further experiments have been reported. The lattice parameters of Mg(NH₃)₂Cl₂ were calculated from laboratory powder XRD data and compared to literature values found by Leineweber *et al.*¹⁸¹. Mg(NH₃)₂Cl₂ identified had slightly elongated *a* parameters and shorter *b* parameters compared to literature values. It was reported¹⁸¹ that the production of magnesium di-ammoniate chloride could be achieved using two methods: by reacting Mg powder and ammonium chloride, heated at 350°C for 1–2 weeks in a sealed autoclave (Eqn. 6-4), or via a decomposition route through Mg(NH₃)₆Cl₂ starting from MgCl₂ and gaseous ammonia at temperatures around 200°C (Eqn. 5-5).

Reaction route <i>(Literature values)</i>	a Lattice parameter (Å)	b Lattice parameter (Å)	c Lattice parameter (Å)
Heating 1: 1 mixture of NH ₄ Cl and MgH ₂ at 205°C for 12 hours	8.167(6)	8.193(3)	3.755(2)
Heating 1: 1 mixture of NH ₄ Cl and MgH ₂ at 215°C for 12 hours	8.162(9)	8.195(6)	3.750(3)
<i>Mg powder and NH₄Cl</i> <i>(Leineweber et al.¹⁸¹, 1999)</i>	8.1810(2)	8.2067(2)	3.7550(1)

Table 5-1: Comparison of the lattice parameters from solid state experiments which have produced Mg(NH₃)₂Cl₂ to literature values from Leineweber et al.¹¹

All other routes to $\text{Mg}(\text{NH}_3)_2\text{Cl}_2$ (Equations 5-4 and 5-5) which has been used as a precursor for a synthesis of a similar compound, hexa-ammoniate chloride ($\text{Mg}(\text{NH}_3)_6\text{Cl}_2$) or produced after subsequent ammonia desorption from $\text{Mg}(\text{NH}_3)_6\text{Cl}_2$, were based on reacting Mg metal or MgCl_2 with gaseous ammonia^{109, 181-183}.



Literature values for the temperatures required for the conversion from the hexa-ammoniate to the di-ammoniate chloride to proceed are varied, ranging from around 120°C up to temperatures of 230°C^{109, 184, 185}. The temperature range at which the di-ammoniate chloride has been found and disappeared as determined by powder XRD in current experiments was in closest agreement with the findings of Christensen *et al.*¹⁸⁴ and Zhu *et al.*¹⁸⁵.

Raising the reaction temperature to 225°C further reduced the residual amounts of starting materials as shown in Figure 5-4. A small amount of MgO appeared after heating to 225°C, and NH_4Cl was no longer observed, approximately 100°C below its literature melting point. After reaction at 225°C, only a small amount of MgH_2 was still observed. Quantitative phase analysis

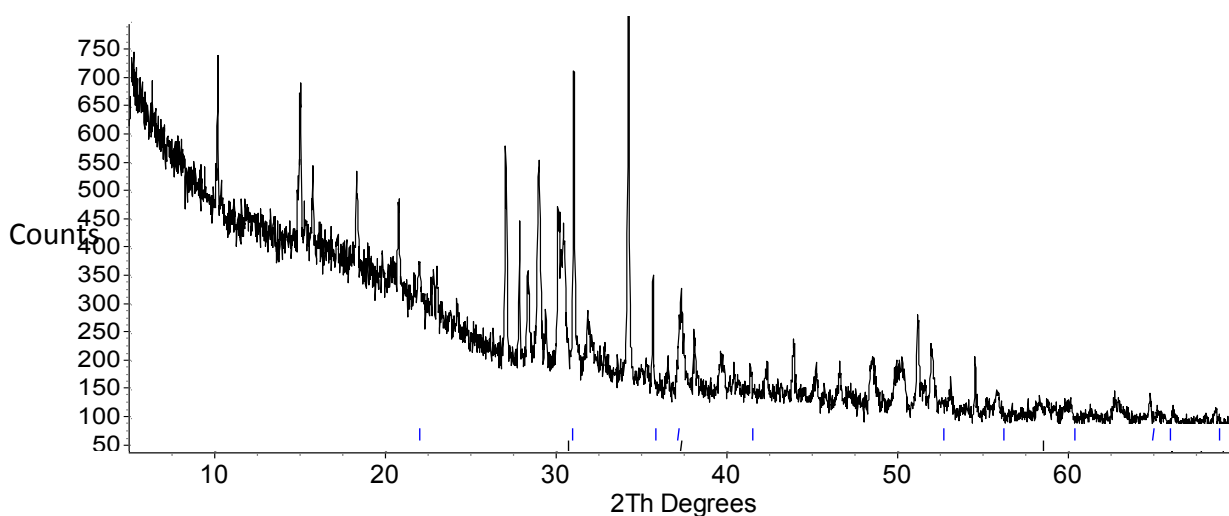


Figure 5-4: Powder XRD pattern of $\text{NH}_4\text{Cl} + \text{MgH}_2$ sample heated at 225°C for 12 hours showing the observed (black) trace with the peak positions indicated for MgH_2 (blue) and MgO (black).

using Topas was run on this pattern to try to assign known phases to this sample. It seemed possible that ammine complexes such as $\text{Mg}(\text{NH}_3)_6\text{Cl}_2$ and/or $\text{Mg}(\text{NH}_3)_2\text{Cl}_2$ might have formed, the latter having been identified previously in Figure 5-3 after reaction at 215°C , but characteristic peaks for either phase were not seen. Further visual comparisons and quantitative phase analysis using Topas were attempted to try and identify any other known phases without success. Possible phases that were considered include an alternative phase (space group $Pm-3m$) of NH_4Cl , MgO , MgCl_2 , $\text{N}_2\text{H}_5\text{Cl}$, MgNH , $\text{Mg}(\text{NH}_2)_2$ and Mg_3N_2 , although at temperatures as low as 200°C the latter would be extremely unlikely.

In a further attempt to identify phases that might be present, discrete reactions were carried out across a temperature range of 225°C to 350°C for 12 hours (Figure 5-5). Reactions for an extended heating duration of 72 hours were also carried out at 185, 200 and 215°C (Figure 5-6) to investigate whether the samples had reached their thermodynamic end point at the shorter reaction time of 12 hours. By increasing the reaction time, it was hoped that the starting material consumption would rise and possible slow reaction kinetics would be overcome. Visual comparison of the variations in the peak shapes, intensities and positioning of peaks in response to slight changes in reaction conditions suggested that the unfitted peaks in Figure 5-4 were not

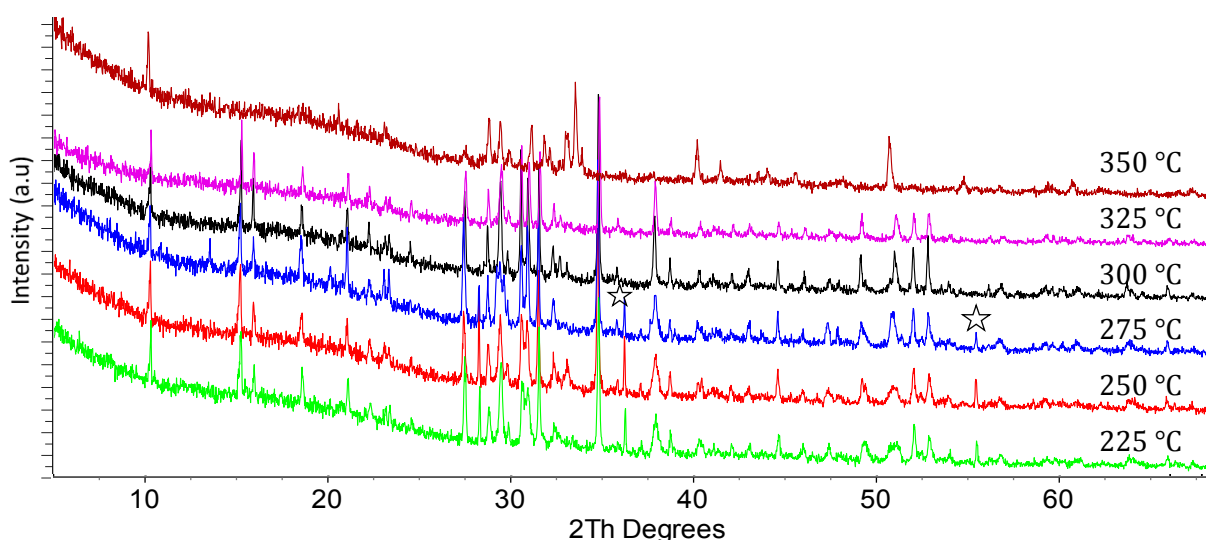


Figure 5-5: Stacked powder XRD plot of $\text{NH}_4\text{Cl} + \text{MgH}_2$ samples heated for 12 hours at 225°C (green) 250°C (red) and 275°C (blue), 300°C (black), 325°C (pink) and 350°C (burgundy).

all generated by a single phase. The stacked powder XRD pattern plot in Figure 5-5 shows how the resulting patterns varied after reaction for 12 hours at the stated temperatures.

The powder XRD patterns of the reactions carried out between 225°C and 325°C were all similar with slight variations in peak shapes and intensities. As the reaction temperature was increased from 275°C to 300°C, some new small peaks were observed and several peaks became sharper. Small amounts of MgH_2 remained in samples that had been heated at temperatures up to and including 275°C as indicated by the starred peaks. Once the reaction temperature was increased to 350°C, the nature of the sample changed significantly, likely indicating a significant decomposition or desorption event. The change in sample makeup that occurred around 350°C, was in a temperature range consistent with the formation of nitride phases and MgCl_2 ¹⁰⁹.

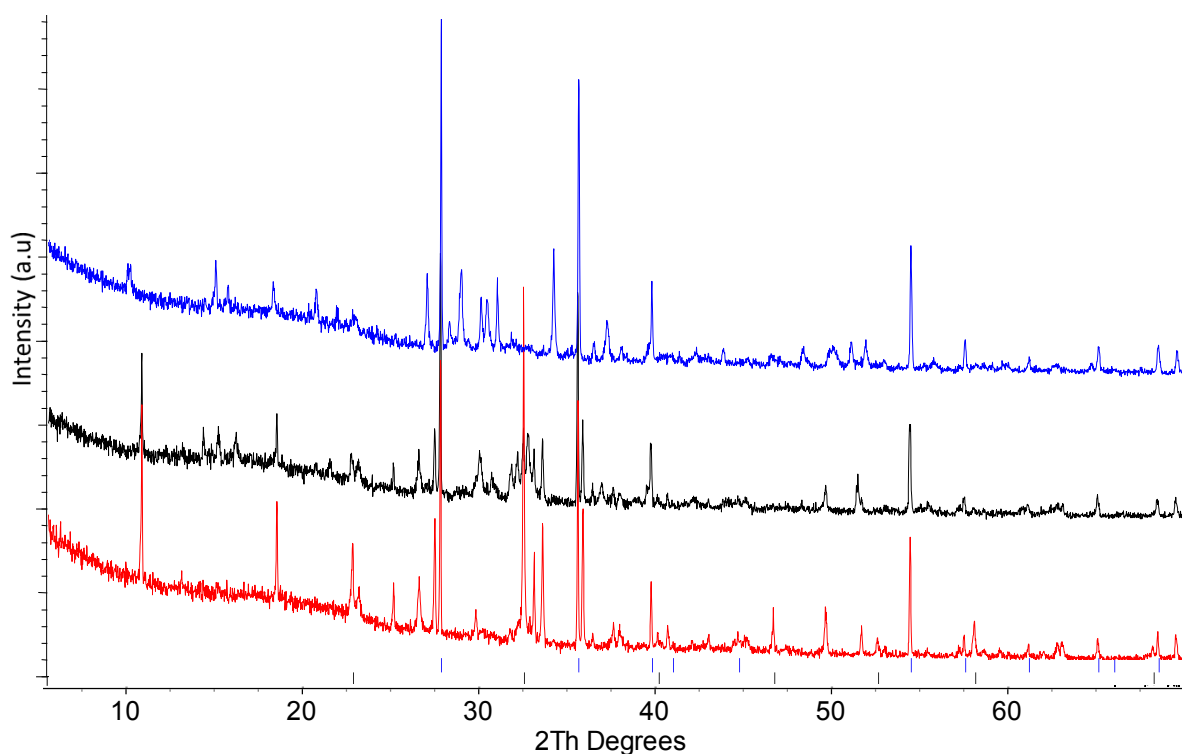


Figure 5-6: Stacked powder XRD plot of $\text{NH}_4\text{Cl} + \text{MgH}_2$ samples heated for 72 hours at 185°C (red), 200°C (black) and 215°C (blue) with the peak positions indicated for MgH_2 (blue) and MgO (black).

A comparison of powder XRD patterns after heating to 72 hours at 185°C, 200°C and 215°C is shown in Figure 5-6. All the patterns show differences from when the same reactions were previously carried out over 12 hours, most notably the experiment carried out at 215°C. The

unidentified peaks in Figure 5-3 and then fitted in Section 5.11 were no longer observed after extended the reaction duration to 72 hours at 215°C and product peaks similar to those in Figure 5-4 are seen. After 72 hours, the sample heated at 200°C has started to display additional peaks, similar to those seen Figure 5-4 which were not previously present after 12 hours of heating at 200°C. The set of product peaks identified in Figure 5-3 (see section 5.11) that were low in intensity after heating for 12 hours at 185°C gained intensity relative to the remaining peaks, indicating consumption of the starting materials, particularly NH_4Cl , had increased after the reaction time was extended to 72 hours. The powder XRD pattern observed after heating to 215°C was very similar to those observed when samples were heated above 225°C for only 12 hours; all NH_4Cl was consumed and new peaks consistent with the patterns in Figure 5-2 were present.

From the subtle variations seen across the additional powder XRD patterns in Figure 5-5 and Figure 5-6, several potential sets of peaks were identified. The pattern recorded after heating for 12 hours at 300°C was chosen for indexing as the starting materials were no longer observed and the peak definition was superior to many other patterns. Peak fitting of all peaks was carried out to refine positions and areas of the peaks and then indexing regimes with selected peaks were run through Topas. Peak selection was carried out by visual inspection of the variation in peak shapes and relative intensities from the additional patterns recorded at varying temperatures and durations.

Initially, the results of the indexing regimes were assessed by the number of unindexed peaks and 'status of the solution' as provided by Coelho in the Topas Technical Reference. As the patterns were thought to include impurities due to the likelihood of multiple phases, solutions with a status lower than 3 were not investigated further. Groups of peaks whose results that auto-indexed to triclinic space groups $P1$ or $\bar{P}1$ were also discounted on the assumption they probably represented sets of peaks from more than 1 phase because of the low symmetry. All the unfitted

peaks were indexed in Set 1 as an example of this. An overview of the indexing results is shown in Table 5-2.

	Peak selection (2Theta° to 2dp)	Status of indexing solution	Number of un-indexed peaks	Space Group	[a b c] lattice parameters (Å)
Set 1	All peaks	1	0	$\bar{P}1$	5.5804, 6.6901, 9.3102 ($\alpha = 112.865$, $\beta = 95.094$, $\gamma = 65.929$)
Set 2	10.20, 15.74, 15.07, 20.80, 29.04, 30.53, 34.31, 37.34, 51.21, 52.04	3	5	$C2$	6.2115, 18.2465, 1.9619 ($\beta = 82.322^\circ$)
Set 3	18.37, 21.97, 24.19, 27.12, 28.35, 30.14, 34.31, 48.44, 50.27	3	4	Cc or $C2$	9.8282, 8.0851, 4.2530 ($\beta = 100.850^\circ$)
Set 4	15.74, 18.36, 20.80, 30.14, 37.34, 48.44, 52.05	3	3	$C222$	11.2753, 3.1380, 4.2740
		3	3	$F222$	11.2128, 4.8066, 3.9815
		3	2	$P2_1/c$	3.0578, 11.2753, 2.7466 ($\beta = 75.928^\circ$)

Table 5-2: Selection of peaks and top 3 (where relevant) indexing solutions for each set of peaks from Topas

After indexing of the peaks selected in Set 2, the c lattice parameter generated seemed unreasonably low and the space group suggested, $C2$, also has low symmetry. Due to the high number of unindexed peaks in this solution, it was likely that too many peaks had been included in the indexing regime. The most realistic indexing solution from the peaks selected in Set 3 also included several unindexed peaks. Although it seems likely that the correct peaks have not been correctly assigned to multiple phases in this powder XRD pattern, the space groups suggested for most of the reasonable solutions identified from the peaks in Sets 3 and 4 were based on face-centred lattices. When the top indexing results were investigated as model-independent Pawley

fits, the modelled fit to recorded data was poor. An example of a modelled fit is shown in Figure 5-7. The space group with highest symmetry ($F222$) and largest c lattice parameter was used. The fit does not appear to have modelled many of the peaks included in the initial indexing regime, suggesting that this selection of peaks likely still belonged to more than one phase. Unfortunately, with the quality of data available, the variations observed in the peaks in the powder XRD patterns were not clear enough to conclusively assign all the peaks to multiple phases.

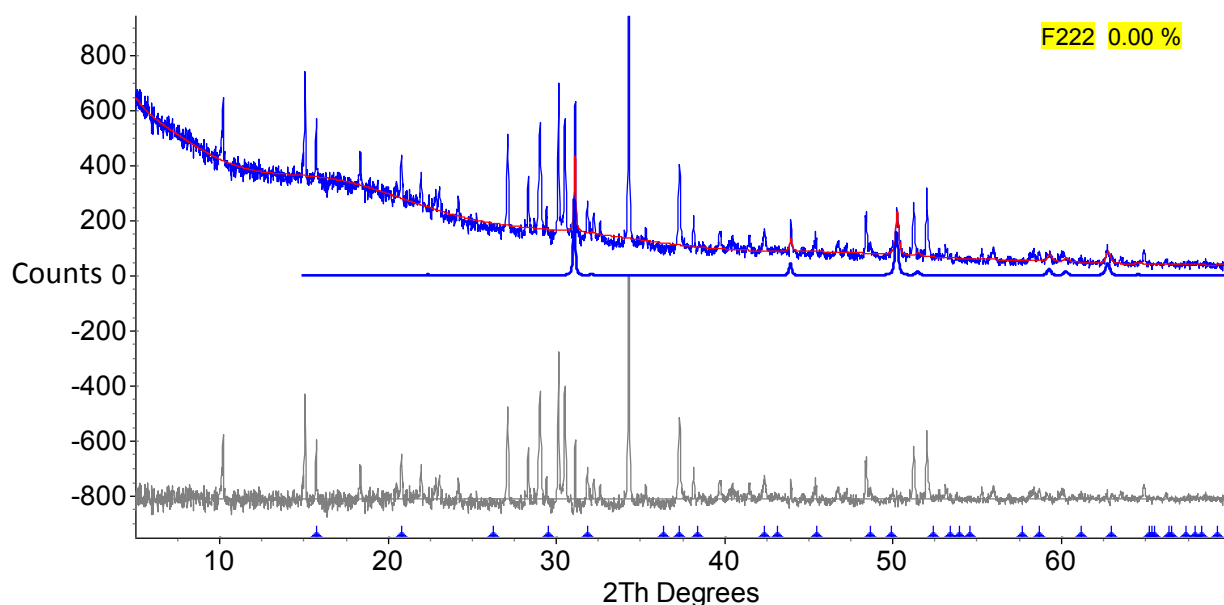


Figure 5-7: Powder XRD pattern of $\text{NH}_4\text{Cl} + \text{MgH}_2$ sample heated at 300°C for 12 hours with the calculated (red) and observed (blue) traces with the peak positions indicated for unknown $F222$ phase (blue highlighted trace).

As an experimentally based solution had not been found, based on the indexing results suggesting a large cell, and the solution with only 2 unindexed peaks was a structure based on space group no. 14, $P2_1/c$ a further literature search was carried out. As large amounts of metal oxides had been seen in Chapters 3 and 4, this time oxygen was also included in the chemistry search. Interestingly a hexahydrate-ammonium magnesium chloride phase was identified, which was solved to space group no. 15, $C2/c$, which is closely related to $P2_1/c$. The lattice parameters of ammonium carnallite¹⁸⁶, $\text{MgCl}_2(\text{NH}_4\text{Cl})(\text{H}_2\text{O})_6$ are $a = 9.300 \text{ \AA}$, $b = 9.550 \text{ \AA}$ and $c = 13.301 \text{ \AA}$, while $\beta = 90.06^\circ$. The characteristics of the resulting powder XRD of ammonium carnallite are similar to the patterns observed in these experiments, but the structural information from this phase does not describe the peaks observed in Figure 5-7. The similarities in the patterns and potentially

indexed phase (Table 5-2, Set 4) could suggest that a similar hydrated magnesium-chloride type phase has been formed but higher quality data would be required to conclusively determine this.

5.3.1.2 *Ex Situ* under flowing ammonia

Brief investigations were made to see if by changing the reaction gas the reaction pathway could be altered, either by the reaction of the components with the ammonia or by suppression of ammonia release due to Le Chatelier's principle. Two reaction temperatures were chosen to coincide with the two major changes in the powder XRD patterns in Section 5.3.1. A sample was heated at 215°C for 12 hours under flowing ammonia and the resulting powder XRD pattern is shown in Figure 5-8.

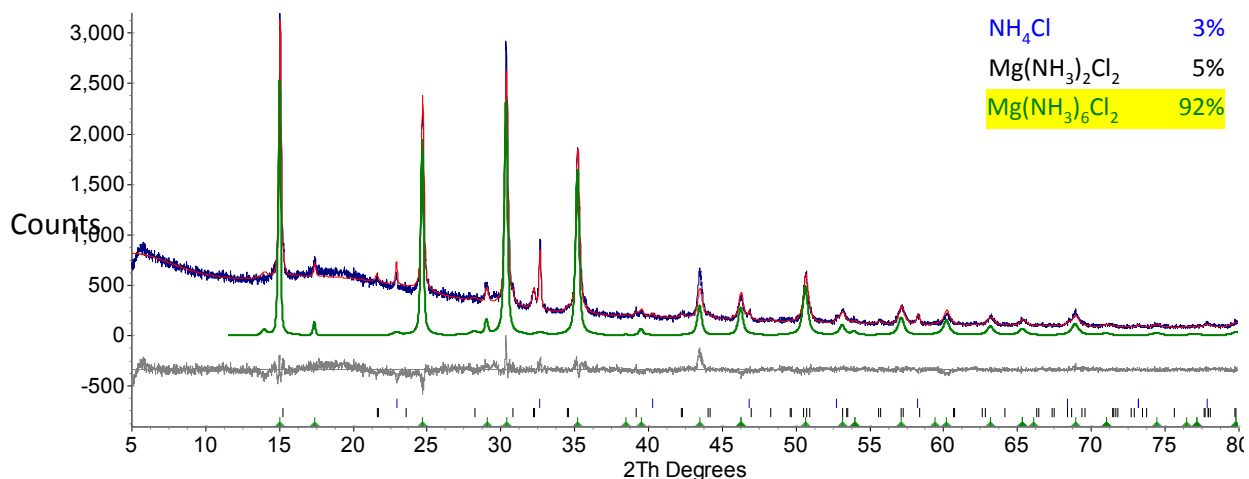


Figure 5-8: Powder XRD pattern of NH_4Cl + MgH_2 sample heated at 300°C for 12 hours under flowing ammonia gas with Rietveld fit showing the difference (grey), calculated (red) and observed (blue) traces with the peak positions indicated for NH_4Cl (blue), $\text{Mg}(\text{NH}_3)_2\text{Cl}_2$ (black) and $\text{Mg}(\text{NH}_3)_6\text{Cl}_2$ (green and highlighted).

The formation of $\text{Mg}(\text{NH}_3)_6\text{Cl}_2$ under these conditions (flowing ammonia gas) was unsurprising as $\text{Mg}(\text{NH}_3)_2\text{Cl}_2$ was identified in Figure 5-4 at 215°C under flowing argon gas. The consumption of starting materials was dramatically improved relative to comparative reactions run under flowing argon gas. The second reaction was carried out at 300°C and the resulting powder XRD pattern is shown in below in Figure 5-9. The peaks assigned to MgH_2 in Figure 5-8 were no longer observed after heating the materials at 300°C. The reaction carried out at 300°C has produced $\text{Mg}(\text{NH}_3)_6\text{Cl}_2$ (highlighted in green) and consumed almost all the starting materials.

However, from the difference trace in Figure 5-9, some additional peaks were observed in the powder XRD pattern suggesting that a further phase was also seen in this sample. According to the literature^{109, 184} under normal conditions (i.e. vacuum or argon) $\text{Mg}(\text{NH}_3)_6\text{Cl}_2$ decomposes between 125°C and 175°C, so it was perhaps slightly surprising that formation of this phase was more successful at 300°C than 215°C. This is likely due to the ammonia vapour pressure in the gas atmosphere during this reaction suppressing the release of ammonia which would accompany a transition from the hexa-ammoniate chloride to the di-ammoniate chloride.

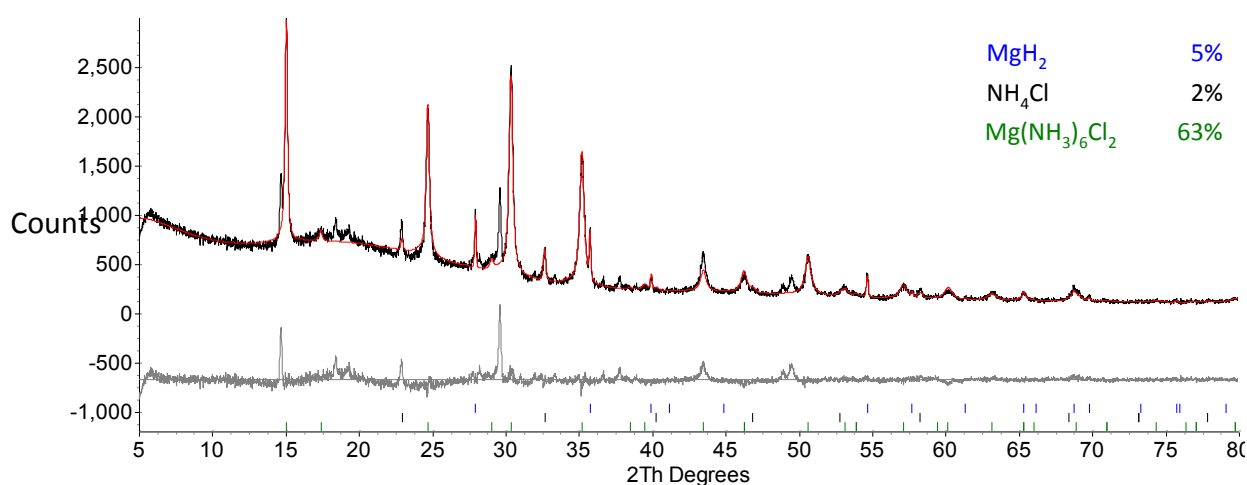


Figure 5-9: Powder XRD pattern of NH_4Cl + MgH_2 sample heated at 300°C for 12 hours under flowing ammonia gas with Rietveld fit showing the difference (grey), calculated (red) and observed (purple) traces with the peak positions indicated for NH_4Cl (blue), $\text{Mg}(\text{NH}_3)_2\text{Cl}_2$ (black) and $\text{Mg}(\text{NH}_3)_6\text{Cl}_2$ (green and highlighted).

The lattice parameter for $\text{Mg}(\text{NH}_3)_6\text{Cl}_2$ reported by Jones *et al.*¹⁰⁹ was 10.12258(3) Å and the calculated lattice parameter using Topas from the data in the pattern in Figure 5-9 was 10.188(1) Å, which represents a small but significant 0.6% increase. These two results have shown that by changing the reaction gas, the reaction pathway has been altered. By reacting the samples under ammonia gas, the sample has demonstrated considerable ammonia uptake to produce $\text{Mg}(\text{NH}_3)_6\text{Cl}_2$, likely from the in-situ formation of MgCl_2 or $\text{Mg}(\text{NH}_3)_2\text{Cl}_2$. The proposed reaction for the $\text{Mg}(\text{NH}_3)_6\text{Cl}_2$ formation is shown below:



These reactions represent a novel method of synthesising the magnesium ammoniate chloride, $\text{Mg}(\text{NH}_3)_6\text{Cl}_2$ from two solid state reactants as other methods have required wet synthesis routes or only used NH_4Cl in a reaction promoter, in very low amounts¹⁸⁰, rather than as a reactant.

5.4 Investigations across a stoichiometry range

As previously suggested in Section 5.3.1, a 1:1 reactant ratio may not be the most appropriate for the reaction of ammonium chloride and magnesium hydride, especially at low temperatures.

5.4.1 Powder X-ray diffraction

Samples across the stoichiometric range $(1-x)\text{NH}_4\text{Cl} + x\text{MgH}_2$, where $x = 0.33, 0.417, 0.50, 0.583$ and 0.66 were heated for 12 hours at 200°C . When the $x = 0.5$ sample was heated at 200°C the resulting powder XRD pattern is shown in Figure 5-10. As noted above both the starting materials remain and clear peaks belonging to an unidentified phase are present for the above values of x except when $x = 0.66$.

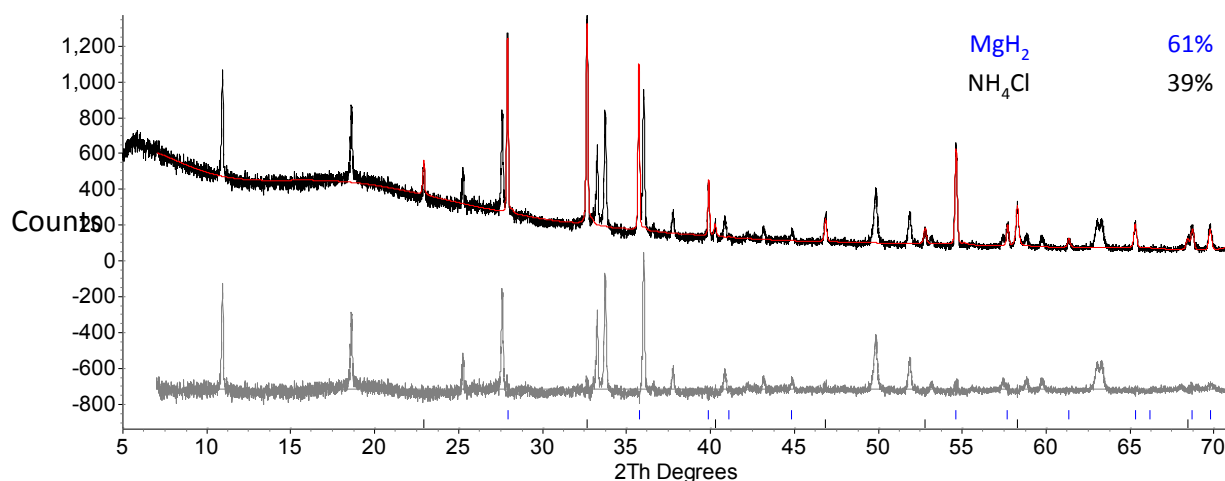


Figure 5-10: Powder XRD pattern of the sample where $x = 0.5$, heated at 200°C for 12 hours, with Rietveld fit showing the difference (grey), calculated (red) and observed (black) traces with the peak positions indicated for MgH_2 (blue), NH_4Cl (black).

Visual inspection of the patterns shows that as the amount of ammonium chloride was increased, an overall reduction in the peak intensity of the peaks associated with the new phase

occurred. When $x = 0.66$ and the NH_4Cl to MgH_2 ratio was decreased, all peaks associated with NH_4Cl had disappeared. In order to investigate the rates of consumption of the starting materials, the mol% of materials present in each sample before and after heating are compared in Figure 5-11 using quantitative phase analysis through Rietveld refinement in Topas.

Only NH_4Cl and MgH_2 were identified, so the total mol% of the two is always 100%. Only values from the range of $0.33 < x < 0.583$ were compared, as these correspond to the range where the new phase was observed. The rate of consumption of the starting materials was not linear across the stoichiometric reaction range. This indicated that the preferred reaction stoichiometry was not 1: 1 and it was likely that varying reactions proceeded depending on if the amount of ammonium chloride or magnesium hydride was greater.

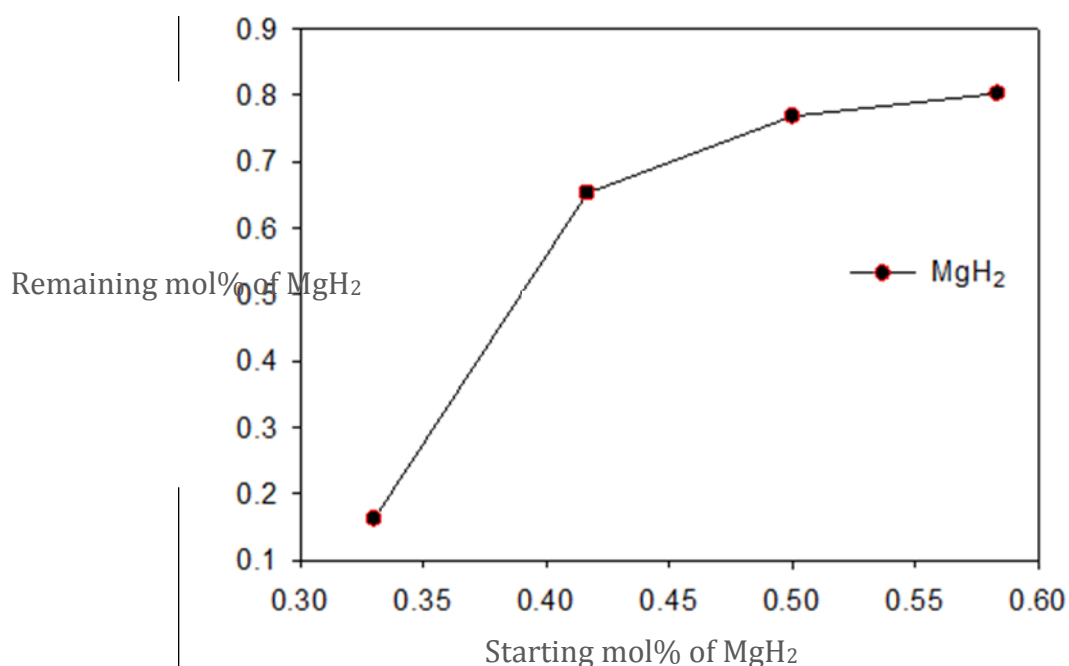


Figure 5-11: Comparison of the resulting mol% of MgH_2 after heating at 200°C for 12 hours against starting mol% of MgH_2

A reasonably stable mid-range area was observed in the graph which indicated that the 'new compound' may be stable over a range of compositions. The structures of $\text{Mg}(\text{NH}_3)_z\text{Cl}_2$ where $z = 2, 6$ were previously identified^{109, 181}, and although potential evidence for the existence of both $z = 1$ and 4 exists¹⁸⁵, no structure has yet been determined for either. The formation of a

magnesium ammoniate chloride where $z = 4$ at temperatures around 200°C would be in good agreement with decomposition temperatures proposed in the literature¹⁸⁵.

5.5 Reactions of NH_4Cl with 2MgH_2

5.5.1 Powder X-ray diffraction

Analysis of the results in Section 5.4 showed that increasing the magnesium hydride content in the sample above $x = 0.583$ changed the reactions that occurred. Experiments at various temperatures were carried out where $x = 0.66$ ($\text{NH}_4\text{Cl} + 2\text{MgH}_2$) to investigate this starting ratio. After a sample ($x = 0.66$) was heated at 200°C for 12 hours, all NH_4Cl was consumed and only MgH_2 remained. The powder XRD recorded showed similar peaks to those seen Figure 5-4. The temperature of heating was increased in order to attempt to determine the nature of this system and to provide clarity for the phase(s) produced in this system as well as a comparison to the $x = 0.5$ system. It was hoped these experiments may help to allocate the peaks to unknown phase(s) to assist with the indexing attempted in Section 5.3.1.1.

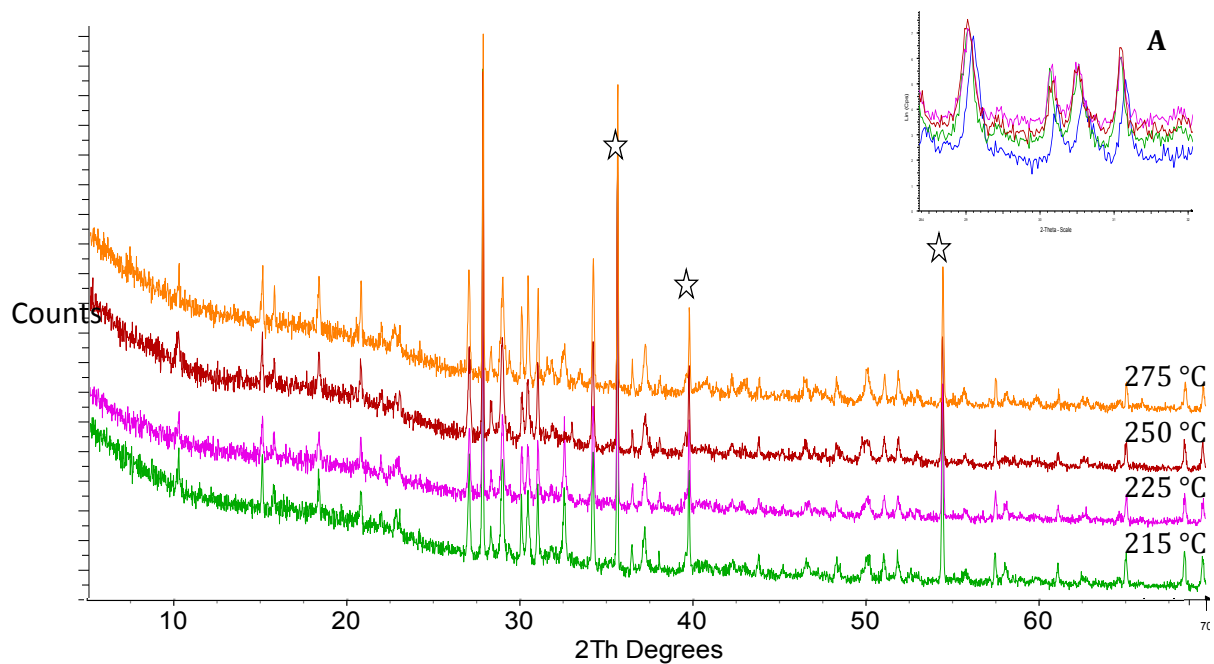


Figure 5-12: Stacked laboratory powder XRD plot of $\text{NH}_4\text{Cl} + 2\text{MgH}_2$ samples heated for 12 hours at 215°C (green), 225°C (pink), 250°C (burgundy) and 275°C (orange) and the expanded section (A) also includes the sample heated at 200°C (blue) for 12 hours.

Several of patterns which were recorded at room temperature after samples were heated at various temperatures between 215°C and 275°C for 12 hours are shown in the stacked powder XRD plot (Figure 5-12). The peaks indicative of MgH_2 are starred to allow easy identification of this starting material. The patterns in Figure 5-12 are very similar to those recorded after the $x = 0.5$ system was subjected to the same heating regimes except an excess of MgH_2 has remained. As the reaction temperature was raised, the relative intensity of peaks corresponding to MgH_2 did decrease and additional peaks in the patterns became sharper. The patterns were more consistent over a larger temperature range in the 1 to 2 system (Figure 5-12) than in the 1: 1 system (Figure 5-5).

A comparison of the pattern observed after heating at 275°C has been made to the pattern observed after heating at 300°C in Figure 5-13. A noticeable change in intensities was observed for some of the peaks in the pattern, especially between 30–35°. As the heating temperature was increased to 300°C most of the peaks were sharp and well defined, however MgH_2 still remained. To consume all the MgH_2 at temperatures below 300°C, a higher ratio of NH_4Cl to MgH_2 is required. Unfortunately these peaks in this patterns could not be assigned to known phases.

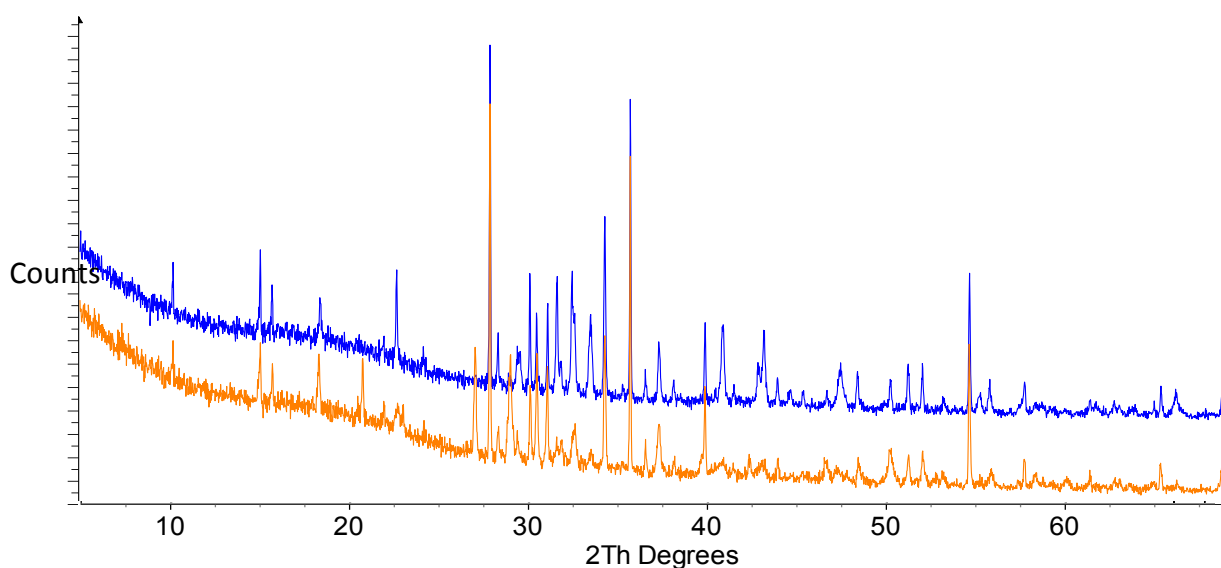


Figure 5-13: Powder XRD plots of $\text{NH}_4\text{Cl} + 2\text{MgH}_2$ samples heated for 12 hours at 275°C (orange) and 300°C (blue) for 12 hours.

5.6 Powder XRD summary

Initially, experiments were carried out across various heating temperatures and durations whilst maintaining stoichiometry of the reactants at 1:1. The resulting powder XRD patterns showed that NH_4Cl and MgH_2 did react with each other under heating, well below each compound's individual melting point, and several compounds were formed at various temperatures. Known compounds which were identified from powder XRD data included magnesium ammoniate chlorides and magnesium imide. Several sets of new peaks appeared in the same positions over a range of temperatures. From the indexing regimes attempted, it was thought that these peaks may belong to a hydrated magnesium ammonium chloride type phase(s). When $x = 0.5$, ammonium chloride was still observed up to reaction temperatures of 225°C alongside an additional set of product peaks indicating that the preferred reaction at this temperature did not consume the reactants in a 1: 1 ratio.

When the same reactions were carried out at the same temperature but the duration of heating increased from 12 hours to 72 hours, the reactions were more complete at lower temperatures than in shorter durations. Many peaks could not be assigned to a known phase. At temperatures around $200\text{--}300^\circ\text{C}$, it seemed possible that $\text{Mg}(\text{NH}_2)_2$ or MgNH could have been formed but these phases have not been conclusively identified; $\text{Mg}(\text{NH}_2)_2$ can readily exist in its amorphous state.

When the stoichiometry of the starting materials was varied with the reaction temperature at 200°C , the new set of peaks were consistent across a range of x ($0.33 \leq x \leq 0.583$). As the ratio of NH_4Cl to MgH_2 was decreased to 1 to 2, a different reaction pathway was followed to that observed when $x < 0.66$. After heating at 300°C , the corresponding powder XRD patterns observed were very similar for all values of x indicating that the same end product was reached regardless of the ratio of the starting materials, however, when $x = 0.66$, excess MgH_2 still remained. The similarities in peak positions, shapes and intensities between the samples heated

at varying temperatures were observed to begin at a lower temperature, around 215°C for the 1:2 system compared to 250°C than the 1:1 system (Section 5.3.1).

The reactions of the samples heated under ammonia according to the powder XRD results were mostly different to those reacted under argon. A novel method of synthesis for almost pure $\text{Mg}(\text{NH}_3)_6\text{Cl}_2$ was identified.

5.7 Raman spectroscopy

Raman spectroscopy was carried out on several samples at room temperature after reaction under a range of temperatures and two reactant gases. Raman data (or IR) was not available for $\text{Mg}(\text{NH}_3)_2\text{Cl}_2$ or $\text{Mg}(\text{NH}_3)_6\text{Cl}_2$ so data from some manganese ammoniates, which are isostructural to the magnesium ammoniate chlorides was used instead for comparison.

Initially full range sweeps were carried out on all samples, and although several Raman active bands were observed in the manganese counterparts, in a range of 100–3000 cm^{-1} ¹⁸⁷, none were observed in these experiments. Raman peaks from the manganese ammoniate chloride ($\text{Mn}(\text{NH}_3)_6\text{Cl}_2$) were observed at 3335, 3255 and 3155 cm^{-1} ¹⁸⁷, which are comparable to the results presented in Table 5-3.

The only spectral features detected were attributed to N–H symmetric and asymmetric stretching modes in the region between 3000 cm^{-1} and 3500 cm^{-1} . The resulting spectra from some samples revealed the absence of any peaks, even if samples appeared to be focused correctly. Raman data from a selection of samples has been tabulated above in Table 5-3.

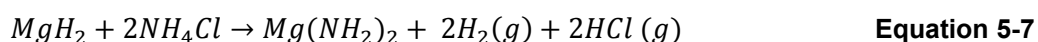
The stretches that could be attributed to the starting material, NH_4Cl , would be expected to appear around 3146 and 3041 cm^{-1} ¹⁸⁸. Experimentally Raman stretches from a sample of NH_4Cl used in this work were observed at 3142, 3048 and 2827 cm^{-1} when recorded at room temperature. No intensity was observed in these areas in any of the Raman spectra reported in

this work, which was in contrast to powder XRD data, which indicated that NH_4Cl was not present in any of the samples tested. This could be due to reasonably large grain sizes which due to the small sampling area of the Raman spectrometer were not detected.

	Heating Regime	Raman Shift (cm^{-1})
	NH_4Cl (Ambient)	2827, 3048, 3142
1	215°C for 12 hours under Ar	3271
2	215°C for 72 hours under Ar	3270, 3327
3	250°C for 12 hours under Ar	3272, 3325
4	325°C for 12 hours under Ar	3276, 3262, 3331, 3325,
5	215°C for 12 hours under NH_3	3264, 3342

Table 5-3: Preliminary Raman data recorded of NH_4Cl + MgH_2 samples.

From previous work using the same equipment,¹⁸⁹ it was found that peaks observed around 3272 cm^{-1} and 3326 cm^{-1} can relate to magnesium amide. These peak positions were in good agreement with the results (3274 cm^{-1} and 3329 cm^{-1}) of Hatrick-Simpers *et al*¹⁹⁰. $\text{Mg}(\text{NH}_2)_2$ is often amorphous, which could explain why it was not been observed through powder XRD. If at higher temperatures, MgNH had been formed, the Raman peaks would have been observed at lower wavenumbers, 3251 and 3199 cm^{-1} ¹⁷¹. A possible route for forming $\text{Mg}(\text{NH}_2)_2$ from the reactants is suggested in Equation 5-7.



If the reaction above was proceeding in samples where $x = 0.5$, it could explain why MgH_2 continued to be observed in the powder XRD patterns (see Figure 5-4) after the ammonium chloride has been consumed. It is then possible that the newly formed magnesium amide could react with remaining ammonium chloride or magnesium hydride or newly produced HCl gas.

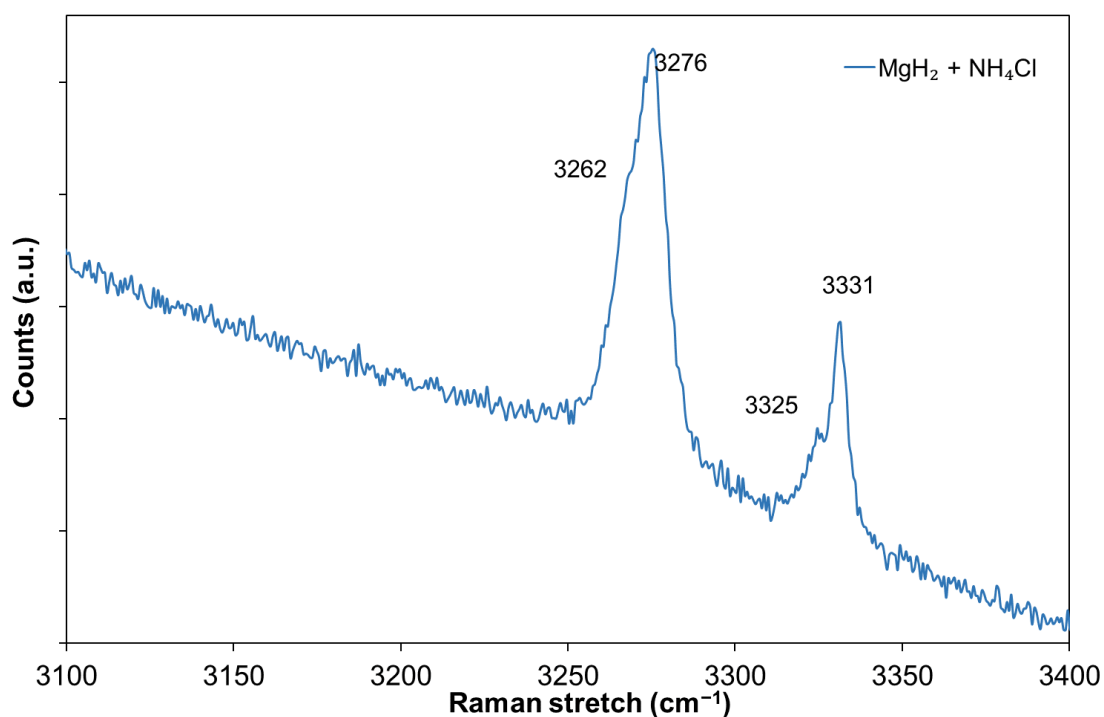


Figure 5-14: Raman spectrum of $\text{NH}_4\text{Cl} + \text{MgH}_2$ heated under flowing argon for 12 hours at 325°C .

An alternative hypothesis is that the sample contains NH_2 type groups which are closely bonded to Mg in a structure but chlorine has been also incorporated which has changed the structure, which would explain why magnesium amide was not visible in the powder XRD patterns. Indeed the formation of $\text{Li}_4(\text{NH}_2)_3\text{Cl}$ has been known for some time⁴⁷, and other compounds¹⁶³ in the same family have also been identified, including some containing Mg. Therefore, in-line with the additional unidentified peaks that have emerged in some of the powder XRD patterns, these spectra could indicate the formation of a magnesium amide type chloride.

As the peaks observed were reasonably broad, although the Raman shift values at the most intense points were close to those corresponding to $\text{Mg}(\text{NH}_2)_2$, additional compounds may also contribute to the spectra. An example of this is shown in Figure 5-14 where additional shoulders are indicated. Similar to the resulting peak overlap in powder XRD patterns, many similar compounds, those including NH_3 , NH_2 or NH often exhibit overlapping Raman peaks as well.

The peaks referenced in sample 5, when the reactants were heated under ammonia, were observed at different wavenumbers to the four other samples. As almost exclusively $\text{Mg}(\text{NH}_3)_6\text{Cl}_2$ was observed in the resulting powder XRD pattern it may be that the location of these peaks is a good representation of this phase.

5.8 Differential scanning calorimetry

5.8.1 Results

DSC experiments were carried out according to Section 2.10 to investigate the thermal properties and to calculate the enthalpies of phase transitions observed in the powder XRD data, and evidenced by gas release and mass loss in TPD-MS and TGA, respectively. Samples of varying stoichiometry were tested, in the region $0.33 < x < 0.66$. DSC datasets were recorded for 5 samples and are compared in Figure 5-16 and Figure 5-17.

In the heating segment of the experiments, an endothermic melt occurred in all samples at temperatures between 175–205°C, which was followed by an exothermic event. From analysis of the shape of the large peak in Figure 5-16, there appeared to be several small changes in the gradient, which provided good evidence for several different transitions taking place. An expanded view of the exothermic peak in Figure 5-16 showed the change in the temperature of the peak as more magnesium hydride was added.

The exothermic event peaked at temperatures around 235°C for all samples, which was in good agreement with powder XRD data where significant changes were observed between 195–240°C. This exothermic event was attributed to a combination of the formation of $\text{Mg}(\text{NH}_3)_2\text{Cl}_2$ and a previously identified novel phase. There was a smooth decrease in peak height and peak temperature as x tended towards 0.58, and as the ratio reached $\text{NH}_4\text{Cl}: 2\text{MgH}_2$ the peak shifted to higher temperature.

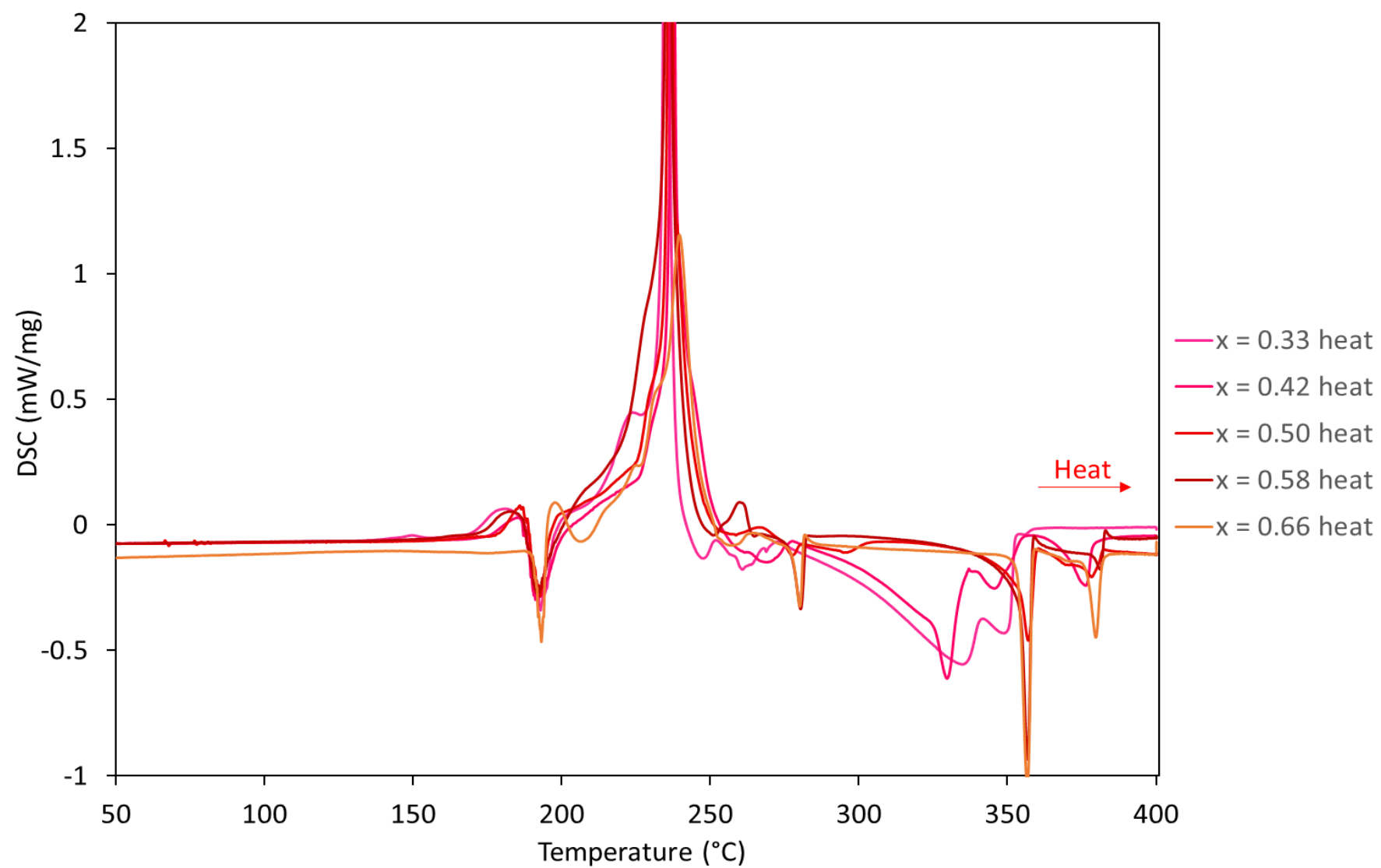


Figure 5-15: DSC heating segment of $(1-x)\text{NH}_4\text{Cl} + x\text{MgH}_2$ when $x = 0.33, 0.42, 0.50, 0.58$ and 0.66 .

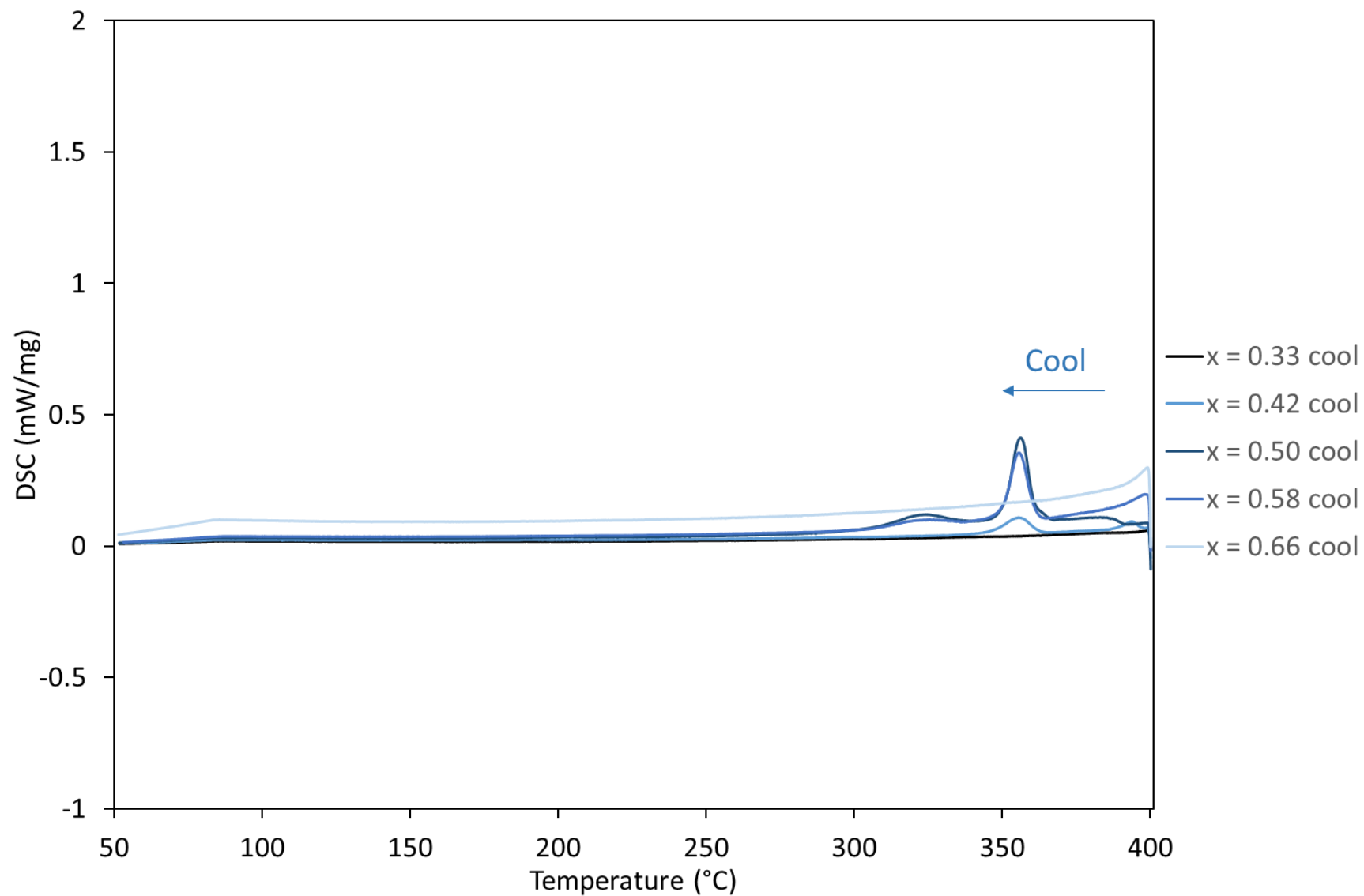


Figure 5-16: DSC cooling segment of $(1-x)\text{NH}_4\text{Cl} + x\text{MgH}_2$ when $x = 0.33, 0.42, 0.50, 0.58$ and 0.66 .

The area under the peak decreased as the magnesium content increased, indicating that the enthalpy of the phase formation(s) had decreased. If less of a phase is formed, the change in heat flow is reduced as this is a quantitative measurement. An increase in the enthalpy change was consistent with powder XRD data, which showed the relative intensity of the peaks corresponding to the unknown phase and $\text{Mg}(\text{NH}_3)_2\text{Cl}_2$ increased as more NH_4Cl was added. As DSC is a quantitative measurement, the largest values would indicate favourable stoichiometry. Unfortunately, as this reaction was likely to release both hydrogen and ammonia and the stoichiometry had not yet been determined for the product of the phase transition or formation corresponding to the large peak (Figure 5-17), these values cannot be converted into kJ mol^{-1} .

x	Temperature of peak ($^{\circ}\text{C}$)	Area of peak (J/g)
0.33	235.0	259
0.42	237.2	328
0.5	236.5	314
0.58	236.0	221
0.66	239.6	157

Table 5-4: Peak temperatures and areas (in Joules per gram of starting materials) of the exothermic peak highlighted in Figure 5-17.

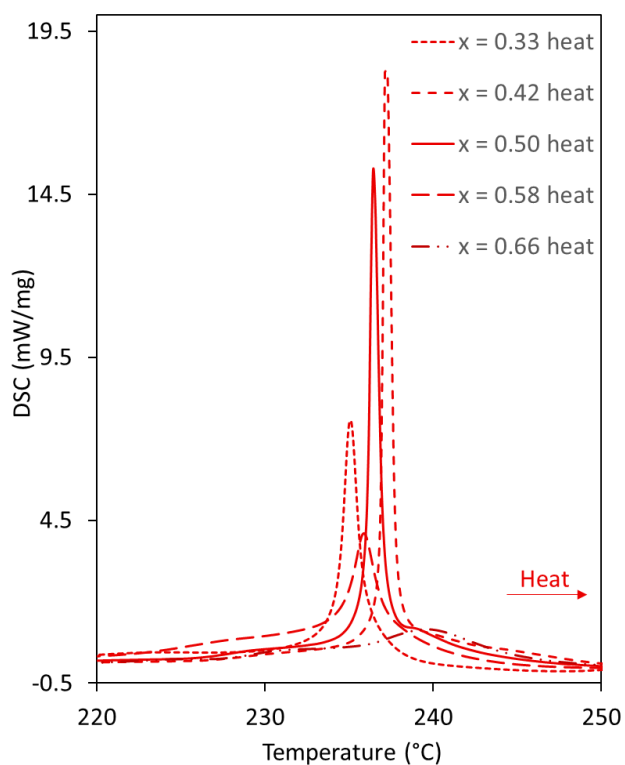


Figure 5-17: Close-up view of the exothermic peak that occurred during the heating segment of the DSC experiments.

At temperatures between 250°C and 350°C , the varying stoichiometry of the samples produced some variations in the heat flow, and several additional smaller endothermic events were observed. The quantity of events is likely due to the production of a mixture of products as the sample is heated, which is in good agreement with powder XRD data (Sections 5.3, 5.4 and

5.4). A further significant melt event was observed at $\sim 360^\circ\text{C}$ when $x \geq 0.42$. When $x \leq 0.42$ the heat flow profile observed at temperatures over 250°C was quite different as the amount of ammonium chloride present in the samples was higher.

During the cooling segment of the experiment a crystallisation was observed when $x = 0.5$ and 0.58 at 360°C (very slight for $x = 0.42$). This event was a mirror of the peak in the heating segment which indicated that after melting a proportion of the sample did not react further at higher temperatures and re-crystallised during cooling. However, as the size of the peak observed in the heating and cooling segments varied for some samples, it was thought that the amount of compound which recrystallized for some samples had reduced which would indicate that further reactions had occurred in the heating segment after melting and the products of subsequent reactions did not re-crystallise at 360°C . A small additional feature was also observed around 330°C when $x = 0.5$ and 0.58 , which suggests that 2 phases were formed. The corresponding peaks in the cooling segments of the runs were smaller than in the heating segment of the experiment.

5.8.2 Summary

DSC data showed several thermal events, both exothermic and endothermic, occurred during the heating stages of all samples. The temperatures of major events, 190°C , 240°C and 360°C corresponded well to significant changes observed in powder XRD data. The area under the biggest exothermic peak in the heating segment decreased as the amount of magnesium hydride in the sample was increased. As this peak had been linked to the formation (crystallisation) of a tetragonal phase and $\text{Mg}(\text{NH}_3)_2\text{Cl}_2$, this indicated that increasing the MgH_2 content in the sample, reduced the quantity of hydrogen-rich phases formed, leaving more MgH_2 unreacted. The endothermic peaks in the heating segment were attributed to melting events which were sometimes accompanied by gas release, (decomposition), further reactions or a phase change, which was likely to be irreversible, which meant the same peak was not observed in the cooling segment.

An exothermic crystallisation event was detected in the cooling segments of the experiment when $x = 0.42, 0.5$ and 0.583 at around 360°C . A sharp exothermic event was observed in the heating segment at the same temperature when $x = 0.5, 0.583$ and 0.66 . The closeness in temperature of the events in the heating and cooling segments may indicate that the transition was reversible in the middle of stoichiometric range, specifically around $x = 0.5$.

5.9 Thermal desorption

5.9.1 TPD-MS

5.9.1.1 $(1-x)\text{NH}_4\text{Cl}$ with $x\text{MgH}_2$

Desorption properties of samples across the stoichiometric range of the $(1-x)\text{NH}_4\text{Cl} + x\text{MgH}_2$ system where $x = 0.33, 0.42, 0.50, 0.58$ and 0.66 were investigated using TPD-MS. Samples were heated at a ramp rate of $2^{\circ}\text{C min}^{-1}$ to 400°C .

As the samples that were prepared all had slightly different masses, the relative intensity of different traces across the stoichiometric range was not directly comparable, hence the use of arbitrary intensity units. However, the relative ratios of hydrogen to ammonia are accurate within a single experiment; more accurate analysis using TGA was carried out in Section 5.9.2 It should be noted that alongside the normal m/z values scanned in TPD-MS as laid out in Section 5.2, in this instance mass channels corresponding to HCl and Cl_2 were also scanned to check for the potential loss of chlorine-containing substances.

The TPD-MS trace when $x = 0.5$ (Figure 5-18) shows that hydrogen was desorbed in several steps, the first and smallest of which began at approximately 175°C and peaked at $\sim 185^{\circ}\text{C}$. The largest peak was at 215°C , with a third hydrogen peak at 270°C .

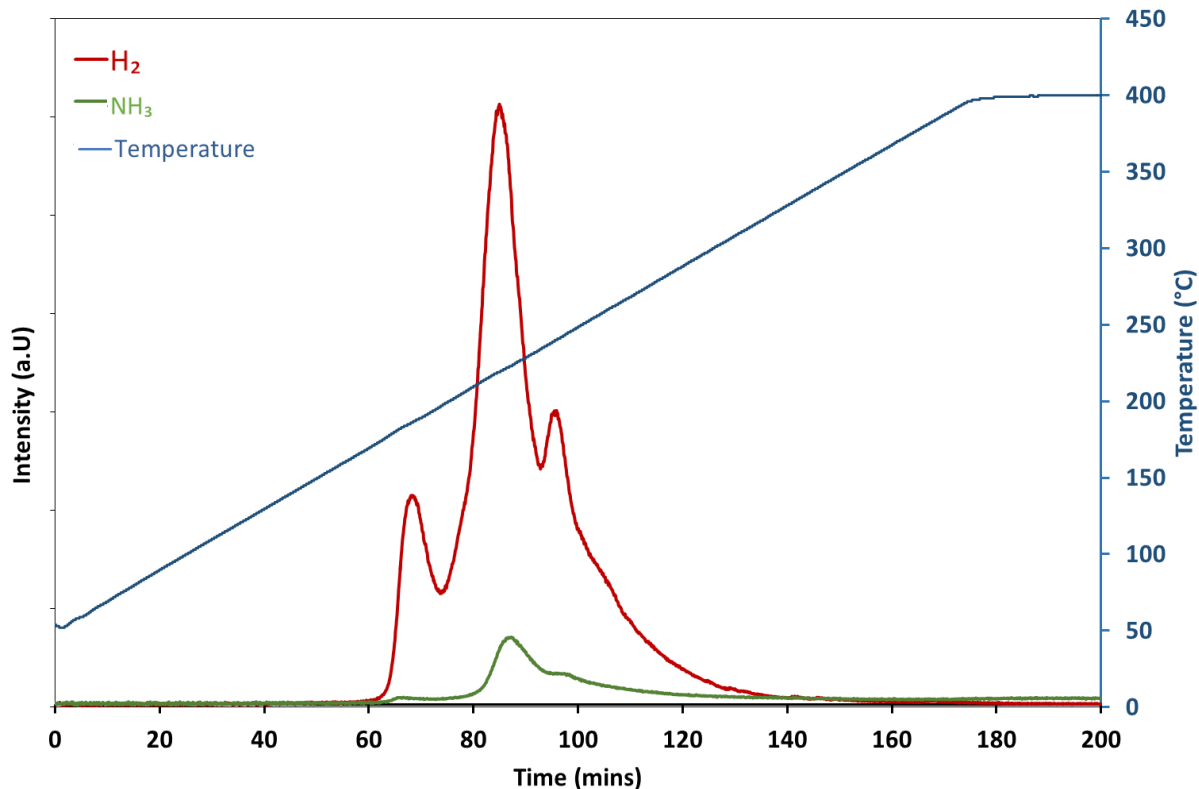


Figure 5-18: TPD-MS trace of $(1-x)\text{NH}_4\text{Cl} + x\text{MgH}_2$ sample heated at 2°C min^{-1} where $x = 0.50$, showing gas release against time, H_2 (red), NH_3 (green) and temperature (blue).

The temperature of the largest desorption peak corresponds to the first major change observed in powder XRD patterns where an unknown phase was identified. The temperature is in the same region that ammonium chloride undergoes a phase transition. Hydrogen desorption indicates that this phase is likely to be a hydrogen-deficient phase.

An ammonia peak was also observed. Although the intensity of the ammonia peak was much lower than the hydrogen peak, because the m/z value of ammonia is 8.5 times that of hydrogen, the mass loss accounted for by the ammonia peak was considerably larger than that accounted for by the hydrogen peak. No traces corresponding to HCl and Cl_2 are displayed because neither of these gases were observed in any of the TPD-MS experiments detailed in Section 5.9.

Next the desorption properties of samples that contained higher amounts of MgH_2 were also tested in TPD-MS experiments and the products were analysed. The TPD-MS traces for $x = 0.58$ and $x = 0.66$ are depicted in Figure 5-19. Both samples show several distinct peaks of

hydrogen release at similar temperatures. Ammonia release was observed from both samples, but a significant amount was observed when $x = 0.66$. This represented a large relative increase in ammonia release in the sample compared to $x = 0.58$ and 0.5 . This was surprising as this sample contained more magnesium hydride than ammonium chloride. The relatively large ammonia release from this sample could have been caused by the *in situ* formation of an ammoniate chloride and then its subsequent decomposition releasing ammonia, although this pathway would have been expected to be more prevalent at higher concentrations of NH_4Cl .

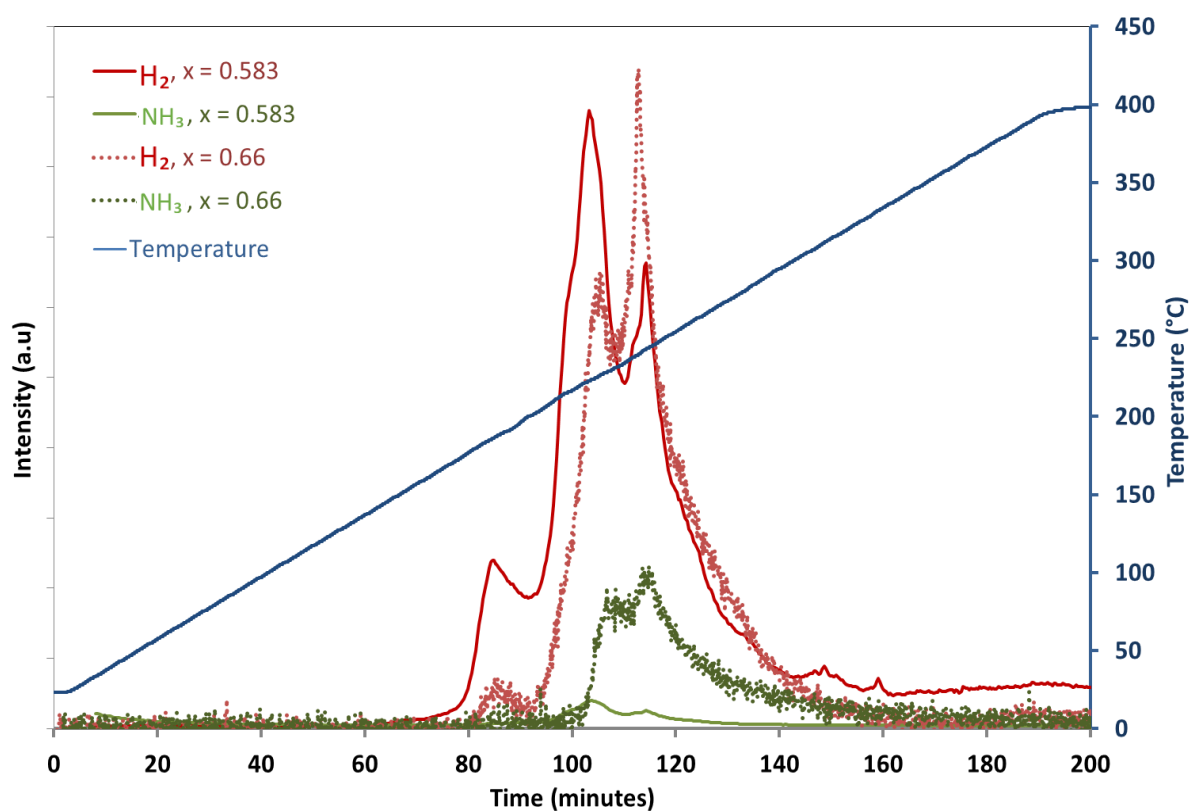


Figure 5-19: TPD-MS trace of $(1-x)\text{NH}_4\text{Cl} + x\text{MgH}_2$ samples heated at 2°C min^{-1} where $x = 0.58$ and 0.66 , showing gas release against time, H_2 (red), NH_3 (green) and temperature (blue).

The hydrogen release profile was similar to that for $x = 0.5$, which showed several hydrogen peaks indicating that multiple hydrogen-producing reactions had occurred. No temperature shift was observed for the first shoulder when $x > 0.5$; the peak remained centred at $\sim 190^\circ\text{C}$ although the intensity of this peak decreased when $x = 0.66$. The largest peaks in the hydrogen profiles corresponding to the samples when $x = 0.583$ and $x = 0.66$ were seen at 225°C and 240°C , respectively.

As the amount of MgH_2 in the sample was increased, the hydrogen released in each step was shifted to a higher temperature range. As the amount of MgH_2 was reduced to $x = 0.417$ and 0.33 , (Figure 5-20) no change in the temperature of the initial hydrogen shoulder was seen; it remained at $\sim 190^\circ\text{C}$.

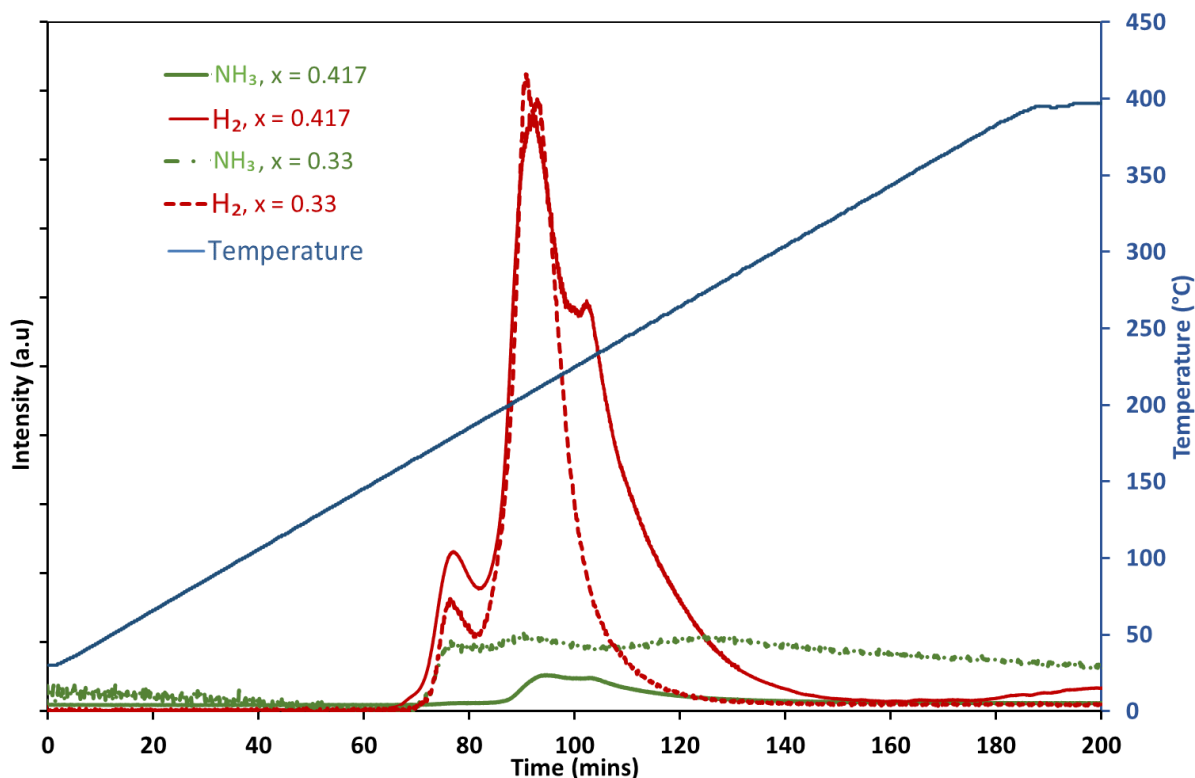


Figure 5-20: TPD-MS trace of $(1-x)\text{NH}_4\text{Cl} + x\text{MgH}_2$ samples heated at 2°C min^{-1} where $x = 0.33$ and 0.42 , showing gas release against time, H_2 (red), NH_3 (green) and temperature (blue).

As the amount of NH_4Cl in the sample was increased ($x = 0.33$), the high temperature peak which was observed at around 240°C when $x = 0.417$, was no longer seen. When $x = 0.33$, the amount of ammonia released at temperatures higher than 180°C was at a constant and significant level, suggesting that by increasing content of NH_4Cl in the sample to $x > 0.417$, the reaction pathway had been changed. As ammonium chloride is the only phase containing nitrogen, the breakdown of this phase must be responsible for ammonia release. However, although ammonium chloride undergoes a phase transition around 190°C , but it has not been found to

decompose until temperatures over 300°C. This phase transition would be in good agreement with the initial desorption temperatures of all the samples in this section.

5.9.1.2 NH_4Cl with alternative hydrides

In addition to a stoichiometric study of the $(1-x)\text{NH}_4\text{Cl} + x\text{MgH}_2$ system, several other hydrides were trialled in order to compare the desorption of the mixtures. As LiH has previously been shown to react more rapidly with ammonia than MgH_2 especially under desorption conditions, this was tested in place of MgH_2 to ascertain if ammonia release could be suppressed. The system tested was $(1-y)\text{NH}_4\text{Cl} + y\text{LiH}$, where $y = 0.66$. To maintain the ratio of hydridic hydrogens to the protons from NH_4Cl , the amount of LiH chosen was $y = 0.66$. Further hydrides investigated also included KH^{104} and CaH_2^{155} , which have all previously been used as replacements for MgH_2 in attempts to improve desorption properties of various systems.

5.9.1.3 $(1-y)\text{NH}_4\text{Cl}$ with $y\text{LiH}$

The TPD-MS data shown in Figure 5-21 showed that hydrogen and ammonia were released in similar amounts when NH_4Cl was heated with LiH. The relative amount of NH_3 to H_2 in this trace was much larger than observed in the desorption experiments of NH_4Cl with MgH_2 indicating that a considerable amount of ammonia has also been produced. This was unexpected as the reaction between LiH and NH_3 that releases hydrogen has been shown to be faster than that of MgH_2 with ammonia. This unexpected result could be due to 'trapping' of ammonia by reaction with MgCl_2 to form $\text{Mg}(\text{NH}_3)_2\text{Cl}_2$ when ammonium chloride is heated with MgH_2 . Although the hydrogen desorption profile in Figure 5-21 was quite different to the TPD-MS profiles in Section 5.9.1.1, the peak temperatures were very similar; with the largest desorption observed at 235°C and earlier features between 180 and 220°C.

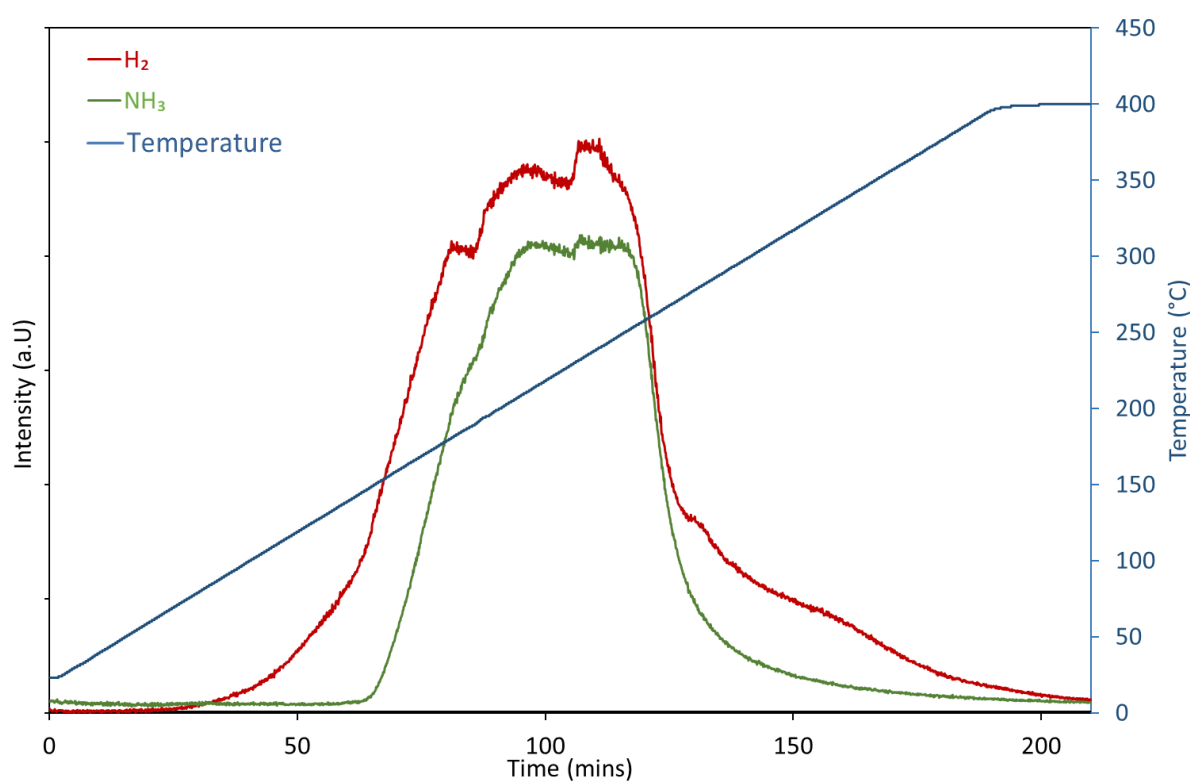


Figure 5-21: TPD-MS trace of $(1-y)\text{NH}_4\text{Cl} + y\text{LiH}$ sample heated at 2°C min^{-1} where $y = 0.66$ showing gas release against time, H_2 (red), NH_3 (green) and temperature (blue).

The similarities in peak temperatures may indicate that the reactions are also comparable. However, significant hydrogen desorption began much sooner than when MgH_2 was replaced by LiH , around 110°C .

5.9.1.4 $(1-z)\text{NH}_4\text{Cl}$ with $z\text{KH}$

The TPD-MS data in Figure 5-22 showed that hydrogen and ammonia were also both released when NH_4Cl was heated with KH . The same hydride ratio was used as in the LiH experiments, however, in contrast to the previous desorption experiments, the intensity of desorbed ammonia was greater than that of hydrogen and the peak also occurred considerably after hydrogen was desorbed, by around 60°C . This result might imply that these starting materials reacted during hydrogen release to form an ammonia- or ammoniate-rich phase, perhaps such as KNH_3NH_2 , which in this case acted as an intermediate, and then subsequently decomposed at a higher temperature resulting in a rapid release of ammonia.

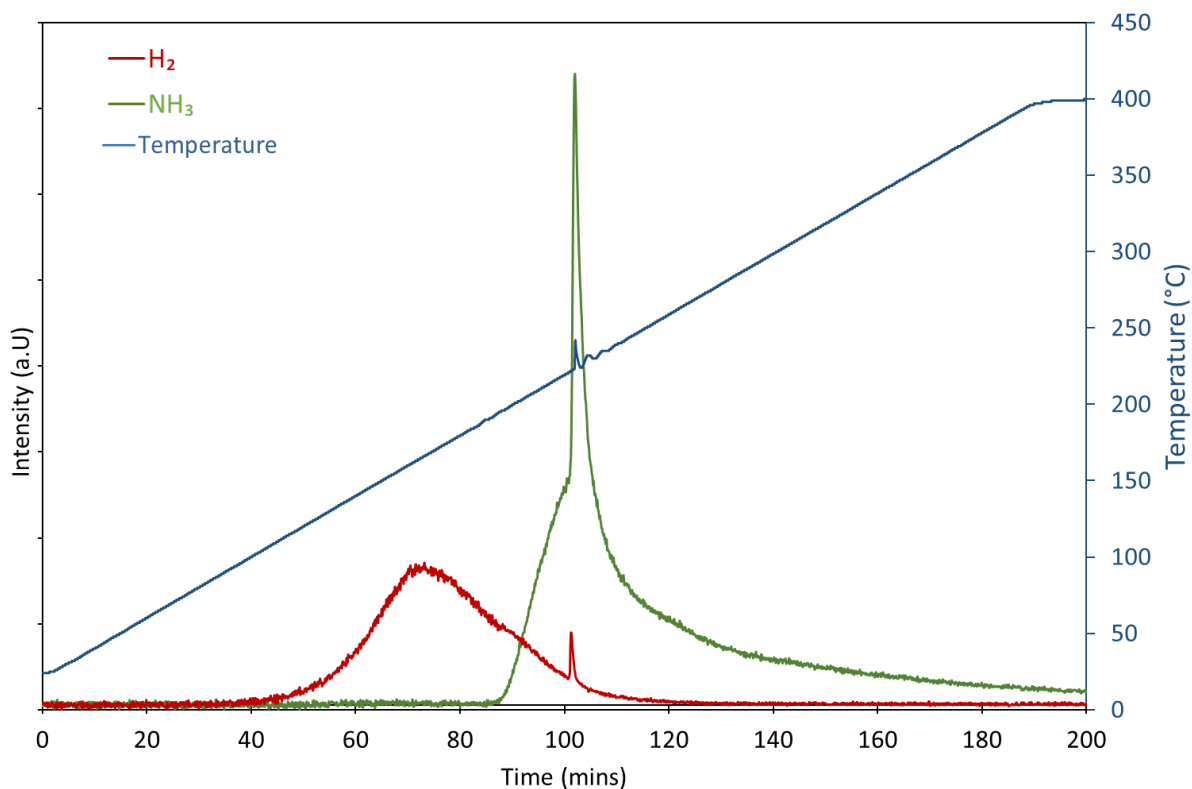


Figure 5-22: TPD–MS trace of $(1-z)\text{NH}_4\text{Cl} + z\text{KH}$ sample heated at 2°C min^{-1} where $z = 0.66$ showing gas release against time, H_2 (red), NH_3 (green) and temperature (blue).

The intense ammonia release was accompanied by a large temperature fluctuation in the temperature trace indicating an exothermic thermodynamic event had occurred. Such a variation in the temperature trace was not seen in any other samples, which would suggest the reaction was not the same as in the NH_4Cl and MgH_2 system. In the reactions of NH_4Cl with both KH and LiH , hydrogen desorption began at considerably lower temperatures than with MgH_2 , around 120°C and peaked at 170°C .

5.9.1.5 $(1-v)\text{NH}_4\text{Cl}$ with $v\text{CaH}_2$

The TPD–MS trace (Figure 5-23) shows that hydrogen and ammonia were also both released when NH_4Cl was heated with CaH_2 . In this case, the temperature at which hydrogen release began was similar to that observed in comparable experiments using MgH_2 . A broad hydrogen release peak was produced which peaked at 260°C and contained several higher temperature peaks.

When MgH_2 and LiH were reacted with ammonium chloride, the reaction temperatures correlated to the phase transition of ammonium chloride around 190°C . Hydrogen release from the reactions of NH_4Cl with CaH_2 and LiH occurred over a larger temperature range than the reactions with MgH_2 .

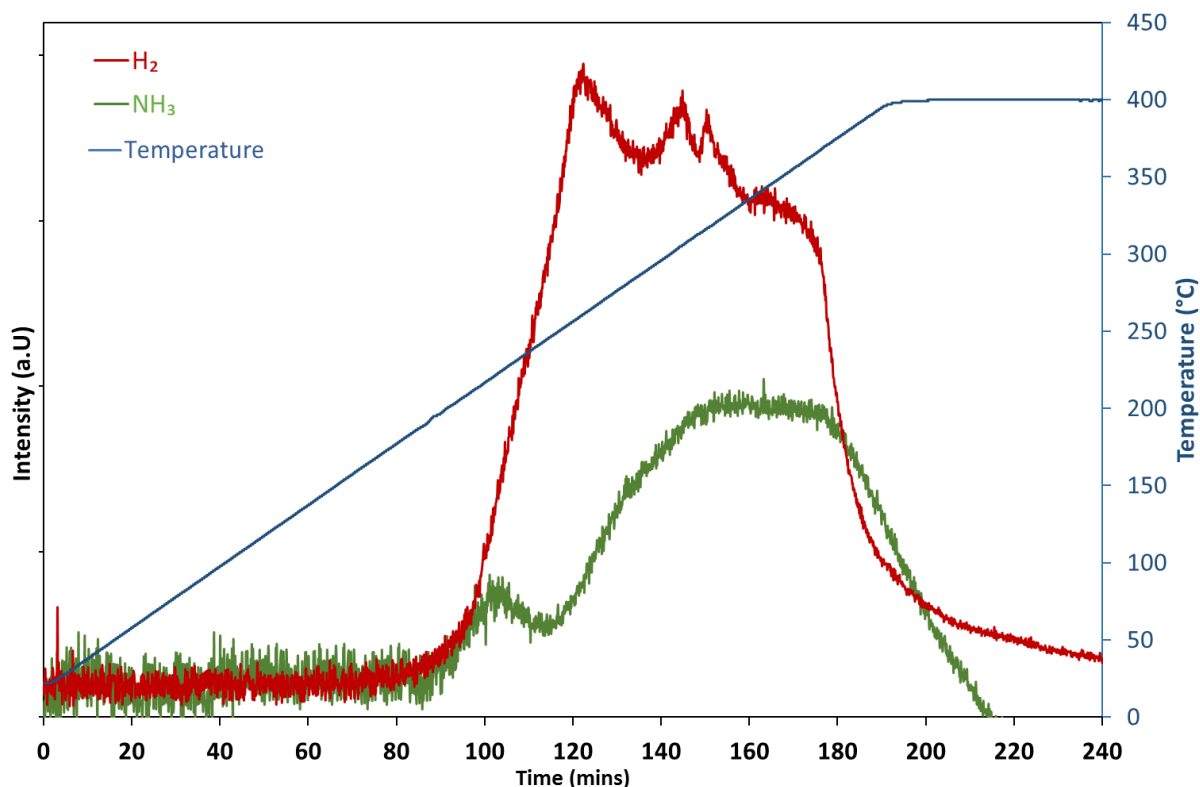


Figure 5-23: TPD-MS trace of $(1-\nu)\text{NH}_4\text{Cl} + \nu\text{CaH}_2$ sample heated at 2°C min^{-1} where $\nu = 0.50$ showing gas release against time, H_2 (red), NH_3 (green) and temperature (blue).

5.9.2 TGA-MS

5.9.2.1 $(1-x)\text{NH}_4\text{Cl}$ with $x\text{MgH}_2$

Gravimetric desorption properties of samples across the stoichiometric range of $(1-x)\text{NH}_4\text{Cl} + x\text{MgH}_2$ system, where $x = 0.33, 0.42, 0.50, 0.58$ and 0.66 were investigated using TGA-MS. Samples were heated to 400°C at 2°C min^{-1} . Unfortunately, mass spectrometry facilities were not available to analyse the gaseous products in the outlet gas stream when the sample $x = 0.33$ was tested.

The mass loss profiles from the samples are compared in Figure 5-24. The trend in the mass loss profiles indicates that the mass loss is directly related to the amount of MgH_2 in the sample. It can be seen that by increasing the MgH_2 content, the total mass losses were reduced when compared to the NH_4Cl rich samples, but all samples followed a very distinct and similar stepwise desorption trend. A lower overall mass loss likely corresponds to lower amounts of ammonia released. However, greater mass loss was observed after the end of the second desorption step when $x \geq 0.58$, potentially indicating that more of the hydrogen released (~ 2.5 wt%) had been shifted to higher temperatures (also seen in Figure 5-19).

Mass loss from all samples began at around 150°C and continued smoothly to approximately 195°C . The gradient then increased and mass loss continued until 220°C when $x \geq 0.58$, 240°C when $x \leq 0.50$ and 260 when $x = 0.33$. The second desorption step accounted for the steepest gradient observed in these TGA experiments, indicating the rate of gas desorption was the fastest.

When the MgH_2 content was high the mass loss during the 2nd step was the least. The samples which had a high MgH_2 content ($x \geq 0.58$) reached an approximate mass loss plateau sooner, (around 280°C) than samples which were ammonium chloride rich (respective plateau around 320°C). A slight bump was observed in most samples at around 370°C , which may have been any remaining MgH_2 fully decomposing.

The total mass lost from the MgH_2 rich samples ($x \geq 0.58$) was ~ 24.5 wt%, whereas the samples containing more NH_4Cl ($x \leq 0.50$) lost around 31 wt%. Clearly, the hydrogen capacity of these samples does not solely account for the mass loss seen in these experiments. The mass losses can be attributed to the release of a combination of H_2 and NH_3 and several reactions that could account for release of these gases were proposed and discussed in Section 5.3. The occurrence of multiple desorption steps was unsurprising and likely caused by several products reacting or

decomposing. This was in good agreement with powder XRD data recorded in Section 5.3, which did not show the formation of a single phase under any reaction conditions.

The appearance of four distinct desorption steps, identified through changes in gradient of the mass loss profile in Figure 5-24 for all samples, was in good agreement with previously recorded TPD-MS data. Three clear hydrogen desorption areas were identified in Figure 5-25 with ammonia appearing under the largest hydrogen peak.

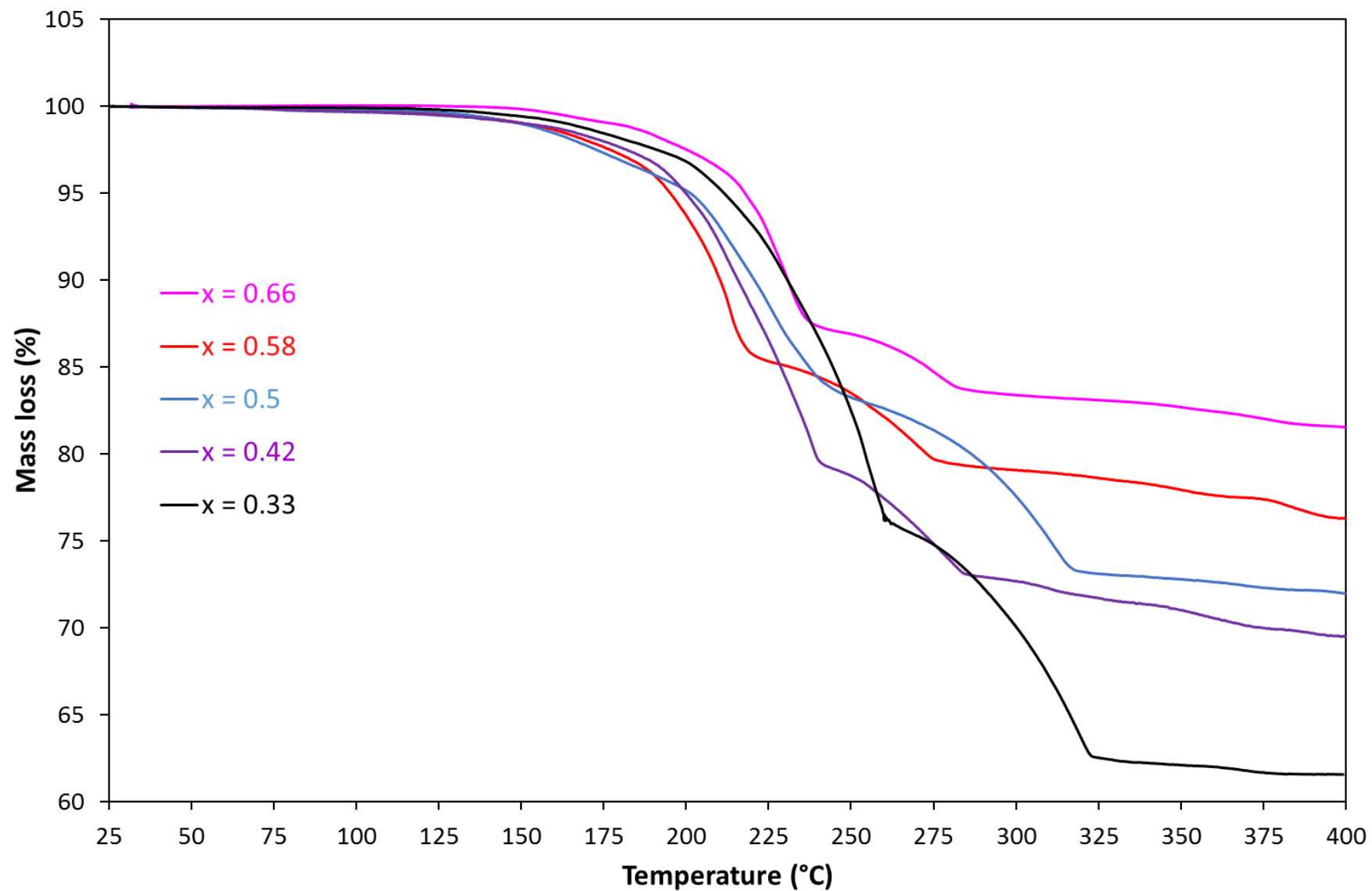


Figure 5-24: TGA mass loss profiles of $(1-x)\text{NH}_4\text{Cl} + x\text{MgH}_2$ samples heated at 2°C min^{-1} where $x = 0.33$ (black), 0.42 (purple), 0.5 (blue), 0.58 (red) and 0.66 (pink).

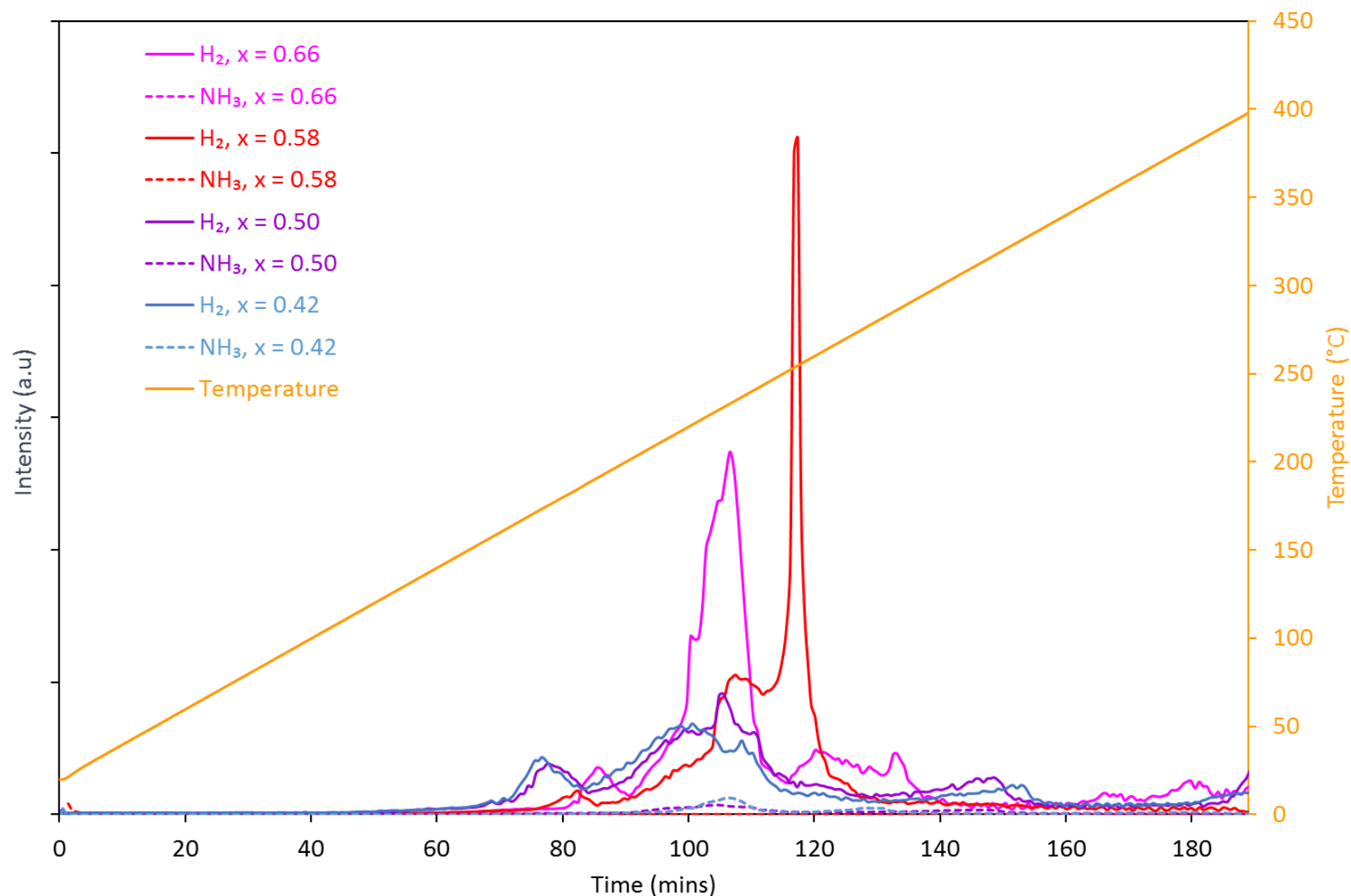


Figure 5-25: MS traces from TGA experiments of $(1-x)\text{NH}_4\text{Cl} + x\text{MgH}_2$ samples heated at heated at 2°C min^{-1} where $x = 0.66$ (pink), $x = 0.58$ (red), $x = 0.50$ (purple), $x = 0.42$ (blue), $x = 0.33$ (black) showing gas release against time, H_2 (solid lines), NH_3 (dashed) and temperature (orange).

The corresponding mass spectrometry traces from the samples are shown in Figure 5-25. Similar to the data observed from most of TPD-MS experiments, the ammonia loss observed via mass spectrometry was undetectable or around 100 times lower than the hydrogen trace for all samples. When the samples were MgH_2 rich, ($x = 0.583$ and 0.66), no trace of ammonia release was observed at all. The hydrogen release from samples where $x = 0.5$ and 0.42 was very similar. As the MgH_2 content was increased to $x = 0.58$, the peak temperature of hydrogen release increased to around 250°C . Then, as the MgH_2 content was further increased the peak temperature was reduced to 235°C . This indicated that when $x = 0.66$, the desorption pathway was quite different which was supported by the changes observed in the powder XRD patterns when $x = 0.66$ was reached.

In order to suggest some equations to account for the gas release occurring in these samples, the number of moles of hydrogen and ammonia released from each sample first need to be calculated. As the TGA is a gravimetric not volumetric technique, and the masses of each compound within the samples varied depending on the starting ratio, the theoretical wt% accounted for by one mol of H_2 and NH_3 was different for each sample. A comparison has been made in Table 5-5 of the total hydrogen content available in each sample and how much mass loss a mole of H_2 or NH_3 would account for when desorbed from a sample in terms of the value of x .

As the starting mass of the samples before TGA experiments was recorded and the gas stream output from the TGA experiments was monitored by mass spectrometry, pseudo-gravimetric calculations using calibrated mass spectrometry data can be performed to resolve the wt% of hydrogen lost from the sample. The temperature-resolved mass loss solely attributed to hydrogen is shown in Figure 5-26. The number of moles of hydrogen (and ammonia by process of elimination) were then calculated (Table 5-6) according to the wt% values in Table 5-5.

Magnesium hydride content (x)	Total H₂ Content (wt% / no. of moles)	Mass loss (wt%) corresponding to a mol of H₂	Mass loss (wt%) corresponding to a mol of NH₃
0.33	7.50 / 5	1.50	12.76
0.42	7.51 / 4.75	1.58	13.44
0.50	7.52 / 4.5	1.67	14.20
0.58	7.53 / 4.25	1.77	15.06
0.66	7.54 / 4	1.89	16.02

Table 5-5: Comparison of theoretical wt% mass loss corresponding to one mole of ammonia and hydrogen when the amount of MgH₂ was varied

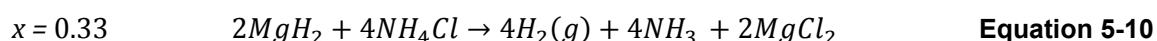
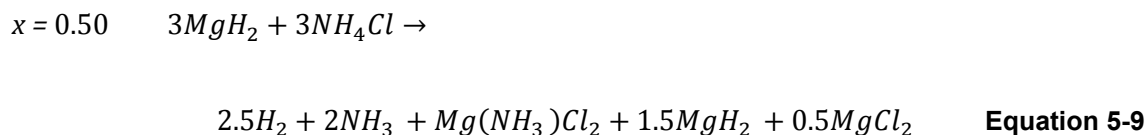
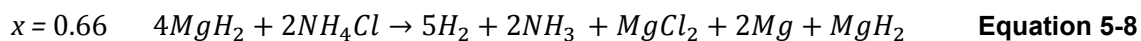
The calculated number of moles of each gas and inferred wt% mass loss of ammonia are displayed in Table 5-6. The ammonia mass loss values were calculated based on the assumption that all remaining mass loss was caused by ammonia. The figures in Table 5-6 show that although the calculated wt% of hydrogen varied (Figure 5-26); the number of moles of hydrogen released in all experiments was very similar.

Magnesium hydride content (x)	Number of moles of H₂	Inferred mass loss (wt%) attributed to NH₃	Corresponding number of moles of NH₃
0.42	2.35	26.78	2
0.50	2.43	23.94	1.7
0.58	2.63	19.36	1.28
0.66	2.30	13.79	0.86

Table 5-6: Comparison of the calculated mass loss in moles attributed to ammonia and hydrogen.

This would suggest that the ammonia release was mainly responsible for the changes in overall mass loss as previously suggested. Some possible equations for desorption reactions for various values of x are suggested taking into account the ratio of hydrogen to ammonia in Table 5-6 and are shown in Equations 5-8 to 5-10. Even though mass spectrometry data was not

available for $x = 0.33$, a hypothesised equation has been presented based on the results available and the trend observed.



While the equation proposed for $x = 0.66$ seems reasonable, when the NH_4Cl content was increased to $x = 0.50$, it became increasingly difficult to account for the chloride content in the sample after desorption without the formation of $Mg(NH_3)_2Cl_2$ in order to roughly maintain the calculated molar ratio of hydrogen to ammonia in Table 5-6.

When $x = 0.33$, the ratio of chloride to magnesium meant that both of these components could be simply accounted for by the formation of $MgCl_2$. As $MgCl_2$ can act as an ammonia sink, through the formation of magnesium ammoniate chloride phases, the equations for the ratio of starting materials can be easily explained. Although ammonia release is shown in Equation 5-10, an in-situ reaction which incorporates the released ammonia during heating, into a solid-state compound could mean that only hydrogen would be observed in the mass spectrometry trace.

The reaction when $x = 0.33$ was the only reaction which could be balanced to consume all starting materials which would suggest that this would be the preferred stoichiometry for this system.

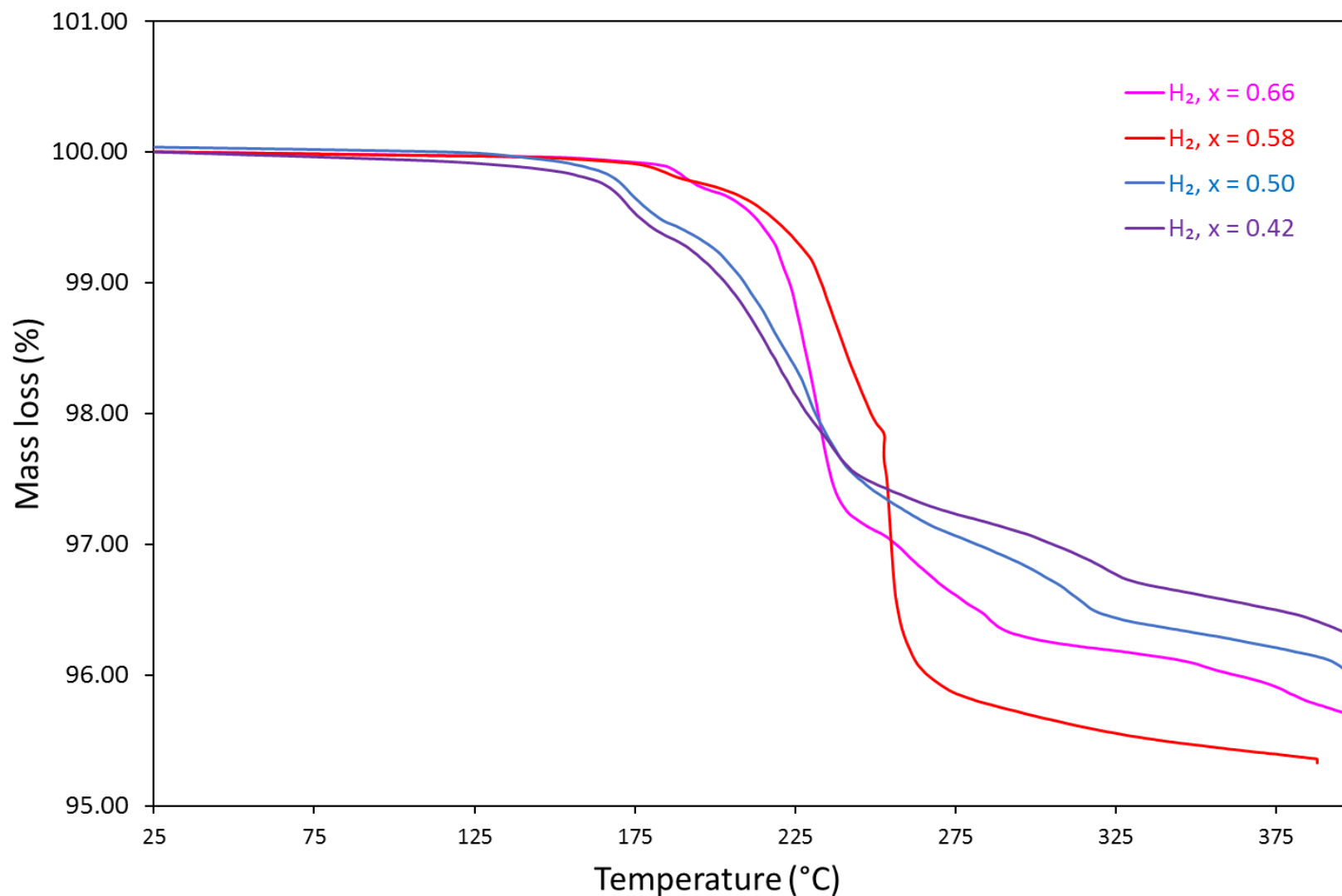


Figure 5-26: Calculated hydrogen mass loss profiles derived from mass spectrometry data of $(1-x)\text{NH}_4\text{Cl} + x\text{MgH}_2$ samples where, $x = 0.42$ (purple), 0.5 (blue), 0.58 (red) and 0.66 (pink).

5.9.3 Post-desorption powder XRD

Room temperature powder XRD data of re-ground samples were collected after a small number desorption experiments. The heating regimes in these experiments were quite different to that used to prepare samples in vertical furnaces, and as such post-desorption powder XRD data often shows considerable differences to samples which were prepared under flowing argon and longer, less variable heating durations. These differences were caused by several factors: the nature of gas flow and equilibrium conditions of the exhaust gases, speed of sample cooling, but mostly the heating duration and ultimate temperature reached. Difficulties were encountered in recording data of some TGA samples due to the small amounts of sample used in these desorption experiments.

Post desorption (TGA) powder XRD was recorded at room temperature of several samples. When $x = 0.42$, a large amount of MgCl_2 was observed and a small amount of NH_4Cl remained in the powder XRD pattern (Figure 5-27). As TGA experiments reach temperatures of 400°C , MgCl_2 would have been the expected major product. Even if phases such as ammoniate chlorides had been formed *in-situ*, ammonia would have been released below 400°C , although due to stoichiometry, a further magnesium containing phase, either MgNH , Mg_2N_3 or Mg metal would have been expected.

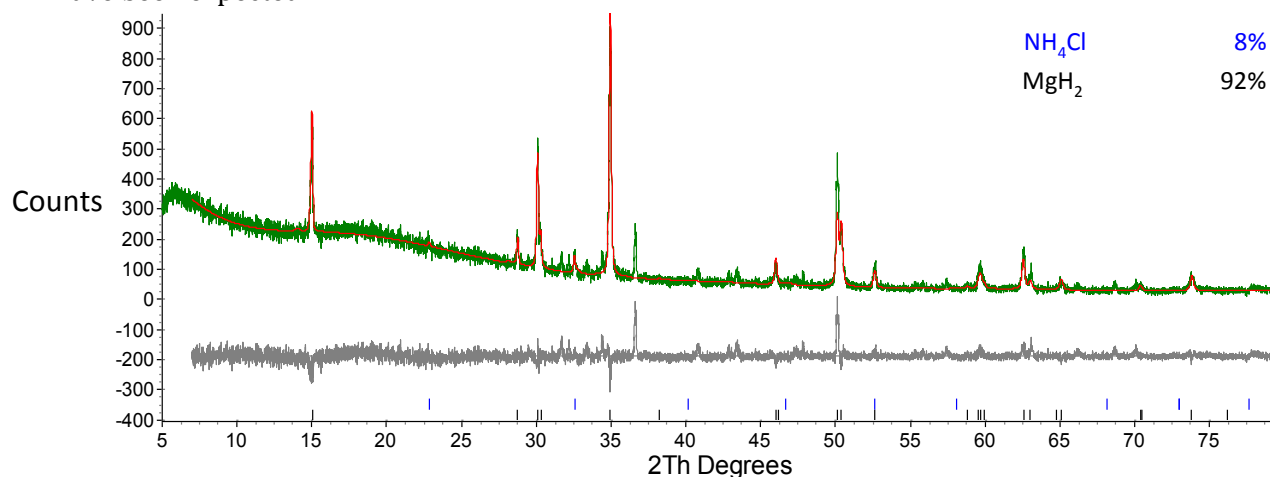
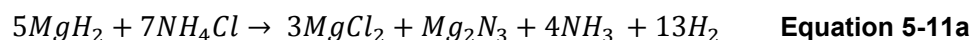
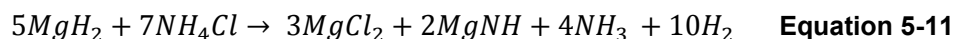


Figure 5-27: Post TGA–MS powder XRD pattern of $(1-x)\text{NH}_4\text{Cl} + x\text{MgH}_2$ sample where $x = 0.42$ and the sample was heated to 400°C . Rietveld fit showing the difference (grey), calculated (red) and observed (green) traces with peak positions indicated for NH_4Cl (blue) and MgCl_2 (black).

Equations leading to these products are suggested in 5-11 and 5-11a.



Post desorption (TPD) powder XRD data was also recorded of the NH_4Cl and $2LiH$ sample (Figure 5-28). The main desorption product was identified as $LiCl$ and low amounts of both starting materials remained. Significant ammonia release during the desorption experiment coupled to the production of $LiCl$ renders this system largely irreversible, as nitrogen needed to trap hydrogen atoms upon hydrogenation to NH_4Cl or imide/amide anions was lost in the form of ammonia. Once formed $LiCl$ is largely unreactive and currently there are no reports that it can form an ammoniate halide type phase like the magnesium cation does.

During work carried out on reactions between $LiNH_2$ and $LiCl$, Davies¹³⁹ identified an additional phase which was refined to a cubic unit cell. The space group was also found to be $Fm\bar{3}m$, but the lattice parameter was found to be $4.6665(3) \text{ \AA}$, between that of Li_2O , $LiCl$ and Li_2NH , the largest of which is $LiCl$, where $a = 5.1295(4) \text{ \AA}$. An additional $Fm\bar{3}m$ phase was identified, where $a = 5.2298(6) \text{ \AA}$. It is likely this phase is related to $LiCl$ with some sort of cross substitution of the anions, but a fit using structural information could not be resolved.

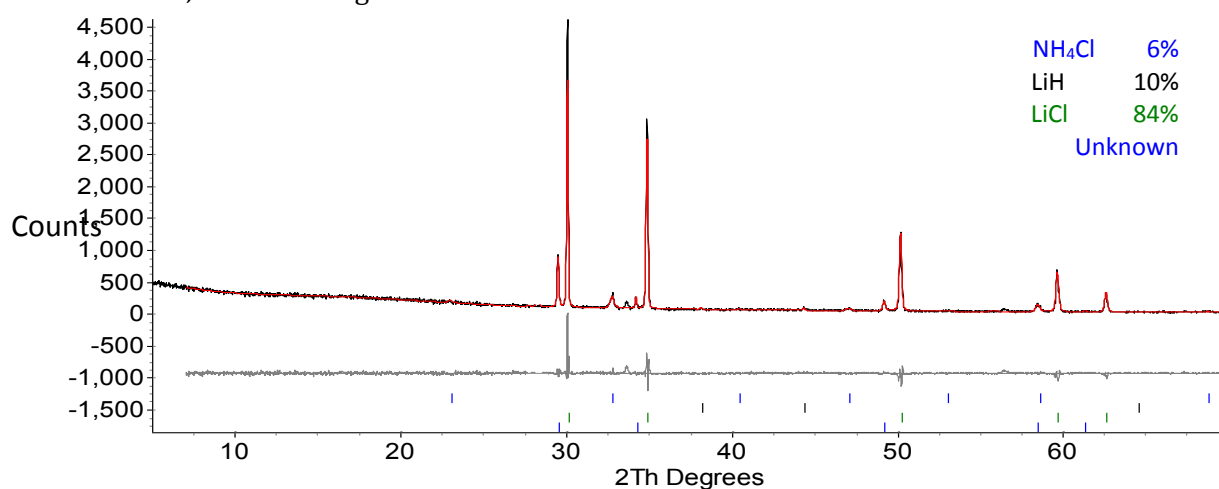
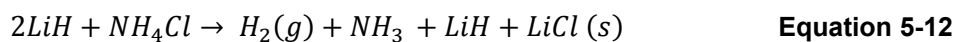


Figure 5-28: Post TPD-MS powder XRD pattern of $NH_4Cl + 2LiH$ sample. Rietveld fit showing the difference (grey), calculated (red) and observed (blue) traces with peak positions indicated for NH_4Cl (blue), LiH (black), $LiCl$ (green) and unknown $Fm\bar{3}m$ phase (blue).

The production of a chloride-containing product is in good agreement with the proposed reaction suggested by Equation 5-12 and would indicate Cl_2 or HCl gas were not produced in this reaction.



5.9.4 Desorption Summary

Two desorption methods, TPD and TGA have been used to measure the desorption characteristics of the same samples. In both cases, although a range of gaseous desorption products were scanned, those observed by mass spectrometry were limited to hydrogen and ammonia. The differences between methods can be accounted for by the setup of equipment; the nature of heating and the gaseous environment that the sample desorbs into can affect the gaseous equilibrium conditions. Many of the resulting mass spectrometry ammonia traces showed little evidence of ammonia desorption, however, the mass losses observed in TGA-MS experiments cannot be accounted for only by hydrogen desorption.

A relative comparison of height of the smaller low temperature hydrogen peak (centred around 190°C) in Figure 5-18, Figure 5-19 and Figure 5-20 shows that the intensity was reduced as the ratio of reactants deviated away from close to $x = 0.5$. As x was reduced across the whole range of samples (Figure 5-18, Figure 5-19 and Figure 5-20), the intensity of the second higher temperature peak at $\sim 240^\circ\text{C}$ was also reduced. All samples tested showed a large hydrogen desorption at around 225°C which was maximised when $x = 0.33$. This correlates well to a significant change in the powder XRD data which was recorded when samples were heated to temperatures around this area.

Overall, TPD-MS data (Section 5.9.1) has shown that multiple reactions involving the release of hydrogen and ammonia occurred for all systems tested. By combining NH_4Cl and MgH_2 , the individual decomposition and desorption properties of each component were altered.

Desorption events for all samples happened at temperatures that are considerably below those expected to be required to thermally decompose either NH_4Cl or MgH_2 .

In some of the repeated TPD–MS experiments, a second area of hydrogen desorption was observed to begin around 360°C and increased in intensity as the temperature increased towards 400°C . It is likely that the second peak may correspond to desorption of any remaining hydrogen from MgH_2 as this has been observed to be reasonably rapid at 375°C under vacuum¹⁷⁷. This could be due to inhomogeneity caused by poor mixing of the sample.

TGA experiments conducted showed that all the samples followed a similar stepwise trend in the masses lost with four steps observed in each mass profile. When the samples were magnesium hydride rich, i.e. $x \geq 0.58$, the mass loss was 8 wt% less than when $x \leq 0.50$. The difference in mass loss was caused by differences in the amount of ammonia release and was mainly accounted for in the 2nd step of mass loss. Despite differences in total mass loss, the samples began to desorb gas at very similar temperatures, around 150°C and lost similar masses in later steps. The total amount of hydrogen desorbed was very similar for all samples (see Table 5-6).

Both desorption methods described above showed that multiple gas release steps occurred at similar temperatures. Considering both the desorption data and post-desorption powder XRD patterns, it is possible that the type of gas lost is a reflection of the ability of the solid-state components in the sample for example MgCl_2 , to react with gaseous ammonia to form compounds that incorporate ammonium ions.

5.10 Rehydrogenation

Rehydrogenation of several samples was attempted in a home-made hydrogenation reactor previously described. The effects of attempted rehydrogenation on samples from TPD-MS and flowing line experiments were compared. The powder XRD pattern in Figure 5-29 was recorded after the attempted rehydrogenation of an NH_4Cl and MgH_2 sample, which had previously been heated to 200°C for 12 hours on a flowing line experiment. The inset powder XRD pattern was added to show that the rehydrogenation experiment changed the composition of the sample. However, as MgH_2 was present in the sample before rehydrogenation, (see inset in Figure 5-29) it cannot be concluded that hydrogen uptake did occur as no other hydrogen containing phases were identified after rehydrogenation.

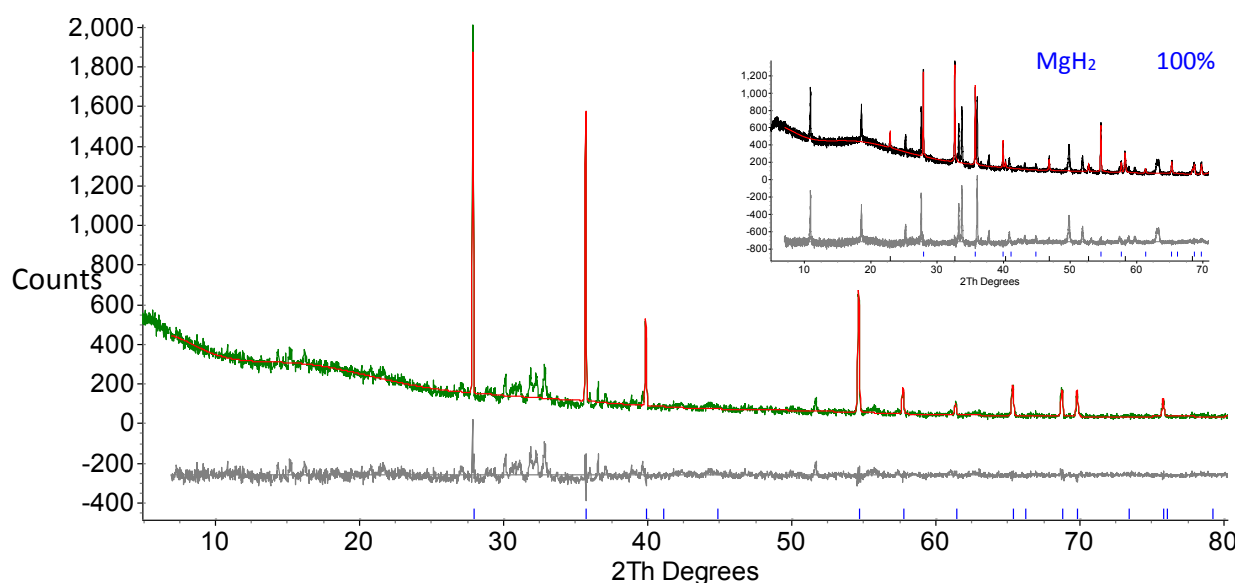


Figure 5-29: Post rehydrogenation powder XRD pattern of NH_4Cl + MgH_2 sample heated to 200°C and held for 24 hours under 100 bar H_2 . Rietveld fit showing the difference (grey), calculated (red) and observed (teal) traces with peak positions indicated for MgH_2 (blue). Inset: powder XRD pattern recorded before rehydrogenation.

The powder XRD pattern in Figure 5-29 was recorded after attempted rehydrogenation of an NH_4Cl and MgH_2 sample that had previously been heated to 325°C for 12 hours on a flowing line experiment. Although a Rietveld fit is not shown for either pattern, few differences were identified between the powder XRD patterns. The intensities of the peaks were very similar in both after both experiments, although the background signal was higher after rehydrogenation.

One additional peak, (indicated) was observed after the rehydrogenation experiment; however, this could not be assigned to a phase. Although hydrogenation did not occur, the hydrogen overpressure stopped any further reactions or degradation of the sample in this experiment.

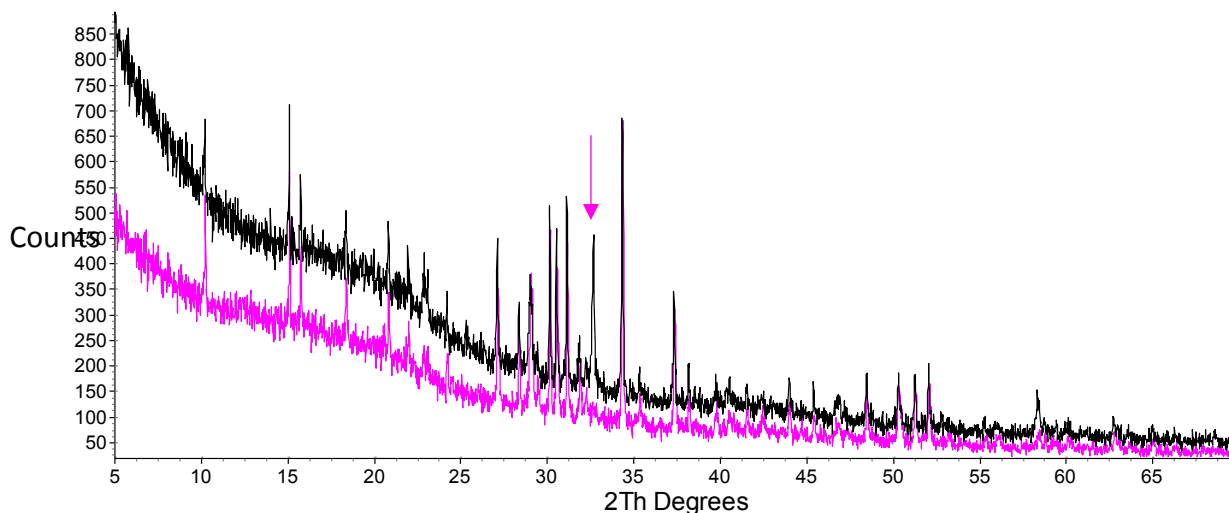


Figure 5-30: Pre- (pink) and post- (black) rehydrogenation powder XRD patterns of an $\text{NH}_4\text{Cl} + \text{MgH}_2$ sample heated to 200°C and held for 24 hours under 100 bar H_2 .

From powder XRD displayed in Figure 5-30 as well as other attempts to re-hydrogenate further samples, it appears that if the sample was initially heated to over 220°C either in flowing line or TPD-MS experiments, the hydrogenations carried out did not change the powder XRD patterns recorded afterwards. This would indicate that when reaction temperatures of over 220°C were used, desorption rendered the samples irreversible. This temperature corresponds well to a large exothermic event in the DSC reaction profiles as well as the largest mass loss step in the TGA profiles, consistent with the hypothesis that once ammonia has been lost from samples, rehydrogenation cannot be achieved.

5.11 Crystal structure determination

A clearly defined set of peaks was observed at low temperatures, and these were clearly visible in Figure 5-2. Further comparisons using the stacked powder XRD plot in Figure 5-5 and visual inspection of the other patterns confirmed that the relative intensities and peak shapes of these peaks seemed consistent at different reaction temperatures and varying stoichiometries.

indicating that a single phase was producing the peaks. Unfortunately, several attempts to synthesise this phase in isolation were unsuccessful.

It was initially thought this phase may belong to the ammoniate-halide family. It has previously been reported that magnesium ammoniate-halides have been formed from reactions between ammonium chloride or ammonia and magnesium hydride. The structures of $\text{Mg}(\text{NH}_3)_6\text{Br}_2$, $\text{Mg}(\text{NH}_3)_6\text{I}_2$ and $\text{Mg}(\text{NH}_3)_x\text{Cl}_2$ where $x = 2$ and 6 have been solved^{109, 187}. Several transition metal ammoniate-halide type compounds, such as $\text{Mn}(\text{NH}_3)_x\text{Cl}_2$ ¹⁸⁷ and $\text{Zn}(\text{NH}_3)_2\text{Cl}_2$ ¹⁹¹ have been synthesised, where $x = 2$ and 6 . These compounds have also been produced including different halides such as bromine and fluorine. These ammoniate-halide type compounds, (where $x = 6$) have been identified as cubic structures belonging to the space group *Fm-3m* with a lattice parameter around 10 Å. The corresponding $\text{Mg}(\text{NH}_3)_6\text{Cl}_2$ phase is also isostructural with these compounds. However, the peaks associated with these known phases were not the same as those observed. Powder X-ray diffraction data of a typical sample including this phase was loaded into a borosilicate capillary and collected at Diamond Light Source on I11 beamline.

5.11.1 Indexing

Investigations using various analysis techniques discussed earlier in Chapter 5 were used to collect information about the desorption products of the reaction(s) and energy changes during the formation of these peaks. This information was used in order to attempt elucidate possible compositions of this new phase and to look at solving the structure.

The peak positions and intensities were assigned and refined using a peak fitting regime in Topas¹¹⁹. The systematic reflection absences in the diffraction pattern indicated that the phase is body centred. Indexing the peak positions through the configuration available in Topas¹⁹² suggested that the most likely space groups were either orthorhombic or tetragonal and included *I222* (23), *Ima2* (46), *I4* (79), *I4₁* (80) and *I4cm* (108). The top indexing solutions are provided in Table 5-7.

Space Group	Number of unindexed peaks	Cell Volume (Å ³)	a Lattice parameter (Å)	b Lattice parameter (Å)	c Lattice parameter (Å)
<i>I4cm</i>	6	400.834	4.9820	$a = b$	16.1495
<i>I4</i>	3	400.834	4.9820	$a = b$	16.1495
<i>Ibcm</i>	7	400.808	16.1496	4.9822	4.9815
<i>Ima2</i>	3	400.790	16.1494	4.9821	4.9814
<i>I4₁</i>	5	400.869	4.9820	$a = b$	16.1510
<i>Ima2</i>	3	400.800	16.1493	4.9816	4.9820
<i>I222</i>	3	400.790	16.1494	4.9820	4.9821

Table 5-7: Top indexing results from Topas²⁷

The lattice parameters from the synchrotron data were refined using a model-independent (Pawley) fit to $a \approx b = 4.98 \text{ \AA}$ and $c = 16.15 \text{ \AA}$ with a unit cell volume of $\sim 400 \text{ \AA}^3$. The c lattice parameter is reasonably large but a big unit-cell is not uncommon in the field of complex hydrides, for example, $\text{Li}_4\text{BH}_4(\text{NH}_2)_3$ ¹⁰² and $\text{Li}_2\text{BH}_4\text{NH}_2$ ¹⁹³, as well as amides such as $\text{Mg}(\text{NH}_2)_2$ all have large unit cell volumes. The number of un-indexed peaks in each space group was considered by graphically comparing the simulated results to the observed data. The improvement in the quality of the calculated fit to observed data when moving from a tetragonal to orthorhombic space group was negligible, indicating that the any orthorhombic distortion (if present) was minimal. Therefore, the higher symmetry tetragonal space groups were selected for Pawley refinements. Comparison of the Pawley refinements using the three tetragonal space groups suggested by Topas gave the best fit to the majority of un-assigned peaks using *I4*. The fit is shown in Figure 5-31.

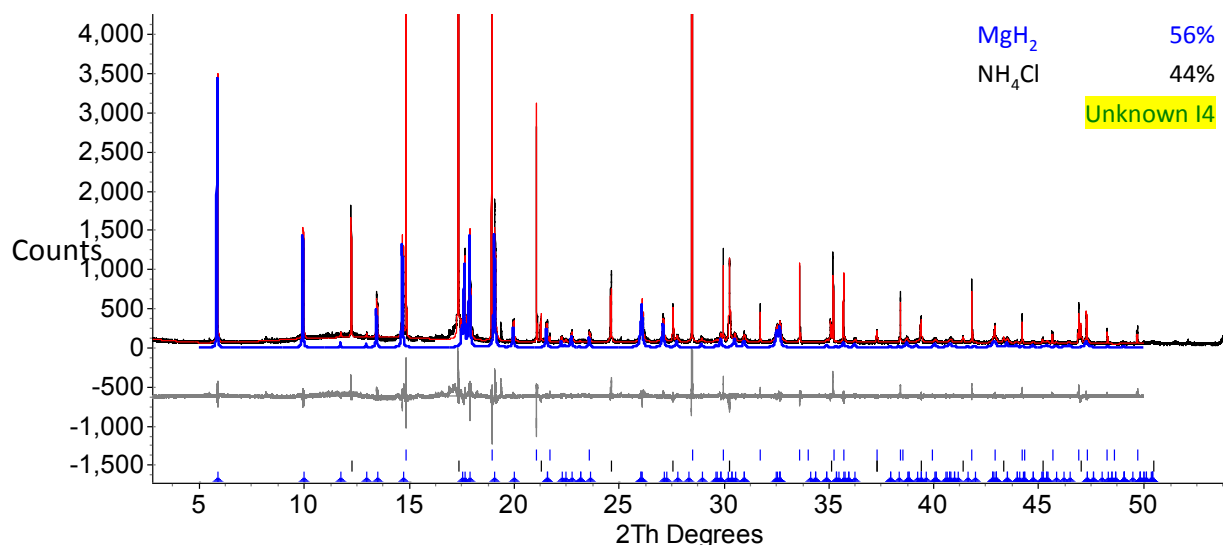


Figure 5-31: Synchrotron powder XRD pattern of NH₄Cl + MgH₂ sample heated at 200°C for 12 hours with a combination of Rietveld and Pawley fits showing the difference (grey), calculated (red) and observed (black) traces with peak positions indicated for MgH₂ (blue), NH₄Cl (black) and the unknown tetragonal phase-space group *I4* (blue and highlighted).

All the body centred space groups which gave rise to different patterns of systematic absences were tested to determine whether other space groups could give an equivalent fit. A graphical depiction of these peak positions arising from these space groups is shown in Figure 5-32. The peak at $\sim 6^\circ$ is a good indication of how well a space group fits to the observed peaks. *I4* matched the most observed peaks, and *P4* was also tested to determine whether any other of the smaller peaks could be indexed by the same unit cell in lower symmetry, but no additional peaks were indexed with this lower symmetry space group. For example, refinements in *I4cm* gave absences at *hkl*s (101), (103), (105) and (107) *etc.*, which were evident in the observed diffraction pattern. Space groups that had equivalent systematic *hkl* absences¹⁹⁴ to the body-centred tetragonal space group, *I4* were consequently the focus for further structure solution work. These were *I4*, *I-4*, *I4/m*, *I422*, *I4mm*, *I-4m2*, *I-42m* and *I4/mmm*.

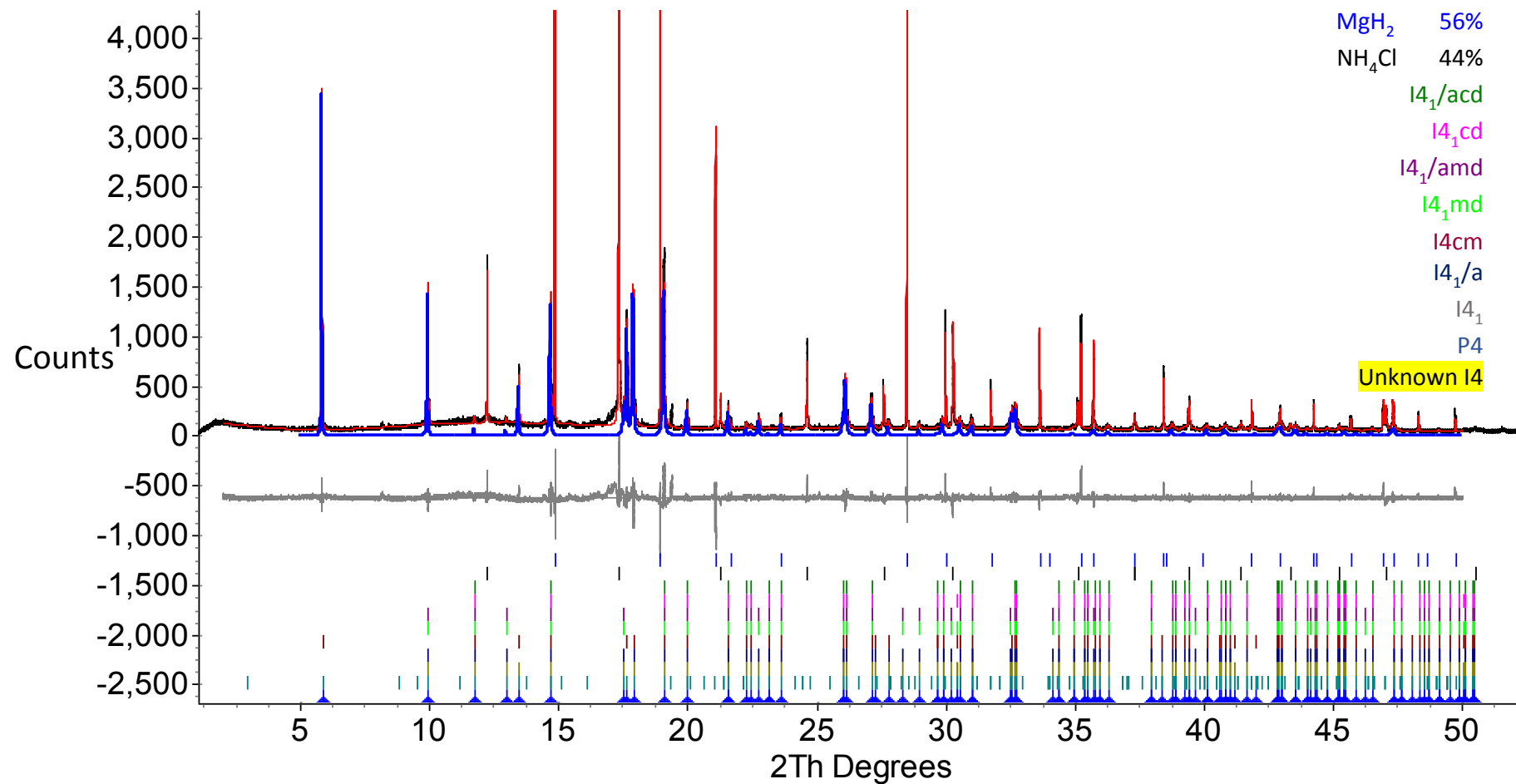


Figure 5-32: Synchrotron powder XRD pattern of NH₄Cl + MgH₂ sample heated at 200°C for 12 hours with a combination of Rietveld and Pawley fits showing the difference (grey), calculated (red) and observed (black) traces with peak positions indicated for MgH₂ (blue), NH₄Cl (black) and peak positions that would correspond to possible body-centred space groups for the unknown tetragonal phase with *I4* (highlighted and blue).

As previously shown in Sections 5.3 and 5.4, this phase was observed across the temperature range 185-215°C, as well as a small composition range. The variation in cell volume (calculated from laboratory powder XRD) was minimal (within 0.7%) over all of the samples containing this phase. The cell parameters and volume derived from several Pawley fits using *I4* from $(1-x)\text{NH}_4\text{Cl} + x\text{MgH}_2$ samples when $x = 0.5$ are listed in Table 5-8.

Temperature heated (°C)	a Lattice parameter (Å)	c Lattice parameter (Å)	Cell Volume (Å ³)
215	4.9741(6)	16.125(3)	398.9(1)
205	4.9747(7)	16.128(3)	399.1(1)
195	4.9625(8)	16.095(3)	396.2(1)
185	4.9748(9)	16.129(3)	399.1(2)

Table 5-8: Variation in lattice parameters and unit cell volume for the unknown tetragonal phase using space group *I4* observed from Pawley refinement of laboratory powder XRD data after heating $(1-x)\text{NH}_4\text{Cl} + x\text{MgH}_2$ samples when $x = 0.5$ for 12 hours.

5.11.2 Producing a model

Ideally, the composition of an unknown phase would be found if a pure phase was formed from known quantities of starting materials. Although it had not been found possible to produce the phase without starting material impurities, the observed remaining wt% and calculated mol% of the starting materials, MgH_2 and NH_4Cl should give an indication to the contents and composition of the unknown phase based on the amounts consumed. Quantitative phase analysis through Rietveld refinement of the known phases gave estimated amounts of MgH_2 and NH_4Cl of approximately 72 mol% to 28 mol% respectively. This meant the products were MgH_2 -rich relative to the 50 mol% to 50mol% starting mixture ratio, indicating that the composition of the unknown phase has a higher component from NH_4Cl than MgH_2 . Desorption data also indicated that the formation of this phase had been accompanied by a desorption event, composed mainly of hydrogen.

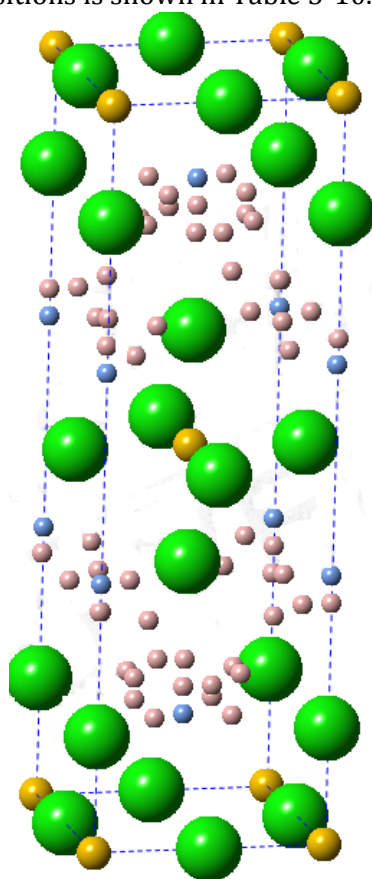
As this phase did not bear many similarities to expected phases, the volumes of the formula units from the starting materials, MgH_2 and NH_4Cl were considered as well as the formula unit volumes from $\text{Mg}(\text{NH}_3)_2\text{Cl}_2$ and $\text{Mg}(\text{NH}_3)_6\text{Cl}_2$, the only known combinations of these elements in a phase of this type. These are displayed in Table 5-9. As the unknown phase preceded the formation of $\text{Mg}(\text{NH}_3)_2\text{Cl}_2$ it was possible that it had a higher hydrogen content. Dependant on the type of cell expected, the Z number of the unknown phase is likely to be 2, 4 or 8.

Phase	Approximate formula unit volume (\AA^3)
MgH_2	31
NH_4Cl (room temperature)	58
NH_4Cl (high temperature)	70
$\text{Mg}(\text{NH}_2)_2$	68
MgNH	36
$\text{Mg}(\text{NH}_3)_2\text{Cl}_2$	126
$\text{Mg}(\text{NH}_3)_6\text{Cl}_2$	264
$\text{Mg}(\text{NH}_4)_2\text{F}_4$	114
$\text{Sr}(\text{NH}_4)_2\text{Cl}_4$	183

Table 5-9: Comparison of formula unit volumes of associated phases in this work.

A literature search was also carried out to examine the possibility of phases which might contain alternative halides as well as nitrogen, hydrogen and magnesium. Interestingly, $\text{Mg}(\text{NH}_4)_2\text{F}_4$, a phase which belonged to space group $I4/mmm$, one of the suggested space groups was found. This phase is a layered perovskite K_2NiF_4 -type structure. The structure of this phase was used as a starting point for the Rietveld refinement of the unknown phase on the assumption that the F^- anion was directly replaced by Cl^- anion. Although there are no reported magnesium ammonium chloride phases there are a few of alkali metal ammonium chlorides known; $\text{Ca}(\text{NH}_4)\text{Cl}_3$ ¹⁹⁵ and $\text{Sr}(\text{NH}_4)_2\text{Cl}_4$.

Initially the atoms were tested on the positions taken from the $\text{Mg}(\text{NH}_4)_2\text{F}_4$ structure, ($R_{\text{wp}} = 16.571$) and the hydrogens were not included in the refinement. The positions of the atoms not on special sites, nitrogen and chlorine positions were allowed to refine ($R_{\text{wp}} = 14.441$) and remained on the same sites. The occupancies of these atoms were then refined. The magnesium and nitrogen sites remained fully occupied whilst the chlorine sites were found to be slightly deficient ($R_{\text{wp}} = 14.211$). The hydrogen positions from the original structure were then added back into the refinement ($R_{\text{wp}} = 13.739$). The Rietveld refinement for cation and anion positions is shown in Table 5-10.



Atom	Site	x	y	z	Occupancy
Mg	2a	0	0	0	1
Cl1	4e	0	0	0.1558 (2)	0.904 (1)
Cl2	4c	0.5	0	0	0.905 (1)
N	4e	0.5	0.5	0.8549 (8)	1
H1	4e	0.5	0.5	0.7675	1
H2	32o	0.7289	0.5613	0.8659	0.25
H3	16m	0.3324	0.6675	0.8659	0.25

Table 5-10: Refined crystallographic data for $\text{Mg}(\text{NH}_4)_2\text{Cl}_4$, Space group $I4/mmm$, $a = 4.98256$ (9) Å, $c = 16.1508$ (3) Å $R_{\text{wp}} = 13.739$, $R_{\text{exp}} = 6.371$, $\chi^2 = 4.648$

Figure 5-33: Structure for $\text{Mg}(\text{NH}_4)_2\text{Cl}_4$ from atomic positions shown in Table 5-10 showing Cl, Mg, N and H positions in green, yellow, blue and pink respectively.

The structure is based around MgCl_2 octahedra centred at $\frac{1}{2}$, $\frac{1}{2}$, $\frac{1}{2}$ in the unit cell. The Cl-Mg-Cl distance in MgCl_2 was very similar to the a lattice parameter in the tetragonal phase so the geometry seems chemically sensible. The final fit to the data is shown in Figure 5-34.

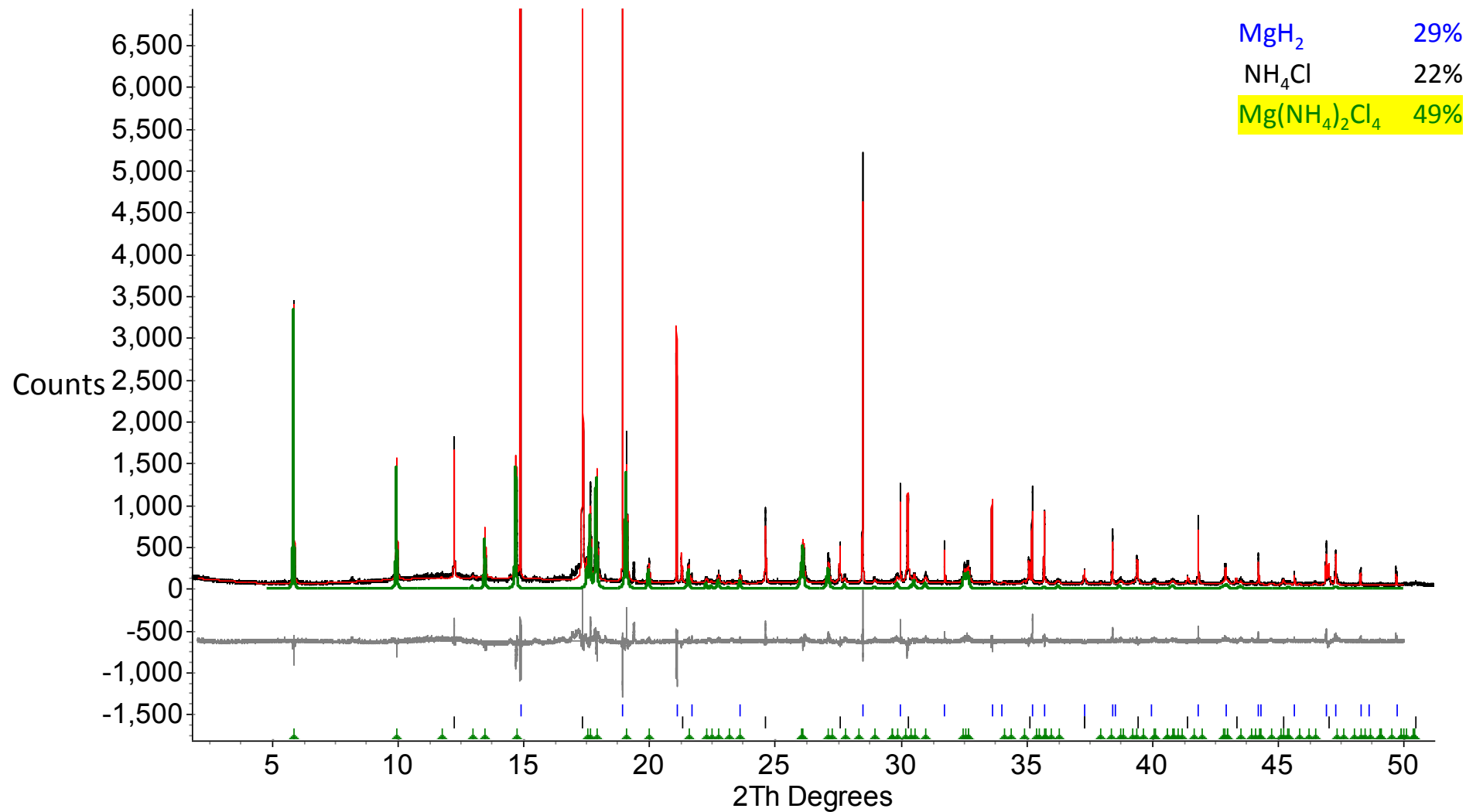


Figure 5-34: Synchrotron powder XRD pattern of NH₄Cl + MgH₂ sample heated at 200°C for 12 hours with Rietveld fit showing the difference (grey), calculated (red) and observed (black) traces with peak positions indicated for indicated for MgH₂ (blue), NH₄Cl (black) and Mg(NH₄)₂Cl₄ (highlighted and green).

A few unfitted peaks were still observed in Figure 5-34. Sublias *et al.*¹⁹⁶ observed a side product, $\text{Mg}(\text{NH}_4)\text{F}_3$ during the synthesis of $\text{Mg}(\text{NH}_4)_2\text{F}_4$, however the peak positions of this phases were not in good agreement with the unfitted peaks produced in this work.

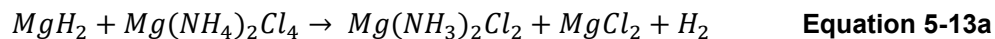
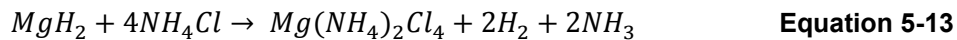
5.12 Discussion

Data have been recorded using a large range of techniques and analysis presented above in Sections 5.3-5.10, mainly in regard to the $(1-x)\text{NH}_4\text{Cl} + x\text{MgH}_2$ system. There is an absence of literature which directly considers the capacity of this solid-state system as a hydrogen store. Some previous work had concentrated on use of the hexa-ammoniate chloride as an ammonia store, but delivers conflicting information about the degree of ammonia desorption at varying temperatures^{109, 184}. This work concentrates on novel structural transitions observed and the varied desorption pathways which can provide both ammonia and hydrogen. The majority of results present a consistent viewpoint of the system and relate temperatures, phase changes, thermal events and corresponding gas releases.

The first change observed in the system was consistently found at 180°C. This correlates closely to the temperature of the phase transition of NH_4Cl ¹⁹⁷. Across a range of x , the formation of a body-centred tetragonal phase was observed in powder XRD patterns. The formation of this phase was preceded by an endothermic event. This was likely due to the ammonium chloride phase transition. The observation of an endothermic event was caused by mass loss (i.e. hydrogen) during a chemical reaction, as the work of gas expansion dominates. The large exothermic peak observed appeared to have several contributing reactions. This was likely due to the crystallisation of the identified tetragonal phase and subsequently a side reaction to form $\text{Mg}(\text{NH}_3)_2\text{Cl}_2$.

According to calculations based on the mass spectrometry data recorded during the TGA experiment, approximately two and half moles of hydrogen were desorbed from most samples. In

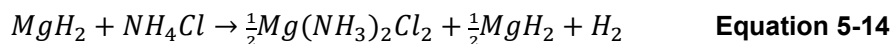
light of the identification of $Mg(NH_4)_2Cl_4$ as the unknown phase, possible equations for the formation of this phase and subsequent reactions to form $Mg(NH_3)_2Cl_2$ are presented in Equations 5-13 and 5-13a.



The reaction proposed in Equations 5-13 and 5-13a offer a potential route of reaction of the reagents and decomposition of phases formed which account for hydrogen and ammonia release observed in desorption experiments. $Mg(NH_4)_2Cl_4$ was observed at lower temperatures in powder XRD experiments, (Figure 5-3:) and crucially before $Mg(NH_3)_2Cl_2$, these reactions would be in good agreement with the suggested equations.

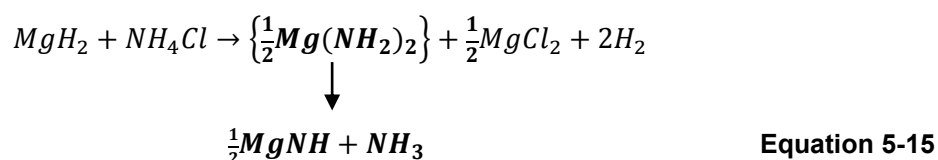
Further desorption from $Mg(NH_3)_2Cl_2$ would likely lead to formation of $MgCl_2$ and ammonia desorption if this was the sole reaction. As both MgH_2 and NH_4Cl were found by powder XRD to remain in many samples after the tetragonal phase was formed, a more probable explanation would be that Equation 5-13 only accounts for part of the sample.

In several samples, $Mg(NH_3)_2Cl_2$ was identified by powder XRD. The formation of $Mg(NH_3)_2Cl_2$ could occur through Equation 5-3 or Equation 5-13a. It appeared to form at slightly higher temperatures than the tetragonal phase, a possible route for when $x = 0.5$ is suggested in Equation 5-14, and previously in Equation 5-3 when $x = 0.33$. When $x = 0.5$ (Equation 5-14) some MgH_2 remains unreacted.

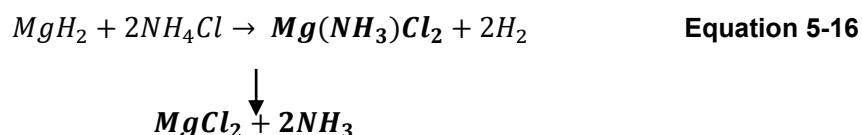


Raman experiments have confirmed the presence of an amide- or possibly ammonium-type phase at lower temperatures; attributed to $Mg(NH_4)_2Cl_4$ or magnesium amide. $Mg(NH_2)_2$ is

often produced as an amorphous product, which may in part explain its absence in powder XRD patterns. If magnesium amide does account for the stretches observed in the Raman experiment a pathway, when $x = 0.5$, that could account for its formation and decomposition is suggested below in Equation 5-15.

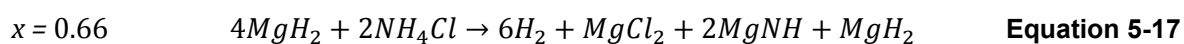


From the data collected when $x = 0.33$, the reactions of the sample are quite different to samples that have a higher magnesium hydride content. This is likely accounted for by the complete desorption pathway below in Equation 5-16.

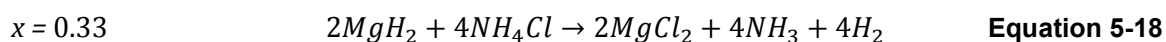


In the two samples where $x \leq 0.42$, a large endothermic feature was observed in the DSC traces, between temperatures of 270°C and 350°C. This was consistent with mass loss and a melting event. When $x \leq 0.42$, due to the ratio of magnesium and chloride, the chances of forming $Mg(NH_3)_2Cl_2$ as a major or sole product are higher than when $x \geq 0.5$. The mass loss is likely to be ammonia from $Mg(NH_3)_2Cl_2$ to produce $MgCl_2$, (or possibly $Mg(NH_3)Cl_2$) and these temperatures are in good agreement with previous desorption findings from this ammoniate system¹⁸⁴. This would also be consistent with TGA data from $x = 0.33$ where the 2nd step of mass loss occurs between 260°C and 325°C. However, this mass loss step only accounts for ~15 wt%, approximately one mole of NH_3 , which implies that $Mg(NH_3)Cl_2$ was more likely to be the product of this reaction. This small endothermic change (gas release) may have been overlapped by the exothermic phase crystallisations.

Li *et al.*¹⁸⁰ suggested that the reaction of MgH₂ with ammonia, where NH₄Cl was used an additive, could directly desorb solely hydrogen, where MgCl₂ and Mg₂N₃ were formed as products, as shown in Equation 5-2. However, even though reaction temperatures of around 400°C were reached in this work, Mg₂N₃ was not observed. If this pathway could be realised when $x = 0.66$, then this system may provide a viable hydrogen store. It is possible that a reaction pathway through magnesium imide where magnesium hydride remains in the sample could occur to enable hydrogen release, but the majority of experiments indicate that significant ammonia release also occurs.



When the ammonium chloride content was increased the pathway through magnesium imide/nitride becomes much less likely due to the difficulty balancing the chloride content in these samples, through the formation of MgCl₂ as gaseous phases containing chlorine were not observed.



As discussed in previous work, the synthesis of Mg(NH₃)₂Cl₂ or Mg(NH₃)₆Cl₂ has not been achieved *via* a solid-state route before. It is documented that the reaction between ammonia and MgCl₂ is reasonably facile and ammonia uptake can begin at temperatures as low as 150°C under 1.5 bar pressure¹⁹⁸.

5.13 Conclusions

During the powder XRD work carried out, a number of unidentified peaks were observed in the diffraction patterns. One new phase, denoted Mg(NH₄)₂Cl₄, was identified and indexed to a body centred cell, with lattice parameters of $a = 4.98 \text{ \AA}$ and $c = 16.15 \text{ \AA}$. The peaks from this phase were present across a temperature range of ~185–225°C and when $0.33 < x < 0.58$, but synthesis

conditions leading to a pure phase, without remaining starting materials were not achieved. Indexing attempts on further patterns suggested some of the unfitted peaks might belong to a face centred phase but this could not be conclusively determined with the quality of data available. There appeared to be similarities in the patterns to powder XRD patterns of ammonium carnallite, so it seems possible that an alternative hydrated ammonium-type magnesium chloride phase could have been formed. Results from Raman spectroscopy and temperature programmed desorption were used to assist in the elucidation of $\text{Mg}(\text{NH}_4)_2\text{Cl}_4$.

Raman data indicated that an amide-type phase was present at ambient temperatures after reactions carried out around 215°C . This could be due to the formation of $\text{Mg}(\text{NH}_2)_2$ or the identified $\text{Mg}(\text{NH}_4)_2\text{Cl}_4$. Raman data collected of a complex phase containing Mg and NH_4^+ ions suggested that a free NH_4^+ ion showed a stretch at 3033 cm^{-1} while a stretch was also observed from the complexed cation at 3015 cm^{-1} ¹⁹⁹. These stretches are close to the ones observed from samples where $\text{Mg}(\text{NH}_4)_2\text{Cl}_4$ was observed. Desorption data concluded that this phase production was accompanied by a gas releasing event. The unknown phase was indexed to a $I4/mmm$ cell and the structure solved to give $\text{Mg}(\text{NH}_4)_2\text{Cl}_4$. It is also possible that another hydrogen-deficient phase may have been made, in a higher temperature range, which has yet to be identified.

Powder XRD data was collected after desorption and hydrogenation experiments. The products identified in powder XRD patterns recorded after desorption experiments varied depending on the method used, TGA or TPD. The materials found in the samples after TGA experiments were more comparable to the products that were expected had desorption followed the suggested pathways, although the products mostly indicated that nitrogen had been lost from the samples, leaving an irreversible system. Powder XRD patterns showed that rehydrogenation experiments on samples that had been heated to temperatures above 220°C were unsuccessful. The post-rehydrogenation powder XRD patterns of samples originally heated at temperatures below 220°C were different to the initial patterns, however, due to MgH_2 being present in both

patterns, it was possible that further desorption occurred during the additional heating cycle, albeit under 100 bar hydrogen pressure.

Desorption and thermogravimetric data across the stoichiometric range of samples were in good agreement with each other and powder XRD. These showed hydrogen and ammonia were lost from all samples across a range where $0.33 < x < 0.66$. Hydrogen release occurred in three clear steps; - desorption started around 180°C and peaked at ~240°C for most samples. Higher starting amounts of MgH_2 promoted lower ammonia release. DSC data showed that several thermal events took place during the heating stages of these experiments which have been attributed to formation and decomposition of a novel tetragonal phase and $\text{Mg}(\text{NH}_3)_2\text{Cl}_2$.

A systematic study using several different analysis techniques has been carried out on a range of samples. All the major phase changes in powder XRD patterns, desorption experiments and DSC thermal events occurred at comparable temperatures. The starting products could not be regenerated after rehydrogenation. From the findings in this work, the $(1-x)\text{NH}_4\text{Cl} + x\text{MgH}_2$ system is not suitable as a reversible hydrogen store although the formation of magnesium ammoniate-chloride phases suggests that this solid-state system may provide alternatives for ammonia absorption and storage.

5.14 Further work

Further experimental work would be carried out to see if the purity of the $\text{Mg}(\text{NH}_4)_2\text{Cl}_4$ phase could be improved, which should assist in structural work on the phase to carry out a full refinement including the hydrogen positions. Additional work on the higher temperature powder XRD patterns observed, specifically those in Figure 5-5 is also needed. The patterns observed were very similar to the one displayed in Figure 5-2 where $\text{Mg}(\text{NH}_3)_2\text{Cl}_2$ was identified but the peaks were at a slightly lower 2θ angle and did not fit easily to the structural model previously proposed for $\text{Mg}(\text{NH}_3)_2\text{Cl}_2$. The phase may be a different ammoniate-chloride or a hydrated ammoniate-

chloride. As it was possible that partially hydrated phase(s) may have been formed, it would be interesting to carry these reactions out under air to see if the phases developed differently. High quality Synchrotron data would be collected for a variety of reaction ratios (NH_4Cl to MgH_2) over a range of temperatures which should allow clearer differentiation of the phases within these samples.

Further work on the reversibility of this system may include investigations into a reaction temperature range, if any, that could be used to desorb hydrogen and lead to a product that has the ability to undergo hydrogenation at moderate temperatures. It would also be interesting to carry out further investigations into reactions under flowing and pressurised ammonia to examine the sorption capabilities of this system and investigate if it is possible to form additional intermediary ammoniates.

6 Summary

The data presented across Chapters 3 and 4 showed that the performance of ball-milled undoped and doped Li-Mg-N-H samples was consistent across a range of measurement techniques. The peak desorption temperatures measured across TGA-MS and DSC desorption experiments as well as the temperatures at which key phases were observed in powder XRD were in good agreement with each other. This suggests that ball-milling a batch of 5-10g produces a material that is of reliable composition, and when sampled helps to give confidence in results where it may have only been possible to carry out the reaction once due to equipment time constraints. Ball-milling removes the sample-to-sample variability that hand-grinding introduces and allows us to study reaction rates with a reduced contribution from large grain sizes and poor diffusion co-efficient.

The effects of ball-milling under different gas pressures, 1 bar argon and 100 bar hydrogen, were marked. The desorption behaviour of the samples was significantly different. This was attributed to the inability of the sample milled under 100 bar hydrogen to undergo a metathesis reaction to form $\text{Mg}(\text{NH}_2)_2$ and LiH as well as the suppression of gas release. The metathesis reaction then occurred preferentially upon heating this sample, rather than hydrogen desorption at low temperatures, around 200°C. The phase of $\text{Li}_2\text{Mg}(\text{NH})_2$ initially formed from the two ball-milled samples was different and this could also be influenced by the choice of desorption conditions, *i.e.* under flowing argon or dynamic vacuum. Low temperature desorption (150–225°C) from the sample ball-milled under 1 bar argon was dominated by the kinetic product, $\beta\text{-Li}_2\text{Mg}(\text{NH})_2$, while $\alpha\text{-Li}_2\text{Mg}(\text{NH})_2$, the thermodynamic product was the only phase observed at similar temperatures from the sample ball-milled under 100 bar hydrogen.

The results from the calcium halide doped samples were compared to the calcium borohydride doped samples examined by Li *et al.*^{90,108}. Although their absolute values of activation energies calculated from undoped ball-milled samples of $2\text{LiNH}_2 + \text{MgH}_2$ and $\text{Mg}(\text{NH}_2)_2 + 2\text{LiH}$ were higher than those seen in this work, the relative decrease observed when 0.1 mole fraction $\text{Ca}(\text{BH}_2)_4$ was added to those samples was ~5% and 16%, respectively. The relative decrease in E_a made to the $2\text{LiNH}_2 + \text{MgH}_2$ sample was similar to that observed upon the addition of 0.1 mole fraction CaCl_2 (Table 4-9), while the improvement made to the $\text{Mg}(\text{NH}_2)_2 + 2\text{LiH}$ -based sample through the addition of $\text{Ca}(\text{BH}_4)_2$ was larger than that made by the CaCl_2 (Table 4-10).

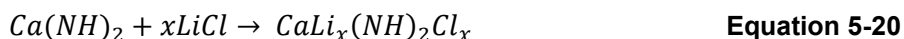
In this study, the peak hydrogen desorption temperatures of the undoped samples ball-milled under 1 bar argon, regardless of reagents, were very similar to those observed by Li *et al.*^{90,108}, 170°C vs ~180°C, respectively. A reduction of 15–20°C in the peak temperature was observed through the introduction of 0.1 mole fraction CaCl_2 or CaBr_2 relative to the undoped samples which the same as the reduction made through the addition of the same amount of $\text{Ca}(\text{BH}_4)_2$. This would indicate the desorption behaviour of these samples was similar.

The metathesis reactions in the calcium halide doped samples did not seem to occur as readily as the calcium borohydride doped samples. Two possible metathesis reactions, depending on the starting materials were suggested by Li *et al.*^{89,90} and these are shown in Equations 5-19 and 5-20. However, no evidence of LiCl and LiBr was observed which would have been expected had the reaction(s) been the same as described by Li *et al.*⁸⁸ which produced LiBH_4 .



In the $\text{Ca}(\text{BH}_4)_2$ doped samples, LiBH_4 was then found to react with LiNH_2 to form $\text{Li}_4\text{BH}_4(\text{NH}_2)_3$ which was identified as a key intermediate in the desorption process by improving

the diffusion of Li⁺ cations. Indications that a bromide analogue, Li₇(NH₂)₆Br had had been formed were observed, but no evidence of a comparable chloride phase was seen in powder XRD patterns. Several of the CaCl₂ doped patterns included an unknown F222 phase which was thought to be similar to CaNH. As a lithium-deficient lithium magnesium nitride phase was identified in many of the samples, it is possible this unknown F222 phase could be a lithium-calcium imide phase also including some chloride anions. A potential stoichiometric formation route is suggested in Equation 5-20, although its likely to be a solid solution range where a small amount of Li⁺ and Cl⁻ are substituted into Ca(NH)₂. This might suggest that Ca(NH₂)₂ was formed in transience and had already reacted after the sample was cooled back to room temperature.



. The hydrogenation capability of the calcium borohydride doped samples appeared to be better than the calcium halide doped samples. Hydrogenation of the CaBr₂-doped sample was more successful than that of the CaCl₂-doped sample, indicating that the formation of a lithium amide halide phase had likely played an important role in the hydrogenation behaviour of these samples. In-depth characterisation studies of the CaBr₂-doped system would be required to fully understand if the signs that the two halide dopants behaved slightly different were correct.

The solid-state reactions $xMgH_2$ and $(1-x)NH_4Cl$ were also examined in this work. Release of both hydrogen and ammonia was observed during the heating of these reagents together. Peaks of an unidentified phase were observed after heating to temperatures between 185–215°C, over a small range of stoichiometries ($0.33 < x < 0.583$) and initially indexed to an *I4* unit cell. The composition of this phase was found to be $Mg(NH_4)_2Cl_x$, which was iso-structural with $Mg(NH_4)_2F_4$. A Rietveld refinement was carried out and the final structure was solved to space group, *I4/mmm*, $a = 4.98256(9) \text{ \AA}$, $c = 16.1508(3) \text{ \AA}$, where $R_{wp} = 13.739$. Ammoniate halides such as $Mg(NH_3)_2Cl_2$ and $Mg(NH_6)_2Cl_2$ were also observed in the course of these reactions.

Identification of further unknown phases in this work was not successful. After attempted hydrogenation of the desorbed samples, the starting products were not observed.

This work has studied the reactions of the Li-Mg-N-H, from two sets of starting materials. The effects of preparation, desorption conditions and various dopants have all been assessed with regards to the desorption properties of these materials. Crude hydrogenation and cycling of samples has also been attempted. The results from multiple techniques provide a broad view of the behaviour of these samples under desorption conditions and demonstrate how sensitive this system is to conditions under which it is examined. Great care should be taken to control the conditions used and also when comparing results to other published work whose experimental techniques are different.

References

1. C. Hammond, *Oxford Science Publications*, 2009, The Basics of Crystallography and Diffraction (3rd Edition).
2. W. I. F. David, *Faraday Discuss.*, 2011, **151**, 399.
3. P. A. Chater, P. A. Anderson, J. W. Prendergast, A. Walton, V. S. J. Mann, D. Book, W. I. F. David, S. R. Johnson and P. P. Edwards, *J. Alloys Compd.*, 2007, **446**, 350.
4. J. Rijssenbeek, Y. Gao, J. Hanson, Q. Huang, C. Jones and B. Toby, *J. Alloys Compd.*, 2008, **454**, 233.
5. J. O. Bockris, *Environment*, 1971, **13**, 51.
6. N. A. Owen, O. R. Inderwildi and D. A. King, *Energy Policy*, 2010, **38**, 4743.
7. S. Shafiee and E. Topal, *Energy Policy*, 2009, **37**, 181.
8. D. Abbott, *Proceedings of the IEEE*, 2010, **98**, 42.
9. J. O. M. Bockris, *Int. J. Hydrogen Energy*, 2002, **27**, 731.
10. J. O. M. Bockris, *Int. J. Hydrogen Energy*, 1999, **24**, 1.
11. http://www.bmw.co.uk/en_GB/topics/discover-bmw/efficientdynamics/hydrogen.html.
12. <http://cafcp.org/>.
13. J. Eichman, J. Brouwer and S. Samuelsen, *Journal of Fuel Cell Science and Technology*, 2010, **7**, 051017.1.
14. http://www.arb.ca.gov/msprog/zevprog/ab8/ab8_report_2015.pdf.
15. T. Q. Hua, R. K. Ahluwalia, J. K. Peng, M. Kromer, S. Lasher, K. McKenney, K. Law and J. Sinha, *Int. J. Hydrogen Energy*, 2011, **36**, 3037.
16. D. J. Tranchemontagne, K. S. Park, H. Furukawa, J. Eckert, C. B. Knobler and O. M. Yaghi, *Journal of Physical Chemistry C*, 2012, **116**, 13143.
17. B. Bogdanovic and M. Schwickardi, *J. Alloys Compd.*, 1997, **253**, 1.
18. K. Tatsumi, I. Tanaka, H. Inui, K. Tanaka, M. Yamaguchi and H. Adachi, *Prism 4: Forth Pacific Rim International Conference on Advanced Materials and Processing*, Vols I and II, Sendai, 2001.
19. T. Umegaki, J.-M. Yan, X.-B. Zhang, H. Shioyama, N. Kuriyama and Q. Xu, *Int. J. Hydrogen Energy*, 2009, **34**, 2303.
20. W. I. F. David, M. O. Jones, D. H. Gregory, C. M. Jewell, S. R. Johnson, A. Walton and P. P. Edwards, *J. Am. Chem. Soc.*, 2007, **129**, 1594.
21. A. Zuttel, P. Wenger, S. Rentsch, P. Sudan, P. Mauron and C. Emmenegger, *J. Power Sources*, 2003, **118**, 1.
22. B. Peng and J. Chen, *Energy & Environmental Science*, 2008, **1**.
23. J. Graetz, *Chem. Soc. Rev.*, 2009, **38**, 73.
24. W. Osborn, T. Markmaitree, L. L. Shaw, R. Ren, J. Hu, J. H. Kwak and Z. Yang, *JOM*, 2009, **61**, 45.
25. Z. T. Xiong, J. J. Hu, G. T. Wu, P. Chen, W. F. Luo, K. Gross and J. Wang, *J. Alloys Compd.*, 2005, **398**, 235.
26. Y. Liu, K. Zhong, K. Luo, M. Gao, H. Pan and Q. Wang, *J. Am. Chem. Soc.*, 2009, **131**, 1862.

27. T. Noritake, M. Aoki, M. Matsumoto, K. Miwa, S. Towata, H. W. Li and S. Orimo, *J. Alloys Compd.*, 2011, **509**, 7553.
28. P. Chen, Z. T. Xiong, L. F. Yang, G. T. Wu and W. F. Luo, *J. Phys. Chem. B*, 2006, **110**, 14221.
29. S. Nayebossadri, *Int. J. Hydrogen Energy*, 2011, **36**, 8335.
30. K.-F. Aguey-Zinsou, J. Yao and Z. X. Guo, *J. Phys. Chem. B*, 2007, **111**, 12531.
31. H. Wu, *J. Am. Chem. Soc.*, 2008, **130**, 6515.
32. B. Li, Y. Liu, Y. Zhang, M. Gao and H. Pan, *Journal of Physical Chemistry C*, 2012, **116**, 13551.
33. J. C. Wang, H. L. Li, S. M. Wang, X. P. Liu, Y. Li and L. J. Jiang, *Int. J. Hydrogen Energy*, 2009, **34**, 1411.
34. H. Y. Leng, T. Ichikawa, S. Hino, N. Hanada, S. Isobe and H. Fujii, *J. Phys. Chem. B*, 2004, **108**, 8763.
35. T. Ichikawa, N. Hanada, S. Isobe, H. Y. Leng and H. Fujii, *J. Phys. Chem. B*, 2004, **108**, 7887.
36. S. Nayebossadri and K.-F. Aguey-Zinsou, *PCCP*, 2011, **13**, 17683.
37. C. Price, J. Gray, R. Lascola and D. L. Anton, *Int. J. Hydrogen Energy*, 2012, **37**, 2742.
38. L.-P. Ma, P. Wang, H.-B. Dai and H.-M. Cheng, *J. Alloys Compd.*, 2009, **468**, L21.
39. P. Chen, Z. T. Xiong, J. Z. Luo, J. Y. Lin and K. L. Tan, *Nature*, 2002, **420**, 302.
40. W. F. Luo, *J. Alloys Compd.*, 2004, **381**, 284.
41. D. J. Bull, N. Sorbie, G. Baldissin, D. Moser, M. T. F. Telling, R. I. Smith, D. H. Gregory and D. K. Ross, *Faraday Discuss.*, 2011, **151**, 263.
42. W. Luo and E. Ronnebro, *J. Alloys Compd.*, 2005, **404**, 392.
43. S. Isobe, T. Ichikawa, S. Hino and H. Fujii, *J. Phys. Chem. B*, 2005, **109**, 14855.
44. Y. H. Hu and E. Ruckenstein, *J. Phys. Chem. A*, 2003, **107**, 9737.
45. P. Chen, Z. T. Xiong, J. Z. Luo, J. Y. Lin and K. L. Tan, *J. Phys. Chem. B*, 2003, **107**, 10967.
46. J. Lu, Z. G. Z. Fang and H. Y. Sohn, *Inorg. Chem.*, 2006, **45**, 8749.
47. P. A. Anderson, P. A. Chater, D. R. Hewett and P. R. Slater, *Faraday Discuss.*, 2011, **151**, 271.
48. Y. Nakamori, S. Orimo and Repeated in an later paper of no use, *Mater. Sci. Eng. B-Solid State Mater. Adv. Technol.*, 2004, **108**, 48.
49. Y. Nakamori and S. Orimo, *J. Alloys Compd.*, 2004, **370**, 271.
50. Y. Nakamori, G. Kitahara and S. Orimo, *J. Power Sources*, 2004, **138**, 309.
51. Z. T. Xiong, G. T. Wu, H. J. Hu and P. Chen, *Adv. Mater.*, 2004, **16**, 1522.
52. L.-P. Ma, H.-B. Dai, Z.-Z. Fang, X.-D. Kang, Y. Liang, P.-J. Wang, P. Wang and H.-M. Cheng, *Journal of Physical Chemistry C*, 2009, **113**, 9944.
53. Y. Nakamori, G. Kitahara, K. Miwa, S. Towata and S. Orimo, *Applied Physics a-Materials Science & Processing*, 2005, **80**, 1.
54. H. Leng, T. Ichikawa and H. Fujii, *J. Phys. Chem. B*, 2006, **110**, 12964.
55. M. Aoki, T. Noritake, Y. Nakamori, S. Towata and S. Orimo, *J. Alloys Compd.*, 2007, **446**, 328.
56. J. Yang, A. Sudik, D. J. Siegel, D. Halliday, A. Drews, R. O. Carter, C. Wolverton, G. J. Lewis, J. W. A. Sachtler, J. J. Low, S. A. Faheem, D. A. Lesch and V. Ozolins, *J. Alloys Compd.*, 2007, **446**, 345.
57. Y. Liu, J. Hu, Z. Xiong, G. Wu and P. Chen, *J. Mater. Res.*, 2007, **22**, 1339.

58. S. Barison, F. Agresti, S. Lo Russo, A. Maddalena, P. Palade, G. Principi and G. Torzo, *J. Alloys Compd.*, 2008, **459**, 343.
59. W. F. Luo and S. Sicksafoose, *J. Alloys Compd.*, 2006, **407**, 274.
60. J. Yang, A. Sudik and C. Wolverton, *J. Alloys Compd.*, 2007, **430**, 334.
61. K. Hoang, A. Janotti and C. G. van de Walle, *Physical Review B*, 2012, **85**.
62. R. Janot, J.-B. Eymery and J.-M. Tarascon, *J. Power Sources*, 2007, **164**, 496.
63. K. J. Michel, A. R. Akbarzadeh and V. Ozolins, *Journal of Physical Chemistry C*, 2009, **113**, 14551.
64. D. Qin, X. Zhao, K. Zhang, J. Lu, H. Zhang and S. Xin, *Rare Metal Materials and Engineering*, 2015, **44**, 355.
65. C. Liang, Y. Liu, H. Fu, Y. Ding, M. Gao and H. Pan, *J. Alloys Compd.*, 2011, **509**, 7844.
66. Y. Chen, C.-Z. Wu, P. Wang and H.-M. Cheng, *Int. J. Hydrogen Energy*, 2006, **31**, 1236.
67. J. Lamb, D. Chandra, W. M. Chien, D. Phanon, N. Penin, R. Cerny and K. Yvon, *Journal of Physical Chemistry C*, 2011, **115**, 14386.
68. Y. Wang and M. Y. Chou, *Physical Review B*, 2007, **76**.
69. E. Weidner, F. Dolci, J. J. Hu, W. Lohstroh, T. Hansen, D. J. Bull and M. Fichtner, *Journal of Physical Chemistry C*, 2009, **113**, 15772.
70. M. Aoki, T. Noritake, G. Kitahara, Y. Nakamori, S. Towata and S. Orimo, *J. Alloys Compd.*, 2007, **428**, 307.
71. C. Liang, M. X. Gao, H. G. Pan, Y. F. Liu and M. Yan, *Int. J. Hydrogen Energy*, 2014, **39**, 17754.
72. Q. Wang, Y. Chen, C. Wu, M. Tao and J. Gai, *Chin. Sci. Bull.*, 2009, **54**, 497.
73. C. Liang, M. X. Gao, H. G. Pan and Y. F. Liu, *Appl. Phys. Lett.*, 2014, **105**.
74. J. Hu and M. Fichtner, *Chem. Mater.*, 2009, **21**, 3485.
75. Y. Nakamori, G. Kitahara, K. Miwa, N. Ohba, T. Noritake, S. Towata and S. Orimo, *J. Alloys Compd.*, 2005, **404**, 396.
76. Y. Nakamori, G. Kitahara, A. Ninomiya, M. Aoki, T. Noritake, S. Towata and S. Orimo, *Materials Transactions*, 2005, **46**, 2093.
77. Z. T. Xiong, G. T. Wu, J. J. Hu, P. Chen, W. F. Luo and J. Wang, *J. Alloys Compd.*, 2006, **417**, 190.
78. W. Luo, J. Wang, K. Stewart, M. Clift and K. Gross, *J. Alloys Compd.*, 2007, **446**, 336.
79. T. Nakagawa, T. Ichikawa, R. Iida, H. Leng, N. Takeichi, T. Kiyobayashi, H. Takeshita and H. Fujii, *J. Alloys Compd.*, 2007, **430**, 217.
80. T. Markmaitree, W. Osborn and L. L. Shaw, *Int. J. Hydrogen Energy*, 2008, **33**, 3915.
81. W. Lohstroh and M. Fichtner, *J. Alloys Compd.*, 2007, **446**, 332.
82. R. R. Shahi, T. P. Yadav, M. A. Shaz and O. N. Srivastava, *Int. J. Hydrogen Energy*, 2008, **33**, 6188.
83. J. Wang, T. Liu, G. Wu, W. Li, Y. Liu, C. M. Araujo, R. H. Scheicher, A. Blomqvist, R. Ahuja, Z. Xiong, P. Yang, M. Gao, H. Pan and P. Chen, *Angewandte Chemie-International Edition*, 2009, **48**, 5828.
84. T. Durojaiye and A. Goudy, *Int. J. Hydrogen Energy*, 2012, **37**, 3298.
85. J. Wang, J. Hu, Y. Liu, Z. Xiong, G. Wu, H. Pan and P. Chen, *J. Mater. Chem.*, 2009, **19**, 2141.

86. M. Matsuo, T. Sato, Y. Miura, H. Oguchi, Y. Zhou, H. Maekawa, H. Takamura and S. Orimo, *Chem. Mater.*, 2010, **22**, 2702.
87. M. Matsuo, A. Remhof, P. Martelli, R. Caputo, M. Ernst, Y. Miura, T. Sato, H. Oguchi, H. Maekawa, H. Takamura, A. Borgschulte, A. Züttel and S. Orimo, *J. Am. Chem. Soc.*, 2009, **131**, 16389.
88. J. Zhang and Y. H. Hu, *Industrial & Engineering Chemistry Research*, 2011, **50**, 8058.
89. B. Li, Y. F. Liu, C. Li, M. X. Gao and H. G. Pan, *J. Mat. Chem. A*, 2014, **2**, 3155.
90. B. Li, Y. F. Liu, J. Gu, Y. J. Gu, M. X. Gao and H. G. Pan, *Int. J. Hydrogen Energy*, 2013, **38**, 5030.
91. H. Y. Leng, Z. Wu, W. Y. Duan, G. L. Xia and Z. L. Li, *Int. J. Hydrogen Energy*, 2012, **37**, 903.
92. H. J. Cao, H. Wang, T. He, G. T. Wu, Z. T. Xiong, J. S. Qiu and P. Chen, *Rsc Advances*, 2014, **4**, 32555.
93. N. S. Gamba, P. A. Larochette and F. C. Gennari, *Rsc Advances*, 2015, **5**, 68542.
94. J. Yang, D. Li, H. Fu, G. Xin, J. Zheng and X. Li, *PCCP*, 2012, **14**, 2857.
95. J. Yang, A. Sudik, D. J. Siegel, D. Halliday, A. Drews, R. O. Carter, C. Wolverton, G. J. Lewis, J. W. A. Sachtler, J. J. Low, S. A. Faheem, D. A. Lesch and V. Ozolins, *Angewandte Chemie-International Edition*, 2008, **47**, 882.
96. A. Sudik, J. Yang, D. J. Siegel, C. Wolverton, R. O. Carter, III and A. R. Drews, *Journal of Physical Chemistry C*, 2009, **113**, 2004.
97. A. Sudik, J. Yang, D. Halliday and C. Wolverton, *Journal of Physical Chemistry C*, 2008, **112**, 4384.
98. J. Hu, M. Fichtner and P. Chen, *Chem. Mater.*, 2008, **20**, 7089.
99. J. Hu, Y. Liu, G. Wu, Z. Xiong, Y. S. Chua and P. Chen, *Chem. Mater.*, 2008, **20**, 4398.
100. J. Hu, E. Weidner, M. Hoelzel and M. Fichtner, *Dalton Trans.*, 2010, **39**, 9100.
101. G. Amica, F. Cova, P. Arneodo Larochette and F. C. Gennari, *PCCP*, 2016, **18**, 17997.
102. P. A. Chater, W. I. F. David, S. R. Johnson, P. P. Edwards and P. A. Anderson, *Chem. Commun.*, 2006, 2439.
103. Y. Liu, Z. Xiong, J. Hu, G. Wu, P. Chen, K. Murata and K. Sakata, *J. Power Sources*, 2006, **159**, 135.
104. C. Li, Y. F. Liu, Y. P. Pang, Y. J. Gu, M. X. Gao and H. G. Pan, *Dalton Trans.*, 2014, **43**, 2369.
105. W. Luo, V. Stavila and L. E. Klebanoff, *Int. J. Hydrogen Energy*, 2012, **37**, 6646.
106. T. Durojaiye, J. Hayes and A. Goudy, *Int. J. Hydrogen Energy*, 2015, **40**, 2266.
107. C. Liang, Y. Liu, Y. Jiang, Z. Wei, M. Gao, H. Pan and Q. Wang, *PCCP*, 2011, **13**, 314.
108. B. Li, Y. F. Liu, J. Gu, M. X. Gao and H. G. Pan, *Chem.-Asian J.*, 2013, **8**, 374.
109. M. O. Jones, D. M. Royse, P. P. Edwards and W. I. F. David, *Chem. Phys.*, 2013, **427**, 38.
110. <http://cnx.org/content/m16927/latest/>.
111. C. Whiston and F. E. Prichard, *X-Ray Methods*, John Wiley & Sons., 1987.
112. R. Jenkins and R. Snyder, *Introduction to X-ray powder diffractometry*, Wiley-Interscience, 1996.

113. V. Pecharsky and P. Z. Zavaliij., *Fundamentals of Powder Diffraction and Structural Characterization of Materials* 2nd Edition edn., Springer, 2009.
114. <http://pd.chem.ucl.ac.uk/pdnn/diff2/kinemat2.htm>.
115. B. H. Toby, *Powder Diffr.*, 2006, **21**, 67.
116. W. I. F. David, *Journal of Research of the National Institute of Standards and Technology*, 2004, **109**, 107.
117. R. A. Young, *The Rietveld Method*, Oxford University Press, 1995.
118. B. A. Arkady Buman, *Building Material Characterization by X-Ray Methods*.
119. A. A. Coelho, Editon edn., 2007.
120. A. J. Churchard, E. Banach, A. Borgschulte, R. Caputo, J. C. Chen, D. C. Clary, K. J. Fijalkowski, H. Geerlings, R. V. Genova, W. Grochala, T. Jaron, J. C. Juanes-Marcos, B. Kasemo, G. J. Kroes, I. Ljubic, N. Naujoks, J. K. Norskov, R. A. Olsen, F. Pendolino, A. Remhof, L. Romaszki, A. Tekin, T. Vegge, M. Zach and A. Zuttel, *PCCP*, 2011, **13**, 16955.
121. H. Pan, S. Shi, Y. Liu, B. Li, Y. Yang and M. Gao, *Dalton Trans.*, 2013, **42**, 3802.
122. Z. T. Xiong, J. J. Hu, G. T. Wu and P. Chen, *J. Alloys Compd.*, 2005, **395**, 209.
123. R. A. Varin, R. Parviz, M. Polanski and Z. S. Wronski, *Int. J. Hydrogen Energy*, 2014, **39**, 10585.
124. R. Parviz and R. A. Varin, *Int. J. Hydrogen Energy*, 2013, **38**, 8313.
125. C. Liang, Y. Liu, K. Luo, B. Li, M. Gao, H. Pan and Q. Wang, *Chemistry-a European Journal*, 2010, **16**, 693.
126. H. J. Cao, J. H. Wang, Y. S. Chua, H. Wang, G. T. Wu, Z. T. Xiong, J. S. Qiu and P. Chen, *Journal of Physical Chemistry C*, 2014, **118**, 2344.
127. X. Y. Zhao, K. Zhang, Z. Q. Cao, J. Lu, H. B. Zhang, S. G. Xin and H. Zhang, *Rare Metal Materials and Engineering*, 2014, **43**, 395.
128. H. Miyaoka, Y. M. Wang, S. Hino, S. Isobe, K. Tokoyoda, T. Ichikawa and Y. Kojima, *Materials*, 2015, **8**, 3896.
129. A. Dunst, V. Epp, I. Hanzu, S. A. Freunberger and M. Wilkening, *Energy & Environmental Science*, 2014, **7**, 2739.
130. W. Li, G. Wu, Z. Xiong, Y. P. Feng and P. Chen, *PCCP*, 2012, **14**, 1596.
131. T. F. Zhang, S. Isobe, M. Matsuo, S. Orimo, Y. M. Wang, N. Hashimoto and S. Ohnuki, *Acs Catalysis*, 2015, **5**, 1552.
132. D. Pottmaier, F. Dolci, M. Orlova, G. Vaughan, M. Fichtner, W. Lohstroh and M. Baricco, *J. Alloys Compd.*, 2011, **509**, S719.
133. A. Sudik, J. Yang, D. Halliday and C. Wolverton, *Journal of Physical Chemistry C*, 2007, **111**, 6568.
134. K. Ohoyama, Y. Nakamori, S. Orimo and K. Yamada, *J. Phys. Soc. Jpn.*, 2005, **74**, 483.
135. H. Jacobs and R. Juza, *Z. Anorg. Allg. Chem.*, 1972, **391**, 271.
136. R. Juza and K. Opp, *Z. Anorg. Allg. Chem.*, 1951, **266**, 325.
137. J. Hu, Z. Xiong, G. Wu, P. Chen, K. Murata and K. Sakata, *J. Power Sources*, 2006, **159**, 116.
138. Y. Kojima and Y. Kawai, *J. Alloys Compd.*, 2005, **395**, 236.
139. R. Davies, University of Birmingham, 2016.
140. B. Paik, H. W. Li, J. H. Wang and E. Akiba, *Chem. Commun.*, 2015, **51**, 10018.
141. L. Xie, Y. Liu, G. Li and X. Li, *Journal of Physical Chemistry C*, 2009, **113**, 14523.
142. H. E. Kissinger, *Anal. Chem.*, 1957, **29**, 1702.

143. F. Torre, A. Valentoni, C. Milanese, C. Pistidda, A. Marini, M. Dornheim, S. Enzo, G. Mulas and S. Garroni, *J. Alloys Compd.*, 2015, **645**, S284.
144. A. S. Bailey, P. Hubberstey, R. W. Hughes, C. Ritter and D. H. Gregory, *Chem. Mater.*, 2010, **22**, 3174.
145. S. Isobe, T. Ichikawa, H. Leng, H. Fujii and Y. Kojima, *J. Phys. Chem. Solids*, 2008, **69**, 2234.
146. Y. Liu, K. Zhong, M. Gao, H. Wang, H. Pan and Q. Wang, *Chem. Mater.*, 2008, **20**, 3521.
147. B. Hughes, University of Birmingham, Editon edn., 2016.
148. G. Linde and R. Juza, *Z. Anorg. Allg. Chem.*, 1974, **409**, 199.
149. R. Juza and E. Eberius, *Naturwissenschaften*, 1962, **49**, 104.
150. J. Hu, Y. Liu, G. Wu, Z. Xiong and P. Chen, *Journal of Physical Chemistry C*, 2007, **111**, 18439.
151. W. Osborn, T. Markmaitree and L. L. Shaw, *J. Power Sources*, 2007, **172**, 376.
152. Y. Liu, C. Liang, Z. Wei, Y. Jiang, M. Gao, H. Pan and Q. Wang, *PCCP*, 2010, **12**, 3108.
153. R. Juza, *Angewandte Chemie International Edition in English*, 1964, **3**, 471.
154. R. D. Shannon, *Acta Crystallographica Section A*, 1976, **32**, 751.
155. Y. Liu, J. Hu, Z. Xiong, G. Wu, P. Chen, K. Murata and K. Sakata, *J. Alloys Compd.*, 2007, **432**, 298.
156. L. Zeng, H. Miyaoka, T. Ichikawa and Y. Kojima, *J. Alloys Compd.*, 2013, **580**, S320.
157. Y. Liu, C. Li, B. Li, M. Gao and H. Pan, *Journal of Physical Chemistry C*, 2013, **117**, 866.
158. T. Sichla and H. Jacobs, *Z. Anorg. Allg. Chem.*, 1996, **622**, 2079.
159. K. Tokoyoda, T. Ichikawa and H. Miyaoka, *Int. J. Hydrogen Energy*, 2015, **40**, 1516.
160. S. Isobe, T. Ichikawa, K. Tokoyoda, N. Hanada, H. Leng, H. Fujii and Y. Kojima, *Thermochim. Acta*, 2008, **468**, 35.
161. K. Tokoyoda, S. Hino, T. Ichikawa, K. Okamoto and H. Fujii, *J. Alloys Compd.*, 2007, **439**, 337.
162. S. Hino, T. Ichikawa, H. Y. Leng and H. Fujii, *J. Alloys Compd.*, 2005, **398**, 62.
163. R. A. Davies and P. A. Anderson, *Int. J. Hydrogen Energy*, 2015, **40**, 3001.
164. R. A. Davies, D. R. Hewett, E. Korciakoski, S. P. Thompson and P. A. Anderson, *J. Alloys Compd.*, 2015, **645**, S343.
165. F. Sun, M. Y. Yan, X. P. Liu, J. H. Ye, Z. N. Li, S. M. Wang and L. J. Jiang, *Int. J. Hydrogen Energy*, 2015, **40**, 6173.
166. Y. Nakamura, S. Hino, T. Ichikawa, H. Fujii, H. W. Brinks and B. C. Hauback, *J. Alloys Compd.*, 2008, **457**, 362.
167. F. Dolci, E. Napolitano, E. Weidner, S. Enzo, P. Moretto, M. Brunelli, T. Hansen, M. Fichtner and W. Lohstroh, *Inorg. Chem.*, 2011, **50**, 1116.
168. R. Nagel, T. W. Gross, H. Gunther and H. D. Lutz, *J. Solid State Chem.*, 2002, **165**, 303.
169. N. S. Gamba, P. Arneodo Larochette and F. C. Gennari, *Rsc Advances*, 2016, **6**, 15622.
170. P. Bouclier, J. Portier and G. Turrell, *J. Mol. Struct.*, 1969, **4**, 1.
171. J. Hu, Z. Xiong, G. Wu, P. Chen, K. Murata and K. Sakata, *J. Power Sources*, 2006, **159**, 120.

172. Y. F. Liu, T. Liu, Z. T. Xiong, J. J. Hu, G. T. Wu, P. Chen, A. T. S. Wee, P. Yang, K. Murata and K. Sakata, *Eur. J. Inorg. Chem.*, 2006, 4368.
173. H. Chu, Z. Xiong, G. Wu, T. He, C. Wu and P. Chen, *Int. J. Hydrogen Energy*, 2010, **35**, 8317.
174. T. Markmaitree and L. L. Shaw, *J. Power Sources*, 2010, **195**, 1984.
175. J. W. Makepeace, H. M. A. Hunter, T. J. Wood, R. I. Smith, C. A. Murray and W. I. F. David, *Faraday Discuss.*, 2016, **188**, 525.
176. B. Bogdanovic and B. Spliethoff, *Int. J. Hydrogen Energy*, 1987, **12**, 863.
177. J. Huot, G. Liang, S. Boily, A. Van Neste and R. Schulz, *J. Alloys Compd.*, 1999, **293**, 495.
178. K. Tokoyoda, S. Hino, T. Ichikawa, K. Okamoto and H. Fujii, *J. Alloys Compd.*, 2007, **439**, 337.
179. L. B. McCusker, R. B. Von Dreele, D. E. Cox, D. Louer and P. Scardi, *J. Appl. Crystallogr.*, 1999, **32**, 36.
180. L. X. Li and J. A. Hurley, *Int. J. Hydrogen Energy*, 2007, **32**, 6.
181. A. Leineweber, M. W. Friedriszik and H. Jacobs, *J. Solid State Chem.*, 1999, **147**, 229.
182. M. Tsubota, S. Hino, H. Fujii, C. Oomatsu, M. Yamana, T. Ichikawa and Y. Kojima, *Int. J. Hydrogen Energy*, 2010, **35**, 2058.
183. Y. Liu, R. Ma, R. Luo, K. Luo, M. Gao and H. Pan, *Materials Transactions*, 2011, **52**, 627.
184. C. H. Christensen, R. Z. Sorensen, T. Johannessen, U. J. Quaade, K. Honkala, T. D. Elmoe, R. Kohler and J. K. Nørskov, *J. Mater. Chem.*, 2005, **15**, 4106.
185. H. L. Zhu, X. Y. Gu, K. H. Yao, L. H. Gao and J. J. Chen, *Industrial & Engineering Chemistry Research*, 2009, **48**, 5317.
186. R. E. Marsh, *Acta Crystallographica Section C-Crystal Structure Communications*, 1991, **47**, 1775.
187. H. Reardon, J. M. Hanlon, M. Grant, I. Fullbrook and D. H. Gregory, *Crystals*, 2012, **2**, 193.
188. F. T. Holmes, *J. Chem. Phys.*, 1936, **4**, 88.
189. A. L. Kersting, University of Birmingham, 2012.
190. J. R. Hattrick-Simpers, J. E. Maslar, M. U. Niemann, C. Chiu, S. S. Srinivasan, E. K. Stefanakos and L. A. Bendersky, *Int. J. Hydrogen Energy*, 2010, **35**, 6323.
191. C. Perchard and A. Novak, *Spectrochimica Acta Part A: Molecular Spectroscopy*, 1970, **26**, 871.
192. A. A. Coelho, *J. Appl. Crystallogr.*, 2003, **36**, 86.
193. P. A. Chater, W. I. F. David and P. A. Anderson, *Chem. Commun.*, 2007, 4770.
194. A. A. Coelho, *Technical Reference, Topas Academic V4.1*, A. A. Coelho, 2007.
195. A. Nagele, K. Gibson, J. Glaser and H. J. Meyer, *Z. Anorg. Allg. Chem.*, 1999, **625**, 1940.
196. D. Miura and T. Tezuka, *Energy*, 2014, **68**, 428.
197. R. Farasat, B. Yancey and S. Vyazovkin, *Journal of Physical Chemistry C*, 2013, **117**, 13713.
198. T. D. Elmoe, R. Z. Sorensen, U. Quaade, C. H. Christensen, J. K. Nørskov and T. Johannessen, *Chem. Eng. Sci.*, 2006, **61**, 2618.
199. V. S. Jayakumar, G. Sekar, P. Rajagopal and G. Aruldas, *physica status solidi (a)*, 1988, **109**, 635.

List of Publications

R. F. Bill, D. Reed, D. Book, P.A. Anderson, *Journal of Alloys and Compounds*. 2015, **645**, S96-S99

Title: Effect of the calcium halides, CaCl₂ and CaBr₂, on hydrogen desorption in the Li-Mg-N-H system